COMPUTATIONAL STUDY OF ADSORPTION AND DIFFUSION IN METAL-ORGANIC FRAMEWORKS

BABARAO RAVICHANDAR

(M.Tech., NIT, India)

A THESIS SUBMITTED

FOR THE DEGREE OF DOCTOR OF PHILOSOPHY

DEPARTMENT OF CHEMICAL AND BIOMOLECULAR ENGINEERING

NATIONAL UNIVERSITY OF SINGAPORE

2009

Acknowledgement

First of all, I would like to extend my sincerest and deepest gratitude to my supervisor Prof. Jiang Jianwen. His constant help, stimulating suggestions and encouragement from the initial to the final stage have enabled me to develop a good understanding of the subject. His enthusiasm, positive outlook and belief in my abilities have helped me go through the difficult phases of research.

I would like to extend my thanks to all the members in Prof. Jiang's research group for their invaluable suggestions, discussions and sharing of technical expertise since the beginning of my PhD study. I also wish to thank Dr. Shaji Chempath for his help during the initial phase of research. My special appreciation is due to Prof. Stanley I. Sandler from the University of Delaware for his comments and suggestions on my research papers.

I would also like to convey my thanks to Prof. Mario S. C. Mazzoni for kindly providing the structure of covalent-organic framework nanotube. My appreciations are due to Prof. Mohamed Eddaoudi and Prof. Yunling Liu for their helpful discussions on the crystallographic structure of zeolite-like metal-organic frameworks.

I would also like to express my sincere thanks to National University of Singapore for providing me the research scholarship.

Finally, I am deeply indebted to my parents and my wife for their love, support and encouragement during my PhD study.

TABLE OF CONTENTS

Summary

Adsorption and diffusion in nanoporous materials lie at the heart of many large-scale industrial applications such as gas separation, storage and selective catalysis. As the number of nanoporous materials to date is extremely large, selecting a promising material from discovery to applications is a challenge. The development of particular technological applications for nanoporous materials requires the fundamental understanding of their microscopic properties. In this sense, computational study plays an important complementary role to experiments by making predictions prior to experimental studies. The selection of a suitable adsorbent is a key step in the design of adsorption-based storage or separation processes. While most studies have focused on zeolites and carbon-based adsorbents, a new class of hybrid materials has been recently developed, i.e. metal-organic frameworks (MOFs) which consist of metal-oxide clusters and organic linkers. MOFs allow the formation of tunable porous frameworks with a wide variety of architectures, topologies and pore sizes. Because of their high porosity and well-defined pore size, MOFs are promising candidates for the storage and separation of gases, ion-exchanges, catalysis, sensing, etc.

In this thesis, molecular simulation techniques such as Monte Carlo and molecular dynamics have been used to elucidate the adsorption and diffusion phenomena of fluids in a wide variety of MOFs.

(1) The adsorption and diffusion of CO_2 and CH_4 were examined in three different nanoporous materials (silicalite, C_{168} schwarzite, and IRMOF-1). IRMOF-1 has a significantly higher adsorption capacity for CO_2 and CH_4 than silicalite and C_{168} schwarzite, however the adsorption selectivity of CO_2 over CH_4 was found to be similar in all the three adsorbents. The permselectivity was calculated based on the adsorption and diffusion selectivity of the mixture, and found to be marginal in

IRMOF-1, slightly enhanced in MFI, and greatest in C_{168} schwarzite. Although IRMOF-1 has the largest storage capacity for CH_4 and CO_2, its selectivity is not satisfactory.

(2) CO_2 storage in a series of MOFs was studied with different characteristics. In addition, covalent-organic frameworks (COFs), a sub-set of MOFs were also considered. Organic linker was revealed to play a critical role in tuning the free volume and accessible surface area, and subsequently determines CO_2 adsorption at high pressures. Due to low framework density and high porosity, COF-105 and COF-108 exhibit the highest storage capacity among the adsorbents studied and even surpass the experimentally reported highest capacity in MOF-177. COF-102 and COF-103 are promising materials with high capacity at low pressures. The gravimetric and volumetric capacity of CO_2 at a moderate pressure correlates well with the framework density, free volume, porosity and accessible surface area of both MOFs and COFs. These correlations are useful for a priori prediction of CO_2 capacity and for the rational screening of MOFs and COFs toward high-performance CO_2 storage.

(3) The adsorption and separation of CO_2/CH_4 mixture were studied in a series of metal-organic frameworks (MOFs) with unique characteristics such as exposed metals (Cu-BTC, PCN-6′ and PCN-6), catenation (IRMOF-13 and PCN-6) and extra-framework ions (*soc*-MOF). The framework catenation leads to constricted pores and additional adsorption sites, and enhances the interaction with the adsorbate. Therefore, catenated IRMOF-13 and PCN-6 exhibit a greater extent of adsorption, particularly for CO_2 at low pressures compared to IRMOF-14 and PCN-6′; however, the opposite was observed to be true at high pressures. It was found that catenated MOFs have a higher selectivity than their non-catenated counterparts. Much higher

selectivity is observed in charged soc-MOF compared with other IRMOFs and PCN structures.

For the first time, the extra-framework ions were characterized and gas separation was examined in a charged MOF, *rho*-ZMOF, with anionic framework. In *rho*-ZMOF, the presence of highly ionic framework enhances the CO_2 capacity at low pressure and in turn increases adsorption selectivity. The selectivity was ~ 1800 for CO_2/H_2, 80 for CO_2/CH_4, and 500 for CO_2/N_2 mixtures. Compared with other MOFs and nanoporous materials reported to date, *rho*-ZMOF exhibits unprecedentedly high selective adsorption for gas mixtures.

(4) The effect of catenation on the separation of alkane isomers mixture was simulated. Competitive adsorption between isomers was observed, particularly at high pressures, in which a linear isomer shows a larger extent of adsorption due to configurational entropy. It was found that both adsorption and diffusion selectivities can be enhanced by catenation, particularly at low pressures.

(5) The microscopic properties of a model drug, ibuprofen, were studied in mesoporous MIL-101 and UMCM-1 based on molecular simulation and first-principle calculations. The loading capacity of ibuprofen in MIL-101 and UMCM-1 is about four times greater than in MCM-41. A coordination bond between the carboxylic group of ibuprofen and the exposed metal site of MIL-101 was observed. In addition, ibuprofen exhibits a smaller mobility in MIL-101 than in UMCM-1 due to strong interaction with the framework.

As a relatively new class of materials, MOFs will continue to attract extensive interest in both academia and industry. They exhibit high potential for adsorptive storage in energy applications as well as separation and purification in industrial applications as illustrated in this thesis.

Nomenclature

σ	collision diameter, Å
$\varepsilon / k_{\mathrm{B}}$	potential well depth, K
q	partial charge
N_{ab}, <N>	absolute adsorption, mmol/g or mmol/cm^3
N_{ex}	excess adsorption, mmol/g or mmol/cm^3
T	temperature, K
V	volume of the system, cm^3
μ	chemical potential
V_{total}	total volume of the adsorbent, cm^3
U_{ad}, U_{total}	total adsorption energy , kJ/mol
U^{o}_{total}	total adsorption energy of a single gas molecule , kJ/mol
U_{intra}	intramolecular energy , kJ/mol
U^{o}_{intra}	intramolecular energy of a single gas molecule , kJ/mol
k_B	boltzmann constant, 1.38066 × 10^{-23} J/K
u^{He}_{ad}	interaction energy between helium and adsorbent, K
q_{st}	isosteric heat , kJ/mol
q^{0}_{st}	isosteric heat at infinite dilution , kJ/mol
K_{H}	Henry's constant, mmol/g/kPa
ρ_{b}	bulk density, g/cm^3
f	fugacity, kPa
f^{o}	fugacity of pure component in standard state, kPa
N_i	maximum loading in site *i*, mmol/g
k_i	affinity constant
P	bulk pressure, kPa
y	mole fraction in gas phase
x	mole fraction in adsorbed phase
ϕ_i	fugacity coefficient of component *i*
γ_i	activity coefficient of component *i*
$D(0)$	diffusivity at infinite dilution, m^2/s

D_f	prefactor, m^2/s
E_a	activation energy, kJ/mol
R	gas constant
D_s	self-diffusivity, kJ/mol
D_c	corrected-diffusivity, kJ/mol
D_t	transport-diffusivity, kJ/mol
Γ	thermodynamic factor
$Đ_i$	maxwell-stefan diffusivity, m^2/s
θ_i	fractional loading of species *i*
Θ_i	loading of species *i*
$\Theta_{i,sat}$	saturation loading of species *i*
$Đ_{ii}^{corr}$	self-exchange coefficient, m^2/s
$Đ_{ij}^{corr}$	binary-exchange coefficient, m^2/s
S_{perm}	permselectivity
S_{diff}	diffusion selectivity
S_{sorp}	sorption selectivity
ρ_f	framework density, g/cm^3
V_{free}	free volume of the adsorbent, cm^3/g
ϕ	porosity of the adsorbent
A_{surf}	surface area of the adsorbent, m^2/g
S	selectivity
k_θ / k_B	bending constant , K/rad^2
θ_o	equilibrium angle
U_{internal}	internal energy, K
U_{external}	external energy, K
E_{bind}	binding energy, kJ/mol
E_{vib}^0	zero-point vibrational energy at 0 K
E_{elec}^0	electronic energy at 0 K

E_{rot}	rotational energy
E_{trans}	translational energy
g (r)	radial distribution function
t	time, ps
h	planck constant (6.62608×10^{-34} J·S)
wt %	weight percentage

Abbreviations

SBU	Secondary Building Unit
MOF-*n*	Metal Organic Framework (with *n* an integer assigned in roughly chronological order)
IRMOF-*n*	Isoreticular Metal Organic Framework (with *n* an integer referring to a member of the series)
MIL-*n*	Materials of Institut Lavoisier (with *n* an integer assigned in roughly chronological order)
UMCM	University of Michigan Crystalline Material
COF-*n*	Covalent Organic Framework (with *n* an integer assigned in roughly chronological order)
ZIF-*n*	Zeolitic Imidazolate Framework (with *n* an integer assigned in roughly chronological order)
TIF-*n*	Tetrahedral-Imidazolate Framework (with *n* an integer assigned in roughly chronological order)
BIF-*n*	Boron-Imidazolate Framework (with *n* an integer assigned in roughly chronological order)
ZMOFs	Zeolite-like Metal Organic Frameworks
TBUs	Tetrahedral Building Units
BDC	Benzene Dicarboxylate
BTC	Benzene Tricarboxylate
BPDC	BiPhenyl DiCarboxylate
PDC	Pyrene DiCarboxylate
DoE	Department of Energy
MMOFs	Microporous Metal Organic Materials

SWNT	Single Walled Carbon Nanotube
NOTT-*nnn*	NOTTingam (with *nnn* an integer assigned in roughly chronological order)
PCN-*n*	Porous Coordination Network (with *n* an integer assigned in roughly chronological order)
MC	Monte Carlo
MD	Molecular Dynamics
EMD	Equilibrium Molecular Dynamics
GCMC	Grand Canonical Monte Carlo
CB-GCMC	Configurational-Bias Grand Canonical Monte Carlo
GEMC	Gibbs Ensemble Monte Carlo
MP2	Møller-Plesset
TZVPP	Triple Zeta Valence Plus Polarization
QZVPP	Quadrupole Zeta Valence Plus Polarization
DFT	Density Functional Theory
LDA	Local-Density Approximation
GGA	Generalized Gradient Approximation
B3LYP	Becke's three parameter, Lee, Yang and Parr
OPLS	Optimized Potential for Liquid Simulations
FF	Force Field
UFF	Universal Force Field
IAST	Ideal Adsorbed Solution Theory
UA	United Atom
AA	All Atom
LJ	Lennard-Jones
LB	Lorentz-Berthelot
MM	Molecular Mechanics
MMFF	Merck Molecular Force Field
AMBER	Assisted Model-Building with Energy Refinement
MS	Maxwell-Stefan
ESP	ElectroStatic Potential
RESP	Restrained ElectroStatic Potential
CHELPG	CHarges from ELectrostatic Potentials using Grid

TraPPE	Transferrable Potentials for Phase Equlibria
EoS	Equation of State
MUSIC	MUlti purpose SImulation Code
DSLF	Dual-Site Langmuir Freundlich
QENS	Quasi Electron Neutron Scattering
WMO	World Meterological Organization
IPCC	Intergovernmental Panel on Climate Change
MFI	Mobil FIve
ZSM-5	Zeolite Socony Mobil
MCM-41	Mobil Composition of Matter
1D,2D,3D	One-Dimension, Two-Dimension, Three-Dimension
soc	Square OCtahedral
ImDC	IMidazolate DiCarboxylate
D8R	Double eight Ring
S8R	Single eight Ring
FH	Feynman-Hibbs
PI	Path Integral
TIP3P	Three Point Transferable Interaction Potential
MSD	Mean Squared Displacement
ETS	Engelhard TitanoSilicate
IBU	IBUprofen
HOMO	Highest Occupied Molecular Orbitals

LIST OF FIGURES

LIST OF TABLES

Chapter 1

Introduction

1.1 Development of Metal-Organic Frameworks

Porous materials are of scientific and technological interest because of their ability to interact with atoms, ions and molecules not only at their surfaces, but also throughout the bulk region. The applications of porous materials thus involve storage, separation, ion exchange, catalysis, etc. Many of these benefit from the pore structures in the materials. The pores are classified according to their sizes: pore sizes in the range of 2 nm and below are called micropores, those in the range of 2 nm to 50 nm are mesopores, and those above 50 nm are macropores. The pore sizes, shapes and volumes in porous materials directly govern their ability for desired function in a particular application. For example, a material with uniform micropores such as zeolite can separate molecules on the basis of their sizes by selectively sieving small molecule from large one [1]. However, inorganic zeolites exist in limited number of structures because of the difficulty in tuning tetrahedral building blocks.

Recently a different approach to prepare porous solids involves the coordination of metal ions to organic 'linker' moieties, thus yielding open framework structures. In fact, these materials have a long history and the earlier examples include transition metal cyanide compounds (Hofmann-type clathrates, Prussian-Blue type structures and Werner complexes). The open frameworks comprising metal–organic units gained renewed considerable interest in 1990s, but the inability of these solids to maintain permanent porosity and avoid structural rearrangements upon guest removal or guest exchange has been a shortcoming [1]. However, metal–organic frameworks

(MOFs), also knows as coordination polymers with permanent porosity have been developed [2,3]. The functionalization or incorporation of organic groups produces a wide variety of MOFs that contain different groups capable of binding guests and/or catalyzing reactions. Unique application possibilities arise from the ability to exploit the building blocks in MOFs to the design of unusual physicochemical properties such as redox potentials, light absorption and magnetic moments. As such, several thousand different MOFs have been synthesized. Compared to other solid-state matters such as zeolites, carbons and oxides, a number of MOFs are known to exhibit high framework flexibility and shrinkage/expansion due to interaction with guest molecules [4]. One of the most striking differences to traditional inorganic materials is probably the total lack of non-accessible bulk volume in MOF structures. It is the absence of dead volume in MOFs that leads to the high porosities and surface areas. A combination of so far unreached porosities, surface areas, pore sizes and also their potential applications in gas storage, separation, catalysis and many other areas [4] have attracted tremendous interest in MOFs inform both academia and industry. A comprehensive review on possible applications of MOFs were recently reported [4-6].

MOFs offer many interesting and promising features over other materials including

- record high surface area
- ultimate porosity with absence of blocked volume
- combined flexible and robust frameworks
- exposure of metal sites
- high mobility of guest species in regular framework nanopores
- fast growing number of novel inorganic-organic chemical compositions

Preparing a porous structure containing vacant space is a mediocre over decades and it is a formidable task to synthesize compounds containing void as nature abhors a vacuum [4]. Hence the pores are usually filled with guest molecules. The nature of the porous structure depends on the way the guest molecules assemble inside the structure and also on their exchange ability with other molecules. However, MOFs can be conceptually designed and assembled based on how building blocks come together to form a net, termed as reticular synthesis by Yaghi [7]. Based on the design strategy of reticular chemistry, a strategy that exploits secondary building units (SBU) [8] as molecular polygons or polyhedra, different MOFs was proposed. Eddaoudi et al. [8] described the secondary building unit (SBU) as metal complexes and cluster entities, in which the ligand coordination nodes and metal coordination environments could be utilized in the transformation of these fragments into various extended porous networks using polytopic linkers. This in turn leads to the design and synthesis of a new class of porous materials with robust structures and high porosity. Moreover, the structure and properties of MOFs can be readily tuned by the judicious choice of metal-oxides and organic linkers. This advantage of tunability is not present in traditional zeolites, in which the pores are confined by rigid tetrahedral oxide skeletons. MOFs are typically synthesized by a self-assembly reaction between various linkers and metal ions under mild conditions. Eddaoudi et al. [2] developed a series of MOFs from the prototype MOF-5 [3] by functionalizing the organic linkers with different groups and expanding its pore size by longer linkers. The resulting 16 highly crystalline materials are as shown in Figure 1.1. They studied CH_4 storage capacity in these MOFs at pressures up to 38 atm at room temperature.

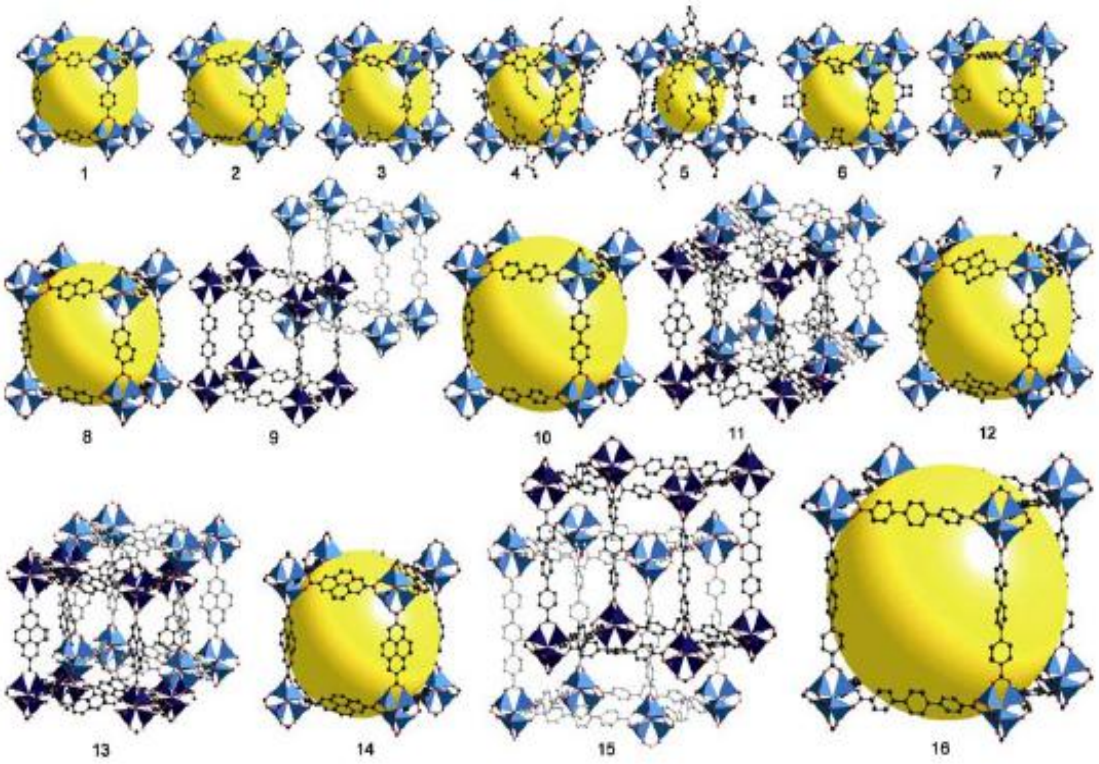

Figure 1.1 Single crystal x-ray structures of IRMOF-n (n=1 to 16), labeled respectively. Color scheme is as follows: Zn (blue polyhedra), O (red spheres), C (black spheres), Br (green spheres in **2**), amino-groups (blue spheres in **3**). The large yellow spheres represent the largest van der Waals spheres that would fit in the cavities without touching the frameworks. All hydrogen atoms have been omitted, and only one orientation of disordered atoms is shown for clarity. Reprinted with permission from [2]. Copyright (2002) American Association for the Advancement of Science. (Appendix A)

As metal sites play a central role in the vast majority of molecular recognition processes, Chen et al. reported the presence of open metal sites by single-crystal X-ray diffraction analysis in a crystalline MOF [9]. The 3D crystalline MOF named as MOF-11 was formed from copolymerization of inorganic square cluster with an organic adamantine tetrahedral cluster, consisting of 3-D channel filled with guest water molecules. Several chiral porous MOFs were synthesized based on chiral ligands for enantioselective applications. As most of the MOFs contain transition elements, new MOFs were developed based on lanthanide elements due to their high coordination number with specific magnetic and luminescence properties [10-12]. The structure of enclathrated water can be an important parameter in understanding the

mechanism of formation of different MOFs. Bharadwaj and co-workers [13-21] examined the stable conformation of different isomers of water cluster in various MOFs. A very large number of MOFs with various pore size, topology and functionality have been synthesized over the years. Figure 1.2 shows the number of MOFs structures reported in Cambridge Structural Database (CSD) from 1978 through 2006.

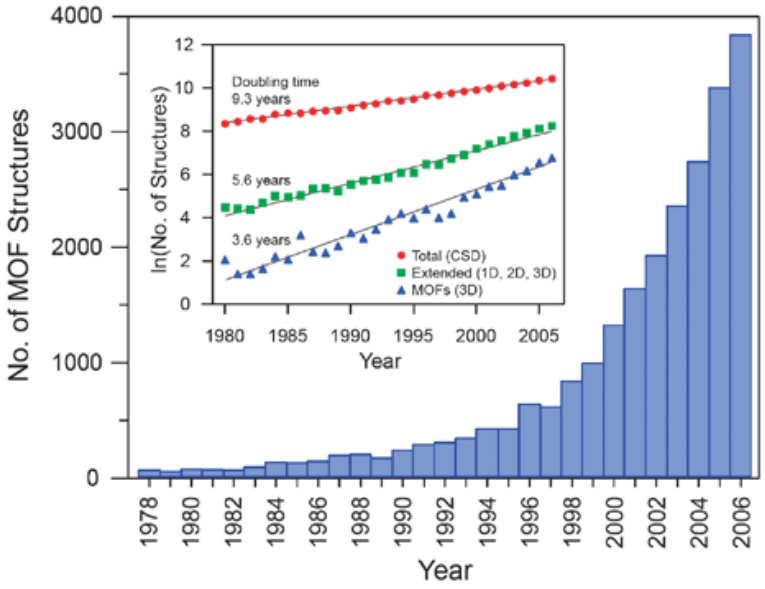

Figure 1.2 Number of MOF structures reported in the Cambridge Structural Database (CSD) from 1978 through 2006. The bar graph illustrates the recent dramatic increase in the number of reports, while the inset shows the natural log of the number of structures as a function of time, indicating the extraordinarily short doubling time for MOF structures compared to the total number of structures archived in the database [22]. Reproduced by permission of The Royal Society of Chemistry. (Appendix A)

Ferey and co-workers first developed a series of 3D rare earth diphosphonates named as MIL-n (Materials of Institut Lavoisier) [23-25]. Later they extended to compounds containing 3D transition metals (M = V, Fe, Ti) and metallic dicarboxylates [26-28]. Serre et al. synthesized the first Cr (III) dicarboxylate MIL-53as (as-synthesized) under hydrothermal conditions [29]. MIL-53as exist in two forms, low-temperature form filled with water molecules and high temperature form, the dehydrated solid. The transition between the hydrated form (MIL-53lt) and the

anhydrous solid (MIL-53ht) is fully reversible and followed by a very high breathing effect. The pores are clipped in the presence of water molecules (MIL-53lt) and reopened when the channels are empty (MIL-53ht). In addition, MIL-53as and MIL-53lt exhibit antiferromagnetic properties. Similar breathing occurs when they change Cr metal with other elements such as Al, Fe and Ga and this is due to the presence of OH groups in the one-dimensional channel which interact with water strongly [30-32]. However, no such breathing occur in vanadium kind of material MIL-47, where there are no OH groups in the skeleton [33]. Ferey et al. [34] used combined targeted chemistry and computational design to create chromium terephthalate based MIL-101 with very large pore sizes and surface area. The pore size is ~ 30-40 Å and exhibits BET surface area of ~ 3900 m^2/g.

One of the outstanding challenges in the field of porous materials is the design and synthesis of chemical structures with exceptionally high surface areas [1]. With the introduction of MOFs, surface areas greater than 3000 m^2/g were reported [2,3]. Chae et al. [35] synthesized a MOF with surface area of 4500 m^2/g higher than the largest surface areas reported in carbons [36] and zeolites [37]. Koh et al. [38] reported a mesoporous MOFs, UMCM-1 (University of Michigan Crystalline Material) with high microporosity. It contains two organic linkers of different topologies, namely, terephthalic acid (H_2BDC) and 1,3,5-tris(4-carboxyphenyl)benzene (H_3BTB). The structure differs dramatically from those based on pure linkers, namely, MOF-177 [35] and MOF-5 [3]. The octahedral geometry of UMCM-1 leads to two types of pores, one is micropore with a dimension of 14 × 17 Å and the other is mesopore with a 1D hexagonal channel of 27 × 32 Å. Koh et al. [39] synthesized a new porous material with microporous and mesoporous cages and reported the BET surface area to be 5200 m^2/g, the highest among any other porous materials to date. In contrast to

spherical or slit-shaped pores usually observed in zeolites and carbons, MOFs incorporate pore with crystallographically well-defined shapes including square, rectangular, triangular and also connected by windows [40-42].

MOFs can be categorized into rigid and flexible/dynamic frameworks. Rigid MOFs are robust and stable porous frameworks with permanent porosity, similar to zeolites and other inorganic porous materials. In contrast, flexible MOFs possess dynamic frameworks that respond to external stimuli, such as pressure, temperature, and guest molecules[43-46]. Inclusion of guest molecules causes structural transformation in MOFs which is usually not observed in zeolite structure. Structural transformations may include stretching, rotational, breathing and scissoring mechanisms, which induce different effects in the structures. Kitaura et al. [47] observed hysteresis in a 3D pillared layer material, which undergoes contraction and expansion during adsorption, with a 27.9% reduction in the cell volume on contraction. The material adsorbs methanol and water but not methane at 298 K, due to the structural transformation in the former. Inclusion of guest molecules in a porous material can cause structural distortion, which is classified into two main categories. One is crystal-to-amorphous transformation which occurs when the framework collapses upon guest removal but regeneration is possible by guest resorption. The other is crystal-to-crystal transformation where guest exchange or removal causes structural change without loss of crystallinity, i.e., unit cell expansion/contraction or scissoring. In MOFs, two processes may occur during adsorption of gas, namely gating and kinetic trapping. Gating occurs when the porous structure changes during adsorption process, going from non-porous to porous at a specific pressure. Kitaura et al. [48] reported a gating phenomenon in $[Cu(4,4'\text{-bipy})(dhbc)_2].H_2O$, which is stable to guest loss. Nitrogen adsorption does not occur at 77 K, however, at 300 K an

abrupt increase in uptake occurs beyond 50 bar referred to as "gate-opening" pressure. At this pressure, structural transformation takes place, i.e., from "close" to "open" structure due to the interaction between framework and guest. Physical adsorption of species on many porous materials produces adsorption isotherms that are virtually completely reversible. However, Zhao et al. [49] reported irreversibility in hydrogen uptake in a MOF at 77 K, whereby all or some of the H_2 is retained on pressure reduction referred to as "kinetic trapping". This is due to the presence of narrow windows, which are considerably smaller than the cavities they connect resulting in the kinetic tapping of H_2 gas by windows.

Covalent Organic Frameworks

A major breakthrough in the development of MOFs is the evolution of covalent-organic frameworks (COFs), which consist of light elements (B, C, N and O) resulting in various 2D and 3D porous framework. Côté et al. [50,51] and El-Kaderi et al. [52] synthesized crystalline, porous COFs solely from light elements such as B, C, O and H. Consisting of organic-linkers covalently bonded with boron-oxide clusters, COFs have salient features such as high thermal stability, large surface area and porosity. These boron-oxide clusters can be regarded as analogous to the metal-oxide clusters in MOFs. With the light elements, COFs have even lower density than MOFs. The co-condensation of boronic acid with hexa-hydroxytriphenylene results in 2D COF-6, -8 and -10 [51]. These 2D COF structures resemble the layered graphite composed of graphene sheets. The inter-layer distances in COF-6, -8 and -10 are 3.399, 3.630 and 3.526 Å, respectively. Alternatively, joining triangular and tetrahedral nodes leads to 3D COF-102, 103, 105 and 108 [52]. COF-108 was reported to have the lowest density (as low as 0.17 g/cm^3), even lower than the highly porous materials MOF-177 (0.42 g/cm^3) and the lowest in any crystalline materials. Similar to carbon nanotube,

armchair or zig-zig 1D COF nanotube (COF_NT) could be constructed by rolling a COF layer in a particular direction. Mazzoni and coworkers [53] tested the stability of COF_NTs by examining the structural and electronic properties using the first-principle calculations. Later, Hunt et al. [54] extended this approach by linking organic units with the strong covalent bonds found in Pyrex (borosilicate glass, B-O and Si-O) to give a porous covalent organic borosilicate framework designated as COF-202. Uribe-Romo et al. synthesized the first 3D crystalline framework (COF-300) constructed solely from C-C and C-N covalent linkages and demonstrated its permanent porosity by studying Ar adsorption at 87 K [55]. Wan et al. reported the synthesis of a new COF, TP-COF based on the condensation reaction of triphenylene and pyrene monomers [56]. TP-COF is highly luminescent, electrically conductive and capable of repetitive on-off current switching at room temperature.

Zeolite-Like Metal Organic Frameworks

Zeolites are inorganic microporous crystalline solids constructed mainly from tetrahedral building units sharing corners. Decoration and expansion of the topological networks of zeolites result in a new generation of high porous MOFs with different terminologies, such as Zeolitic-Imidazolate Frameworks (ZIFs), Tetrahedral-Imidazolate Frameworks (TIFs), Boron-Imidazolate Frameworks (BIFs) and Zeolite-like Metal-Organic Frameworks (ZMOFs). MOFs with topologies similar to the purely inorganic zeolites exhibit unique properties such as the presence of extra-large cavities (not present in zeolites), chemical stability and ion-exchange capability.

Tian et al. [57] reported a novel MOF with large pores based on expanding a zeolite topology by construction of metal-organic a tetrahedral building block TX_4 with four connections, in which the T-X-T angle is about 145º, T is cobalt (II) ion and X is imidazole linker. Usually such a building block leads to diamond-like topology

that is often unstable owing to framework interpenetration. Similarly, Tian et al. [58-61] synthesized several MOFs based on cobalt and zinc imidazolates, with some of the structures exhibiting zeolite topologies. Huang et al. [62] established a new strategy to develop zeolite-type MOFs with large pores by using a simple imidazolate ligand with a smaller substituent such as a methyl or ethyl group at the 2-position resulting in SOD and ANA topologies [63]. They also developed a SOD-type MOFs using benzimidazolate as linker [64]. Park et al. [65] synthesized a series of ZIFs by copolymerization of either Zn (II) or Co (II) with imidazolate-type linkers. The resulting ZIF structures are based on the nets of aluminosilicalite zeolites in which the tetrahedral Si (Al) and O are replaced with transition metal ion and imidazolate linkers. Hayashi et al. [66] reported the first metal-organic analogues, ZIF-20, ZIF-21 and ZIF-22 based on FAU or LTA topologies. They found that replacing carbon atoms in imidazolate linker with nitrogen at key positions has a profound impact on whether or not LTA structure is achieved. Banerjee et al. [67] developed twenty-five different ZIFs structures, 10 of which have two different links and 5 have topologies yet unobserved in zeolites. They found that out of these twenty-five ZIFs, ZIF-68, -69 and -70 show high thermal stability (up to 390 ºC) and chemical stability in organic and aqueous media. Wang et al. [68] reported two porous ZIFs, ZIF-95 and ZIF-100 with enlarged structures and complexity that was previously unknown in zeolites. Zhang et al. [69] demonstrated a new synthetic method based on the cross-linking of various presynthesized boron imidazolate complexes with monovalent cations like Li^+ and Cu^+ into extended frameworks. They named the compound as boron imidazolate frameworks (BIFs). Recently, Wu et al. [70] synthesized five 4-connected zeolitic metal imidazolate frameworks by fine-tuning of synthesis parameters such as solvent ratio and named as tetrahedral-imidazolate frameworks (TIFs). Based on the

interaction of ligands, different topologies are obtained, which is not the case in zeolites.

Liu et al. [71] reported the first example of a 4-connected MOF with topology of *rho*-zeolite and anionic in nature. It was synthesized by metal-ligand-directed assembly of In atoms and 4,5-imidazoledicarboxylic acid (H_3ImDC). In *rho*-ZMOF, each In atom is coordinated to four N and four O atoms of four separate doubly deprotonated H_3ImDC (HImDC) to form an eight-coordinated dodecahedron. Each independent HImDC is coordinated to two In atoms resulting in two rigid five-membered rings via N-, O-hetero-chelation. The structure is truncated cuboctahedra (α-cages) containing 48 In atoms, which link together through double eight-membered rings (D8MR). The substitution of oxygen in *rho*-zeolite with HImDCs generates a very open-framework with extra-large cavity of 18.2 Å in diameter. Unlike *rho*-zeolite [63] and other *rho*-aluminosilicate or aluminophosphate, *rho*-ZMOF contains twice as many positive charges (48 vs. 24) in a unit cell to neutralize the anionic framework. Figure 1.3 shows two different zeolite-like metal-organic frameworks constructed based on the molecular building block approach. Similarly, Sava et al. [72] used this approach based on rigid and directional single-metal-ion tetrahedral building units (TBUs) to synthesize different ZMOFs. They are built from heterofunctional organic linkers, such as pyridine derivatives with carboxylate substituents in different positions.

Incorporating functional groups into MOFs is a greater challenge because of the reactivity of such groups with metal ions, particularly under solvothermal conditions. Cohen et al. [73-76] reported an alternative method where a MOF was first synthesized and then functionalized using suitable chemical reagents and termed this approach as “postsynthetic modification”.

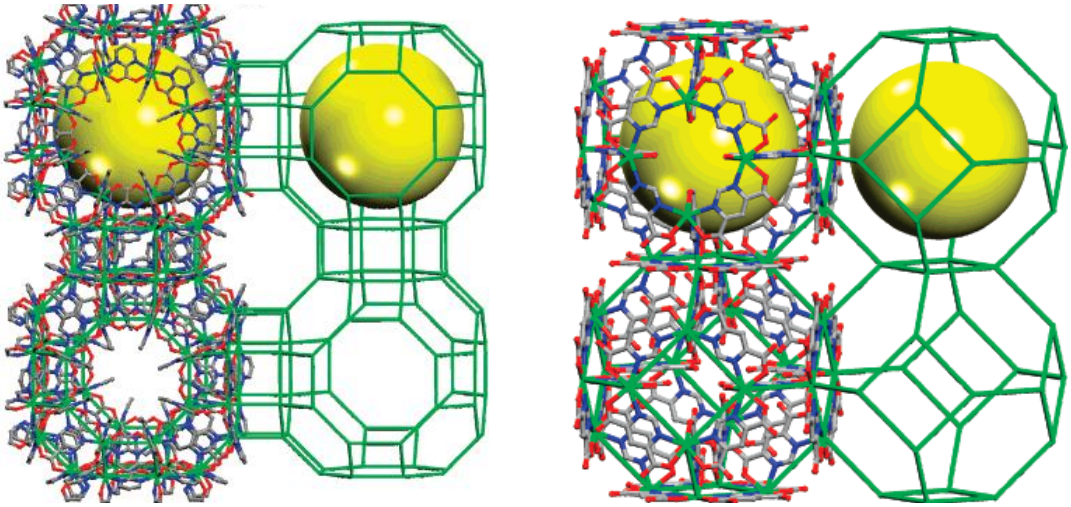

Figure 1.3 Single-crystal structure of *rho*-ZMOF (left) and sod-ZMOF (right). Hydrogen atoms and quest molecules are omitted for clarity. In - green, C - gray, N - blue, O - red. The yellow sphere represents the largest sphere that can be fit inside the cage, considering the van der Waals radii. Adapted with permission from [72]. Copyright (2008) American Chemical Society. (Appendix A)

They modified IRMOF-3, composed of 2-amino-1, 4-benzenedicarboxylic acid and Zn_4O clusters, with linear alkyl chain anhydrides and isocynates to produce amide and urea functionalized systems. These modifications affect the physical and chemical properties of IRMOF-3, including its microporosity. Based on the results three important findings were demonstrated. First, amino-benzenedicarboxylic acid (NH_2-BDC) can act as a substituent for BDC in a number of MOFs. Second, postsynthetic modification is a general strategy to functionalizing MOFs that can be applied to a variety of MOF structures. Third, the topology and chemical or thermal stability of a MOF can influence the type of chemical reaction and reagent that can be used for postsynthetic modification [77]. Recently, Wang et al. [78] presented a critical review on postsynthetic modification of MOFs.

1.2 Industrial Applications

MOFs have been explored for their interesting properties including optic [71,79-81], magnetic [82-84] and electronic properties [85-88], as well as their potential

applications such as catalyst [89-92], ion-exchange [71,72,93-95], gas storage and separation [96-98], sensing [99-101], polymerization [102,103] and drug-delivery [104-106]. A brief discussion on the application of MOFs, particularly in gas adsorption, separation and catalysis is summarized below.

1.2.1 Gas Storage

Gas storage in nanoporous materials is becoming increasingly important with applications ranging from energy and environment to biology and medicine. Porous materials such as zeolites and carbon materials have been extensively studied for the storage of different gases and some have been industrially used. With very high porosity and surface area, MOFs are proved to be robust in storage applications. Gas storage in MOFs is attracting a great deal of attention, particularly H_2 and other gases such as CH_4 and CO_2. H_2 is considered as friendly energy carrier as it is free of carbon and abundantly available from water. A key issue for the practical utilization of H_2 for on-board use is the development of safe and high-capacity systems for H_2 storage. The U.S. Department of Energy (DOE) has set the targets for on-board H_2 storage as of 6.0 wt% and 45 g/L by 2010, and 9.0 wt% and 81 g/L by 2015 [107]. As the major component of natural gas fuel, CH_4 is considered as a promising alternative fuel for vehicular application. The U.S DOE has defined a storage target of 180 v/v (the volume of gas adsorbed at standard temperature and pressure per volume of the storage vessel) for CH_4 storage at 35 bar.

Over the past few years, numerous studies have been reported in MOFs toward H_2 storage for vehicular applications. For instance, Rowsell et al. [108] carried out H_2 adsorption on a set of MOF materials and found the impact of internal surface area and the number of rings in organic link on storage capacity. They observed that the adsorption capacity in MOFs can be further increased by altering the chemical nature

of organic component. Chen et al. [109] highlighted the synthesis and H_2 adsorption in a MOF named MOF-505 based on NbO topology with two kind of pores, open metal sites, permanent porosity. Ferey and his group [110] studied H_2 storage properties of nanoporous metal-benzenedicarboxylate containing trivalent Cr or Al denoted as MIL-53. They found that these solids exhibit H_2 storage capacity of 3.8% and 3.1 wt%, respectively, at 77 K and 1.6 MPa.

Pan et al. [111] explored a new type of microporous metal coordination materials (MMOMs) with pore dimensions comparable to the molecular diameter of H_2. MOMMs are very similar to single walled carbon nanotubes (SWNTs) in physical characteristic, however they possess several advantageous over SWNTs promising for H_2 adsorption. For example, MMOMs incorporate metals that can bind H_2 much more strongly than graphitic carbon. The open channels in MMOMs are perfectly ordered, allowing the effective access of H_2 to interior space. In addition, the structures of these materials, including the metal building unit, pore dimension, shape, size and volume, can be systematically tuned for modifying and improving H_2 uptake and adsorption/desorption properties.

Rowsell and Yaghi [112] highlighted a comprehensive study on the strategies that enhance H_2 storage in MOFs. They reported different strategies for improving H_2 uptake in MOFs, including the optimization of pore size and adsorption energy by linker modification, impregnation, catenation, and the inclusion of open metal sites and lighter metals. Following this, numerous experimental studies have been reported on the effect of catenation and inclusion of open metal sites on H_2 uptake in MOFs. For example, Rowsell and Yaghi [113] measured H_2 storage capacities of various MOFs and found that catenated MOFs show higher uptake at pressures below 1 bar. Dinca et al. [114,115] synthesized a MOF with exposed Mn^{2+} and exchanged with

other metals ions, where the metals were unsaturated and an increase in H_2 storage capacity was observed. Wang et al. [116] reported a new porous coordination network, PCN-12 exhibiting the highest H_2 uptake (3.05 wt%) at 77 K and 1 bar. Vitillo et al. [117] reported a MOF, CPO-27-Ni, with the highest heat of adsorption of -13.5 kJ/mol, the highest yet observed for a MOF. Recently, Dinca and Long [118] reviewed in detail the experimental studies for H_2 adsorption in MOFs with open metal sites.

Li and Yang [119,120] suggested a new technique, dissociation/spillover to enhance H_2 storage in MOFs. They demonstrated that it is possible to increase storage capacity in nanostructured carbons by using a catalyst to dissociate H_2. By using this technique, they found an increase in storage capacity of H_2 in IRMOF-8 to 1.8 wt% at 298 K and 10 MPa, an enhancement factor of 3.1 and the storage was totally reversible. Similarly, enhancement of H_2 storage by using hydrogen spillover with bridges was carried out. They found that the storage capacity of IRMOF-8 to be 4 wt% at 298 K and 10 MPa and eight times higher than that of pure IRMOF-8 under the same conditions. To date, the highest excess H_2 uptake were found in MOF-5 (7.1 wt %) [121], MOF-177 (7.0 wt %) [113], COF-102 (6.75 wt%) [97] and NOTT-102 (7.1 wt%) [122] at 77 K. Long and co-workers [123] reported a critical review on H_2 uptake in MOFs.

Eddaoudi et al. [2] synthesized various MOFs and studied gas storage, particularly CH_4 storage. They proposed a strategy based on reticulating metal ions and organic carboxylate links into extended networks in which pore size and functionality could be varied systematically. As a prototype of MOFs, MOF-5 was constructed from Zn_4O clusters and benzene links. The three-dimensional structure of MOF-5 can be functionalized with the organic groups -Br, -NH_2, -OC_3H_7, -OC_5H_{11}, -C_2H_4, -C_4H_4

and the pore size can be expanded with long molecular struts biphenyl, tetrahydropyrene, pyrene and tetraphenyl. They synthesized an isoreticular series of 16 highly crystalline materials with open space up to 91.1% of the crystal volume and pore size from 3.8 to 28.8 Å. One member of this series exhibited a high capacity for CH_4 storage of 240 cm^3 (STP)/g at 36 atm and ambient temperature. Later Düren et al. [124] investigated the adsorption characteristics of CH_4 in several IRMOFs, zeolites, MCM-41 and carbon nanotubes, as well as molecular squares. They found a correlation between the adsorption of CH_4 at 35 and 298 K with the surface area and suggested that the ideal adsorbent for CH_4 storage should have a large surface area, high free volume, low framework density and strong CH_4-adsorbent interactions. Ma et al. [125] reported a microporous MOF, PCN-14 based on anthracene derivative consisting of nanoscopic cages. High pressure CH_4 adsorption study showed that PCN-14 exhibits an absolute CH_4-adsorption capacity of 230 v/v, which is 28% higher than the DOE target of 180 v/v [126] at ambient temperature.

In addition to gas storage for energy application, the removal of gases from environment is also important. For example, burning of fossil fuels in automobile and power plant releases a huge amount of CO_2 in the atmosphere. CO_2 emissions contribute global warming, sea-level rise, and an irreversible increase in the acidity level of oceans with the undesirable impact on the environment. In this regard, Yaghi and Millward [98] tested the storage capacity of CO_2 at room temperature in nine MOFs, representing a cross section of framework characteristics such as square channel (MOF-2), pores decorated with open metal sites (MOF-505 and $Cu_3(BTC)_2$), hexagonally packed cylindrical channels (MOF-74), interpenetration (IRMOF-11), amino-and alkyl–functionalized pores (IRMOFs-3 and -6), and the extra-high porosity frameworks (IRMOF-1 and MOF-177). Llewellyn et al. [127] reported high uptake of

CO_2 and CH_4 in chromium-based MIL-101 using different activation procedures. Similarly, Chowdhury et al. [128] studied the gas adsorption in MIL-101 at three different temperatures 283, 319 and 351 K using a standard gravimetric method. Active metal sites and sites inside the pores of supertetrahedra act as a major adsorption sites for gases like CO_2, CH_4, C_3H_8, SF_6 and Ar. For all gases considered in their study, the enthalpy of adsorption was found to be lower than those in purely siliceous zeolites such as silicalite indicating a weaker between the adsorbates and MIL-101 framework. Recently, Furukawa and Yaghi [97] measured CO_2 storage capacity in various 1D, 2D and 3D structures of covalent organic frameworks (COFs) [51,52] and showed that 3D COFs structures outperform 1D and 2D COFs. For instance, CO_2 uptake in COF-102 and COF-103 is around 1010 mg/g and 1200 mg/g at 55 bar and 298 K. These uptakes are larger than in most MOFs reported to date and comparable to that in MOF-177 (1490 mg/g at 40 bar and 298 K) [98] and MIL-101(Cr) (1760 mg/g at 50 bar and 298 K) [127].

Apart from gas storage in MOFs for energy application, MOFs can also be useful for medical applications. Xiao et al. [129] showed MOFs with accessible metal sites can bind with biologically important gas NO. The high porosity of MOFs offers the advantage of high adsorption and delivery capacity of NO almost five times greater than zeolites. MOFs are less stable than polymers and zeolites, however, their applicability in biological applications is yet to be proved. Mickinlay et al. [130] showed an exceptionally high adsorption capacity and water-triggered delivery of NO in two porous MOFs. MOFs are also tested for the storage and delivery of drug, for example MIL-101 exhibited a remarkably high dosage capacity of ibuprofen up to 1.38 g/g MIL-101 [106], larger than that reported in MCM-41 [104]. The sorption and

in vitro delivery of ibuprofen were also examined in MIL-53 and the loading was about 0.22 g/g MIL-53 and independent of metal type (Cr, Fe) [105].

1.2.2 Gas Separation

In gas separation, the efficiency depends on temperature, pressure and nature of the adsorbates and adsorbent. Many porous materials were explored as adsorbents, such as aluminosilicate zeolites, carbon and metal-oxide molecular sieves, aluminophosphates, activated carbon, activated alumina, carbon nanotubes, silica gel, pillared clay, inorganic and polymeric resins; some of which are now used commercially [131]. Exploitation of better adsorbents which can be easily tuned to meet the specific application can improve the performance of industrial processes. Compared to other structures, MOFs can be easily tuned with infinitely large numbers structures. Some MOFs have been demonstrated being potentially useful in gas separation.

Chen et al. [132] designed MOF-508 with pores that can be tuned to match alkane molecular sizes and found highly selective chromatographic separation of alkanes in this MOF. Separation of linear and branched isomers of pentane and hexane were examined in detail, because of their availability and industrial relevance in petroleum refining. Pan et al. [133] studied the separation of hydrocarbons in microporous MOFs (MMOFs). Compared to zeolites, the MMOF structures are typically composed of aromatic rings and other organic moieties. Their pore structures can be designed and modified to yield the desired shape, size, and surface characteristics. They designed and synthesized a group of MMOFs that have 3D or 2D structures built upon paddle-wheel metal clusters (nodes) and a V-shaped dicarboxylate ligand. These structures contain irregular-shaped micro channels with alternating large cages (or chambers) and small entrances (or necks) that connect these cages. One of the

MMOFs developed has unique property to separate normal C_2, C_3 and *n*-C_4 olefins and alkanes from all branched alkanes and all normal hydrocarbons above C_4.

Dybtsev et al. [134] reported a new MMOF from manganese formate with permanent porosity, high thermal stability and high selective gas sorption properties. It selectively adsorbs H_2 and CO_2 but not N_2 and other gases of larger kinetic diameters and the selectivity appears to be due to the smaller aperture of the channels. The selective adsorption of H_2 over N_2 was also reported in other MOFs such as PCN-13 [135], $Mg_3(ndc)_3$ [136] and Cu (F-pymo)$_2$ [137]. Synthetic zeolites and carbon molecular sieves have been used as solid adsorbents for non-cryogenic air separation to produce either oxygen or nitrogen. Metal–complex–based materials have been examined as possible candidates for gas separation and purification. One of the first robust MOFs, Cu-BTC, with a microporous structure was developed [138]. Followed by this synthesis, Wang et al. [139] developed an improved synthesis process for large scale manufacture of Cu-BTC. In this material a series of sorption properties of different gases has been studied. Ma et al. [140] reported a coordinative linked interpenetrated MOF, PCN-17, which has porous structure containing large cages linked by relatively small apertures and retain its porosity at temperature as high as 480ºC. It selectively adsorbs H_2 and O_2 over N_2 and CO. This material may thus be suitable for the separation of N_2 and O_2, the separation of H_2 over CO in fuel-cell applications.

Although the pore size and shape of an adsorbent determine adsorption selectivity as discussed above, the interaction of guest-surface interaction is also important. In this case, the selectivity is related to adsorbate properties such as polarity, quadrupole moment and H-bonding. One such example is the selective adsorption of C_2H_2 over CO_2 in $Cu_2(pzdc)_2(pyz)$ [141], where pzdc is pyrazine-2,3-dicarboxylate and pyz is

pyrazine. The sorption of both the gases at 270, 300 and 310 K showed that this MOF selectively adsorbs C_2H_2 over CO_2 at low pressures and room temperature. C_2H_2 binds strongly to the MOF surface than CO_2 due to H-bonding between C_2H_2 molecules and surface the O atoms. Selective adsorption based on the hydrophobic/hydrophilic properties of pores was observed in Zn (tbip) [142], (tbip-5-tert-butyl isophthalic acid), $Zn(bdc)(ted)_{0.5}$ [143], (bdc -1,4 benzene dicarboxylate, ted-triethylenediamine) and CID-1 [144], (CID-coordination polymer with interdigitated structure). These MOFs selectively adsorb MeOH, EtOH and dimethyl ether over H_2O. Several MOFs selectively adsorb CO_2 over CH_4 because CO_2 has a large quadrupole moment whereas CH_4 has none. For example, Mn(ndc) (ndc-napthalenedicarboxylate) [145] is a 3D microporous MOF with 1D channels which contain unsaturated metal sites. The adsorption measurement shows that CO_2 is more adsorbed than CH_4 at ambient temperature. Similarly, Bae et al. [146] reported selective adsorption of CO_2 over CH_4 in a carborane based-MOF with coordinatively unsaturated metal sites. Recently, Mu et al. [147] synthesized a new 2D interpenetrating MOF with unsaturated metal sites and uncoordinated carboxylic group, exhibiting a high selectivity (~ 13) for CO_2 over CH_4.

In recently developed ZIFs, high storage capacity for CO_2 and selective adsorption of CO_2 over CO were identified. For example, in ZIF-68, ZIF-69 and ZIF-70 [67], CO_2 and CO adsorption isotherms show that all these ZIFs have high affinity and capacity for CO_2, which is further confirmed in a breakthrough experiment of stream containing 50:50 v/v binary mixture of CO_2 and CO at room temperature. In ZIF-95 and ZIF-100 with large cavities and highly constricted pores, a higher affinity was found for CO_2 over CH_4, CO and N_2 [148]. The high selectivity for CO_2 is due to the combined effects of the aperture sizes and the strong quadrupolar interactions of CO_2

with the N atoms present on the pore surface and also related to the higher condensability of CO_2 than other gases.

1.2.3 Catalysis

One of the demonstrated applications of MOFs is heterogeneous catalysis. Fujita et al. first reported MOF-based catalyst in a 2D square network material for the cyanosilylation of aldehydes and imines [148]. Evans et al. explored the design and synthesis of thermally and hydrolytically robust, single-crystalline, chiral porous MOFs based on metal biphosphonates [149]. They also reported the catalytic properties of a series of homochiral porous lamellar lanthanide biphosphonates. Seo et al. reported the synthesis of a homochiral MOF that allows the enantioselective inclusion of metal complexes in its pores and catalyses a transesterfication reaction in an enantioselective manner [150]. Wu et al. reported the synthesis of a highly porous homochiral MOF and its application in heterogeneous asymmetric catalysis and stereo selectivity rivaling its homogeneous counterparts [151]. Ravon et al. studied the Friedel-Crafts tert-butylation of both toluene and biphenyl in a cubic compound MOF-5 [152]. They found the catalytic activity of MOF-5 is attributed to encapsulated zinc-hydroxide clusters or to a hydrolytically degraded form of the parent materials. Kaskel and co-workers [153,154] showed that the Lewis acid sites in HKUST-1 can catalyze the cyanosilylation of benzaldehyde or acetone. Similarly, they studied the catalytic activity of MIL-101 and found that MIL-101 is much more active than HKUST-1 as a catalyst for the cyanosilylation of benzaldehyde due to the greater Lewis acidity of Cr (III) vs. Cu (II). Alaerts et al. [155] investigated the behavior of HKUST-1 as acid catalyst.

Eddaoudi and coworkers [156] encapsulated cationic porphyrins in rho-ZMOF during synthesis and achieved more than 60% loading. They demonstrated that the

encapsulated free-base porphyrin could be metallated with Mn, Co, Zn or Cu ions and showed the catalytic activity towards the oxidation of cyclohexane in Mn-metallated porphyrin. Hasegawa et al. [157] synthesized a catalytic MOF which consists of identical pairs of networks, single cadmium ions, octahedrally ligated by pyridyl nitrogen. They found that the MOF is capable of base-catalyzing the Knoevenagel condensation of benzaldehyde with malononitrile. Ferey and co-workers [158] modified the interior of MIL-101 via Cr(III) coordination with the N atoms of ethylenediamine molecules. They tested the catalytic activity of MIL-101 for Knoevenagel condensation of benzaldehyde with nitriles.

1.3 Scope of the Thesis

Development of technological applications based on nanoporous materials requires fundamental understanding of their properties at a microscopic level. With ever growing computational power, molecular simulations are playing increasingly important role in the development of new materials. Simulations at the molecular scale can provide microscopic pictures that otherwise are experimentally inaccessible or difficult to obtain. In conjunction with experiment, fundamental insight gained from molecular simulations can assist the rational design of novel materials and products. In addition, this approach can be extended to hypothetical structures not yet prepared in experiments. Because of the predictability of the synthesis routes to MOFs and the nearly infinite number of variations possible, molecular simulations are attractive for screening new MOFs before experimental synthesis and testing. The main goal of this thesis is to understand adsorption and diffusion phenomena in MOFs using molecular simulation techniques in conjunction with quantum chemical computations; and subsequently provide structure-function relations for the screening

and design of high-performance MOFs toward important applications. The objectives are summarized as follows.

- To investigate the storage capacity of pure CO_2 and CH_4 and the separation of CO_2/CH_4 mixture in different types of nanoporous materials (IRMOF-1, silicalite and C_{168} schwarzite).
- To study the effects of metal-oxide, organic linker and topology on the storage capacity of CO_2 in various MOFs and COFs, and compare with zeolites and carbon nanotubes.
- To analyze the effects of different characteristics such as unsaturated metal sites, interpenetration and extra-framework ions on the adsorption selectivity of CO_2/CH_4 mixture. The role of electrostatic interactions on both adsorption and selectivity are also analyzed.
- To understand the effect of extra-framework ions on gas adsorption and separation of mixtures. The location and dynamics of extra-framework ions in a charged MOF is characterized. The selective separations of CO_2 to mimic post-combustion and pre-combustion capture and upgrading of natural gas are investigated.
- To investigate the effect of catenation on the separation of alkane isomer mixtures. Adsorption and diffusivity of alkane isomer mixtures are predicted in catenated and non-catenated MOFs.
- To study the adsorption and diffusion of a model drug (ibuprofen) in mesoporous MIL-101 and UMCM-1. The energetics and dynamics of ibuprofen in the MOFs are unraveled at the molecular level.

1.4 Organization of the Thesis

The thesis is organized into ten chapters, including the Introduction discussing the development of MOFs and their applications, particularly for gas storage, separation and catalysis in Chapter 1. A comprehensive literature review highlighting the current modeling studies in MOFs for gas storage, adsorption separation and diffusion is presented Chapter 2. A brief introduction about simulation techniques employed in the thesis is discussed in Chapter 3. The results and discussions pertaining to the objectives mentioned above are discussed in Chapters 4 through 9.

More specifically, Chapter 4 describes the storage and separation of CO_2 and CH_4 in IRMOF-1, silicalite and C_{168} schwarzite. The role of different metal-oxide, organic linkers and topology on CO_2 storage capacity in various MOFs are discussed in Chapter 5. In Chapter 6, the effects of different characteristics such as open metal sites, interpenetration and extra-framework ions on the adsorption selectivity of CO_2/CH_4 mixtures, including the effect of electrostatic interactions on selectivity are addressed. In Chapter 7, characterization of the extra-framework ions and gas separation in a charged MOF are investigated. In Chapter 8, the effect of catenation on the separation of alkane isomer mixtures is explored and compared with non-catenated MOFs. Adsorption and diffusion of ibuprofen in mesoporous MOFs is presented in Chapter 9. Finally, the concluding remarks and the recommendations for future studies are discussed in Chapter 10.

Chapter 2

Literature Review

Chapter 1 summarizes the experimental studies on the applications of MOFs. In this Chapter, a literature review on molecular modeling of MOFs for gas adsorption and diffusion are presented.

2.1 Single-Component Adsorption

2.1.1 H_2 Storage

H_2 is considered as an ideal energy carrier and clean fuel for the future. A key issue for the practical utilization of H_2, e.g. in mobile applications, is the development of safe and high-capacity systems for H_2 storage. The U.S. Department of Energy (DoE) has set the targets for on-board H_2 storage as of 6.0 wt% and 45 g/L by 2010, and 9.0 wt% and 81 g/L by 2015 [107]. The mentioned gravimetric figures refer to H_2 storage system as a whole, which includes all of the hardware (e.g. tank, valves, cooling or heating systems if needed, insulation, etc.). Hence the actual capacity of H_2 storage material might need to be significantly higher than the system targets. Considerable research has been undertaken over the past two to three decades to determine H_2 storage capacity in different carbon nanostructures such as activated carbon, graphite, carbon nanofibres, carbon nanotubes, fullerenes and also in zeolites, metal hydrides and MOFs. Several techniques such as Monte Carlo, molecular dynamics and first-principle approaches have been employed to examine H_2 adsorption in different classes of materials and in turn guide to rational design of adsorbent materials that can meet storage targets.

Ab initio calculations have been reported to investigate the interaction of H_2 with MOFs and COFs. Hüber et al. [159] studied the H_2 interaction with MOFs using the approximate resolution of the identity Møller-Plesset (MP2) [160-162] calculations and triple zeta valence basis set (TZVPP) [163]. They estimated the binding energies between H_2 and various substituted benzenes such as C_6H_6, C_6H_5F, C_6H_5OH, $C_6H_5NH_2$, $C_6H_5CH_3$, C_6H_5CN. The binding energies of H_2 to benzene and naphthalene are 3.91 and 4.28 kJ/mol, respectively, indicating that enlarging the aromatic systems increases the interaction energy. Sagara et al. [164,165] calculated the binding energy of H_2 with organic linker and metal-oxide part in IRMOF-1 using MP2 with the quadrupole zeta QZVPP [163] basis set. In addition, they also calculated H_2 interaction with organic linkers in various MOFs (IRMOF-1, IRMOF-3, IRMOF-1-4NH_2, IRMOF-6, IRMOF-8, IRMOF-12, IRMOF-14, IRMOF-18 and IRMOF-993) and found that the larger linkers bind more H_2 molecules and addition of NH_2 or CH_3 group to each linker increases the binding energy up to 33%. Han et al. [166] performed MP2/QZVPP calculation to find the binding energy of H_2 with different metal oxides and found that the substitution of metal sites from Zn to Mg and Be does not change the configuration, with Mg cluster showing the higher binding energy.

Even though density functional theory (DFT) has been widely used to study the interactions of molecules with surfaces, it fails to describe weak physisorption interaction largely because the dispersion forces and the van der Waals interactions are not properly accounted in DFT theory. DFT calculations within the local-density approximation (LDA) give notably higher binding energies than the generalized gradient approximation (GGA). The hybrid Becke-three-parameter Lee-Yang-Parr (B3LYP) DFT method gives a qualitatively incorrect prediction of H_2 binding. Both

LDA and GGA methods are inaccurate in predicting the binding energy when compared to more accurate MP2 method. As MP2 calculations are impractical for realistic MOF systems, the combined LDA and GGA calculations provide a cost-effective way to assess the H_2 binding capability in MOFs [167]. Several polar aromatic molecules in addition to a model for metal-oxide corner of MOF were studied to predict the H_2 binding properties using the Perdew-Wang exchange correlation functional and MP2 calculations, and the computed binding energies were found to be in good agreement with experimental observations. Corrected binding energies between H_2 molecule and a model for MOF-5 were calculated with Perdew-Wang exchange correlation functional and 6-311++G** basis set [168].

Grand canonical Monte Carlo (GCMC) simulations are commonly used to predict gas adsorption in confined space. Sagara et al. [169] studied the uptake of H_2 in MOF-5 using GCMC simulation and found that the predicted results overestimated experimental data. Yang and Zhong [170] simulated H_2 adsorption isotherm in IRMOF-1, IRMOF-8 and IRMOF-18 by refitting the parameters using OPLS-AA force field (OPLS-AA) [171] and obtained better agreement with experimental results. Similarly, Yang and Zhong [172] simulated H_2 isotherm in IRMOF-1 and Cu-BTC at 298 K up to 70 bar and extended their simulations to MOF-508 with open metal sites. The presence of open metal sites was found to have a favorable impact on H_2 uptake, but the uptake was still low at room temperature. Garberoglio et al. [173] predicted H_2 adsorption isotherms in various MOFs namely, MOF-2, MOF-3, IRMOF-1, IRMOF-5, IRMOF-8 and IRMOF-14 using UFF [174] and DREIDING force fields [175]. They found the simulation results agreed better with experiments by taking into quantum effects, however, overestimated in IRMOF-1 and underestimated in IRMOF-8 at 1 bar and 77 K without the quantum effects. Frost et al. [176] used GCMC simulations to

predict the adsorption isotherm of H_2 in ten different non-interpenetrating MOFs. The calculated results reveal the existence of three different adsorption regimes: at low pressures, H_2 uptake correlates with the heat of adsorption; at intermediate and higher pressures, the surface area and free volume correlates with the uptake. Jung et al. [177] studied the effect of catenation on H_2 adsorption in catenated MOFs using GCMC and found that the small pores generated by catenation play a significant role to densely confine H_2 molecules, therefore, the capacity in catenated frameworks is higher than that of the non-catenated counterparts. Similarly, Ryan et al. [178] reported the effect of catenation on H_2 uptake in MOFs and found the catenation can be beneficial for improving H_2 storage in MOFs at cryogenic temperature and low pressures, however not necessarily at room temperature.

To improve H_2 storage capacity in MOFs, Zhang et al. [179] designed new hypothetical MOFs by exchanging the organic linker in MOF-5 with oxalate and introducing –F, –Cl, $–CF_3$ and $–CCl_3$ to tune the electro negativity of the linkers. They simulated H_2 adsorption isotherm up to 1 bar and 77 K and found that the proposed MOFs show higher H_2 uptake at low pressures. Frost and Snurr [180] investigated how to improve the H_2 storage to meet the current DoE targets. They artificially increased the H_2 –MOF Lennard-Jones attraction and found that the gravimetric H_2 uptake of 6 wt % could be achieved in a MOF with a free volume between 1.6 and 2.4 cm^3/g. In MOFs with free volumes less than 1.5 cm^3/g or void fraction of less than 75%, isosteric heats larger than 20 kJ/mol would be required to achieve 6 wt%. Garberoglio [181] simulated H_2 uptake in different COFs consisting of lighter element like C, B, Si, O and H. H_2 adsorption isotherm in 3-dimensional COFs (COF-102, COF-10, COF-105 and COF-108) at 77 and 298 K showed a higher capacity in COF-105 at 77 K and COF-108 at 298 K. Similar work was reported by Klontzas et al. [182]

showing a gravimetric H_2 uptake of 21 wt% at 77 K and 100 bar in COF-108 and 4.5 wt % at room temperature and 100 bar.

Most GCMC studies have used empirical force fields like UFF [174], DREIDING [175] and OPLS-AA [171] to predict the adsorption of H_2 in different MOFs and COFs. Recently Goddard and his co-workers [183-185] developed accurate non-bonded interactions between H_2 –MOF (or COFs) and H_2-H_2 from high level *ab initio* calculations. Based on the *ab initio* force field, they showed accurate H_2 adsorption isotherms in IRMOF-1 and MOF-177 and 2D- and 3D-COFs. For instance, their simulations in IRMOF-1 indicated H_2 adsorption of 1.28 wt % at 77 K and 1 bar, close to experimental 1.30 wt % under the same conditions and showed 4.17 wt % and 4.89 wt % at pressures of 20 and 50 bar, which are also comparable to experimental results. In COF-5 the simulation data are also in excellent agreement with the experimental results. As none of the studies reported for H_2 adsorption in MOFs and COFs meet the DoE targets, several strategies were proposed to improve the storage capacity of H_2 in MOFs and COFs.

Rowsell and Yaghi [112] discussed six strategies for high H_2 adsorption in MOFs, such as high porosity with appropriate pore size, impregnation, catenation, open metal sites, light metals and functionalized linkers. Using GCMC simulation based on *ab initio* force field, Han et al. [185] found a large heat of adsorption for H_2 (8.8 kJ/mol) in COF-1 due to appropriate pore size, showing a high uptake of 1.7 wt % at 0.1 bar which is higher than other COFs such as COF-5, COF-102, COF-103, COF-105 and COF-108. At 300 K, however, COF-1 shows a low H_2 storage ~ 0.78 wt % at 100 bar. Yaghi and co-workers [112] suggested the insertion of another adsorbate molecule in large-pore MOFs to create appropriate pore size for high H_2 adsorption. Using this approach, Han et al. [175] obtained C_{60} loaded MOF-177 using GCMC simulation at

300 and 1 bar using the standard DRIEDING force field. They found H_2 uptake at low pressures increases by the inclusion of C_{60} into MOF-177 at 77 K and 300 K, however, at high pressures it decreases due to the reduction in pore volume. Another way of reducing pore size in MOFs is framework catenation. As discussed earlier, Jung et al. and Ryan et al. studied the effect of catenation on H_2 uptake at 77 and 300 K and found the catenation increases the adsorption of H_2 at 77 K, but not at 300 K.

In addition to tune the pore size of MOFs to improve H_2 storage capacity, open metal sites in MOFs can also be used to enhance the binding energy of H_2. Few theoretical studies have been reported to calculate the binding energy of H_2 with the open metal sites in MOFs and indicated that the binding energy of H_2 can be tuned up to 10-50 kJ/mol by using different transition metals in MOF systems [186-188]. Doping alkali elements on the organic linker parts of MOFs and COFs was considered as another strategy to improve the H_2 uptake at 300 K. Han et al first proposed the Li-doped MOFs as practical H_2 storage materials using *ab initio* based GCMC simulations. They found the predicted isotherms for H_2 in Li doped MOFs are significantly improved compared to MOFs without Li. For instance, at 300 K and 20 bar the Li-doped MOF-C30 stores 3.89 wt % excess H_2 and reaches up to 5.16 wt % at 100 bar [189]. Similar theoretical works have been reported to study the binding energy of H_2 in Li-doped MOFs [190-194]. Recently, Cao et al. [195] simulated H_2 adsorption in Li-doped COFs using *ab initio* based force field and GCMC simulations. They reported exceptionally high uptake of H_2 at 298 K and 100 bar in COF-105 (6.84 wt %) and COF-108 (6.73 wt %). They also suggested that doping Li with COFs is a promising approach to enhance H_2 storage capacity.

2.1.2 CH_4 Storage

Natural gas, which consists mainly of CH_4, is considered as an alternative fuel for traditional fossil fuels. The U. S. DoE has set a storage target of 180 v/v (the volume of gas adsorbed at standard temperature and pressure per volume of the storage vessel) at 35 bar [126]. Düren et al. investigated CH_4 storage in several IRMOFs as well as molecular squares, zeolites, MCM-41 and carbon nanotubes [124]. They found a correlation between CH_4 adsorption at 35 bar and 298 K with the surface area and suggested that an ideal adsorbent for CH_4 storage should have a large surface area, high free volume, low framework density and strong adsorbent-adsorbate interactions. Based on these criteria, they proposed a hypothetical structure having different linkers showing high uptake of CH_4 [124]. Wang simulated CH_4 adsorption in a series of IRMOFs namely IRMOF-1, -6, -8, -10 and -14, Cu-BTC, CPL-28, CPL-522 and Cu (AF_6) $(bpy)_2$. Similar to that observed by Düren et al., the surface area was found to play a dominant role in CH_4 adsorption at room temperature and moderate pressure. The heat of adsorption correlated well with the pore size at low loadings and surface area, and free volume at high loadings [196]. Jhon et al. [197] studied CH_4 adsorption in alkoxy-functionalized variations of IRMOF-1. Propoxy substituted IRMOF-1 was synthesized by Eddaoudi et al. [2] and named as IRMOF-4. Alkoxy-functionalized IRMOF-1 was first structurally optimized and then CH_4 adsorption was performed using GCMC simulations. It was found that the constricted pores by the alkoxy-functionalized linkers promoted CH_4 adsorption at low to moderate pressures but the saturation capacities were decreased. The propoxy-functionalized IRMOF-1 showed the largest volumetric adsorption at low to moderate pressures due to the presence of longer linker and small pore.

2.1.3 CO_2 Storage

Kawakami et al. [198] simulated CO_2 adsorption in $Zn_3(bdc)_3$ at 78 K using *ab* initio method to calculate the charges of framework and CO_2 molecule. They found that the value of charges on the framework have a substantial effect on the saturation capacity of CO_2. The predicted adsorption isotherms overestimate experimental results and were attributed to the defects in experimental samples. Walton et al. [199] calculated the adsorption isotherms of CO_2 in IRMOF-1 at different temperatures and compared with experiments. They predicted the inflection and steps in the adsorption isotherms and the simulation results match qualitatively with experiments. They showed that the inclusion of electrostatic interaction between CO_2 molecules is required to capture the inflection in the adsorption isotherms. In addition, Walton et al. [199] predicted the adsorption isotherms of CO_2 in IRMOF-3 and MOF-177 at 298 K and found good agreement with experiments. The main conclusion from this study is the inclusion of framework charges has little effect on the adsorption of CO_2 in different MOFs.

Yang et al. [200] predicted CO_2 adsorption isotherms in various MOFs (Cu-BTC, IRMOF-1, -8, -10, -11, -14, -16, MOF-177 and Mn-MOF) by fitting parameters to match experimental data. They found that the amount of CO_2 in MOFs at low pressures correlated well with the isosteric heat. At moderate pressure of 30 bar, the uptake of CO_2 is related to both free volume and surface area. They also found that the electrostatic interactions between CO_2 and the framework atoms enhance the adsorption by ~ 20-30 % at low pressures and decrease to ~ 3 % at high pressures compared with the neutral framework. Ramasahye et al. [201-203] calculated CO_2 adsorption in MIL-53 (Al) and MIL-53 (V). They used the charges computed form DFT calculation and a three site model for CO_2. They predicted the adsorption isotherms and enthalpies of adsorption in two different structures of MIL-53 (Al),

namely narrow-pore MIL-53np (Al) and large-pore MIL-53lp (Al) forms, having the same chemical identity but different pore widths of 8.3 and 13.8 Å, respectively. The simulated enthalpy in MIL-53np (Al) matches experimental results at low pressures, while the enthalpy in MIL-53lp (Al) agrees with experimental data at high pressures. This finding is consistent with the structural transition from narrow-pore form to the large-pore form in MIL-53(Al) during CO_2 adsorption. They also calculated CO_2 adsorption isotherms at 303 K for pressure up to 30 bar in the two structural forms of MIL-53(Al) and concluded that the μ_2-OH groups in MIL-53(Al) is the main factor for structural transition. The calculated adsorption isotherm for CO_2 in MIL-53(V) overestimates experimental results probably due to the presence of incomplete solvent molecules in experiment samples. In addition, Ramasahye et al. [204] used DFT to probe the different adsorption sites for CO_2 adsorption in MIL-53(Al, Cr) and MIL-53(V).

2.1.4 Other Gases

Kawakami et al. [198] simulated N_2, O_2 and Ar adsorption in $Zn_3(bdc)_3$ and compared the predicted N_2 adsorption with experimental data up to 1 atm. They found that the predictions were 1.7 times larger than experimental data. They also observed the formation of O_2 magnetic chain due to the confinement of O_2 position and orientation by the $Zn_3(bdc)_3$ pores. Vishnyakov et al. [205] investigated Ar adsorption in Cu-BTC using GCMC simulations and experimental measurements at 87 K. They adjusted the force field parameters in their simulations to match experimentally determined Henry's constant. The simulated isotherms using UFF [174] agree well with experiments over most loadings but over-predicted the saturation loading. The preferential adsorption sites were identified, first in the side pockets and followed by condensation in the main channels. Dubbeldam et al. [206] studied adsorption

isotherms for Ar and N_2 in IRMOF-1 at 78 K. They scaled down the simulated adsorption isotherms by a factor 0.725 to match experiment data and also identified the adsorption sites for Ar and N_2 in IRMOF-1. The positions and occupations of the adsorption sites match well with experiments. The molecules are localized around their crystallographic sites at 30 K, however, at 300 K they are quite dispersed inside the pore. The preferential adsorption site were also identified for many gases such as Ar, N_2, CO_2, CH_4, H_2, C_2H_6 and C_3H_8, which are near to the ZnO_4 cluster with the organic linkers pointing outward.

Walton et al. [207] calculated BET surface areas in various IRMOFs, IRMOF-1, -6, -10, -14, -16 and -18 using the adsorption isotherms of N_2 and found good agreement with the accessible surface areas estimated from crystal structures. They concluded that by careful choosing of pressure range, BET method can be used to obtain the surface areas of MOF materials. Yang et al. [208] simulated the adsorption isotherms of N_2 and O_2 in Cu-BTC and adjusted the potential parameters to match experimental adsorption isotherms at 295 K and pressure up to 1 bar. Later they used these potentials to study mixture adsorption. Garberoglio et al. [173] predicted the adsorption isotherms of Ar in Cu-BTC at 87 K and in manganese formate at 78 K. The simulated result agrees well with experiment in Cu-BTC at low pressure, however, overestimated at high pressure by a factor of ~ 30 %. In manganese formate, the predicted isotherm is a factor of ~ 50 larger than experimental value. Since the experiment was conducted at temperature lower than the triple point of Ar (83. 8 K), the discrepancy may arise due to the formation of bulk like Ar clusters on the adsorbent surface. Similarly, Garberoglio et al. [181] simulated Ar adsorption in COF-102 and COF-103 at 87 K using UFF and DRIEDING force fields and compared with experiments. The predicted adsorption overestimated experiments by

~ 25 % upon saturation and worse at low pressures. The author mentioned the possible discrepancy might be due to a number of effects, including defects in the crystal structure, inaccurate solid-fluid interaction potentials and structure change upon adsorption at high loadings.

Cao et al. [195] used first-principle calculations performed at MP2 level of theory to calculate the interaction parameters of Ar and H_2 with various COFs and predicted adsorption isotherms of Ar in COF-102 and COF-103 at 87 K. They obtained reasonably good agreement with experiments compared with the results obtained by Garberoglio et al [181]. Liu and co-workers [209] calculated N_2 adsorption isotherm at 77 K in Cu-BTC to obtain the surface area and pore volume. The calculated isotherm matches well with the experiment samples of Cu-BTC activated by a novel method. However, poor agreement was observed when compared with other groups using different activation procedures [210]. They also compared simulated isotherms of N_2 at 253 and 298 K with experiments up to a maximum pressure of 60 bar. The simulated isotherms underestimated experimental data, as attributed to the ignorance of charge-quadrupole interactions of N_2 with framework atoms.

2.2 Multi-Component Adsorption

Experimental measurement of single-component adsorption isotherms in MOF and other nanoporous material is straight-forward, however, measuring mixture adsorption is much more complicated and time consuming. For practical applications of adsorption separation, information on mixture adsorption is important. Molecular simulations have been extensively used to predict mixture adsorption in MOFs. Düren and Snurr [211] reported CH_4/n-C_4H_{10} mixture adsorption in IRMOFs-1, -8, -10, -14 and -16 at room temperature and pressure up to 40 bar. They simulated pure CH_4,

C_4H_{10} and their mixture adsorption in MOFs to study the effect of linkers on adsorption. CH_4 shows a type-I isotherm, whereas C_4H_{10} isotherm is more complex, showing sharp jumps. Mixture selectivity of n-C_4H_{10} over CH_4 increases by reducing the pore size and increasing the number of carbon atom in the linker. Based on this, they proposed a hypothetical structure with a 9,10-anthracenedicarboxylate linker and named it IRMOF-993. Predicted selectivity in this structure is as high as 2500. Jiang et al. [212] examined mixture adsorption of C_1-nC_5 linear alkanes and C_5 isomers in IRMOF-1, silicalite and (10,10) carbon nanotube. They found that the enthalpy effect dominates at low pressures, favoring long alkane over short alkane and linear alkane over branched alkane, while at high pressures entropy effects become important, favoring adsorption of short alkane.

Yang et al. [208] predicted adsorption separation of CO_2 from $CO_2/N_2/O_2$ mixtures, a representative of flue gas in Cu-BTC. They reported a selectivity of 20 at room temperature at a total pressure of 5 MPa. Similarly, Wang et al. [213] performed simulation in Cu-BTC for the separation of CO_2 from CO and olefins from paraffins mixtures. For an equimolar mixture, the selectivity of CO_2 over CO is ~ 25 at a pressure of 5 MPa, whereas the selectivity of C_2H_4 from CO_2 is ~ 2 under the same conditions. Wang et al. [214] predicted mixture selectivity of $CO_2/CH_4/C_2H_6$ mixture in manganese-formate MOFs. They found that the selectivity of CO_2/CH_4 mixture is larger than that in IRMOF-1 and Cu-BTC [215] and higher than most carbon and zeolite materials. Martin-Calvo et al. [216] studied the adsorption and separation of natural gas considering two- and five-component mixtures in IRMOF-1 and Cu-BTC. They found that the adsorption capacity is higher in IRMOF-1 and adsorption selectivity of CO_2 over CH_4 and N_2 is higher in Cu-BTC. Yang and Zhong [172] performed GCMC simulations to investigate the separation features of Cu-BTC and

IRMOF-1 for mixtures of CO_2, CH_4 and H_2. The adsorption selectivity varies depending on the structure topology and the interaction strength of the framework with adsorbates. Selectivity of CH_4 over H_2 in an equimolar mixture at room temperature and pressure of 5 MPa was found to be ~ 6 and ~ 12 in IRMOF-1 and Cu-BTC, respectively. In IRMOF-1, the selectivity of CH_4 over H_2 is nearly independent of pressure. On the other hand, the selectivity of CO_2 over H_2 shows a different trend in Cu-BTC, which initially decreases and then increases, reaching a maximum and finally decreases at high pressures. At a pressure of 5 MPa, the selectivity of CO_2/H_2 is around 40 and 110 in IRMOF-1 and Cu-BTC. Ideal adsorbed solution theory (IAST) has been tested to compare the mixture selectivity with simulation results. For CH_4/H_2 mixture, IAST predicts the mixture selectivity quite accurately upon comparing with the simulation, however, for CO_2/H_2 mixture the prediction from IAST is poor. The discrepancy can be attributed to the difference in size and the interaction strength of adsorbates with MOFs.

The siting and segregation of complex alkane mixtures were simulated in MOF-1, which suggested new possibilities for the design of highly selective adsorption sites in MOFs and removing low RON alkanes from mixed stream [217]. Alkanes in Cu-BTC were studied by infrared microscopy and simulation, and strong inflection characteristics were found in the isotherms due to the preferential locations close to the mouths of octahedral pockets [218]. Liu et al. [219] performed simulation to study the effect of interpenetration on mixture separation in MOFs. They chose different MOFs with and without interpenetration (IRMOFs -10, -12, -14 and IRMOFs -9, -11 and -13) to compare the adsorption selectivity of CH_4/H_2 mixtures at room temperature. The results showed that the selectivity is greatly enhanced in the interpenetrated framework compared to its non-interpenetrated counterparts due to the

formation of small pore size, resulting in increased interaction. Recently, Liu et al. [220] performed a systematic simulation study to compare the separation of CO_2/N_2 and CH_4/N_2 mixtures in two classes of nanoporous materials, zeolites and MOFs. Three zeolites (MFI, LTA and DDR) and seven MOFs (Cu-BTC, MIL-47 (V), IRMOFs-1, -12, -14, -11 and -13) were chosen for study. The results showed that MOFs are better for gas storage and their separation performance is comparable to zeolites. They also tested the applicability of IAST to predict mixture selectivity based on single-component isotherms and found a reasonable good agreement between IAST and simulation results in both zeolites and MOFs.

2.3 Diffusion

In gas separation in porous materials, diffusion is also important. A number of simulation studies have been reported for gas adsorption in MOFs. Skoulidas, for the first time, reported the gas diffusion study in HKUST-1 using molecular dynamics (MD). The results showed that the transport diffusivity of Ar in HKUST-1 differs from the self-diffusivity by two orders of magnitude at high loadings. Indeed, the diffusion in HKUST-1 is similar to that in silica zeolites in magnitude, concentration and temperature dependence [221]. Skoulidas and Sholl further examined the self- and transport diffusion of light gases such as Ar, CH_4, CO_2 and N_2 in MOF-2, MOF-3, MOF-5 and Cu-BTC. They found the transport diffusivities of Ar, CH_4 and N_2 increase as a function of pore loading in MOF-5, however, the transport diffusivities of CO_2 are a non-monotonic function of pore loading [222]. Sarkisov et al. [223] simulated the self-diffusivities of CH_4, *n*-C_5H_{12}, *n*-C_6H_{14}, *n*-C_7H_6 and cyclo-C_6H_{14} in MOF-5. An interesting conclusion is that the predicted diffusivities in MOFs are in similar magnitude to those in silica zeolites. Jhon et al. [197] measured self-

diffusivities of CH_4 in alkoxy-functionalised IRMOFs, which were decreased compared to those in IRMOF-1 due to the steric effect.

A comprehensive review on understanding the diffusion of adsorbed molecules in crystalline nanoporous materials was highlighted by Sholl [224]. Most of the studies related to diffusion in MOFs excluded the lattice dynamics by freezing the framework. Amirjalayer et al. [225] predicted the self-diffusion of benzene in both rigid and flexible MOF-5. They found that the self-diffusion of benzene is higher in rigid MOF than a flexible one. This value is quite comparable with the experimental reported value of Stallmach et al. [226]. Dubbeldam et al. [227] used a flexible force field to investigate the negative thermal expansion of IRMOFs-1, -10 and -16. Greathouse and Allendorf [228,229] developed a flexible force field to model the interaction of water with IRMOF-1 and later reported MD simulations on several hydrocarbons to validate this force field in IRMOF-1.

Diffusion properties of H_2 are also important together with the adsorption capacity for practical H_2 storage. Yang and Zhong [170] reported H_2 diffusion in IRMOFs-1, -8 and -18 and found that the self-diffusivity of H_2 in IRMOF-18 is smaller than in IRMOFs-8 and -1 due to the steric hindrance of the pendant CH_3 groups. In addition, the diffusivity of H_2 is larger in IRMOF-8 than in IRMOF-1 due to the relatively larger pore size. Skoulidas and Sholl [222] studied H_2 diffusion in IRMOF-1 and found the self-diffusivity of H_2 decreases as a function of loading, whereas transport diffusivity increases monotonically. Liu et al. [230] calculated the self-diffusivity of H_2 in ten different MOFs with and without catenation and showed that the catenation reduces diffusivity by a factor of 2-3 fold at room temperature and high free volume increases diffusivity. Liu et al. [231] simulated self- and transport diffusivities of H_2 in $[Zn(bdc)(ted)_{0.5}]$-based MOFs synthesized in their lab and found that the diffusivity of

H_2 is comparable to that in IRMOF-1 at 298 K. Salles et al. [232] calculated the self-diffusivity in two MOFs, MIL-47 (V) [33] and MIL-53 (Cr) [29] and showed that H_2 diffusivity is about 2 orders of magnitude greater than in zeolites, supported by the quasielastic neutron scattering experiment. Garberoglio and Vallauri [233] reported the self- and transport diffusivities of H_2 in 2D-COFs (COF-6, COF-8 and COF-10) [51] and found that the diffusivity is one order of magnitude greater than in MOFs.

Mixture diffusion in MOFs is essential to predict the possible utility of MOFs in chemical separations. Measuring mixture diffusion experimentally is challenging, in this regard molecular simulations play a useful role in predicting mixture diffusion in nanoporous materials. However, simulation study on mixture diffusion in MOFs is rare. We reported the first simulation study for mixture diffusion in IRMOF-1, which will be discussed later in Chapter 4 [234]. Seda et al. [235] predicted the adsorption and diffusion of H_2/CH_4 mixture in Cu-BTC and tested several correlations for transport properties in nanoporous materials. Seda et al. [236,237] further used atomically detailed simulations to examine the performance of MOFs as membranes for the separation of CO_2/CH_4, CO_2/H_2 and CH_4/H_2 in MOF-5 and Cu-BTC. They validated this method in screening additional MOFs, IRMOFs-8, -9, -10 and -14, $Zn(bdc)(ted)_{0.5}$, and COF-102 to examine the chemical diversity and interpenetration on the performance of MOFs membranes for gas separation.

Chapter 3

Simulation Methodology

3.1 Interaction Potential

Interaction potential plays a central role in molecular simulations; therefore, it should be accurately modeled. In a simulation system, the total interaction energy U^{total} can be decomposed into two contributions,

$$U^{total} = U^{bonded} + U^{non-bonded} \tag{3.1}$$

where U^{bonded} is the intramolecular energy within a molecule and $U^{non-bonded}$ is the intermolecular energy arising between different molecules.

The non-bonded intermolecular energy usually consists of three terms,

$$U^{non-bonded} = U^{vdW} + U^{Coulombic} \tag{3.2}$$

where U^{vdW} is the van der Waals interaction energy and $U^{Coulombic}$ is the coulombic interaction energy.

The bonded intramolecular energy is sum of the following terms,

$$U^{bonded} = U^{stretching} + U^{bend} + U^{torsion} \tag{3.3}$$

where $U^{stretching}$ is the bond stretching energy, U^{bend} is the bond bending energy for the angle formed by two successive chemical bonds, and $U^{torsion}$ is the torsional energy due to the dihedral angles formed by four successive atoms in a chain.

The van der Waals interaction is usually mimicked by Lennard-Jones (LJ) potential,

$$U_{LJ}(r) = 4\varepsilon \left[\left(\frac{\sigma}{r} \right)^{12} - \left(\frac{\sigma}{r} \right)^{6} \right] \tag{3.4}$$

where σ is the collision diameter and ε is the well depth. For a system composed of different types of atoms, the total Lennard-Jones interaction energy is

$$U_{LJ}(r) = \sum_{\substack{i,j \\ i<j}} 4\varepsilon_{ij} \left[\left(\frac{\sigma_{ij}}{r} \right)^{12} - \left(\frac{\sigma_{ij}}{r} \right)^{6} \right] \tag{3.5}$$

where ε_{ij} and σ_{ij} depend on the pair of atoms considered and are generally derived from ε_i and σ_i of pure components by appropriate combining rules, for instance, the most widely Lorentz-Berthelot rules

$$\sigma_{ij} = \frac{\sigma_i + \sigma_j}{2} \tag{3.6}$$

$$\varepsilon_{ij} = \sqrt{\varepsilon_i \varepsilon_j} \tag{3.7}$$

The coulombic interaction is modeled by the Coulomb's law,

$$U^{Coulomb} = \sum_{\substack{i,j \\ i<j}} \frac{1}{4\pi\varepsilon_o} \frac{q_i q_j}{r_{ij}} \tag{3.8}$$

where q_i and q_j are the charges in atoms i and j. The atomic charges are usually estimated by quantum chemical methods.

On the basis of different functional forms and various resources used to optimize potential parameters, there are numerous force fields have been developed over the years suitable for a particular class of molecules, e.g., Universal Force Field [174] (for organics, main group elements and organometallic systems) Dreiding II [175] (for organics, biological compounds, main group elements, and polymers), CVFF class II force fields [238] (for proteins and organics), PCFF [238] (for polymers and materials science applications), Burchart and BKS [239] (for zeolites), specialty force fields for sorption [240]. Other newly developed force fields include MM2 [241], MM3 [242-245], MM4 [246-248], AMBER [249], CHARMM [250], Tripos [251]. A general force field should be able to cover a broad range of elements in the periodic table and

used for various compounds. UFF is one such a force field designed for simulating molecules containing any combination of elements. The parameters were defined by combining atomic parameters and empirical rules. They expected to yield reasonable predictions of molecular structures, whereas predicting other molecular properties such as vibration frequencies and conformation properties are limited. Many well-parameterized force fields such as MM3, MM4, CHARMM, AMBER and MMFF (Merck Molecular Force Field) were designed primarily for biologically interesting molecules. However, these force fields give very poor results for adsorption in nanoporous materials.

No matter which interaction potential and force field are used, simulation is always performed on a finite system. To minimize the subsequent surface or heterogeneous effect, periodic boundary conditions are commonly exerted. The minimum-image convention is used to calculate the interaction energy during simulation, with potential truncated at a cutoff distance smaller than half of the box length. For system where coulombic interaction is present, the potential decays with distance, the interaction is handled using Ewald summation in which the interactions from infinite periodic array of simulation cells are summed with the aid of Fourier transformation.

3.2 Monte Carlo

The basic principles of Monte Carlo (MC) simulations used in the thesis are described. The more detailed descriptions have been well documented in several books [252-254].

3.2.1 Canonical Ensemble

Canonical ensemble or NVT ensemble is an assembly of systems, in which the number of particles, temperature and the volume are constant. Each system in the ensemble can share its energy with a heat reservoir or heat bath. The system is allowed to exchange energy with the reservoir, and the heat capacity of the reservoir is assumed to be so large as to maintain a fixed temperature for the coupled system.

For MC simulation in canonical ensemble, sample distribution is performed according to the Metropolis scheme. The algorithm generates random trial moves from a old state (*o*) to a new state (*n*). If $P_B(o)$ and $P_B(n)$ denote the probability of finding the system in the state (*o*) and (*n*), respectively, and $\alpha(o \to n)$ and $\alpha(n \to o)$ denotes the conditional probability to perform a trial move from $(o \to n)$ and $(n \to o)$, respectively, then the probability $P_{acc}(o \to n)$ is related to $P_{acc}(n \to o)$ by

$$P_B(o)\alpha(o \to n)P_{acc}(o \to n) = P_B(n)\alpha(n \to o)P_{acc}(n \to o) \tag{3.9}$$

The probability of generating a particular configuration is constant and independent of the conformation of the system.

$$\alpha(o \to n) = \alpha(n \to o) = \alpha \tag{3.10}$$

Introducing this condition in the detailed balance, equation 3.9 gives the acceptance rule as

$$P_{acc}(o \to n) = \min\left[1, \frac{P_B(n)}{P_B(o)}\right] \tag{3.11}$$

In adsorption studies, MC simulations are particularly convenient for computing equilibrium thermodynamic quantities such as the isosteric heat and Henry's constant. In addition, MC simulations provide detailed structural information, in particular, the location and distribution of adsorbed molecules in the pores. Adsorption quantities are usually computed in the grand canonical ensemble as described below.

3.2.2 Grand Canonical Ensemble

In Grand Canonical Monte Carlo (GCMC) simulation, the chemical potential (μ), volume (V), and temperature (T) are fixed. At equilibrium, the chemical potentials of adsorbate in the bulk phase and adsorbed phase are equal. The pressure in the bulk phase can be calculated from an equation of state and it is thus directly related to the chemical potential in the adsorbed phase. The ensemble average number of molecules in the nanoporous material $\langle N \rangle$ is computed directly from the simulation. By performing simulations at various chemical potentials, one obtains the adsorption isotherm at a given temperature. Experimental adsorption isotherm yields the excess number of molecules adsorbed in the porous medium which is not, in principle, directly comparable to $\langle N \rangle$.

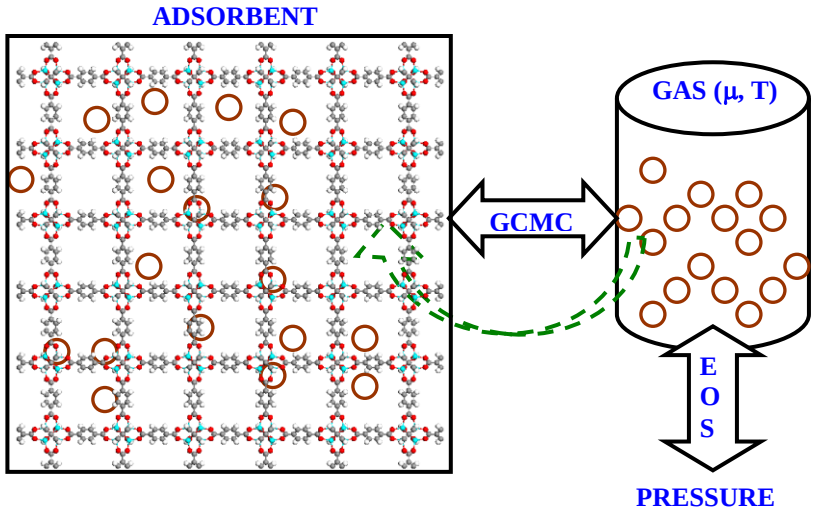

Figure 3.1. Schematic representation of GCMC simulation. Adsorbent in contact with a reservoir that imposes constant chemical potential and temperature by exchanging particles and energy. Equation of state is used to calculate the pressure of gas.

A schematic representation of GCMC simulation is illustrated in Figure 3.1. Three types of moves are usually performed. The first is a displacement and/or rotation, in which the new move is accepted with a probability

$$P_{acc}(o \to n) = \min\left(1, \exp\left\{-\beta\left[U(n) - U(o)\right]\right\}\right) \tag{3.12}$$

where β is the inverse temperature $1/k_BT$, k_B is Boltzmann's constant. U is the potential energy, and 'o' refers to old state and 'n' refers to new state. In the second type, a new molecule is inserted in to the system at a randomly chosen position. The new configuration is accepted with a probability

$$P_{acc}(N \to N+1) = \min\left[1, \frac{fV\beta}{(N+1)} \exp\left\{-\beta\left[U(N+1) - U(N)\right]\right\}\right] \tag{3.13}$$

where f is the gas fugacity, V is the volume of the simulation box, N is the number of molecules present before the attempted insertion. In the third type, a molecule is randomly chosen to be deleted with a probability

$$P_{acc}(N \to N-1) = \min\left[1, \frac{N}{fV\beta} \exp\left\{-\beta\left[U(N-1) - U(N)\right]\right\}\right] \tag{3.14}$$

In normal GCMC, insertions are attempted throughout the entire volume of the simulation box. Nevertheless, part of the volume is occupied by adsorbent atoms and inaccessible to sorbate molecules. Therefore a preferred region exists where the sorbate molecules could be inserted energetically favorable with increased acceptance rate. In this case, the acceptance rules for insertions and deletions must be altered to ensure that microscopic reversibility is satisfied and that the grand canonical ensemble is still correctly sampled. For the adsorption of long-chain molecules in a porous material, the configurational-bias (CB) scheme [255] is often used based upon the Rosenbluth sampling scheme [256]. The chain molecule is inserted bead by bead into the pore. First, a number of candidate positions are generated for the atom to be inserted. One of these positions is then selected according to the energy contributions from the external degrees of freedom of the molecule. When the molecule is constructed, a Rosenbluth weight is accumulated and used in the acceptance rule. This procedure was shown by Smit [257,258] for the adsorption of united-atom (UA)

linear alkanes and later extended to branched alkanes [259,260] and to all-atom (AA) alkanes [261]. The CB-GCMC scheme is primarily for flexible chain molecules, and other bias has to be used in the case of rigid molecules. For aromatic molecules, different biased schemes such as cavity-bias [262,263], energy-bias, energy/cavity-bias [264] and orientational-bias [263-271] GCMC schemes have been used.

3.1.3 Gibbs Ensemble

Gibbs Ensemble Monte Carlo (GEMC) method was first introduced for the simulations of phase equilibria in bulk systems by Panagiotopoulos [272]. Considering a macroscopic system with two phases co-existing at equilibrium, Gibbs ensemble simulation is performed in two microscopic regions without the interface. The thermodynamic requirements for phase coexistence require the equality of temperature, pressure, chemical potentials of all components in the two phases. Temperature of the system is specified in advance in GEMC simulation. Three types of MC moves are performed in order to satisfy the three conditions mentioned, namely, displacement of particle with in each region to satisfy internal equilibrium, coupled volume change to satisfy equality of pressures, and swap particles between regions to satisfy equality of chemical potential. The acceptance criteria for GEMC were originally derived from fluctuation theory. Detailed statistical mechanical definition of the ensemble can be found in Smit et al. [273] and Smit and Frenkel work [253]. GEMC methods were modified to study the equilibrium properties of adsorbed fluid in nanospace. The method includes the pore-bulk GEMC [274], the pore-pore GEMC [274], the constant pressure pore-bulk GEMC method [275] and the gauge cell method [276,277].

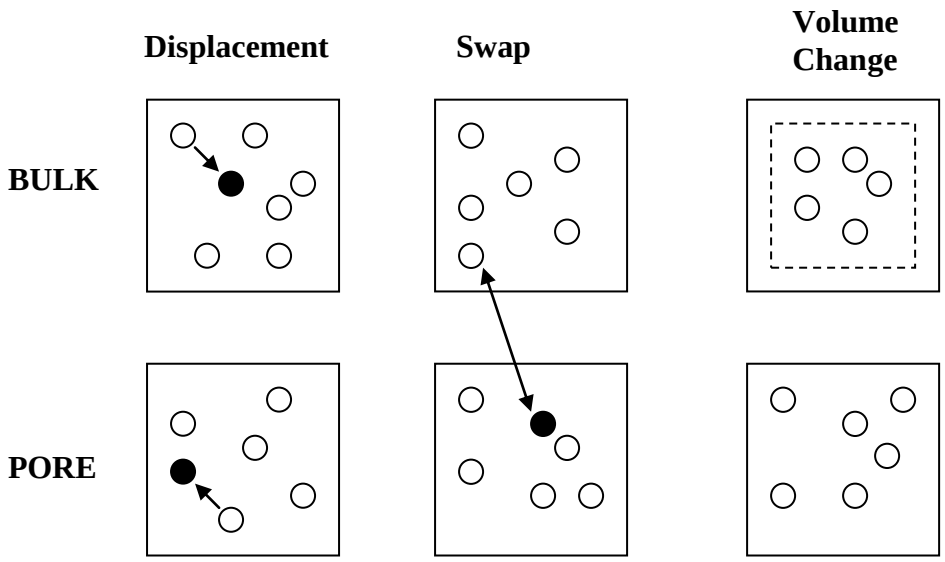

Figure 3.2. Three types of move attempted in constant pressure-GEMC. Volume changes only in the cell representing the bulk fluid.

In constant-pressure GEMC, two simulation cells are used one for the adsorbent and the other for bulk fluid. The total number of the particles, volume of the adsorbent and temperature are fixed. Rather than fixing the volume of the bulk fluid, the pressure is fixed. A schematic representation of constant-pressure GEMC simulation is illustrated in Figure 3.2. Three types of trial moves are implemented randomly, namely displacement in each phase, swap between two phases, and volume change of the bulk phase. For displacement, the number of particle in each phase is fixed and the trial move is accepted using the Metropolis scheme. Creation of a particle in the adsorbed phase (A), corresponding to deletion in the bulk (B) phase, is accepted with a probability of

$$\min\left\{1, \exp\left[-\beta(\Delta U_A + \Delta U_B)\right] N_B V_A / (N_A + 1) V_B\right\} \qquad (3.15)$$

where $\beta = 1/k_B T$, N_A, N_B refers to the number of particles in the adsorbed and bulk phase, V_A, and V_B refers to the volume of the adsorbent and bulk phase. Similarly, the probability of acceptance for deletion of a particle in the adsorbed phase and its creation in bulk phase is

$$\min\left\{1, \exp\left[-\beta(\Delta U_A + \Delta U_B)\right] N_A V_B / (N_B + 1) V_A\right\} \tag{3.16}$$

The acceptance probability for the trial volume change in the bulk phase is

$$\min\left\{1, \exp\left[-\beta \Delta U_B + \beta P \Delta V_B + N_B \ln(1 + \Delta V_B / V_B)\right]\right\} \tag{3.17}$$

3.3 Molecular Dynamics

Understanding the diffusion of molecules in a porous material is important, as the diffusion behavior in confined space is differently from bulk phase. Diffusion in pores can be classified in a number of different regimes depending on the pore diameters. In a large pore over 50 nm or more in diameter, collisions between the molecules occur more frequently than collisions with the pore wall. This type of diffusion is usually referred as molecular diffusion or fickian diffusion. With decreasing pore size, the number of collisions with the wall increases. As the pore size becomes smaller than the mean free path (the average distance travelled by a molecule between two collisions), the diffusion behaves in Knudsen regime, which is normally for pores with diameter between 2 and 50 nm. At even smaller pore, in which the diameter is comparable to the molecular size and molecules continuously experience the interaction with the pore, configurational diffusion occurs.

Molecular dynamics (MD) simulates the time evolution of molecules by solving Newton's equation of motion. Structural and thermodynamics properties can be calculated from an equilibrium MD simulation. The Newton's second law states

$$F_i = m_i a_i \tag{3.18}$$

where F_i is the force acting on the particle i, m_i and a_i are the particle's mass and acceleration, respectively. Since we are interested in the time evolution of the particle, eq. 3.18 can be expressed in terms of displacement r with respect to time t.

$$\frac{\mathrm{F_i}}{m_i} = \frac{d^2 r_i}{dt^2} \tag{3.19}$$

The trajectory of the system can be obtained by solving eq. 3.19. To integrate eq. 3.19, several finite difference schemes have been proposed and are discussed in detail elsewhere. In particular, the Verlet algorithm is probably most widely used for integrating the equation of motion in MD simulation. The basic equation in the Verlet algorithm is

$$\mathrm{r}(t+\Delta t) = \mathrm{r}(t) + \mathrm{v}(t)\Delta t + \mathrm{a}(t)\Delta^2 t \tag{3.20}$$

The time step Δt is chosen such a way that the integration is accurate enough and the total energy of the system is conserved. The average properties of the system can be determined from the trajectory obtained over a sufficient period of time.

Diffusion can be characterized into self-, corrected and transport diffusion at different length scales [278]. Self-diffusivity describes the mobility of individual molecules, also called tracer diffusivity, can be estimated from the mean-squared displacement based on the Einstein relation [279]

$$D_s(c) = \lim_{t\to\infty} \frac{1}{6t} \left\langle \frac{1}{N} \sum_{k=1}^{N} \left| \mathbf{r}_k(t) - \mathbf{r}_k(0) \right|^2 \right\rangle \tag{3.21}$$

where c is concentration, $\mathbf{r}_k(t)$ is the position of kth molecule at time t, N is the number of molecules. This definition applies to both single and multi-component systems. At a macroscopic scale, Fick law of diffusion gives the phenomenological relation between flux **J** and concentration gradient ∇c ,

$$\mathbf{J} = -D_t(c)\nabla c \tag{3.22}$$

The transport or Fickian diffusivity D_t can be evaluated from the corrected diffusivity $D_c(c)$ and thermodynamic correction factor $\Gamma(c)$

$$D_t(c) = D_c(c)\Gamma(c) \tag{3.23}$$

with

$$\Gamma(c) = \left(\partial \ln f / \partial \ln c\right)_T \tag{3.24}$$

where f is the fugacity of fluid in equilibrium with the adsorbed phase at a concentration c. $\Gamma(c)$ at a given temperature T can be evaluated from equilibrium adsorption isotherm. The corrected diffusivity $D_c(c)$, also called jump diffusivity, can be written as

$$D_c(c) = Lk_BT / c \tag{3.25}$$

where L is the phenomenological coefficient, k_B is Boltzmann's constant. Note that corrected diffusivity is equal to the Maxwell-Stefan diffusivity for system with only one species. From the linear response theory, L is related to the flux autocorrelation function by

$$L = \frac{1}{3Vk_BT}\int_0^\infty \left\langle \mathbf{j}(0)\cdot\mathbf{j}(t)\right\rangle dt \tag{3.26}$$

where V is system volume, $\mathbf{j}(t)$ is the microscopic current defined as the sum of molecular velocities

$$\mathbf{j}(t) = \sum_{k=1}^{N} \mathbf{v}_k(t) \tag{3.27}$$

The microscopic current is an equilibrium property and can be directly obtained from MD simulation. Equation 3.26 is the Green-Kubo form, and the equivalent Einstein form can be found elsewhere [278]. The above expression can be extended to multicomponent systems. Self-, corrected and transport diffusivities are concentration dependent and generally not equal to each other unless at infinite dilution,

$$D_s(0) = D_t(0) = D_c(0) = D(0) \tag{3.28}$$

Chapter 4

Adsorption and Diffusion of CO_2 and CH_4 in Three Different Types of Nanoporous Materials

4.1 Introduction

Combustion of fossil fuels has generated huge amount of greenhouse gas CO_2. The relationship between anthropogenic emission of CO_2 and increased temperature has been well recognized, and the effect of increasing atmospheric CO_2 concentration on global warming is now regarded as one of the most pressing environmental issues. To reduce the atmospheric level of CO_2 while minimizing the world economic impact, four strategies have been proposed: 1) carbon sequestration, 2) less carbon-intensive fuels, 3) more energy-efficient methods, and finally 4) increased conservation. It is expected that CO_2 sequestration to be implemented in the coming 30 years will be both economically and environmentally attractive [280], and several approaches have been developed such as chemical conversion, solvent absorption, deep sea deposition, and adsorption in porous media. Compared to the commonly used purification technique of CO_2 absorption, adsorption is technically feasible, affordable, and energy efficient [281].

In the long run, use of less carbon-intensive fuels, e.g. natural gas, will help in reducing overall CO_2 emissions. The major component in natural gas is CH_4, thus it is essential to find a suitable adsorptive material for CH_4 storage. On the other hand, CO_2 is often found as a major impurity in natural gas [282], and its presence can reduce the energy content of natural gas. Consequently, in addition to the storage of pure CO_2 and CH_4, it is also important to separate their mixture.

The selection of a suitable adsorbent is a key step in the design of adsorption-based storage or separation processes. A number of experimental and simulation studies have been reported on the adsorption of gases in various adsorbents and many of these have been summarized in two recent books [283,284]. Most studies have focused on zeolites and carbon-based adsorbents. Inorganic porous materials, such as zeolites in which the Si-O and Al-O bonds have tetrahedral oxide skeletons, generally can be produced in only a limited range of structures. Recently, a new class of porous materials have been developed, the metal organic frameworks (MOFs), which consist of metal-oxide clusters and organic linkers [2,7,285]. MOFs allow for the formation of flexible porous frameworks with a wide variety of architectures, topologies and pore sizes. They provide almost unlimited opportunities to develop, control, and tune structures for specific applications [5]. Due to their high porosity and well-defined pore size, MOFs are promising candidates for the storage of gases, the separation of mixtures, and ion-exchange [286].

In this work, atomistic simulations were used to investigate the storage capacity for pure CO_2 and CH_4 and their binary mixtures in three different adsorbents: silicalite, C_{168} schwarzite, and IRMOF-1. Each of them has a well defined three-dimensional periodic structure with nano-sized channels, and each represents a typical class of nanoporous material. The mixture diffusion was also studied in the three adsorbents, as well as the permselectivity based on the adsorption and diffusion selectivity of binary mixture. In Section 4.2 the models used for the different adsorbents and the two adsorbates are described. In Section 4.3 the simulation methods are briefly described. The results and discussion are briefly explained in Section 4.4, followed by summary in Section 4.5.

4.2 Models

Silicalite

Usually denoted as MFI, silicalite is an Al-free zeolite existing in three distinct crystal forms: monoclinic, *Pnma* and $P2_12_12_1$ orthorhombic structures. In this work, the *Pnma* orthorhombic structure is considered. The unit cell has 96 Si atoms and 192 O atoms, and the lattice constants are $a = 20.06$ Å , $b = 19.80$ Å , and $c = 13.36$ Å . As shown in Figure 4.1a, MFI consists of two types of channels with 10-membered rings, one is straight and the other is zig-zag (sinusoidal).

These channels have diameters of approximately 5.4 Å . This implies that an adsorbate molecule with a van der Waals diameter of about 5.4 Å or less can fit inside these channels. A unit cell has two straight channels, two zigzag channels, and two channel intersections. The potential parameters and atomic charges for MFI are taken from the work of Hirotani et al. [287] as listed in Table 4.1, which had been optimized to reproduce the experimental heats of adsorption. It is worthwhile to note that in most of the previous simulation studies of adsorption in zeolites, the short-ranged dispersion interaction of Si atoms was neglected because of its weak contribution and thus only electrostatic interaction was taken into account. To model the framework fully atomistically, in this work both the dispersion and electrostatic interactions were considered for the O and Si atoms.

(a) MFI

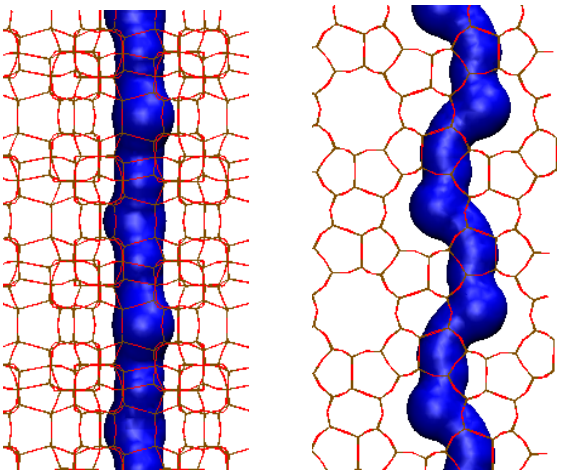

(b) C_{168}

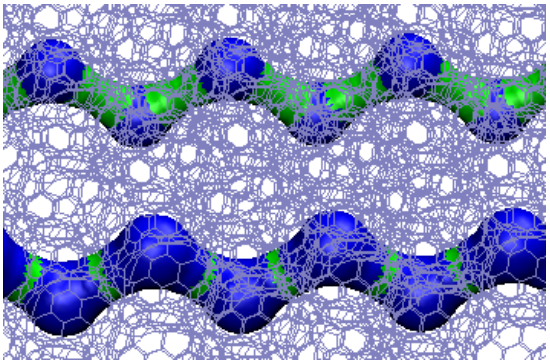

(c) IRMOF-1

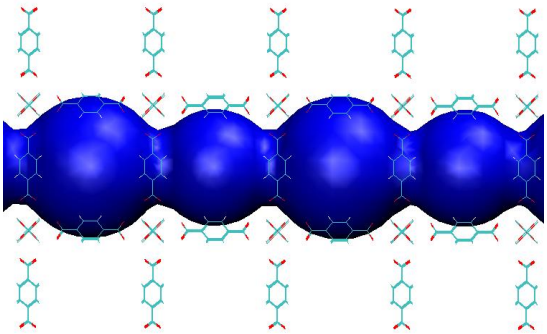

Figure 4.1. Nano-sized channels in MFI, C_{168}, and IRMOF-1. (a) MFI has one straight channel and one zig-zag channel (b) C_{168} has two zig-zag channels. (c) IRMOF-1 has one straight channel.

C_{168} schwarzite

Nanoporous carbon membranes are amorphous and do not have well-defined structures, consequently, the hypothetical C_{168} schwarzite [288] is used in this work to represent the nanoporous carbon. C_{168} schwarzite has a simple periodic structure with well-defined channels, and carbon-surface curvatures are similar to those in realistic samples. In addition to the primary six-membered rings, there are also five-, seven-, and eight-membered rings. The unit cell of the C_{168} schwarzite has a length of 21.8 Å and 672 carbon atoms. As shown in Figure 4.1b, there are two types of channels in C_{168} schwarzite with average diameters of approximately 7 and 9 Å , respectively. The channels in the same layer are isolated from each other, but they are connected with those in the neighboring layers by channel intersections.

IRMOF-1

IRMOF-1 is an isoreticular MOF and also known as MOF-5 [7]. It has a lattice constant of 25.832 Å , a crystal density of 0.593 g/cm^3, a free volume of 79.2%, and a surface area of 2833 m^2/g [98]. For simulation, the atomic coordinates of the crystal were taken from experimental x-ray crystallographic data [3]. IRMOF-1 has a formula of $Zn_4O(BDC)_3$, where BDC is 1,4-benzenedicarboxylate [2]. Each oxide-centered Zn_4O tetrahedron is edge-bridged by six carboxylate linkers resulting in an octahedral $Zn_4O(O_2C–)_6$ building unit, which reticulates into a three-dimensional cubic structure. As shown in Figure 4.1c, there is one type of straight channel in IRMOF-1 with sizes of 15 and 12 Å along the channel. The dispersive interactions of the atoms in IRMOF-1 are modeled by the universal force field [174]. All adsorbent structures are shown in Figure 4.2.

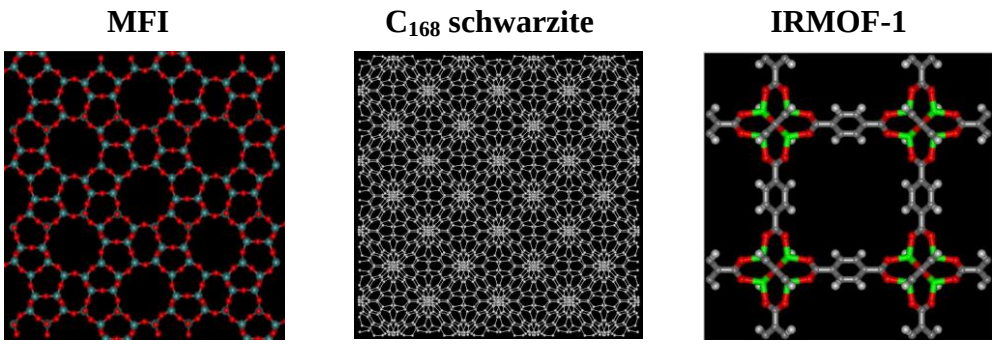

Figure 4.2. Schematic representations of MFI, C_{168} schwarzite and IRMOF-1.The structures are not drawn to scale their actual sizes.

TABLE 4.1. LJ and Coulombic potential parameters for MFI, C_{168} and IRMOF-1[174, 287-288]

Adsorbent	site	σ(Å)	ε / k_B (K)	q (e)
MFI	**O**	2.708	128.21	–0.400
	Si	0.677	18.60	+0.800
C_{168}	**C**	3.40	28.00	0
IRMOF-1	**Zn**	2.462	62.343	ESP Charges as shown in Figure 4.3
	C	3.431	52.791	
	O	3.118	30.166	
	H	2.571	22.122	

Atomic Partial Charge

The concept of atomic charges is solely an approximation, and no unique straightforward method is currently available to determine the atomic charges on a rigorous level. Commonly used methods are based on Mulliken population analysis [289], the ElectroStatic Potential (ESP) [290], the Restrained ElectroStatic Potential (RESP) [291] and the CHarges from ELectrostatic Potentials using Grid (CHELPG) [292]. Mulliken's method is from the wave functions and usually overestimates the charges. In the ESP method, the electrostatic potentials are fitted at grids located with equal density on different layers around the molecule. The RESP method sets the charges on the buried atoms to zero by using a penalty function in the fit, and hence

showed improvement over the ESP method. Similar to the ESP method, the electrostatic potentials are calculated in the CHELPG method at grids distributed on a cubic lattice.

The ESP method was used to estimate the atomic charges of IRMOF-1. It has been recognized that quantum mechanically derived charges fluctuate largely with small basis sets. However, they tend to converge beyond a basis set of 6-31G(d). As a consequence, 6-31G(d) basis set was used for all atoms except the transitional metals, for which LANL2DZ basis set was used. LANL2DZ is a double-zeta basis set and contains the effective pseudo-potentials to represent the potential of the nucleus and core electrons experienced by the valence electrons. All DFT computations were carried out with Gaussian 03 programs [293]. Figure 4.3 shows the cluster and the estimated charges in IRMOF-1. The cluster was cleaved from IRMOF-1 unit cell with dangling bonds terminated by CH_3 group.

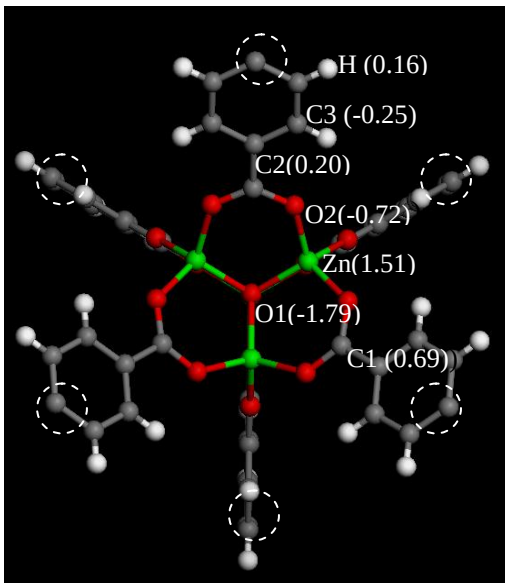

Figure 4.3. Atomic-centered partial charges in an IRMOF-1 cluster from B3LYP/6-31g(d) computation. The cleaved clusters are terminated by methyl group to maintain hybridization.

CH_4 was modeled by the united-atom model, which has been demonstrated to give comparable adsorption isotherms for alkane adsorption in MFI, but with less

computational effort compared to the all-atom model [294]. The intermolecular potential parameters of CH_4 given in Table 4.2 are from the TraPPE force field, developed to reproduce the critical parameters and saturated liquid densities of alkanes [295]. The interactions between CH_4 and adsorbent was modeled using the Lennard-Jones (LJ) potential, and the Lorentz-Berthelot mixing rules [296] was used to calculate cross interaction parameters.

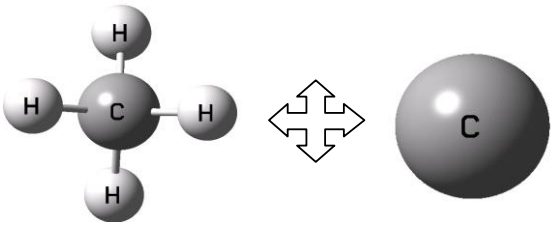

Figure 4.4. Schematic representation of united-atom model for CH_4

CO_2 was represented as a three-site rigid molecule. The intrinsic quadrupole moment is described by the partial charge model. The partial charge on the C atom is 0.576*e*, and to maintain electro neutrality, the partial charge on O atom is –0.288*e*. The CO bond length is 1.18 Å , and the bond angle ∠OCO is 180°. The CO_2–CO_2 intermolecular interactions are modeled as a combination of LJ and coulombic potentials with the potential parameters [288] given in Table 4.2, which are very close to the elementary physical model fitted to the experimental vapor-liquid equilibrium data of bulk CO_2 [297].

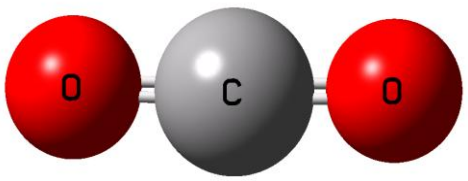

Figure 4.5. Schematic representation of three-site atom model for CO_2

TABLE 4.2. LJ and Coulombic potential parameters for CH_4 and CO_2

Adsorbate	site–site	σ (Å)	ε / k_B (K)	q (e)
CH_4	CH_4	3.73	148.0	0
CO_2	C	2.789	29.66	+0.576
	O	3.011	82.96	–0.288

4.3 Methodology

GCMC simulations at fixed temperature T, volume V, and adsorbate chemical potential μ were carried out for the adsorption of pure CO_2 and CH_4 and their mixture in MFI, C_{168} schwarzite, and IRMOF-1. GCMC simulation allows one to directly relate the chemical potential in adsorbed and bulk phases and so it has been widely used for the simulation of adsorption. The adsorption was investigated at room temperature 300 K. The non-ideal behavior of the bulk pure gas and gas mixture was described by the Peng-Robinson equation of state (PR EoS) [298]. For CO_2/CH_4 mixture, the binary interaction parameter in the PR EoS was assumed to be zero.

The simulation box representing MFI contained 12 ($2 \times 2 \times 3$) unit cells, while for C_{168} schwarzite and IRMOF-1, 8 ($2 \times 2 \times 2$) unit cells were used. No finite-size effect was found in larger simulation box. All the three adsorbents were treated as rigid with atoms frozen during simulations, and the periodic boundary conditions were used in three dimensions to mimic the crystalline periodicity. A spherical cutoff length of 19.0 Å was used in all simulations to evaluate the intermolecular LJ interactions without long range corrections. The coulombic interaction between CO_2 and adsorbent was accounted for using Ewald sum technique [299]. For CO_2 molecules, the coulombic interaction was calculated directly on the basis of the centre-of-mass cutoff of 19.0 Å, because CO_2 molecule is neutral with quadrupole moment, which

converges rapidly with cutoff distance. To accelerate the simulation, the LJ and coulombic interactions between adsorbate and adsorbent were calculated on the basis of a pre-tabulated energy map with a grid of 0.2 × 0.2 × 0.2 Å cubic mesh constructed throughout the unit cell of adsorbent. The same procedure was employed in the subsequent molecular dynamics simulations mentioned later in this chapter.

The number of Monte Carlo trial moves used in a typical simulation was 6 million, though additional moves were used at high pressures. The first half of these moves were used for equilibration and the second half were used for calculating the ensemble averages. For pure CH_4, three types of moves were randomly attempted, translation, insertion, and deletion. For pure CO_2, an additional move, rotation, was also included. For CO_2/CH_4 mixture, in addition to the above mentioned moves, species exchange was also included with equal probability to ensure microscopic reversibility. In this latter move, a randomly selected sorbate molecule is exchanged with the other type of sorbate molecule. While this move is not a requirement in GCMC for mixtures, its use allows faster equilibration and reduces statistical errors after equilibration [300].

At specified T, V, and μ, GCMC simulation gives the absolute number of molecules adsorbed N_{ad}. However, experiment data are usually reported as the excess amount of adsorption N_{ex}. To make a comparison, the experimental N_{ex} was converted into N_{ad} by

$$N_{ad} = N_{ex} + \rho_b V_{free} \tag{4.1}$$

where ρ_b is the density of bulk gas calculated with PR EoS, and V_{free} is the free volume within adsorbent for adsorption estimated from

$$V_{free} = \int_V \exp[-u_{ad}^{He}(\mathbf{r})/k_B T]\, d\mathbf{r} \tag{4.2}$$

where u_{ad}^{He} is the interaction between a single helium atom and adsorbent. In this calculation, s_{He} = 2.58 Å and e_{He}/k_B = 10.22 K were used [301]. Note that the free volume detected by helium is temperature dependent and usually the room temperature is chosen [302]. The porosity of an adsorbent can be estimated by V_{free}/V_{total}, with V_{total} the total occupied volume.

From the loading dependence of the total adsorption energy U_{ad}, the isosteric heat of adsorption q_{st} was calculated [303] as the difference between the enthalpy of adsorbate in gas phase H_b and the partial molar energy of the adsorbed phase [304-306]

$$q_{st} = H_b - \left(\frac{\partial (U_{ad} - U_{intra})}{\partial N_{ad}} \right)_{T,V} \tag{4.3}$$

where H_b can be approximated as RT, U_{ad} includes contributions from both adsorbate–adsorbent and adsorbate–adsorbate interactions, U_{intra} is the intramolecular energy of the adsorbate molecules and is equal to zero for rigid molecules. The partial derivative in equation (4.3) can be calculated by fluctuation theory or direct differentiation of the simulation results. In this work, the latter was used.

Diffusion can be characterized into self-, corrected- and transport diffusion. The details of calculating the various diffusivities are discussed in Chapter 3. MD simulations were carried out in a canonical ensemble (NVT) with the Nosé-Hoover thermostat [252]. A time step of 1 fs was used for CH_4, 0.3 fs for CO_2 and mixture to achieve better energy conservation. All the three adsorbents were assumed to be rigid and the framework atoms were fixed during simulation. It is important to note, however, diffusion can be influenced by the framework flexibility. Diffusion in zeolites is usually accelerated in a flexible model due to the increased possible

pathways for molecular jump [307]. Nevertheless, a reduction of diffusion is observed in flexible carbon nanotube by taking into account the energy exchange between diffusing molecules and the nanotube [308]. The activation energy of benzene in IRMOF-1 is considerably smaller in a flexible framework compared to a rigid one and hence diffusion is higher in the former case. This is attributed to the correlation motion of the benzene with the organic linker phenylene rings, which leads to an increase of the population of benzene in the A-cell pockets [225]. The final configurations of MC simulations for adsorption of pure CH_4, CO_2 and equimolar CH_4/CO_2 mixture were taken as the initial configurations for the MD simulations. For pure CH_4 and CO_2 at 300 K, MD simulations were performed for a total period of 2.5 - 5.0 ns with an equilibration period of 1.0 - 3.5 ns. Ten independent runs were performed at each loading in order to obtain the desired level of statistical accuracy. During the production run, the atomic coordinates were written to disk every 1 ps and then used to calculate the averaged D_s from the Einstein relation. The molecular velocities were written to disk every 0.1 ps, and then used to calculate the flux autocorrelation function and phenomenological coefficient with an upper limit of 30 ps. As demonstrated in the literature [309,310], with even a short limit of 10 ps, the flux autocorrelation function decays to zero and the integral converges to a constant. In addition, the diffusivities at infinite dilution were calculated for CH_4 and CO_2 in all the three adsorbents at various temperatures. To do this, the MD simulation as described above with at least forty molecules in the box was performed by turning off the adsorbate-adsorbate interactions. For CH_4/CO_2 mixture, MD simulations were performed at 300 K for a total period of 8 ns, with the first half left out for equilibration and the second half for ensemble average. The potential and kinetic energies were monitored during simulation to ensure equilibration.

4.4 Results and Discussion

First, the pure and mixture adsorption isotherms and selectivities are presented in the three nanostructures. Then, the simulation results for diffusivity of pure CH_4 and CO_2 are shown at infinite dilution, as well as the activation energies of diffusion. The self-, corrected- and transport diffusivities of pure CH_4 and CO_2 at 300 K are shown as a function of loading. The correlation effects of diffusion are examined and used in the MS formulation for predictions, which are then compared with simulation results. Finally, the simulated and predicted self-diffusivities of CH_4/CO_2 binary mixture are presented at 300 K and the permselectivity for mixture is evaluated.

4.4.1 Adsorption of Pure and Binary Components

4.4.1.1 Limiting Properties

Table 4.3 gives the density and porosity of MFI, C_{168} schwarzite, and IRMOF-1; as well as the limiting heats of adsorption q_{st}^0 and Henry constants K_H of pure CO_2 and CH_4 in each adsorbent. The density decreases in the order of MFI > C_{168} > IRMOF-1, which is opposite to the porosity. For CO_2 and CH_4, both q_{st}^0 and K_H are largest in C_{168}, and are smallest in IRMOF-1. The fact that the limiting properties in C_{168} are larger than in the less porous MFI indicates that there is no direct relation between adsorption affinity and porosity. In a given adsorbent, both q_{st}^0 and K_H of CO_2 are larger than those of CH_4, implying that CO_2 is more strongly adsorbed. This is not unexpected because CO_2 is a three-site molecule and has a greater interaction with adsorbent. Also for CH_4 in MFI, our simulated q_{st}^0 is consistent with several reported values [311-314]. For CO_2 in MFI, q_{st}^0 is in close agreement with previous experimental (24.07 kJ/mol) [312] and simulation results [288,314]; however, slightly

lower than one reported value (27.2 kJ/mol) [315]. For CH_4 in IRMOF-1, again, our q_{st}^0 agrees well with the reported simulated values [124,212].

TABLE 4.3. Density and Porosity of MFI, C_{168}, and IRMOF-1. Limiting Adsorption Properties of Pure CH_4 and CO_2.

Adsorbent	Density (g/cm^3)	Porosity	Adsorbate	q_{st}^0 (kJ/mol)	K_H (mmol/g/kPa)
MFI	1.793	0.37	CH_4	19.42	0.010
			CO_2	22.91	0.022
C_{168}	1.294	0.67	CH_4	26.78	0.218
			CO_2	35.67	1.215
IRMOF-1	0.593	0.82	CH_4	10.31	0.0046
			CO_2	14.38	0.0093

4.4.1.2 Adsorption Isotherms

Simulated and experimentally available measured adsorption isotherms of pure CO_2 and CH_4 separately in MFI, C_{168} schwarzite, and IRMOF-1 are shown in Figure 4.6 as a function of the bulk pressure. All isotherms are of type I (Langmuirian), which is the characteristic of a microporous adsorbent with pores of molecular dimensions (below 2 nm) [316]. In MFI, the extent of CO_2 adsorption is consistently greater than that of CH_4. The simulated isotherms match closely with the experimental results [287,311] for both CH_4 and CO_2, though deviations are observed at high pressures for CH_4 adsorption. In IRMOF-1, CO_2 adsorption is again consistently larger than CH_4 adsorption, as in MFI. At low pressures, the adsorption of both CO_2 and CH_4 is nearly negligible in IRMOF-1, since their interactions with the IRMOF-1 framework are weak, as evidenced from q_{st}^0 and K_H in Table 4.3. The simulated isotherms are in accord with previous simulation results [212], and experiment data [98,124], especially, at low pressures. At high CO_2 pressures, simulation slightly overestimates the measured values. The reason could be that in our

work IRMOF-1 was considered to be a perfect crystal, whereas experimental samples may contain impurities and defects leading to a decrease in the storage capacity. In addition, the empirical force fields used may not be accurate enough to describe such a small discrepancy.

In C_{168} schwarzite, CO_2 is preferentially adsorbed at low pressures because CO_2 has three interactions sites and is more energetically favored. At high pressures near saturation, the smaller molecule CH_4 can fit into the partially occupied pores more easily; as a consequence of this entropic effect, CH_4 is adsorbed more. However, CO_2 is consistently greatly adsorbed than CH_4 in MFI and IRMOF-1 over the entire pressure range considered in the study, in which the saturation has not been approached. Nevertheless, it is expected that at even higher pressures close to saturation, CH_4 will have greater adsorption due to the entropic effect.

A dual-site Langmuir-Freundlich (DSLF) equation [317]

$$N^{o}(f) = \frac{N_1 k_1 f^{n_1}}{1 + k_1 f^{n_1}} + \frac{N_2 k_2 f^{n_2}}{1 + k_2 f^{n_2}} \tag{4.4}$$

was used to fit the adsorption isotherm of pure gas, where f is the fugacity of bulk gas at equilibrium with adsorbed phase, N_i is maximum loading in site i (= 1 and 2), k_i is the affinity constant, and n_i is used to characterize the deviation from the simple Langmuir equation. As shown in Table 4.4, the fitted parameters will then used to predict the adsorption of mixture. There is no restriction on the choice of the model to fit the adsorption isotherm, but data over the pressure range under study should be fitted very precisely. The fitted isotherms are shown as solid lines in Figure 4.6, and the adjustable parameters are given in Table 4.4. For CO_2 and CH_4 in each adsorbent, the fit is nearly perfect.

TABLE 4.4. Parameters in the Dual-Site Langmuir-Freundlich Equation fitted to Adsorption of pure CH_4 and CO_2.

Adsorbent	Adsorbate	N_1	k_1	n_1	N_2	k_2	n_2
MFI	**CH_4**	0.52	3.97×10^{-3}	1.23	2.74	3.88×10^{-3}	1.03
	CO_2	1.79	8.47×10^{-3}	0.62	2.51	3.98×10^{-3}	1.03
C_{168}	**CH_4**	0.75	1.97×10^{-5}	2.79	7.17	0.033	0.90
	CO_2	8.03	0.025	0.27	5.99	0.181	0.94
IRMOF-1	**CH_4**	22.32	1.80×10^{-4}	1.03	5.19	4.83×10^{-8}	2.15
	CO_2	19.83	2.56×10^{-4}	1.16	11.55	1.60×10^{-12}	4.02

A comparison of CH_4 adsorption isotherms in the three different adsorbents is presented in Figure 4.6a as a function of pressure. It can be seen clearly that among the three adsorbents, the greatest extent of adsorption is in IRMOF-1, which is not saturated even at the highest pressure considered here. This indicates that IRMOF-1 has a very high storage capacity for CH_4. Also the simulation results of CH_4 in MFI and IRMOF-1 are in good agreement with experimental data. For CH_4 in C_{168} schwarzite no experimental data is available.

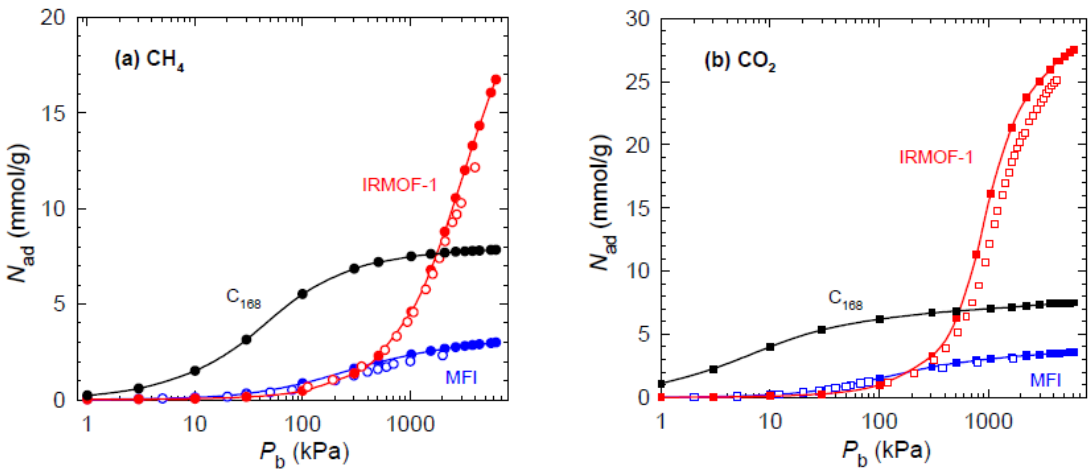

Figure 4.6. Adsorption isotherms of (a) CH_4 and (b) CO_2 in MFI, C_{168}, and IRMOF-1 as a function of bulk pressure. The filled symbols are simulation results, the lines are fits of the dual-site Langmuir-Freundlich equation to simulation results, and the open symbols are experimental data.

Figure 4.6b shows the simulated and experimental adsorption isotherms for CO_2 in MFI, C_{168} schwarzite, and IRMOF-1. Similar to that observed for CH_4, there is greater adsorption of CO_2 in IRMOF-1 than in MFI and C_{168} schwarzite. Recently, the US Department of Energy (DoE) set the storage target for CH_4 at 35 bar as 180 v/v [126], which is the excess volume of CH_4 adsorbed at the standard temperature and pressure per volume of the storage vessel. Our simulated excess adsorption of CH_4 at 35 bar is 140.3 v/v, slightly greater than the experimental result of 121.9 v/v [124]. Though the predicted CH_4 storage in IRMOF-1 is lower than the DoE target, the capacity is significantly higher than in MFI and C_{168} schwarzite. Based on this observation, IRMOF-1 could be an ideal starting material for the storage of CH_4 [124], as well as for CO_2. With a proper choice of an organic linker, it may be possible to design an MOF with enhanced storage capacity and reach the DoE target.

4.4.1.3 Isosteric Heats of Adsorption

Figure 4.7a shows the isosteric heats q_{st} of CO_2 and CH_4 adsorption in MFI. Consistent with the adsorption isotherm, CO_2 has a higher heat of adsorption than CH_4. With increasing loading, q_{st} initially increases, passes through a maximum at high loading, and finally decreases, though the extent of the change for CH_4 is weaker. This type of behavior has been observed in experimental studies, for example, in the adsorption of Xe in zeolites X and Y [318], Ar in $AlPO_4$-5 [319], and CH_4 in a fcc–structured silica gel [302]. The initial increase in q_{st} is attributed to the cooperative attractive interactions between adsorbate molecules, while the interaction between adsorbate and adsorbent remains nearly unchanged. The additional adsorbed adsorbate molecules must occupy the less favorable sites leading to a weaker adsorbate-adsorbent interaction, and the adsorbate-adsorbate interaction becomes less

attractive due to their shorter separation distance. As a consequence, q_{st} tends to decrease at high loadings. Also included in Figure 4.7a are the experimentally determined q_{st} at low loadings [311-313,315]. While our simulated limiting heats of adsorption q_{st}^{0} as listed in Table 4.3 well reproduce the measured values, the heats of adsorption q_{st} at low loadings seem to be underestimated. Figure 4.7b shows q_{st} of CO_2 and CH_4 in C_{168} schwarzite. The heat of adsorption in C_{168} schwarzite shows different behavior with increasing coverage, q_{st} first decreases to a minimum, then increases to a maximum and finally decreases.

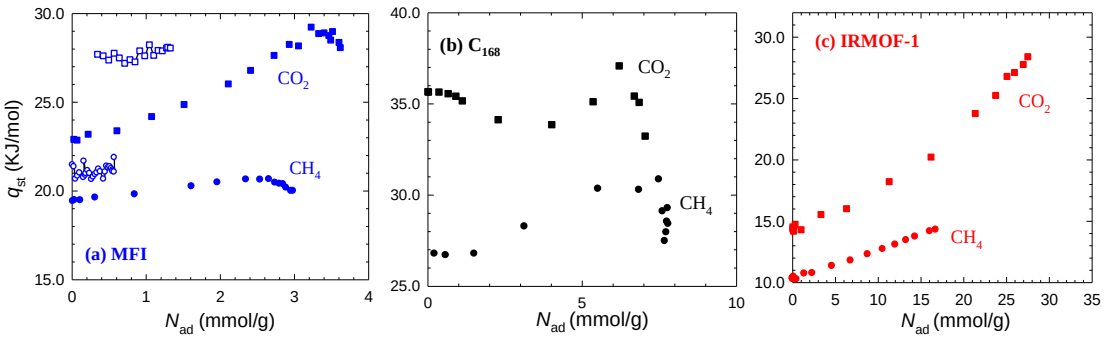

Figure 4.7. Isosteric heats of adsorption of pure CH_4 and CO_2 in MFI, C_{168}, and IRMOF-1. Legends are as in Figure 4.6.

Such behavior is not unusual and has been observed experimentally in the adsorption of N_2 and CO in $AlPO_4$-5 [319], CH_4 in a silica gel with a hard sphere structure [302], Ar in chabazite [320], and CH_4 in activated carbon [321]. The initial decrease of q_{st} is a consequence of the heterogeneous character of the C_{168} schwarzite surface, in which the more energetically favorable sites for adsorption are occupied first, and then the less favorable sites are occupied as the loading increases. Figure 4.7c shows q_{st} of CO_2 and CH_4 in IRMOF-1. The adsorption has not approached saturation, as a result, q_{st} increases monotonically with loading simply because of the

increased cooperative interaction between adsorbate-adsorbate. However, a decrease in q_{st} is expected at high loadings.

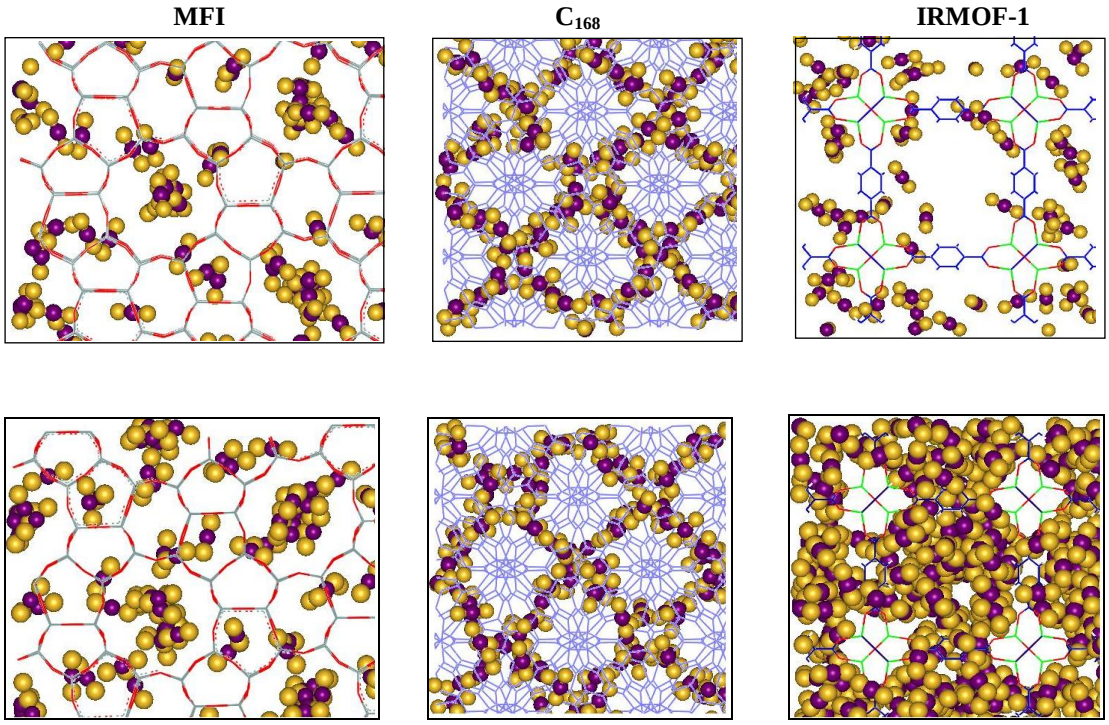

Figure 4.8. Snapshots of pure CO_2 adsorption in MFI, C_{168}, and IRMOF-1 at 500 kPa (top) and 2000 kPa (bottom).

Figure 4.8 shows the equilibrium snapshots of the adsorbed CO_2 molecules at 500 and 2000 kPa in all the three adsorbents. In MFI, CO_2 are adsorbed mostly in the straight channels at a low pressure, however, at a high pressure CO_2 is also adsorbed in the zig-zag channels. In C_{168} schwarzite, CO_2 molecules occupy both the small and larger channels. As observed previously [288], on going from a low to a high pressure, the distribution of adsorbed CO_2 molecules changes from continuous in both channels to localized first in small channels and then in large channels. With increasing pressure, the adsorbate-adsorbate attraction first increases at low pressures, but then decreases. This is because as the number of admolecules increases, the channels become crowded and the separation distance between the admolecules decreases. In a competitive balance between energetic and entropic effects, a

phenomenon similar to a first-order phase separation occurs, leading to the localized distribution in the channels, first in the small channels at modest pressures and then in the large pores at high pressures [288]. In IRMOF-1, CO_2 molecules are concentrated around the metal-oxide tetrahedra. At a high pressure, CO_2 molecules also enter the straight channels within the framework.

4.4.1.4 Adsorption Isotherms of Binary Components

For adsorption of a gas mixture, the equilibrium condition is the equality of fugacity in the gas and adsorbed phases [321].

$$P y_i \phi_i = x_i \gamma_i f_i^{\circ} \tag{4.5}$$

where P is bulk pressure, y and x are the molar fraction in gas and adsorbed phases, respectively. The fugacity coefficient of component i in gas phase is ϕ_i calculated by PR EoS, f_i° is the fugacity of pure component i in a standard state, and γ_i is the activity coefficient of component i in the adsorbed phase.

If a perfect mixing is assumed in the adsorbed phase and hence $\gamma_i = 1$, we can use the ideal-adsorbed solution theory (IAST) [321] to predict the adsorption of a mixture based on the information from pure components only. The standard state is specified by the surface potential Φ_i given by the Gibbs adsorption approach,

$$\Phi_i = -RT \int_0^{f_i^{\circ}} N_i^{\circ}(f_i)\, d \ln f_i \tag{4.6}$$

where $N_i^{\circ}(f)$ is the adsorption isotherm of pure component i. The mixing process is carried out at a constant surface potential $\Phi_1 = \Phi_2 = \cdots = \Phi$.

Figure 4.9 shows the adsorption isotherms for an equimolar mixture CH_4/CO_2 in MFI, C_{168} schwarzite, and IRMOF-1 as a function of total bulk pressure. The closed symbols are from simulation and the lines are from IAST theory. In all adsorbents,

CO_2 is more preferentially adsorbed than CH_4 as expected due to the stronger interaction between CO_2 and surfaces. Again, in IRMOF-1 the loading at low pressures is negligible. The agreement between IAST predictions and simulation results is generally good, particularly, at low pressures because IAST becomes exact in the Henry law limit [321]. However, at high pressures IAST either underestimates or overestimates the results compared to simulation. This may be attributed to the assumption intrinsically used in IAST, that is, that the adsorbed phase of mixture is an ideal phase with perfect mixing. Improved predictions can be obtained by removing this assumption.

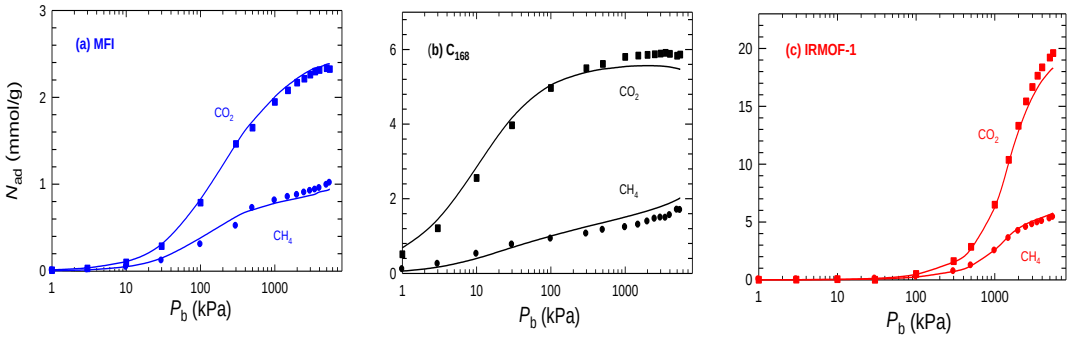

Figure 4.9. Adsorption of an equimolar mixture of CH_4 and CO_2 in MFI, C_{168}, and IRMOF-1 as a function of bulk pressure. The filled symbols are simulation results, and the lines are IAST predictions.

Adsorption selectivity in a binary mixture of component *i* and *j* is defined as

$$S_{i/j} = \left(\frac{x_i}{x_j}\right)\left(\frac{y_j}{y_i}\right) \tag{4.7}$$

where x_i , y_i are the mole fractions of component *i* in the adsorbed and bulk phase respectively. Although the general trend of selectivity can be properly estimated from simulation, it is remarked that the value of selectivity may not be as accurate as

isotherm, because a slight deviation in the number of adsorbed molecules may result in a larger deviation in selectivity.

Figure 4.10 shows the simulated adsorption selectivity of an equimolar mixture of CO_2 and CH_4 in MFI, C_{168} schwarzite, and IRMOF-1 as a function of total bulk pressure. It is worthwhile to point out that at a fixed total bulk pressure, selectivity is only a weak function of the bulk phase composition [322]. In all the three adsorbents, when the bulk pressure is close to zero, the simulated selectivity is approximately equal to the ratio of the Henry constants, $K_H(CO_2)/K_H(CH_4)$. In MFI, the selectivity increases slowly at low pressures, then decreases at modest pressures, and finally increases slightly at high pressures. In C_{168} schwarzite, the selectivity drops at high pressures since CO_2 nearly reaches saturation while there is still a slight increase in CH_4 adsorption. In IRMOF-1, the selectivity first remains nearly constant and then increases as pressure increases, which are consistent with the adsorption behavior described earlier. The selectivity in C_{168} schwarzite is the highest among the three adsorbents, though the adsorption capacity in IRMOF-1 is the highest.

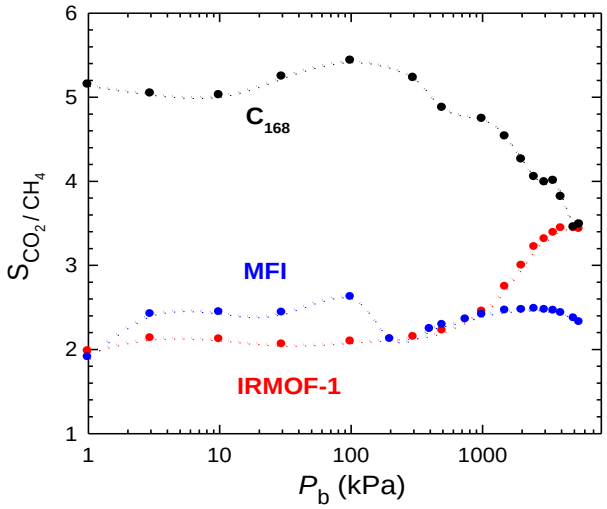

Figure 4.10. Adsorption selectivity of an equimolar mixture of CH_4 and CO_2 in MFI, C_{168}, and IRMOF-1as a function of bulk pressure from simulation. The dotted lines are to guide the eye.

4.4.2 Diffusion of Pure Components

4.4.2.1 Diffusivities at Infinite Dilution

Figure 4.11 shows diffusivities at infinite dilution $D(0)$ for CH_4 and CO_2 separately in MFI, C_{168} and IRMOF-1 as a function of the inverse temperature. The results are the average of ten independent runs with a standard deviation within 5%. As given in Table 4.5, for the three adsorbents under consideration, the porosity increases in the order of MFI < C_{168} < IRMOF-1. In accordance with the increasing trend of porosity, $D(0)$ generally increases in the same order for both CH_4 and CO_2 because of the increased free space for molecules to move. At temperatures lower than 300 K, however, $D(0)$ in MFI becomes slightly greater than in C_{168}. Therefore, porosity is not the only factor influencing the diffusivity. Our simulated $D(0)$ at 300 K given in Table 4.5 generally matches well with the reported simulation and experimental values. For CH_4 in MFI, $D(0)$ agrees well with the simulation results from a number of groups [305,323-325]. For CH_4 in IRMOF-1, $D(0)$ is also in good agreement with a simulation result [222], but both are almost an order of magnitude lesser than the measured value by Stallmach et al. [226] For CO_2 in MFI, $D(0)$ is comparable to the measured value from QENS ($0.6 \sim 0.7 \times 10^{-8}$ m^2/s) [326], though a bit higher than the value simulated by Krishna et al [323] For CO_2 in IRMOF-1, $D(0)$ is slightly higher than the simulated value of Skoulidas et al [222]. The discrepancy for CO_2 might be due to the different potential parameters used. C_{168} schwarzite is a hypothetical structure for nanoporous carbons, no experimental data are available for comparison with our results.

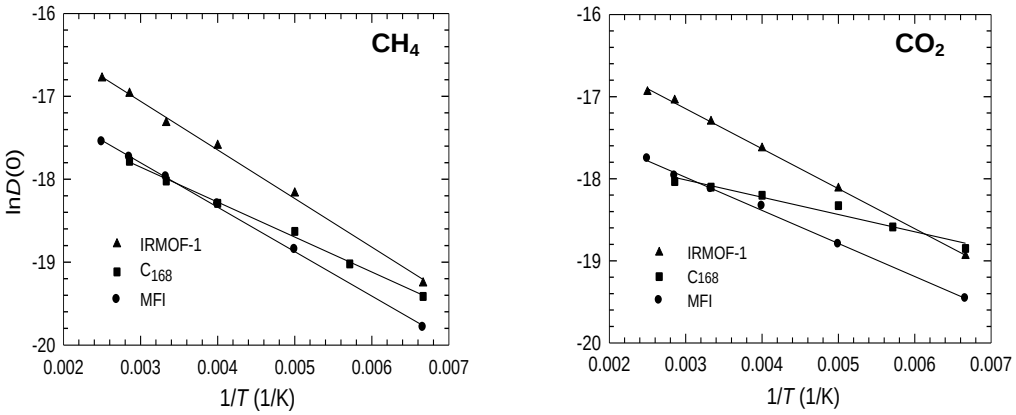

Figure 4.11. Diffusivities $D(0)$ at infinite dilution as a function of inverse temperature for pure CH_4 and CO_2 in MFI, IRMOF-1 and C_{168}. Symbols are from simulations, and lines are the Arrhenius fits to the symbols.

In nanoporous materials, the steric effect and surface interaction play a dominant role. Diffusion is normally interpreted as an activated process and can be described by the Arrhenius relation

$$D(0) = D_f \exp\left(\frac{-E_a}{RT}\right) \tag{4.8}$$

where D_f is the prefactor, E_a is the activation energy and R is the gas constant. By fitting the simulated $D(0)$ at various temperatures using eq. 4.8, D_f and E_a can be correlated. The lines in Figure 4.11 are the Arrhenius fits to the simulation data. As listed in Table 4.5, D_f for CH_4 is greater than CO_2 in all the three adsorbents, simply because CH_4 is a lighter molecule compared with CO_2. As a result of the high porosity, in IRMOF-1 D_f for both CH_4 and CO_2 is found to be almost one order of magnitude greater than in MFI and C_{168}. Our simulated E_a for CH_4 in MFI (4.45 kJ/mol) is in good agreement with experimental value (5.69 kJ/mol) [327].

TABLE 4.5. Diffusivities $D(0)$ at 300 K (10^{-8} m^2/s), Prefactors D_f (10^{-8} m^2/s), and Activation Energies E_a (kJ/mol) at Infinite Dilution for CH_4 and CO_2 in MFI, C_{168} and IRMOF-1.

Adsorbent	Adsorbate	Porosity	$D(0)$	D_f	E_a
MFI	CH_4	0.37	1.56	9.28	4.45
	CO_2		1.31	5.18	3.35
C_{168}	CH_4	0.67	1.51	6.24	3.50
	CO_2		1.35	2.81	1.75
IRMOF-1	CH_4	0.82	3.37	22.6	4.88
	CO_2		3.01	15.4	4.05

Stallmach et al [226] found E_a for CH_4 in IRMOF-1 as around 8.5 kJ/mol, which is almost twice the simulated value (4.88 kJ/mol). The discrepancy in both $D(0)$ and E_a in IRMOF-1 may be due to the defects present in the porous structure used in experiments, however, which were not taken into account in simulations. Our simulated E_a for CO_2 in MFI (3.35 kJ/mol) is smaller than one available experimental value (5.8 kJ/mol). Note that, however, the experimental condition was not at infinite dilute, instead, the loading was approximately two molecules/unit cell [326]. A molecule must overcome the free energy barrier to move from one site to another. The barrier as reflected in the activation energy is lower for either CH_4 or CO_2 in C_{168} schwarzite compared with that in MFI and IRMOF-1. In particularly, the estimated E_a for CO_2 in C_{168} (1.75 kJ/mol) is considerably lower. As further discussed below, this is because CO_2 is a slender molecule and readily mobile particularly in C_{168} channels.

4.4.2.2 Self-diffusivities

Figure 4.12 shows the loading dependence of self-diffusivities D_s for CH_4 and CO_2 in the three adsorbents. The loadings considered here for IRMOF-1 are substantially lower than the saturation loading. The error bars indicate the uncertainties in our simulation. As seen, D_s for both CH_4 and CO_2 in each adsorbent

decreases monotonically as loading increases. This belongs to type I behavior as characterized by Karger and Pfeifer [328], in which five types of diffusion behavior were demonstrated with increased loading. The observed type I behavior is very common in nanoporous materials, due to the enhanced steric hindrance to the motion of a tagged particle by the neighboring particles as loading increases. At a loading of around 3 mmol/g for either CH_4 or CO_2, D_s in IRMOF-1 is about twice of that in C_{168}, and almost one order of magnitude greater than that in MFI. The decrease rate in D_s (the slope) is closely related to the adsorbent porosity. The lower the porosity, the faster is the decrease rate. Our simulated values of D_s for CH_4 in MFI agree well with the experimental results of Caro et al. [329], though at high loadings the experimental results are slightly greater than the simulation results. Note that the reported experimental data in the literature may be conducted at different conditions, particularly, at different loadings. Therefore, experimental data should be carefully chosen to compare with simulation results.

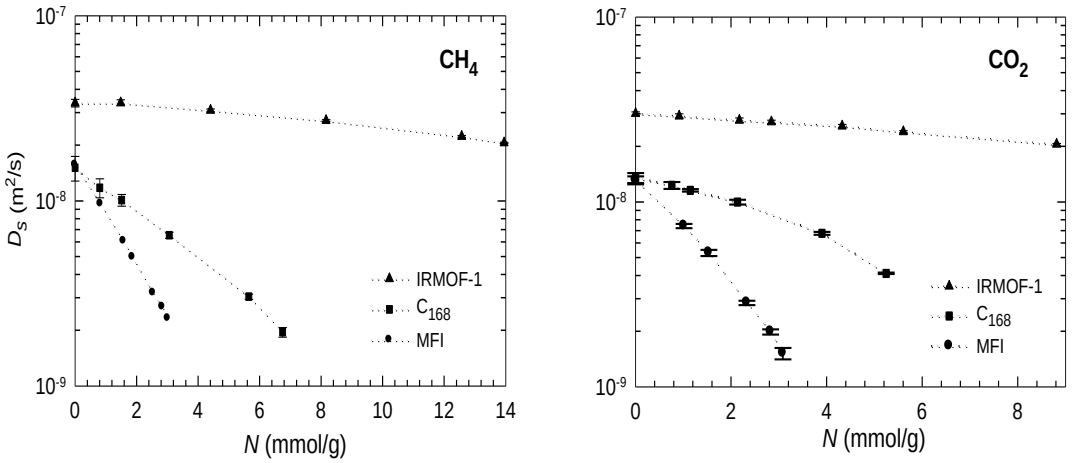

Figure 4.12. Self-diffusivities D_s as a function of loading for pure CH_4 and CO_2 in MFI, IRMOF-1 and C_{168}. Symbols are from simulations with dotted lines to guide the eye.

Physically, a decrease in D_s can be interpreted in terms of free energy variation as proposed recently by Beerdsen et al. [330] based on the classification of framework topologies. For the three nanostructures MFI, IRMOF-1 and C_{168}, they all consist of

mutually intersecting channels and can be classified as intersecting channel-type structures. In such type of structures, free energy rises as loading increases and in turn causes the decrease in D_s. Nevertheless, the magnitude of decease depends on many factors for a given structure, e.g., porosity might be a key indicator. In addition, pore volume and pore size, surface area also play a role.

In IRMOF-1 with the largest porosity among the three structures, the increase in free energy barrier upon sorption is not significant compared to MFI and C_{168}. This leads to the slowest decrease in D_s for both CH_4 and CO_2 in IRMOF-1. Without exception, however, D_s would approach zero in any framework near saturation because of the negligibly available free volume. That is, in this situation all the vacant sites within a framework are almost fully occupied, molecules are difficult to jump into a different location, leading to a vanishingly small diffusivity. A closer look in Figure 4.12 informs us that D_s of CH_4 is greater than that of CO_2 in MFI or IRMOF-1 over the entire range of loading. This is attributed to the fact that CO_2 is a heavier molecule than CH_4. Nevertheless, D_s of CO_2 in C_{168} is greater than CH_4 over the entire range of loading except at infinite dilution. The reason is probably the free energy barrier for hopping in C_{168} channels is lower for CO_2, a more slender molecule as compared with CH_4. This can be evidenced from the simulated activation energies shown in Table 4.5, in which E_a for CO_2 in C_{168} is only half of that for CH_4. Similar behavior was observed for diffusion of CH_4 and CO_2 in CHA and DDR zeolites [323].

4.4.2.3 Corrected-diffusivities

Figure 4.13 shows the corrected diffusivities D_c for CH_4 and CO_2 in MFI, IRMOF-1 and C_{168}. The error bars denote the statistical uncertainties in calculating D_c, which are apparently greater than those in Figure 4.12 for D_s. This is because D_s a particle property, whereas D_c is a collective system property. One can usually obtain

accurate D_s from a single sufficiently long MD run, but need more independent runs to obtain accurate D_c. At a given loading, D_c of CH_4 has the largest value in IRMOF-1 and similar value in MFI and C_{168}. This is partially different from Figure 4.14, in which D_s decreases with reducing porosity of the structure. For CO_2 in the three structures, D_c and D_s follow the same trend, although the variation between D_c in different structures is less.

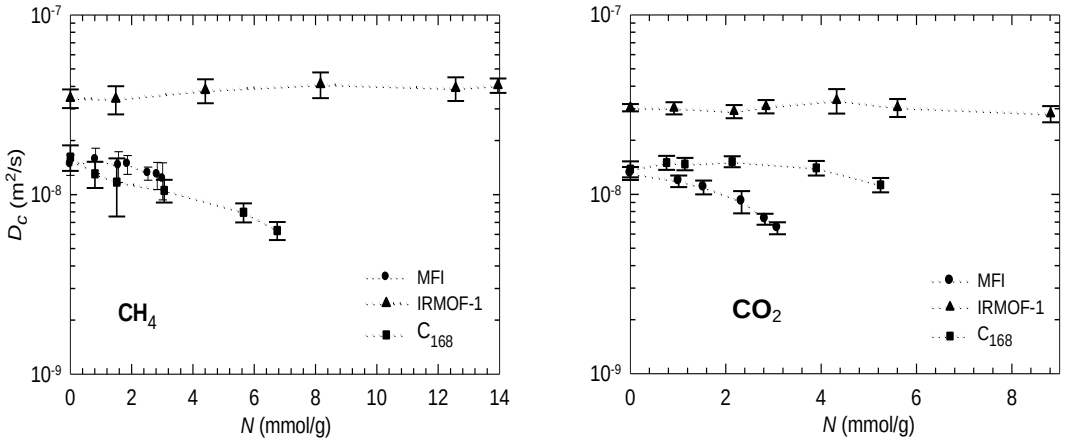

Figure 4.13. Corrected diffusivities D_c as a function of loading for pure CH_4 and CO_2 in MFI, IRMOF-1 and C_{168}. Symbols are from simulations with dotted lines to guide the eye.

As a function of loading, D_c exhibits much less dependent on loading compared to D_s. Despite some fluctuations, D_c for CH_4 in IRMOF-1 and MFI, and for CO_2 in IRMOF-1 and C_{168} approximately remain constant over the range of loading under study. Therefore, D_c for each of this case is roughly equal to the diffusivity at zero-loading, i.e. $D_c = D(0)$. This, indeed, is the Darken approximation in which D_c is simply regarded to be independent of loading. In principle, D_c would approach zero or become comparable to solid diffusion at the maximum loading irrespective of the topology of the confinement [331]. Therefore, the Darken approximation is valid in a given region and usually referred to as the weak confinement scenario, as of Ar in silicalite [332]. On the other hand, D_c for CH_4 in C_{168} and for CO_2 in MFI decreases

approximately linearly with loading. Similar behavior was found for CF_4 and SF_6 in silicalite [332], and can be referred to as the strong confinement scenario.

The loading dependence of D_c varies from weak to strong confinement scenario. The scenario depends on the degree of confinement, adsorbate size and molecular interaction, all of which determine the energy barrier, frequency and distance for molecular jump. Both CH_4 and CO_2 in IRMOF-1 show weak confinement scenario. This is because the energy barrier for diffusion in the highly porous IRMOF-1 is not significantly affected by loading at low and moderate loadings. Although CH_4 has a larger kinetic diameter than CO_2, the latter is linear and can align perpendicular to the channels in MFI. The channels could be blocked to some extent by CO_2 and the energy barrier for CO_2 jump is higher than CH_4. As a result, in MFI CO_2 shows the strong confinement scenario and CH_4 shows the reversed behavior. C_{168} channels in the same layer are isolated from each other, when diffusing molecules jump between different layers they must pass through the channel intersections. CO_2 is a slender molecule and the energy barrier of jump in the intersections is lower compared with CH_4, as evidenced from the considerably lower activation energy. Consequently, CH_4 instead of CO_2 in C_{168} shows the strong confinement scenario. Similar loading dependence was observed by Krishna et al [323] for CO_2 and CH_4 in CHA and DDR zeolites. Krishna et al. [333] have shown that the loading dependence of corrected diffusivity in zeolites is closely related to the topology, connectivity and molecule-molecule interactions, leading to a decrease or increase in energy barrier for diffusion.

4.4.2.4 Transport-diffusivities

Transport diffusivity D_t is related to corrected diffusivity D_c as given in eq. 4.9

$$D_t(c) = D_c(c)\Gamma(c) \tag{4.9}$$

in which the thermodynamic factor Γ can be calculated from adsorption isotherm. In our study on the adsorption of CH_4 and CO_2 in MFI, IRMOF-1 and C_{168} [334], the adsorption isotherms were fitted using a dual–site Langmuir–Freundlich equation (DSLF). Differentiation of the DSLF equation yields Γ in Figure 4.14. With increasing loading, Γ of CH_4 increases sharply in MFI, moderately in C_{168}, and marginally in IRMOF-1. For CO_2, Γ also increases in MFI and C_{168}, but with smaller value compared with CH_4. Nevertheless, Γ of CO_2 in IRMOF-1 is nonmonotonic, initially decreases and then increases with loading, as shown in the inset.

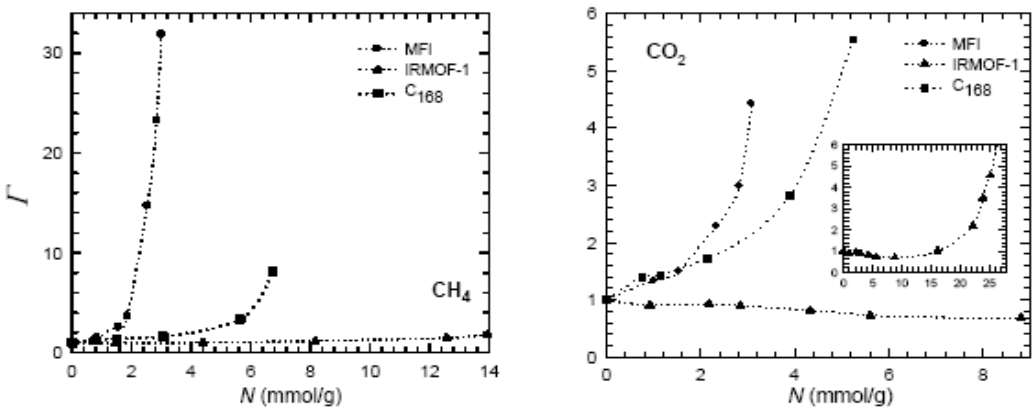

Figure 4.14. Thermodynamic factor Γ as a function of loading for pure CH_4 and CO_2 in MFI, IRMOF-1 and C_{168} (the inset is for CO_2 in IRMOF-1 at high loadings). Symbols are from simulation with dotted lines to guide the eye.

Figure 4.15 shows D_t for CH_4 and CO_2 in the three adsorbents. As seen, the values of D_t do not follow the magnitude of porosity. At a loading of 3 mmol/g, D_t for CH_4 in MFI is almost one order of magnitude greater than in IRMOF-1 and C_{168}, and D_t for CO_2 is nearly identical in the three adsorbents. As loading increases, D_t becomes greater in most cases. For CH_4 in MFI, though D_c is nearly independent of loading, D_t rises quite rapidly as Γ increases rapidly with respect to loading. For CH_4 in IRMOF-1, however, D_t rises slowly due to a marginal change of Γ in the highly porous framework, particularly at low loadings. The rise of D_t for CH_4 in C_{168} is monotonic though it is less than in MFI. For CO_2 in MFI, Γ is found to be less than

CH_4 in MFI and consequently D_t rises slowly. In C_{168}, D_t of CO_2 is quite similar to that of CH_4 at low loadings, but at high loadings it is larger due to the substantial increase in Γ. Unlike other cases, D_t of CO_2 in IRMOF-1 is nonmonotonic as a function of loading attributed to the variation of Γ demonstrated in Figure 4.14. At low loadings, Γ decreases with loading and hence D_t drops. In contrast, at high loadings Γ rises and consequently D_t is expected to increase, which was not calculated in this work because of the required extremely long simulation but observed by Skoulidas and Sholl [222].

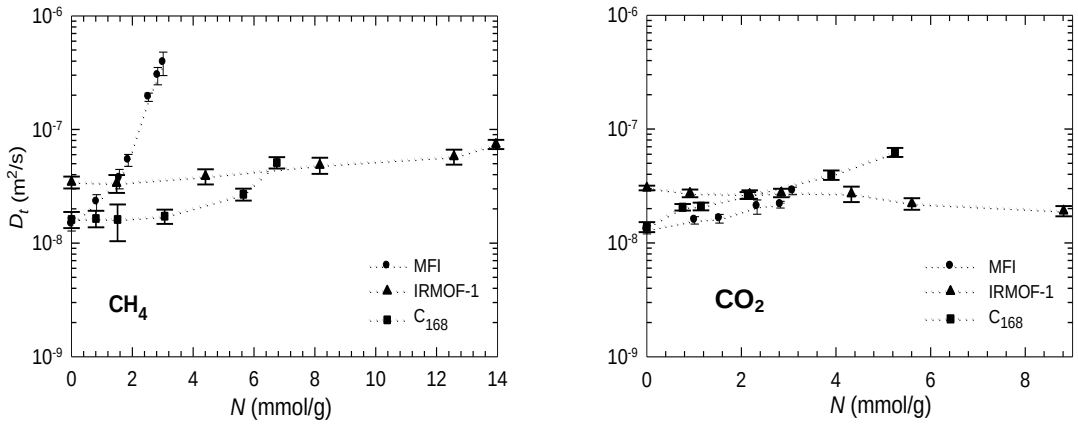

Figure 4.15. Transport diffusivities D_t as a function of loading for pure CH_4 and CO_2 in MFI, IRMOF-1 and C_{168}. Symbols are from simulation with dotted lines to guide the eye.

4.4.2.5 Correlation Effects

As mentioned earlier, self-diffusivity D_s is a particle property, but corrected diffusivity D_c is a collective property. Difference arising between D_s and D_c is due to the correlation effects in the diffusing particles. One evidence is that at non-zero loading, D_s is always less than D_c. The ratio of D_s/D_c is a rough indicator for the strength of correlation, in which the smaller the ratio, the stronger is the correlation. As loading increases, D_s/D_c decreases in the three structures, implying an enhancement of correlation effects. At high loadings, D_s/D_c are as low as 0.19 in

MFI, 0.31 in C_{168} and around 0.47 in IRMOF-1. This suggests that the correlation effects reduce with increasing porosity of the adsorbent.

TABLE 4.6. Saturation Loadings $\Theta_{i,sat}$ (mmol/g), Adjustable Parameters α_i and β_i in Eq. 4.11 for CH_4 and CO_2 in MFI, C_{168} and IRMOF-1.

Adsorbent	Adsorbate	$\Theta_{i,sat}$	α_i	β_i
MFI	CH_4	6.25	0.2838	1.752
	CO_2	6.38	0.3509	1.823
C_{168}	CH_4	11.85	0.8336	2.123
	CO_2	10.64	0.3387	0.159
IRMOF-1	CH_4	45.49	0.4400	0.926
	CO_2	42.23	0.6810	1.513

In the Maxwell-Stefan (MS) formulism, Krishna and Paschek [335] have derived an expression to evaluate the correlation effects in system with a single species *i*,

$$\frac{1}{Đ_{ii}^{corr}} = \frac{1}{\theta_i}\left(\frac{1}{D_{i,s}} - \frac{1}{Đ_i}\right) \tag{4.10}$$

where $Đ_i$ is the MS diffusivity equal to D_c, as mentioned earlier, for a system with single species. θ_i is the fractional occupancy defined as $\Theta_i / \Theta_{i,sat}$, in which $\Theta_{i,sat}$ is the saturation loading of species *i*. Using the grand canonical MC simulation, the saturation loadings for CH_4 and CO_2 separately in MFI, IRMOF-1 and C_{168} have been estimated and listed in Table 4.6. $Đ_{ii}^{corr}$ is called the self-exchange coefficient, generally deceases with loading. More often, $Đ_{ii}^{corr}/Đ_i$ is used to characterize the correlation effects; the lower the value of $Đ_{ii}^{corr}/Đ_i$, the stronger are the correlation effects. A large value of $Đ_{ii}^{corr}/Đ_i$ signifies the weak correlations between molecular jumps. In particular, when $Đ_{ii}^{corr}/Đ_i \to \infty$, the correlation effects vanish and this is the facile exchange scenario. Eq. 4.10 allows one to calculate $Đ_{ii}^{corr}$ if $D_{i,s}$ and $Đ_i$ are known. Once calculated, then $Đ_{ii}^{corr}$ can be used to describe binary diffusion and be a

starting point for quantitatively predicting the cross-species coefficients in mixtures.

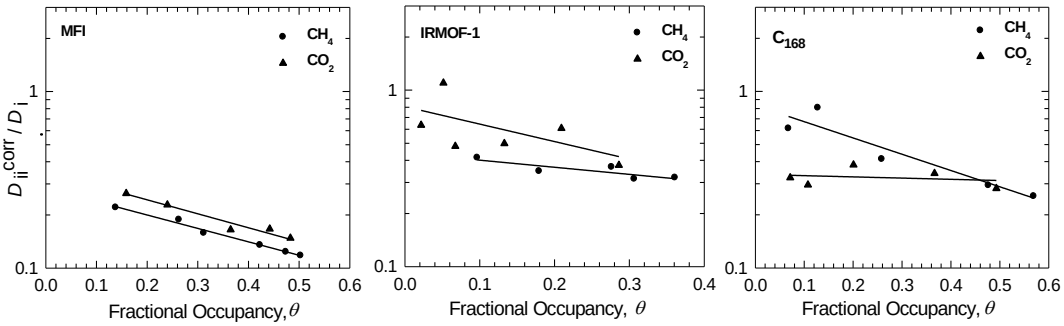

Figure 4.16. Correlation coefficients $Đ_{ii}^{corr}/Đ_i$ as a function of fractional occupancy for pure CH_4 and CO_2 in MFI, IRMOF-1 and C_{168}. Symbols are predictions from simulated D_s and D_c using equation eq. 4.10, and lines are the fits using the empirical equation eq. 4.11.

With $D_{i,s}$ and $Đ_i$ from MD simulation and $\Theta_{i,sat}$ from MC simulation, $Đ_{ii}^{corr}$ or $Đ_{ii}^{corr}/Đ_i$ were calculated through eq. 4.10 for CH_4 and CO_2 separately in MFI, IRMOF-1 and C_{168}. Figure 4.16 shows such estimated $Đ_{ii}^{corr}/Đ_i$ as symbols versus the fractional occupancy. It can be seen that $Đ_{ii}^{corr}/Đ_i$ decreases with increasing loading for both CH_4 and CO_2 in all the three structures, suggesting the enhanced correlation effects at higher loadings. This is consistent with the indication of D_s/D_c observed above, attributed to the fewer vacant sites and the stronger adsorbate-adsorbate interactions at high loadings [323]. As discussed earlier, D_s/D_c increases in order of MFI < C_{168} < IRMOF-1, consistent with the increasing order of the porosity, and consequently the correlation effects reduces. $Đ_{ii}^{corr}/Đ_i$ exhibits similar order and again reveals that the correlation effects decreases from MFI, C_{168} to IRMOF-1, i.e., with increasing porosity. We find no direct connection exists between the strength of correlation with the confinement scenario. For example, both CH_4 and CO_2 in MFI have small $Đ_{ii}^{corr}/Đ_i$ indicating strong correlation, but they show different scenarios, weak for CH_4 and strong for CO_2. Although CH_4 in C_{168} has a larger $Đ_{ii}^{corr}/Đ_i$ than

CO_2 and hence a smaller correlation, it exhibits the strong confinement scenario. In IRMOF-1, $Đ_{ii}^{corr}/Đ_i$ of CO_2 is higher than CH_4, but both belong to the weak confinement scenario.

An exponential relation was used to describe $Đ_{ii}^{corr}/Đ_i$

$$\frac{Đ_{ii}^{corr}}{Đ_i} = \alpha_i \exp(-\beta_i \theta_i) \tag{4.11}$$

Above equation was fitted to the simulated $Đ_{ii}^{corr}/Đ_i$ and the fits are shown by the lines in Figure 4.16. The values of the two adjustable parameters α_i and β_i are listed in Table 4.6. From eq. 4.10, it was observed that if D_s and D_c are very close at a given loading, $Đ_{ii}^{corr}$ may be very large. For this particularly reason, some points were not included in eq. 4.10 to fit. As seen, the fits match fairly well with the simulated data.

With the adjustable parameters in eq. 4.11 and based on the loading dependence of D_c or equivalently $Đ_i$ in Figure 4.13, the MS formulation can be used to predict diffusivities. Under the weak confinement scenario, $Đ_i$ remains nearly constant for CH_4 in IRMOF-1 and MFI and for CO_2 in IRMOF-1 and C_{168}; consequently, the Darken approximation can be used

$$Đ_i = D_i(0) \tag{4.12}$$

Under the strong confinement scenario, D_c decreases approximately linearly with loading for CH_4 in C_{168} and for CO_2 in MFI, and can be described by

$$Đ_i = D_i(0)(1-\theta_i) \tag{4.13}$$

Combining eq. 4.10-4.13, D_s can be predicted at a given loading. Substituting eq. 4.12 or 4.13 into eq. 4.9 allows us to predict D_t. Figure 4.17 shows the simulated and predicted D_s, D_c and D_t as a function of loading for pure CH_4 and CO_2 in MFI, IRMOF-1 and C_{168}. The predictions generally agree well with the simulated results.

Due to the correlation effects, in all cases D_c are greater than D_s. As a product of D_c and thermodynamic factor, D_t are greater than D_c in all cases except for CO_2 in IRMOF-1 because of the reason mentioned earlier.

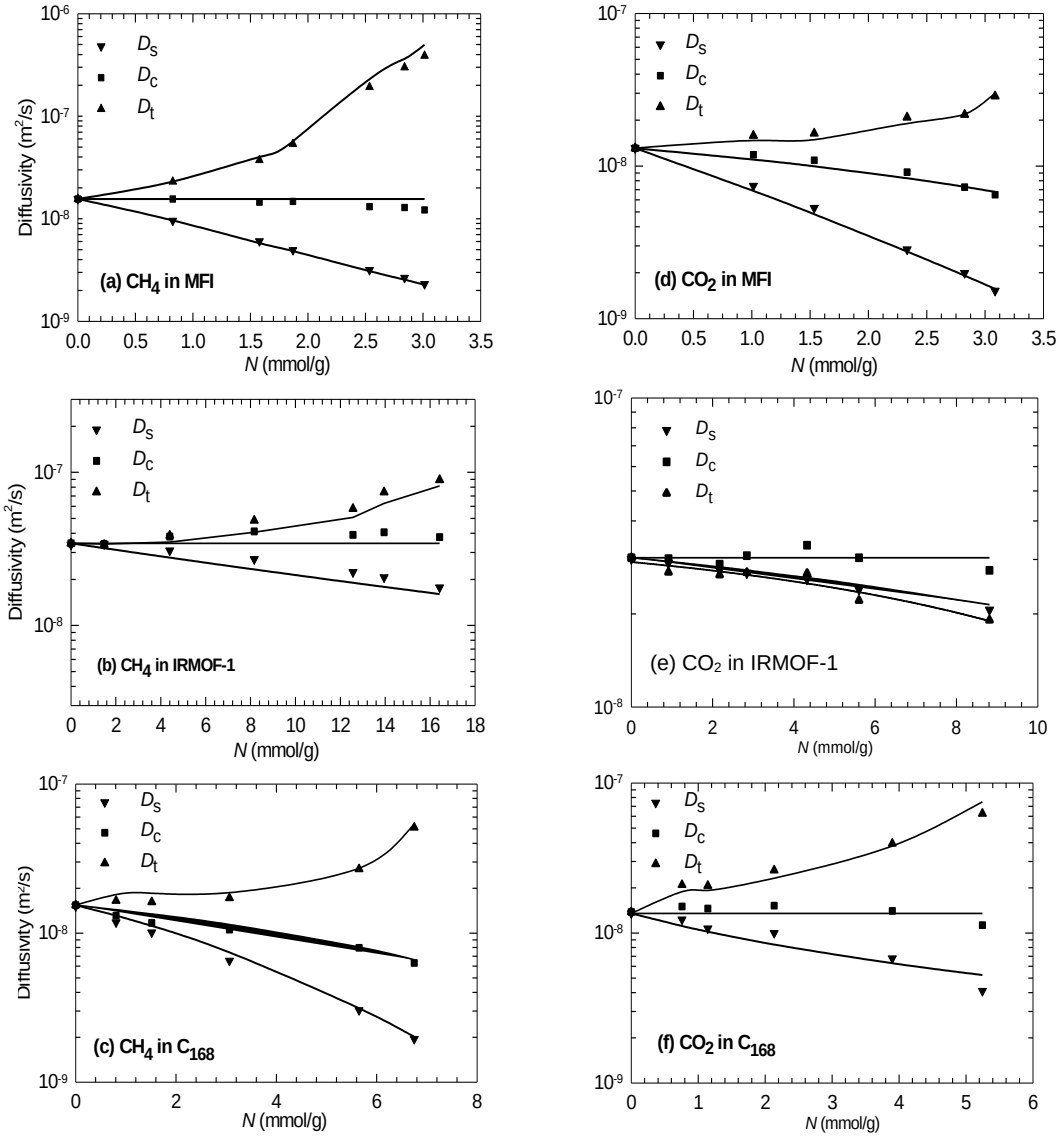

Figure 4.17. D_s, D_c and D_t as a function of loading for pure CH_4 and CO_2 in MFI, IRMOF-1 and C_{168}. Symbols are from simulation, and lines are from MS formulation.

4.4.3 Diffusion of Binary Components

4.4.3.1 Self-diffusivities

Based on the adsorption of equimolar mixture from bulk phase, MD simulations were performed to examine the self-diffusivities for CH_4/CO_2 mixture in MFI, IRMOF-1 and C_{168} at 300 K. Figure 4.18 shows the simulation snapshot of the

adsorbed mixture in the frameworks at a total loading of 3mmol/g. In MFI, most molecules are in the straight channels. In IRMOF-1, CO_2 molecules are preferentially adsorbed near the corners due to the high density of the framework atoms therein. In C_{168}, more CO_2 molecules are observed to adsorb in the channels.

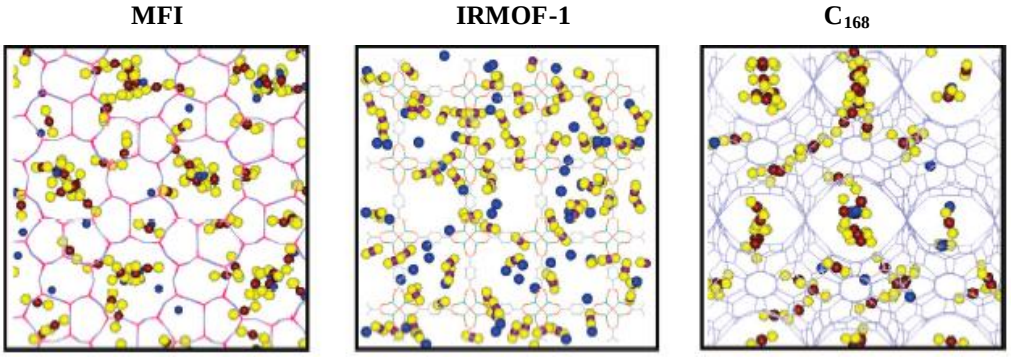

Figure 4.18. Snapshot of CH_4 and CO_2 mixture in MFI, IRMOF-1 and C_{168} at a total loading of 3mmol/g. CH_4: blue, $C(CO_2)$: purple, $O(CO_2)$: yellow.

Krishna and Paschek [335] developed a generalized MS formulation to predict the self-diffusivities $D_{i,s}$ in multicomponent mixtures. In a binary mixture, $D_{i,s}$ is

$$D_{1,s} = \frac{1}{\frac{1}{Đ_1} + \frac{\theta_1}{Đ_{11}^{corr}} + \frac{\theta_2}{Đ_{12}^{corr}}} \qquad D_{2,s} = \frac{1}{\frac{1}{Đ_2} + \frac{\theta_1}{Đ_{21}^{corr}} + \frac{\theta_2}{Đ_{22}^{corr}}} \tag{4.14}$$

where $Đ_{ii}^{corr}$ is the self-exchange coefficient and $Đ_{ij}^{corr}$ is the binary-exchange coefficient. In this formulation, sorption thermodynamics or in other words thermodynamic factor plays no role in determining $D_{i,s}$ in binary mixture. In contrast, $D_{i,s}$ is more strongly influenced by the correlation effects. In most previous studies in zeolites, the binary exchange coefficient $Đ_{ij}^{corr}$ was calculated using the logarithmic interpolation suggested by Krishna and Wesselingh [336].

$$Đ_{ij}^{corr} = \left[Đ_i\right]^{\Theta_i/\Theta_i+\Theta_j} \left[Đ_j\right]^{\Theta_j/\Theta_i+\Theta_j} \tag{4.15}$$

Skoulidas et al. [337] showed that unequal saturation capacities violate the symmetry assumption in $Đ_{ij}^{corr}$ as possessed by the Onsager reciprocal relation, and consequently proposed the following relationship for the binary-exchange coefficients

$$\Theta_{j,sat} Đ_{ij}^{corr} = \Theta_{i,sat} Đ_{ji}^{corr} \tag{4.16}$$

A more general interpolation was further proposed by Skoulidas et al. [337]

$$\Theta_{j,sat} Đ_{ij}^{corr} = \left[\Theta_{j,sat} Đ_{ii}^{corr}\right]^{\Theta_i/\Theta_i+\Theta_j} \left[\Theta_{i,sat} Đ_{jj}^{corr}\right]^{\Theta_j/\Theta_i+\Theta_j} \tag{4.17}$$

Equation 4.17 reduces to eq. 4.15 when the saturation capacities are equal and $Đ_{ii}^{corr}/Đ_i = 1$. Equation 4.17 has been demonstrated to be valid for mixture diffusion in zeolites and carbon nanotubes [338-340]. Coppens and Iyengar [341] tested the consistency of MS formulation when predicting $D_{i,s}$ in zeolites with strong adsorption sites. By assuming $Đ_{ii}^{corr}/Đ_i = 1$, they found that the MS formulation works well in silicalite upon comparison with simulation. For other systems with pore network differing from silicalite, it is necessary to assume $Đ_{ii}^{corr}/Đ_i \neq 1$, as suggested by most of the earlier studies [332,337,342].

With eq. 4.11 for $Đ_{ii}^{corr}$, eq. 4.12 or 4.13 for $Đ_i$, and eq. 4.17 for $Đ_{ij}^{corr}$, the self-diffusivities $D_{i,s}$ for CH_4/CO_2 mixture in MFI, IRMOF-1 and C_{168} were predicted. Equation 4.15 and 4.16 were also tested for $Đ_{ij}^{corr}$ and then used in prediction, however, eq. 4.17 is found to be superior. Furthermore, it is worthwhile to point out that when eqs. 4.15 and 4.17 are generalized for binary mixture, the fractional occupancy θ_i needs to be substituted by $(\theta_1 + \theta_2) = (\Theta_1/\Theta_{1,sat} + \Theta_2/\Theta_{2,sat})$.

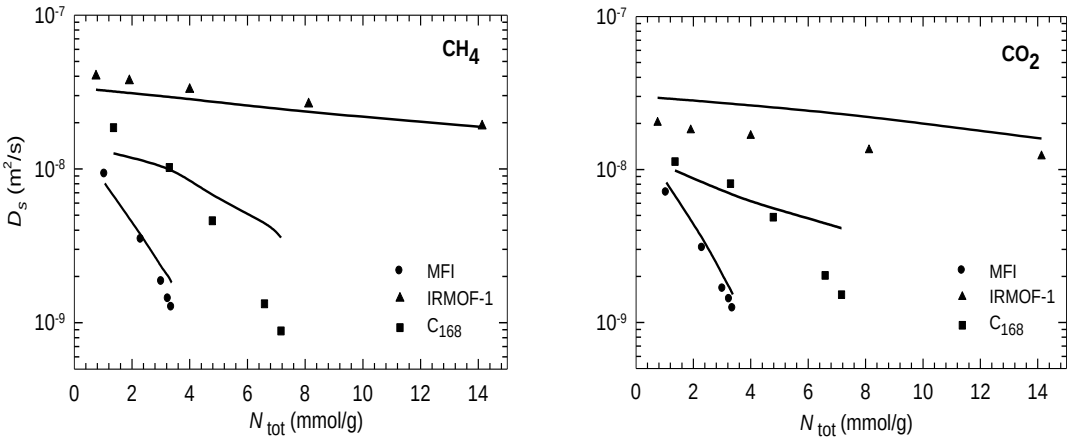

Figure 4.19. Self-diffusivities D_s of CH_4 and CO_2 in MFI, IRMOF-1 and C_{168} as a function of total loading for equimolar mixture. Symbols are from simulation and lines are from MS formulation.

Figure 4.19 shows the simulated and predicted $D_{i,s}$ of CH_4/CO_2 mixture. For each component, $D_{i,s}$ decreases consistently with loading and the decreases rate is faster in a less porous adsorbent. In MFI, $D_{i,s}$ of CH_4 is found to be greater than CO_2 at low to moderate loadings, whereas at high loadings CH_4 and CO_2 have close $D_{i,s}$. In IRMOF-1, D_s of CH_4 is greater than that of CO_2 at all loadings considered. Nevertheless, D_s of CO_2 in C_{168} is greater than that of CH_4 since CO_2 is a more slender molecule and the free energy barrier for CO_2 hopping in C_{168} is lower. The predictions are found to be in fairly good agreement with the simulation results, particularly, for both CH_4 and CO_2 in MFI and for CH_4 in IRMOF-1. In zeolites and carbon nanotubes, a number of simulation studies have validated the predictions of MS formulation for mixture diffusivities from the single-component data [332,335,338,339,342]. In this study, we further show that MS formulation is also successful in predicting the diffusion of mixture in MOF.

4.4.4 Permselectivity

The separation factor of a mixture across membrane is characterized by permselectivity, which depends on solubility selectivity – an equilibrium property,

and diffusivity selectivity – a transport property. In a binary mixture, permselectivity can be approximated as

$$S_{\text{perm}} = S_{\text{diff}}\ S_{\text{sorp}} = \frac{D_{1,s}}{D_{2,s}} \frac{\Theta_1}{\Theta_2} \tag{4.18}$$

where $S_{\text{diff}} = D_{1,s} / D_{2,s}$ is the diffusion selectivity, the ratio for the self-diffusivity of component 1 to component 2. $D_{1,s}$ and $D_{2,s}$ are the self-diffusivities obtained from the simulation of binary mixture. $S_{\text{sorp}} = \Theta_1 / \Theta_2$ is the sorption selectivity, the ratio for the loading of component 1 to component 2 in mixture. Earlier, the adsorption and sorption selectivity for the equimolar mixture of CH_4/CO_2 in MFI, IRMOF-1 and C_{168} were discussed. CO_2 is preferentially adsorbed than CH_4 in all the three adsorbents. S_{sorp} at low pressures is larger in C_{168} compared to MFI and IRMOF-1; however, approximately the same in all the three adsorbents at high pressures. Combining with S_{diff} as shown in Figure 4.20, S_{perm} is calculated based on the equimolar mixture of CO_2 /CH_4 in MFI, IRMOF-1 and C_{168}, as shown in Figure 4.21. Note that the largest loading simulated is close to saturation in MFI and C_{168}, but not in IRMOF-1. S_{perm} in MFI has an overall value of about 2.0, it increases marginally with loading and then decreases slightly at high loadings. There is a slight increase of S_{perm} in IRMOF-1 over the range of loading considered, and the overall value of S_{perm} is close to unity. Despite the largest storage capacity among the three structures, IRMOF-1 shows poor permselectivity. In C_{168}, S_{perm} increases as the loading increases, primarily because of the rise in S_{sorp}. But at high loadings, S_{perm} drops due to the decrease in S_{sorp} as a result of competitive adsorption between CH_4 and CO_2. Being a smaller molecule, CH_4 is preferentially adsorbed than CO_2 at high loadings because of entropic effects. Though the permselectivity in C_{168} schwarzite is predicted to be higher than in

IRMOF-1 and MFI, it is not sufficiently high for efficient separation from a practical point of view.

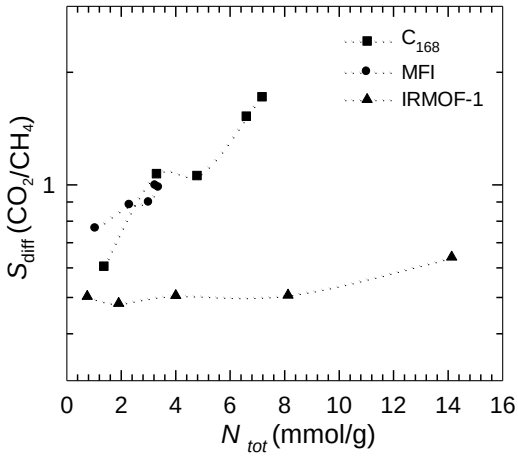

Figure 4.20. Diffusion selectivity of CO_2 over CH_4 in MFI, IRMOF-1 and C_{168} as a function of total loading based on the self-diffusivity of equimolar mixture. Dotted lines are to guide the eye.

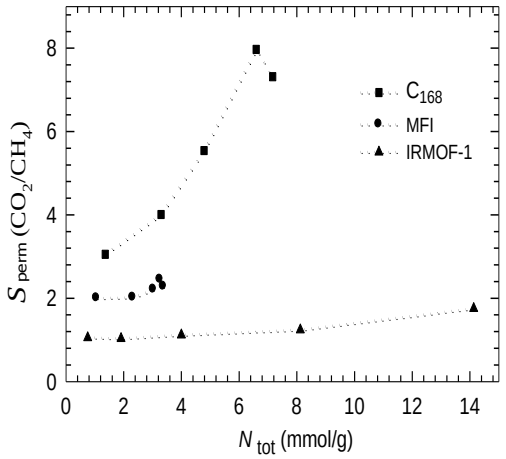

Figure 4.21. Permselectivity of CO_2 over CH_4 in MFI, IRMOF-1 and C_{168} as a function of total loading based on the adsorption of equimolar mixture. Dotted lines are to guide the eye.

4.5 Summary

Monte Carlo and molecular dynamics simulations have been used to study the adsorption and diffusion of pure and mixed CO_2 and CH_4 in three nanosized porous adsorbents, silicalite, C_{168} schwarzite, and IRMOF-1. The simulated adsorption

isotherms and isosteric heats are consistent with available experimental data. Compared to silicalite and C_{168} schwarzite, the adsorption capacity of pure CH_4 and CO_2 separately in IRMOF-1 is substantially higher. CO_2 is preferentially adsorbed over CH_4 from their binary mixture in all three adsorbents. Predictions from the ideal-adsorbed-solution theory based on the adsorption of only pure gases agree well with the simulation results. Even though the storage capacity of IRMOF-1 is greater than silicalite and C_{168} schwarzite, the adsorption selectivity of CO_2 over CH_4 is found to be close in all the three adsorbents.

In the limit of infinite dilution, the diffusivities at various temperatures show a good Arrhenius relation and used to estimate the activation energies. The activation energy of CO_2 in C_{168} is considerable smaller, implying a lower free-energy barrier for the slender CO_2 in C_{168}. The self-, corrected- and transport diffusivities at different length scales are computed as a function of loading. The self-diffusivities belong to type I behavior in that they decrease with increased loading due to the steric effect, and the decrease rate is faster in a less porous structure. The corrected diffusivities exhibit the weak and strong confinement scenarios. In the former, they remain nearly constant for both CH_4 and CO_2 in IRMOF-1, for CH_4 in MFI and CO_2 in C_{168}; while in the latter, they decreases approximately linear for CH_4 in C_{168} and CO_2 in MFI. As a product of the corrected diffusivity and thermodynamic factor, transport diffusivities generally increase except a nonmonotonic behavior of CO_2 in IRMOF-1. The correlation effects in diffusion are estimated from the simulated self- and corrected diffusivities, and found to reduce with increasing porosity of the three adsorbents, that is, in the order from MFI, C_{168} to IRMOF-1. There is no direction connection between the strength of correlation and the confinement scenario. Strong correlation effects do not necessarily suggest the strong confinement scenario, and vice versa. From the MS

formulation, the predicted self-, corrected- and transport diffusivities for pure CH_4 and CO_2 in the three adsorbents are found to agree well with the simulated results. In CO_2/CH_4 binary mixture, the self-diffusivities for both components also exhibit type I behavior, i.e., decrease with loading. Predictions of the self-diffusivities are in fairly good agreement with the simulation results in the three adsorbents. Therefore, in addition to zeolites and carbon-based materials, the MS formulation is proved to be applicable in predicting mixture diffusion in IRMOF-1 and can be extended to other MOFs.

From the adsorption and diffusion selectivity calculated using binary mixture, permselectivity is estimated as a function of loading. As loading rises, the permselectivity in IRMOF-1 slightly increases with an overall value close to unity. Similar trend is observed in MFI, though the value is a bit larger. In C_{168}, the permselectivity is the greatest but appears to drop at a high loading. Though IRMOF-1 has the largest storage capacity for CH_4 and CO_2, its selectivity is poor. C_{168} schwarzite, considered as a hypothetical model for nanoporous carbon membranes, is shown to be more selective compared with IRMOF-1 and MFI, but insufficient for practical separation. Nevertheless, as the functionality of MOFs can be altered readily by tailoring metal-oxide and organic linker, a wide variety of MOFs can be explored to achieve a high capacity for CO_2 storage and desired selectivity for CO_2/CH_4 mixture, as well as for other industrially important mixtures.

Chapter 5

Storage of CO_2 in Metal-Organic and Covalent-Organic Frameworks

5.1 Introduction

According to the recent report by the World Meteorological Organization (WMO), atmospheric concentrations of greenhouse gases such as CO_2, CH_4 and NO reached new high in 2007. In particular, CO_2 concentration in the atmosphere has increased by a third over preindustrial levels, from about 280 ppm to 385 ppm [343]. The impact of CO_2 emissions is already seen in the increase of global temperature, the change of snow cover, and the decrease in upper ocean pH. Recent estimations by the Intergovernmental Panel on Climate Change (IPCC) [343] indicate that large reduction from current CO_2 emissions will be required by mid-century if we are to stabilize atmospheric concentrations of CO_2, even at levels substantially higher than the current but low enough to limit the predicted global average temperature rise up to 2 °C.

MOFs are considered as ideal materials for gas storage compared to zeolites and carbons. Millward et al. [98] studied the storage capacity of CO_2 in a series of MOFs using gravimetric method. They selected nine compounds that represent a cross section of framework characteristics such as square channel (MOF-2), pores decorated with open metal sites (MOF-505 and $Cu_3(BTC)_2$), hexagonally packed cylindrical channels (MOF-74), interpenetration (IRMOF-11), amino- and alkyl-functionalized pores (IRMOFs-3 and -6), and extra-high porosity frameworks (IRMOF-1 and MOF-177). MOFs can be easily tuned to vary pore size and

functionality to suite a particular application, resulting in infinite number of porous crystalline structures. Therefore, in order to screen MOFs for high efficacy storage application, molecular modeling can be a useful tool to complement experiments. In this study, different kinds of MOFs and COFs were chosen with characteristics such as varying metal-oxide, organic linker, topology, and pore size to quantitatively assess the storage capacity of CO_2 and to develop structure-function correlations. To examine the effect of cations, CO_2 adsorption in pure silicalite and Na-exchanged ZSM-5 with different Si/Al ratio were compared.

Initially, the storage capacity of CO_2 in three different adsorbents: silicalite (with varying Si/Al ratio), SWNT and IRMOF-1 were investigated. Then different MOFs with varying characteristics were chosen to study the uptake of CO_2. Finally, COFs considered as sub-class of MOFs were characterized for CO_2 storage. In Section 5.2 the models used for the different adsorbents and adsorbate are described. In Section 5.3 the Monte Carlo simulation method is briefly described. The adsorption isotherms of pure components, isosteric heats of adsorption, Henry constants, and density contours are presented in Section 5.4, followed by summary in Section 5.5.

5.2 Models

Silicalite and Na-ZSM-5

Silicalite (MFI) is an Al-free zeolite existing in three distinct crystal forms: monoclinic, *Pnma* and $P2_12_12_1$ orthorhombic structures. In this work, the *Pnma* orthorhombic structure was considered. The unit cell has 96 Si atoms and 192 O atoms, and the lattice constants are $a = 20.06$ Å , $b = 19.80$ Å , and $c = 13.36$ Å . MFI consists of two types of channels with 10-membered rings, one is straight and the other is zig-zag (sinusoidal). These channels have diameters of approximately 5.4 Å .

A unit cell has two straight channels, two zigzag channels, and two channel intersections [344]. For Na^+-exchanged ZSM-5 zeolites, there are charge balancing nonframework Na^+ cations in addition to the framework Si, O and Al atoms. Two Na-ZSM-5 zeolites were considered here with two different Si/Al ratios (23 and 11), in which Si atoms were substituted with Al atoms at T12 sites. The potential parameters and atomic charges for MFI and Na-ZSM-5 were adopted from the work of Hirotani et al. [287] as listed in Table 5.1, which had been optimized to reproduce the experimental heats of adsorption. It is worthwhile to note that in most of the previous simulation studies of adsorption in zeolites, the short-ranged dispersion interaction of Si atoms was neglected because of its weak contribution, and thus only electrostatic interaction was taken into account. To model the fully atomistic framework, in this work both the dispersion and electrostatic interactions were considered for O and Si atoms.

MFI **Na-ZSM-5 (23)** **Na-ZSM-5 (11)**

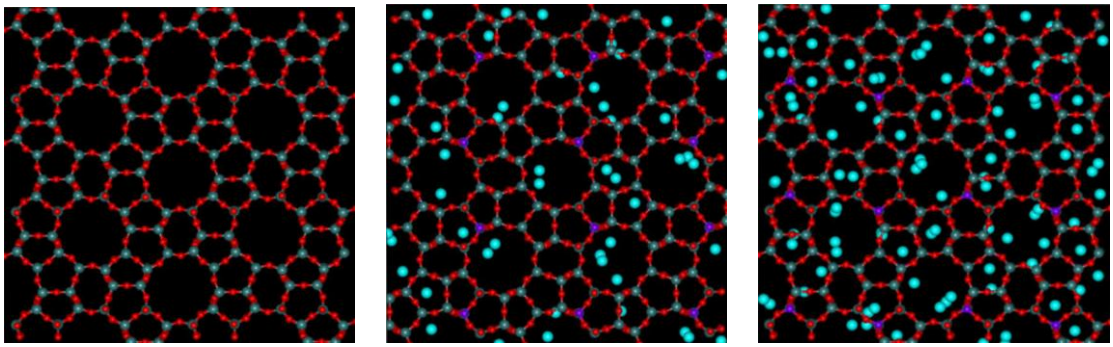

SWNT

Carbon nanotube is a seamless cylinder rolled-up by graphene sheet [345]. On the basis of experimental observation, carbon nanotubes exist as hexagonal bundles with the nanotube number between 100 and 500 or in the order of 20 [346,347]. A homogeneous bundle was mimicked in this study using hexagonally aligned armchair (10, 10) single-walled carbon nanotube (SWNT). Each (10, 10) SWNT has a diameter

of 13.56 Å and the van der Waals gap between nanotubes is 3.2 Å [346,347]. There are three types of energetically favorable adsorption sites within the bundle, the annular layer and center inside the nanotube and the interstitial channels between the nanotubes. The charge on C atom was assumed to be zero and the LJ potential was used to model the dispersive interaction on C atom [348] and listed in Table 5.1.

SWNT

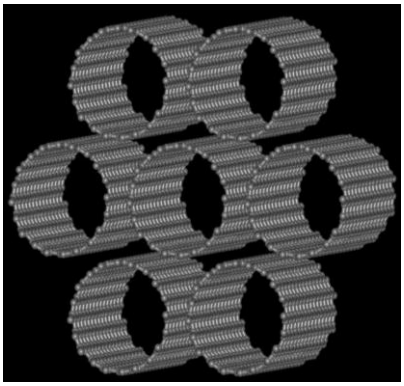

MOFs

IRMOF1 is an isoreticular MOF and also known as MOF-5 [7]. It has a lattice constant of 25.832 Å , a crystal density of 0.593 g/cm^3, a free volume of 79.2%, and a surface area of 2833 m^2/g [98]. IRMOF-1 has a formula of $Zn_4O(BDC)_3$, where BDC is 1,4-benzenedicarboxylate [3]. Each oxide-centered Zn_4O tetrahedron is edge-bridged by six carboxylate linkers resulting in an octahedral $Zn_4O(O_2C-)_6$ building unit, which reticulates into a three-dimensional cubic structure. IRMOF1 is a prototype of isoreticular MOF and other IRMOFs can be obtained by tailoring the metal oxide and organic linker, as schematically demonstrated in Figure 5.1. Specifically, Mg-IRMOF1 and Be-IRMOF1 were constructed by replacing Zn_4O in IRMOF1 with lighter Mg_4O and Be_4O. From *ab initio* calculations, Han et al. [166] found that the substitution of Zn with Mg or Be does not change the basic configuration of the metal oxide and the crystal structure remains stable. Although

Mg-IRMOF1 and Be-IRMOF1 are not yet reported experimentally, the objective is to examine whether CO_2 storage is affected by varying the metal oxide. IRMOF1-$(NH_2)_4$ was constructed by adding four amino groups onto the four available positions of the BDC linker in IRMOF1. Compared with IRMOF3 in which only one amino group is present [2], more groups are introduced in IRMOF1-$(NH_2)_4$ to check the effect of functional groups. IRMOF10 and IRMOF14 were constructed by replacing BDC in IRMOF1 with biphenylene dicarboxylate (BPDC) and pyrene dicarboxylate (PDC), respectively. From BDC to BPDC and PDC, the organic linker becomes longer in length and also bigger in size. The pore diameters are 16.7 and 20.2 Å in IRMOF10, and 14.7 and 20.1 Å in IRMOF14 [2]. IRMOF13 was constructed by interpenetrating framework. Despite the identical metal oxide and organic linker in IRMOF13 and IRMOF14, they differ in the topology. The pore diameter in IRMOF13 is reduced to 12.4 and 8.7 Å due to the interpenetration [2].

A new type of MOF with fluorine (F-MOF1) was also considered. F-MOF1 consists of six-connected tetranuclear (Ag_4Tz_6) clusters (where Tz represents triazolate) linked by three-coordinated Ag centers [349]. There are two types of channels, one with a semirectangular shape of size ~ 12.2 × 7.3 Å and the other one with diamond-shape of size ~ 6.6 × 4.9 Å. The experimentally determined surface area is 810.5 m^2/g and the pore volume is 0.324 cm^3/g. In addition, University of Michigan Crystalline Material-1 denoted as UMCM-1 was studied for CO_2 adsorption. UMCM-1 consists of Zn_4O clusters linked together by two BDC and four BTB linkers arranged in an octahedral geometry. It consist of two types of pore, one is micropore with an dimension of approximately 14 x 17 Å [38] and the other one is mesopore with an 1D hexagonal channel of dimension 27 x 32 Å neglecting the van der Waal's radii of the atoms in both case.

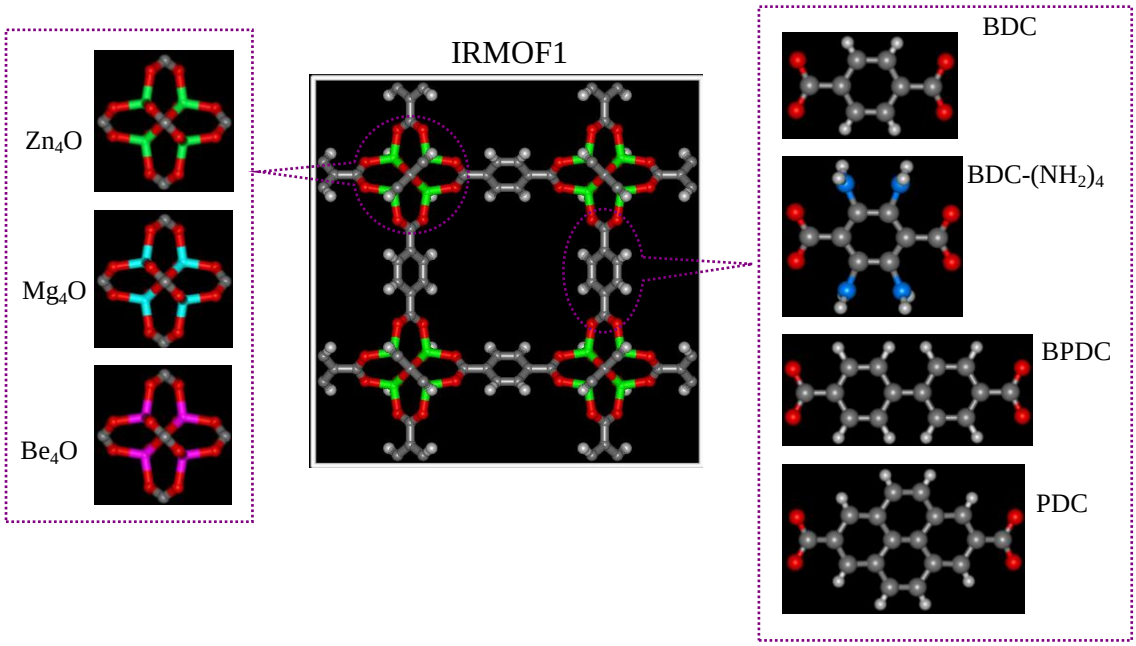

Figure 5.1. Schematic tailoring the metal oxide and organic linker in IRMOF1. Zn: green, Mg: cyan, Be: purple, O: red, N: blue, C: grey, H: white.

COFs

COFs can exist in 3D, 2D and 1D as shown in Figure 5.2. Co-condensation of boronic acid with hexahydroxytriphenylene results in 2D COF-6, -8 and -10 [51]. COF-6 and -8 have pore sizes of 8.6 and 16.4 Å, respectively; whereas COF-10 has pore size of 31.7 Å. These 2D COFs resemble the layered graphite composed of graphene sheets. The inter-layer distances in COF-6, -8 and -10 are 3.399, 3.630 and 3.526 Å, respectively. Alternatively, joining triangular and tetrahedral nodes lead to 3D COF-102, -103, -105 and -108 [52]. COF-102 has a cubic structure with a lattice constant of 27.18 Å and a crystal density 0.41 g/cm^3. The largest cavity in the center of COF-102 is 5.66 Å from the nearest H atoms. COF-103 is identical to COF-102, except that the tetrahedral C atoms are replaced by Si atoms. COF-105 and COF-108 were reported to have the lowest density (as low as 0.17 g/cm^3), even lower than the highly porous materials MOF-177 (0.42g/cm^3). COF-108 has two types of cavities namely 9.34 and 15.46 Å from the center C atom excluding the van der Waals radii.

In general, the pores in 3D COFs are not spherical but fully accessible to all the edges and faces in the framework. Similar to carbon nanotube, armchair or zig-zig 1D COF nanotube (COF_NT) could be constructed by rolling a COF layer in a particular direction. Mazzoni and coworkers tested the stability of COF_NTs by examining the structural and electronic properties using the first-principles calculations [53]. A hexagonal COF_NT bundle is constructed to explore its capacity for CO_2 storage. Each COF_NT has a diameter of 16.8 Å and the van der Waals gap (distance between two neighboring nanotubes) is 3.2 Å. There exist three types of energetically favorable adsorption sites within the bundle, the annular layer and center inside the nanotube and the interstitial channels between the nanotubes.

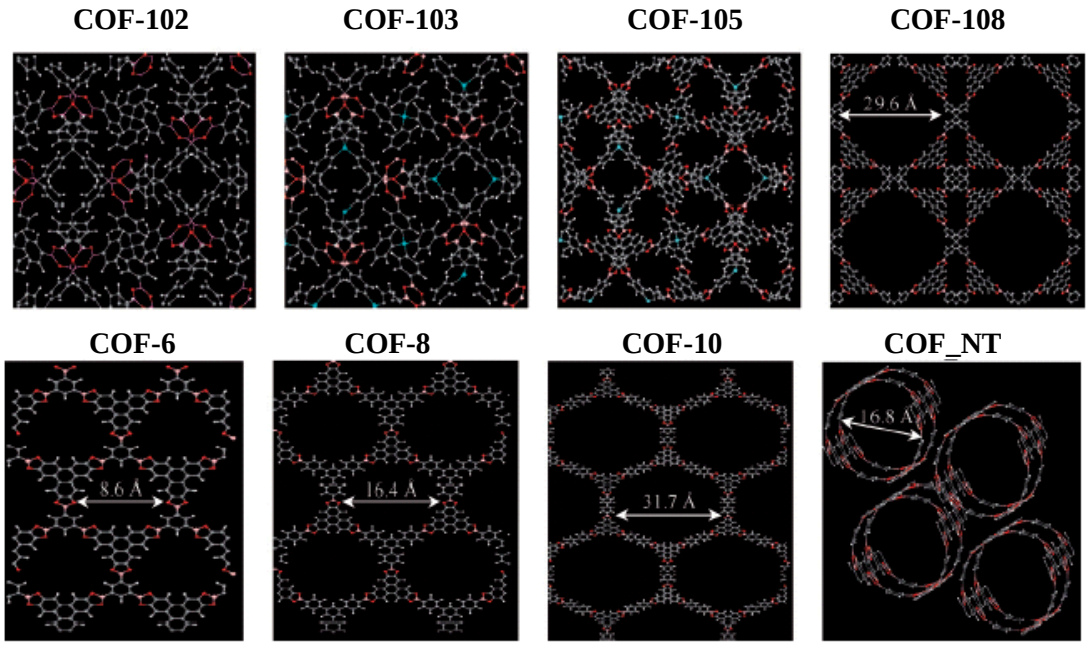

Figure. 5.2. Atomic structures of COF-102, COF-103, COF-105, COF-108, COF-6, COF-8, COF-10 and COF_NT. The structures are not drawn to scale. B:pink, C: grey, O: red, Si: cyan, H: white.

The dispersive interactions of all the toms in MOFs and COFs were modeled by the Universal Force Field [174] and listed in Table 5.1. Similar model as described in Section 4.2 was used for CO_2 with the potential parameters listed in Table 4.2. The atomic partial charges of the MOFs and COFs were estimated from fragmental

clusters as shown in Figure 5.3. B3LYP density-functional theory (DFT) and 6-31G(d) [350] basis set were used with the Gaussian 03 suite of programs [293].

TABLE 5.1. LJ and Coulombic potential parameters for ZSM-5, SWNT, MOFs and COFs [174, 287, 348].

Adsorbent	Site	σ(Å)	ε / k_B (K)	q (e)
ZSM-5	**O**	2.708	128.21	–0.400
	Si	0.677	18.60	+0.800 (Si/Al = ∞)
				+0.766 (Si/Al = 23)
				+0.732 (Si/Al = 11)
	Al	1.016	19.11	+0.575 (Si/Al = 23)
				+0.549 (Si/Al = 11)
	Na	2.655	15.08	+1
SWNT	**C**	3.40	28.00	0
MOF/COF	**Zn**	2.462	62.343	ESP Charges on structure as shown in Fig. 5.2
	Mg	2.691	55.807	
	Be	2.446	42.735	
	Ag	2.805	18.100	
	B	3.638	90.498	
	C	3.431	52.791	
	N	3.261	34.691	
	O	3.118	30.166	
	F	2.997	25.138	
	H	2.571	22.122	

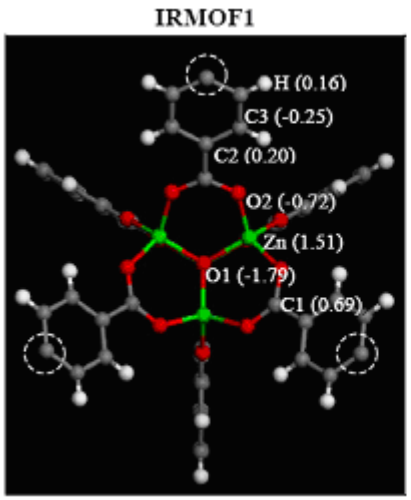

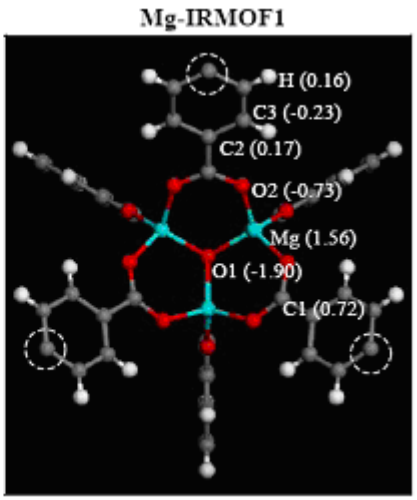

Be-IRMOF1

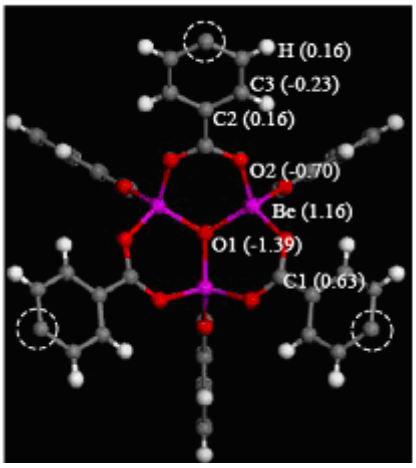

IRMOF1-$(NH_2)_4$

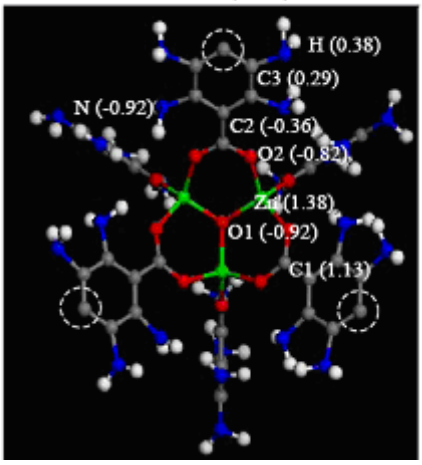

IRMOF10

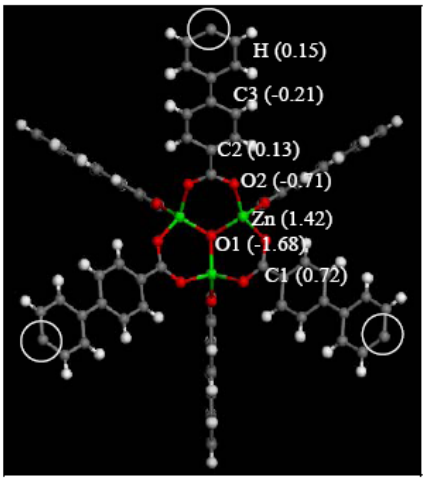

IRMOF13 and IRMOF14

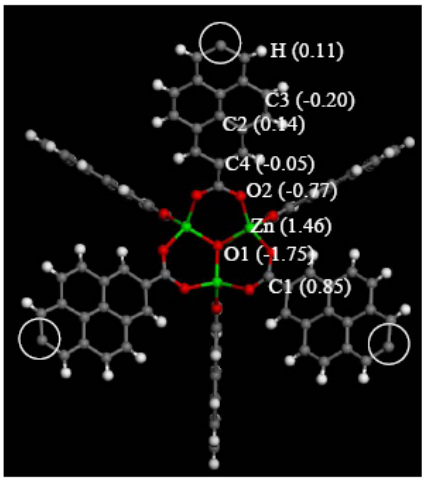

UMCM-1

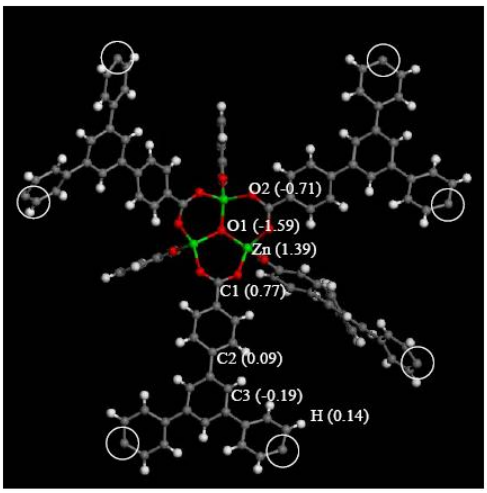

F-MOF1

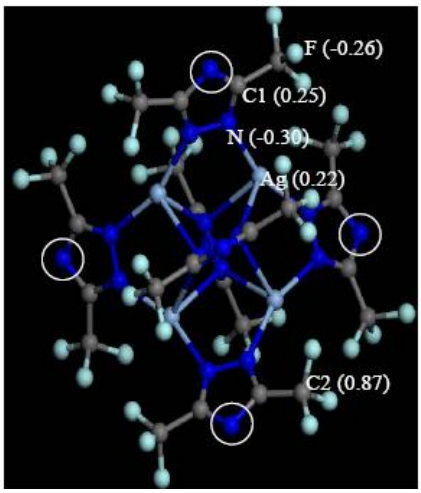

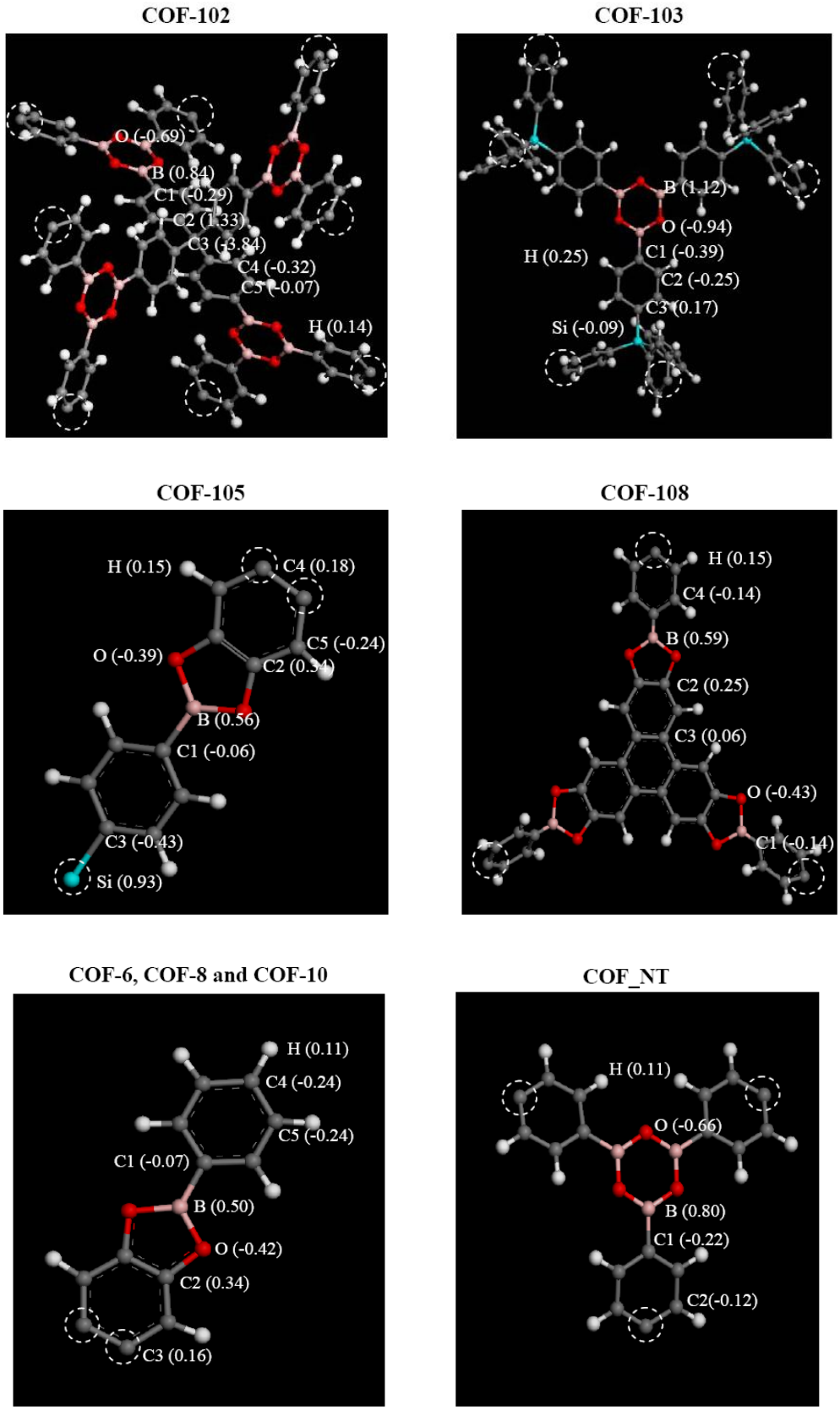

Figure 5.3. Atomic charges in MOFs and COFs. Different cluster models are used in density-functional theory calculations for MOFs and COFs. The cleaved clusters are terminated by methyl group to maintain correct hybridization.

5.3 Methodology

Most simulation studies for adsorption have used GCMC method at fixed chemical potential μ, volume V and temperature T [252]. The chemical potential as an input in GCMC, however, has to be converted into pressure for comparison with experimental data. This has to be implemented using empirical equation of state or additional simulation. Here, GEMC simulation was used directly at a given pressure. Two simulation boxes were used one for adsorbent and other for bulk adsorbate. The total number of adsorbate molecules was fixed, but molecules can be transferred from one box to the other. The volume of the adsorbent was fixed, while the bulk phase was allowed to change at fixed bulk pressure. Jiang and Sandler have used GEMC simulation to study the adsorption of pure O_2, N_2 and their mixtures in carbon-based materials and found perfectly consistent results between GEMC and GCMC simulations [322,351]. The beauty in GEMC simulation is that one can directly obtain the uptake at a desired bulk pressure, as well as the bulk density and enthalpy. The latter are needed to calculate the excess adsorption and heat of adsorption.

As our study was on the low-energy equilibrium configurations, the adsorbent structures were assumed to be rigid during simulations. Structural flexibility allowing local small movements would not be expected to give significantly different results. The simulation box representing MFI and ZSM-5 contained 12 ($2\times2\times3$) unit cells. The simulation box varied from ($1\times1\times1$) to ($3\times3\times1$) unit cells for MOFs and ($1\times1\times1$) to ($2\times2\times8$) unit cells for COFs. The periodic boundary conditions were exerted in all three directions. A spherical cutoff length of 15.0 Å was used to calculate the LJ intermolecular interactions with the tail correction added. Coulombic interactions were evaluated by the Ewald sum with an infinity dielectric constant in

the surrounding. The Ewald sum consists of a real-space sum, a reciprocal-space sum and a self-interaction sum [253]

$$U_{\text{ele}} = \frac{1}{8\pi\varepsilon_0}\sum_{i=1}^{N}\sum_{j=1}^{N}\sum_{|\mathbf{n}|=0}^{\infty}{}' q_i q_j \frac{\operatorname{erfc}(\alpha|\mathbf{r}_{ij}+\mathbf{n}|)}{|\mathbf{r}_{ij}+\mathbf{n}|} + \frac{1}{2\varepsilon_0 V}\sum_{k\neq 0}\frac{1}{k^2}\exp\left(\frac{-k^2}{4\alpha^2}\right)\sum_{i=1}^{N}\sum_{j=1}^{N} q_i q_j \cos(\mathbf{k}\cdot\mathbf{r}_{ij}) - \frac{\alpha}{4\pi\sqrt{\pi}\,\varepsilon_0}\sum_{i=1}^{N} q_i^2 \tag{5.1}$$

where erf(x) is the error function, erfc(x) is the complementary error function and erfc(x) = 1 – erf(x). The atomic distance is $\mathbf{r}_{ij} = \mathbf{r}_i - \mathbf{r}_j$. The lattice points contain $\mathbf{n}$ = (n_xL_x, n_yL_y, n_zL_z) with the integers n_x, n_y, n_z and the box lengths L_x, L_y, L_z. The prime indicates $i \neq j$ when $\mathbf{n}$ = 0. The reciprocal wave vectors are determined by $\mathbf{k} = 2\pi$ (n_x/L_x, n_y/L_y, n_z/L_z) and $k = |\mathbf{k}|$. A balance between accuracy and computing time is governed by the real/reciprocal space partition parameter α and the cutoff k in the reciprocal space. Usually α is chosen in such a way that erfc(αr) decreases rapidly with r, and thereby the sum in real space at $\mathbf{n}$ = 0 converges within the cutoff distance. The cutoff k is chosen to ensure rapid convergence of the reciprocal-space sum. In our work, α was chosen to be 0.2 Å^{-1} and k is 8, a dimensionless parameter.

Four types of trial moves were conducted randomly in the GEMC simulation including displacement and rotation in each phase, swap between the two phases, and volume change of the bulk phase. The number of trial moves in a typical simulation was 2×10^7, though additional trial moves were used at high coverages. The first 10^7 moves were used for equilibration, and the second 10^7 moves to obtain ensemble averages. The block transformation method was used to estimate the statistical uncertainties of the simulated averages [252]. Unless otherwise mentioned, the uncertainties were smaller than the symbol size in the figures presented.

To precisely characterize adsorption process, the isosteric heat of adsorption rather than the adsorption isotherm is usually used to ascertain the adsorption mechanism as the isosteric heat is more sensitive to the change of adsorption energy. The isosteric heat q_{st} was calculated [302] from

$$q_{st} = H_b - \left[\frac{\partial (U_{total} - U_{intra})}{\partial N_{ab}} \right]_{T,V} \tag{5.2}$$

where H_b is the enthalpy of adsorbate in the bulk phase obtained directly from GEMC simulation. In most GCMC simulation studies, H_b is simply assumed to be RT in which R is gas constant. This is acceptable when the bulk phase behaves as an ideal gas, but not accurate at high pressures/low temperatures. U_{total} is the total adsorption energy including contributions from both adsorbate-adsorbent and adsorbate-adsorbate interactions, U_{intra} is the total intramolecular energy of the adsorbate and N_{ab} is the molar number of adsorbed molecules.

Canonical ensemble (NVT) simulation was also performed to estimate the isosteric heat of adsorption and Henry constant at infinite dilution. A single adsorbate molecule was subjected to three types of trial moves employed in the NVT simulation, namely, translation, rotation and regrowth. The isosteric heat at infinite dilution was calculate from

$$q_{st}^0 = RT - \left(U_{total}^0 - U_{intra}^0 \right) \tag{5.3}$$

where U_{total}^0 is the total adsorption energy of a single molecule with adsorbent and U_{intra}^0 is the intramolecular interaction of a single gas molecule in bulk phase.

The Henry constant K_H was calculated from

$$K_H = \frac{N_A}{RT} \frac{\int \exp[-\beta u_a(\mathbf{r}, \varpi)] \, d\mathbf{r} d\varpi}{\int \exp[-\beta u_{intra}(\mathbf{r}, \varpi)] \, d\mathbf{r} d\varpi} \tag{5.4}$$

where N_A is the Avogadro constant, $\beta = k_B T$ and k_B is the Boltzmann constant, $u_a(\mathbf{r}, \varpi)$ is adsorption energy of gas. The two integrals give the excess chemical potentials of a single adsorbate molecule in adsorbent and in bulk phase, respectively. From the regrowth trial move, which is equivalent to the Widom test–particle insertion method [352], the excess chemical potential was evaluated.

Experimental adsorption isotherm is usually reported in the excess amount N_{ex}, while simulation gives the absolute amount N_{ab}. To convert from N_{ab} to N_{ex}, we used

$$N_{ex} = N_{ab} - \rho_b V_{free} \tag{5.5}$$

where ρ_b is the density of bulk adsorbate, which is readily obtained from GEMC simulation. V_{free} is the free volume in adsorbent available for adsorption and estimated from

$$V_{free} = \int_V \exp[-u_{ad}^{He}(\mathbf{r})/k_B T]\, d\mathbf{r} \tag{5.6}$$

where u_{ad}^{He} is the interaction between Helium and adsorbent, in which s_{He} = 2.58 Å and e_{He}/k_B = 10.22 K [353]. Note that the free volume detected by Helium is temperature dependent, and usually the room temperature was chosen. The ratio of free volume V_{free} to the occupied volume V_{total} gives the porosity ϕ of adsorbent. In addition, the accessible surface area A_{surf} was estimated. In our calculation, a probe molecule with a diameter equal to 3.30 Å (kinetic diameter for CO_2) was rolled over the framework surface. All simulations were performed at 300 K using in-house developed code.

5.4 Results and Discussion

First, the capacity in IRMOF1, as a prototype MOF, was compared with those in MFI and carbon nanotube. In addition, Na^+ cations were introduced into MFI to examine whether the introduction of nonframework cations could enhance capacity. Carbon nanotube is the iconic molecule in nanoscience and nanotechnology and has been proposed as a good candidate for storage because of the hollow interior. By comparing adsorption in these three families of nanoporous materials, IRMOF1 has the highest capacity for CO_2 storage. Then, a series of IRMOFs were considered with variations in metal oxide, organic linker, functional group and framework topology, as well as F-MOF1. In addition, a variety of COFs existing in 3D, 2D and 1D structure, consisting of light elements were also investigated. To establish the relations between adsorbent structure and CO_2 adsorption, finally the capacities at 30 bar were correlated with framework density, free volume, porosity and accessible surface area.

5.4.1 Adsorption in MFI, SWNT and MOFs

5.4.1.1 Structural and Limiting Properties

For characterization of adsorbent structure, the framework density ρ_f , free volume V_{free}, porosity ϕ, accessible surface area A_{surf} for each adsorbent were calculated and listed in Table 5.2. Also listed are the isosteric heat q_{st}^0 and Henry constant K_H for CO_2 adsorption at infinite dilution. The extent of adsorption in the Henry regime depends primarily on the interaction strength between CO_2 and adsorbent, which is reflected in q_{st}^0 and K_H. The predicted q_{st}^0 in MFI agrees well with the measured values of 21.7 ~ 24.1 kJ/mol [354]. In MFI, SWNT, IRMOF1-$(NH_2)_4$ and IRMOF13, both q_{st}^0 and K_H are pronouncedly larger than in all other adsorbents, because of the

relatively higher ρ_f, smaller V_{free}, ϕ and A_{surf}. The inorganic MFI and SWNT consist of narrow pores, therefore, interact with CO_2 strongly. By adding $-NH_2$ group or interpenetrating framework into IRMOF1, the adsorbent structure varies, particularly, the pore becomes constricted. Specifically, V_{free} drops from 1.39 cm^3/g in IRMOF1 to 0.97 and 1.00 cm^3/g, respectively, in IRMOF1-$(NH_2)_4$ and IRMOF13. Similarly, A_{surf} drops from 3742 to 2601 and 2869 m^2/g. Upon CO_2 adsorption, distance between CO_2 molecule in the constricted pore is shorter and CO_2 interacts more strongly with the adsorbent. Consequently, adsorption is enhanced in IRMOF1-$(NH_2)_4$ or IRMOF13 compared to IRMOF1.This was also observed by Jung et al in which IRMOF13 showed a stronger binding energy for H_2 adsorption at 77 K [177].

Table 5.2. Framework density, free volume, porosity, accessible surface area, heat of adsorption and Henry constant in MFI, SWNT and MOFs.

	ρ_f (g/cm^3)	V_{free} (cm^3/g)	ϕ	A_{surf} (m^2/g)	q_{st}^0 (kJ/mol)	K_H ($mmol/cm^3/kPa$)
MFI	1.79	0.21	0.37	691	23.86	0.052
SWNT	1.33	0.39	0.52	693	22.89	0.077
IRMOF1	0.59	1.39	0.82	3742	15.65	0.007
Mg-IRMOF1	0.47	1.76	0.82	4738	15.66	0.007
Be-IRMOF1	0.42	1.95	0.82	5270	14.05	0.005
IRMOF1-$(NH_2)_4$	0.74	0.97	0.72	2601	20.25	0.018
IRMOF10	0.33	2.73	0.90	4953	13.46	0.004
IRMOF13	0.75	1.00	0.75	2869	26.22	0.077
IRMOF14	0.37	2.44	0.91	4823	15.36	0.006
UMCM-1	0.39	2.28	0.89	4470	14.90	0.006
F-MOF1	1.76	0.23	0.40	842	16.49	0.007
COF-102	0.41	2.02	0.85	5172	16.54	0.013

Nevertheless, as we shall see below that the enhancement in CO_2 adsorption is only true in the Henry regime, but not at high pressures. In IRMOF1, Mg-IRMOF1, Be-IRMOF-1, IRMOF10, IRMOF14, UMCM-1 and F-MOF1, q_{st}^0 and K_H are approximately in the same magnitude, despite the high density of F-MOF1. This implies that CO_2 adsorption at infinite dilution is not distinctly changed by varying the metal oxide and organic linker in IRMOF1. The pore size remains almost the same or increase slightly upon substitution of Zn_4O by Mg_4O or Be_4O, or BDC by BPDC and PDC. Therefore, the interaction of CO_2 with adsorbent is not significantly altered.

5.4.1.2 Adsorption Capacity and Isosteric Heats

MFI, SWNT and IRMOF1 represent three different classes of nanoporous materials. Figure 5.4 show the gravimetric and volumetric adsorption isotherms of CO_2 as a function of bulk pressure. In MFI the simulated results match closely with the experimental data [287]. In IRMOF1 good agreement is observed at low pressures between simulation and experiment, whereas at high pressures simulation slightly overestimates [98]. The reason could be that in our work IRMOF1 is considered as a perfect crystal; nevertheless, experimental samples may contain impurities and defects leading to a decrease in adsorption. Consistent with q_{st}^0 and K_H in Table 5.2, CO_2 adsorption at low pressures is less in IRMOF1 compared to MFI and SWNT as the interaction of CO_2 with IRMOF1 is weaker. The opposite is true at high pressures; however, at 1000 kPa CO_2 uptake in IRMOF1 is almost three - five fold greater than in MFI and SWNT. IRMOF1 has a substantially smaller ρ_f, larger V_{free}, ϕ and A_{surf}; consequently, more space is available for adsorption in IRMOF1 that can accommodate more CO_2 at high pressures. At the highest pressure of this study (5000

kPa), CO_2 adsorption reaches saturation in MFI and SWNT, whereas not in IRMOF1. We can conclude that IRMOF1 has a significantly higher capacity than MFI and SWNT for CO_2 storage. Figure 5.4 also reveals that the inclusion of framework charges in IRMOF1 only leads to a slightly higher adsorption. Figure 5.5 shows a similar role of the framework charges in IRMOF13 and IRMOF14. The observation here is consistent with the study by Walton et al. [199].

As mentioned above, the structure of MOF can be tailored over a wide atomic range. One can enhance the capacity even higher with a proper choice of the building block in MOF. Despite the considerable interest in SWNT for gas storage, our simulation results reveal that the use of SWNT is not feasible for CO_2 storage, since the physisorption is considered here for CO_2 in SWNT with relatively weak disperse interactions. If SWNT is functionalized by surface coating or interior doping, interactions between CO_2 and SWNT become stronger or chemisorption might occur and thus the capacity increases.

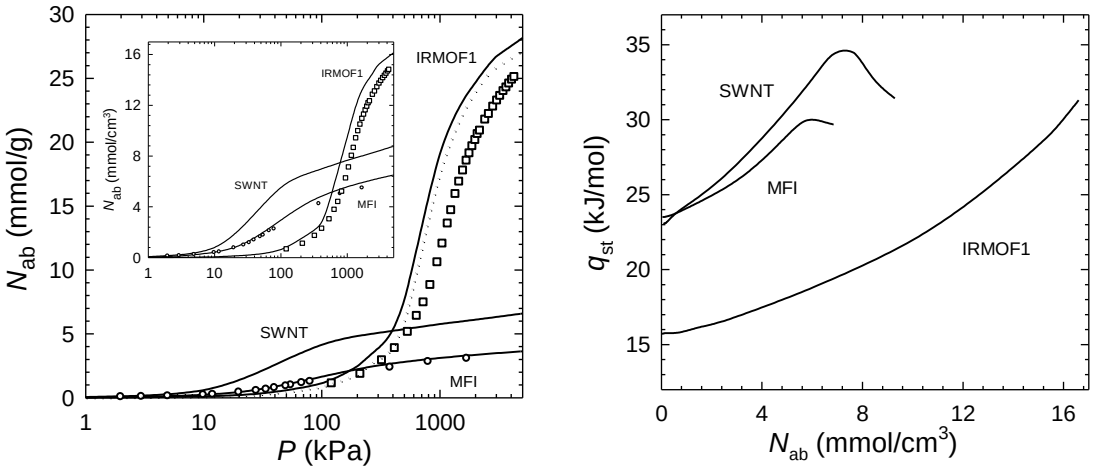

Figure 5.4. (Left) Gravimetric and volumetric (in the inset) isotherms of CO_2 adsorption in MFI, SWNT and IRMOF1 as a function of bulk pressure. The lines are simulation results and the symbols are experimental data [98,287]. The dotted line refers to adsorption in IRMOF1 without charges in the framework. (Right) Heats of CO_2 adsorption in MFI, SWNT and IRMOF1 as a function of loading.

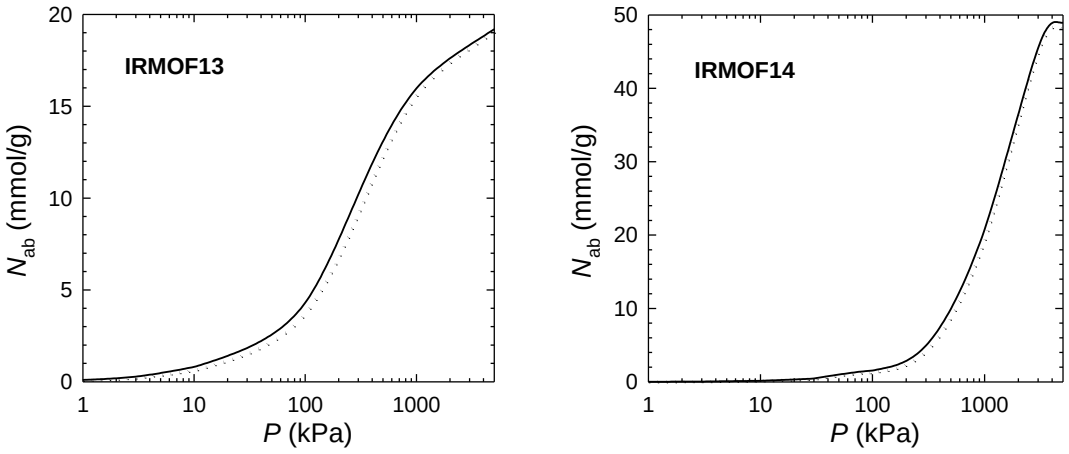

Figure 5.5. Gravimetric isotherms of CO_2 adsorption in IRMOF13 and IRMOF14 from simulations. The solid and dotted lines refer to adsorption with and without charges in the frameworks, respectively. Inclusion of the framework charges leads to a slightly higher adsorption.

The isosteric heats of CO_2 adsorption in MFI, SWNT and IRMOF1 are shown in Figure 5.4 as a function of loading. There results are estimated from eq. 5.2 and nearly identical to those from eq. 5.3 at infinite dilution, as they should be. In MFI and SWNT, q_{st} initially rises with loading, passes through a maximum and finally drops. There are two contributions to q_{st} , one from the adsorbate-adsorbent interaction and the other from the adsorbate-adsorbate interaction. The initial increase in q_{st} is due to the cooperative attraction between adsorbate molecules, while the adsorbate-adsorbent interaction remains essentially unchanged. Nevertheless, the further adsorbed adsorbate molecules must occupy the less favorable sites leading to a weaker adsorbate-adsorbent interaction and also the adsorbate-adsorbate interaction becomes less attractive because of the steric constraint. As a consequence, q_{st} drops at high loadings. Different behavior is observed for q_{st} in IRMOF1, in which q_{st} rises monotonically as the loading increases. This is because CO_2 adsorption in IRMOF1 has not reached saturation and the cooperative attraction between adsorbate-adsorbate

increases with loading. However, a drop in q_{st} is expected at high loadings close to saturation (not shown in Figure 5.4).

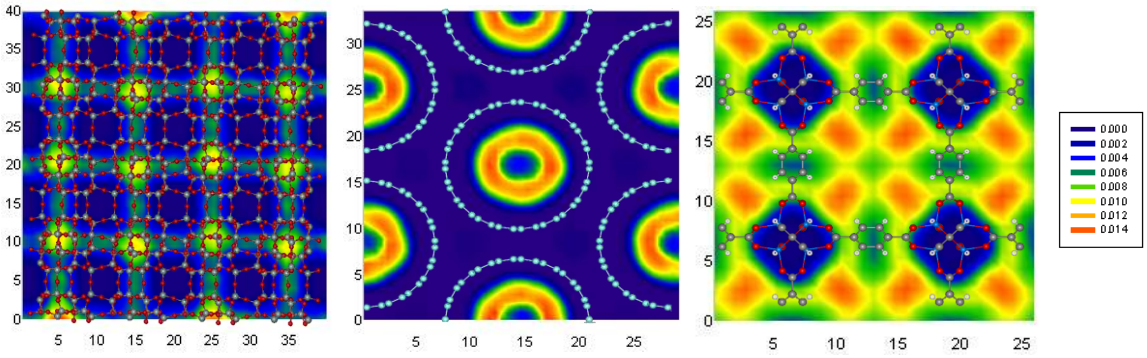

Figure 5.6. Density distribution contours for the center-of-mass of CO_2 molecules in MFI, SWNT and IRMOF1 at 1000 kPa.

To identify the favorable locations for CO_2 adsorption, Figure 5.6 shows the density distribution contours in the *xy* plane of MFI, SWNT and IRMOF1 at 1000 kPa. The contours were generated by accumulating the centers-of-mass of CO_2 molecules in 100 equilibrium configurations. CO_2 adsorption in MFI occurs mostly in the straight channels at 1000 kPa, but can be in both straight and zigzag channels at high pressures. In SWNT, CO_2 is exclusively adsorbed at the annular layer and the center inside the nanotubes. The annual layer in (10, 10) SWNT is the most favorable adsorption site, followed by the center [351]. At high pressures, intercalation is observed into the interstitial channels among the nanotubes. Because of the narrow channel, CO_2 molecules therein exhibit an interesting needle-like alignment. In IRMOF1, the strongest adsorption site is toward the metal-oxide cluster. At 1000 kPa CO_2 is preferentially adsorbed around the corners of Zn_4O clusters. However, the metal-oxide sites represent only a small portion of the framework, consequently, at high pressures adsorption occurs mainly in the central pores. This observation has been validated experimentally for Ar and N_2 in IRMOF1 [206].

5.4.1.3 Effect of Cations

It has been recognized that the nonframework cations in zeolites can enhance the extent of adsorption, particularly for molecules with polar or quadrupolar moment. Figure 5.7 shows the isotherms of CO_2 adsorption in MFI and Na-ZSM-5 (23) and Na-ZSM-5 (11). MFI is aluminium-free (Si/Al = ∞) ZSM-5 zeolite and no cation exists. In contrast, there are 4 Na^+ cations per unit cell in Na-ZSM-5 (Si/Al = 23) and 8 in Na-ZSM-5 (Si/Al = 11). A substantial increase in CO_2 adsorption is observed at low pressures upon adding Na^+ cations into MFI. The presence of cations largely increases the electrostatic interaction for CO_2 in the framework, which in turn increases adsorption. With further decrease of Si/Al ratio and hence increase in the number of Na^+ cations, CO_2 adsorption increases slightly from Na-ZSM-5 (23) to Na-ZSM-5 (11). At high pressures, the enhancement of CO_2 adsorption is not distinct. This is because the available volume for adsorption is indeed less in the presence of Na^+ cations, which becomes a predominant factor to determine capacity at high pressures. Our results reveal that the introduction of cations into adsorbent can increase CO_2 capacity only at low pressures.

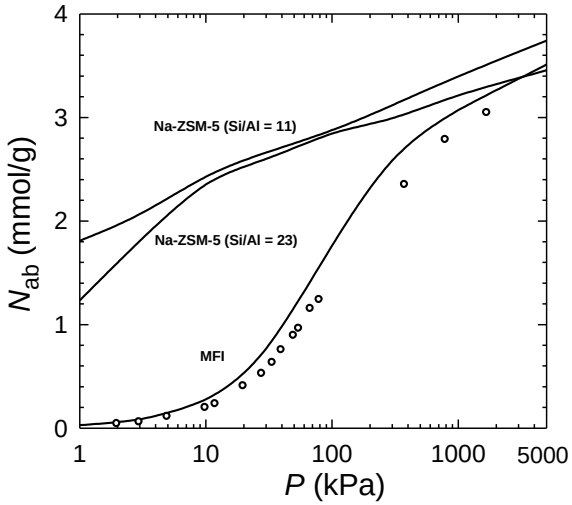

Figure 5.7. Isotherms of CO_2 adsorption in MFI, Na-ZSM-5 (23) and Na-ZSM-5 (11). The lines are simulation results and the symbols are experimental data [287].

5.4.1.4 Adsorption in MOFs

Adsorption capacity in IRMOF is affected by varying the metal oxide, functional group, organic linker and framework topology. Figure 5.8 shows the excess adsorption isotherms of CO_2 in a series of IRMOFs (IRMOF1, Mg-IRMOF1, Be-IRMOF1, IRMOF1-$(NH_2)_4$, IRMOF10, IRMOF13 and IRMOF14) as well as in UMCM-1, F-MOF1 and COF-102. In terms of the gravimetric basis, COF-102, IRMOF13 and IRMOF1-$(NH_2)_4$ show higher adsorption at low pressures compared to other adsorbents. In particular, there is a steep rise for CO_2 adsorption in COF-102. The packing of atoms in COF-102 is rather compact and hence COF102 has a significant overlap of spaces with attractive interaction with CO_2. This has been recently observed from a simulation study for CH_4 adsorption in different COFs.[181] IRMOF13 contains interpenetrated framework with constricted narrow pores, as a result, the interaction with CO_2 is strong. In IRMOF1-$(NH_2)_4$, the amino groups have a high affinity with CO_2 through the hydrogen bonding or interaction with the lone electron pair. This affinity is the basis for CO_2 absorption in amine solution, in which CO_2 shows high selectivity. Nevertheless, adsorption is strong at low pressures does not necessarily imply the same case at high pressures close to saturation. Indeed IRMOF13 and IRMOF1-$(NH_2)_4$ have far lower extent of saturation adsorption than all other MOFs considered here except F-MOF1. This is because the increased framework density and decreased free volume and surface area by interpenetrating framework or adding functional group. Specifically, the framework density increases from 0.59 g/cm^3 in IRMOF1 to 0.75 g/cm^3 in IRMOF13 and to 0.74 g/cm^3 in IRMOF1-$(NH_2)_4$. The free volume decreases from 1.39 cm^3/g in IRMOF1 to 1.00 and 0.97 cm^3/g, respectively, in IRMOF13 and IRMOF1-$(NH_2)_4$. Similar decrease is observed in the surface area. F-MOF1 was reported to hold the highest capacity for O_2

and among the best for H_2 at 77 K [349], but its capacity for CO_2 is found to be poor due to the significantly small free volume and surface area.

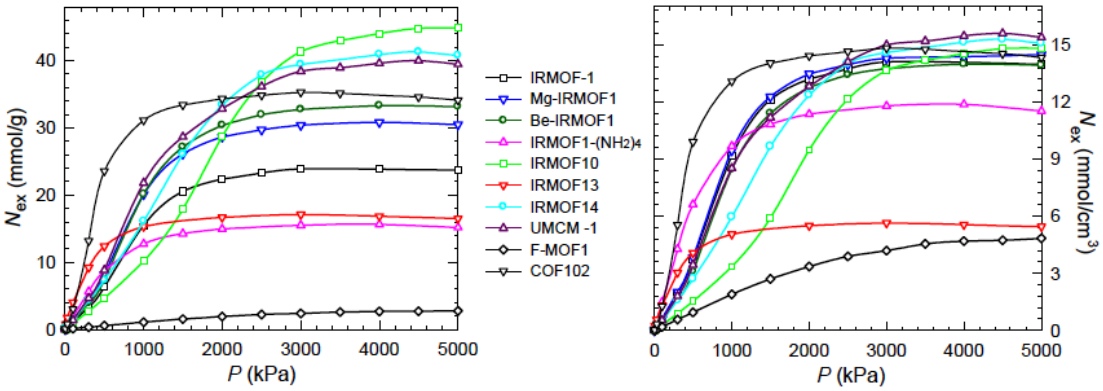

Figure 5.8. Gravimetric (left) and volumetric (right) isotherms of CO_2 adsorption in IRMOF1,Mg-IRMOF1, Be-IRMOF1, IRMOF1 $(NH_2)_4$, IRMOF10, IRMOF13, IRMOF14, UMCM-1, F-MOF1 and COF-102.

Substitution of the metal oxide Zn_4O in IRMOF1 by Mg_4O or Be_4O, the gravimetric adsorption rises, particularly at moderate and high pressures. This is primarily due to the presence of light metal Mg or Be, the framework density reduces from 0.59 g/cm^3 in IRMOF1 to 0.47 and 0.42 g/cm^3 in Mg-IRMOF1 and Be-IRMOF1, respectively. The reduction in density leads to the increase of free volume and surface area per unit mass, despite the identical porosity. Varying the organic linker from BDC in IRMOF1 to BPDC in IRMOF10 and to PDC in IRMOF14, the framework density reduces from 0.59 to 0.33 and 0.37 g/cm^3 in IRMOF10 and IRMOF14, respectively. In contrast, the porosity increases from 0.82 to 0.90 and 0.91, the free volume increases significantly from 1.39 to 2.73 and 2.44 cm^3/g, and the surface area increases from 3742 to 4953 and 4823 m^2/g. Similarly, using two different linkers namely BDC and BTB, the surface area and free volume increases and also a subsequent decrease in framework density is observed in UMCM-1.Consequently, IRMOF10, IRMOF14 and UMCM-1 have larger capacity for CO_2 adsorption at high pressures compared to other adsorbents, although the adsorption is lower at low

pressures. Since the pores in an adsorbent are almost fully filled at high pressures and adsorption approaches saturation, the adsorbent with a larger free volume has more space to accommodate molecules and hence exhibits higher capacity. CO_2 capacity predicted in IRMOF10, IRMOF14 and UMCM-1 is even greater than in MOF177, which was reported experimentally as 33 mmol/g [98].

The gravimetric capacity can be converted into the volumetric capacity using the framework density for each adsorbent given in Table 5.2. In terms of volumetric basis, the trend for CO_2 adsorption is observed to be different in certain sense. Though the gravimetric capacities at saturation in IRMOF1, Mg-IRMOF1, Be-IRMOF1, IRMOF10, IRMOF14, UMCM-1 and COF-102 are not the same, the volumetric capacities are close to each other due to the cancelling effect of the framework density. Taken both gravimetric and volumetric capacities into consideration, IRMOF10 and IRMOF14 turn out to be the best for CO_2 storage as a combination of high uptake and low framework density. The organic linker appears to play a key role, therefore, varying the organic linker to increase the free volume and surface area might be advisable to increase adsorption capacity. COF102 shows a fairly large capacity, though the gravimetric capacity is less than in IRMOF10 and IRMOF14. However, the pressure required to reach saturation in COF-102 is considerably lower, which is advantageous for operation from safety point of view. Consequently, storage of CO_2 in COF-102 or other COFs is also promising, which will be discussed in the following section. As observed on gravimetric basis, the volumetric capacities in IRMOF1-$(NH_2)_4$ and IRMOF13 at high pressures are also lower than the prototype IRMOF1, particularly in IRMOF13. Therefore, adding functional group or interpenetrating framework is not helpful to enhance capacity at high pressures. Finally, the capacity in F-MOF1 turns out to be the lowest in both gravimetric and volumetric basis.

5.4.2 Adsorption in COFs

5.4.2.1 Structural and Limiting Properties

Table 5.3 lists the framework density ρ_f, free volume V_{free}, porosity ϕ and accessible surface area A_{surf} for various COFs as well as the isosteric heat q_{st}^0 and Henry constant K_H, which reflect the affinity with framework at infinite dilution. The 3D COFs particularly COF-105 and COF-108 have the lowest ρ_f and largest V_{free}, ϕ and A_{surf}; followed by 1D COF_NT and then 2D COFs. COF-102 and COF-103 have similar structures except that Si atoms replace the tetrahedral C atoms in COF-102. The presence of Si atoms in COF-103 slightly increases the affinity of CO_2 with the framework and in turn leads to a higher q_{st}^0 and K_H. Though ρ_f and ϕ of COF-105 and COF-108 are nearly the same, q_{st}^0 is higher in COF-105. This is due to the relatively more compact atomic packing in COF-105 than in COF-108 that enhances the interaction strength with CO_2. In 2D COFs with layered structures, q_{st}^0 and K_H are sensitive to the inter-layer distance. With a short distance (3.399 Å), ρ_f, q_{st}^0 and K_H in COF-6 are significantly larger than all other COFs attributed to the overlap of attractive space between CO_2 and the framework. With increasing distance in COF-8 (3.630 Å) and COF-10 (3.526 Å), q_{st}^0 and K_H decrease. In 1D COF_NT, q_{st}^0 and K_H are comparable to or slightly larger than in 3D COFs, but lower than in 2D COFs.

Table 5.3. Framework density ρ_f, free volume V_{free}, porosity ϕ, accessible surface area A_{surf}, heat of adsorption q_{st}^0 and Henry constant K_H in various COFs.

Adsorbent	ρ_f (g/cm^3)	V_{free} (cm^3/g)	ϕ	A_{surf} (m^2/g)	q_{st}^0 (kJ/mol)	K_H (mmol/cm^3/kPa)
COF-102	0.41	2.02	0.85	5172	16.54	0.013
COF-103	0.39	2.20	0.86	5366	18.13	0.014
COF-105	0.18	5.22	0.94	6636	21.98	0.012
COF-108	0.17	5.59	0.95	6298	14.22	0.003
COF-6	1.07	0.47	0.50	1288	32.79	0.517
COF-8	0.71	0.86	0.61	1911	24.81	0.043
COF-10	0.48	1.62	0.78	2214	24.14	0.034
COF_NT	0.49	1.59	0.78	3509	20.91	0.022

5.4.2.2 Adsorption Isotherms in COFs

Figure 5.9 shows the excess adsorption isotherms of CO_2 in COFs. At low pressures, there is a steep rise in 2D COFs due to the constricted pores within the layered structures, particularly in COF-6. At high pressures, however, the saturation capacities in 2D COFs are lower than in 3D COFs because of the smaller available free volumes. COF_NT has a close saturation capacity with COF-10 as they possess approximately the same free volume. In 3D COFs, COF-102 and COF-103 show higher adsorption at low pressures than COF-105 and COF-108. This is due to the compact packing of atoms, which in turn increases the interaction strength of CO_2 with the adsorbent. The framework density decreases from 0.39 g/cm^3 in COF-103 to 0.18 g/cm^3 in COF-105 and 0.17 g/cm^3 in COF-108. In contrast, the porosity increases from 0.86 to 0.94 and 0.95, the free volume increases significantly from 2.20 to 5.22 and 5.59 cm^3/g, and the surface area increases from 5366 to 6636 and 6298 m^2/g.

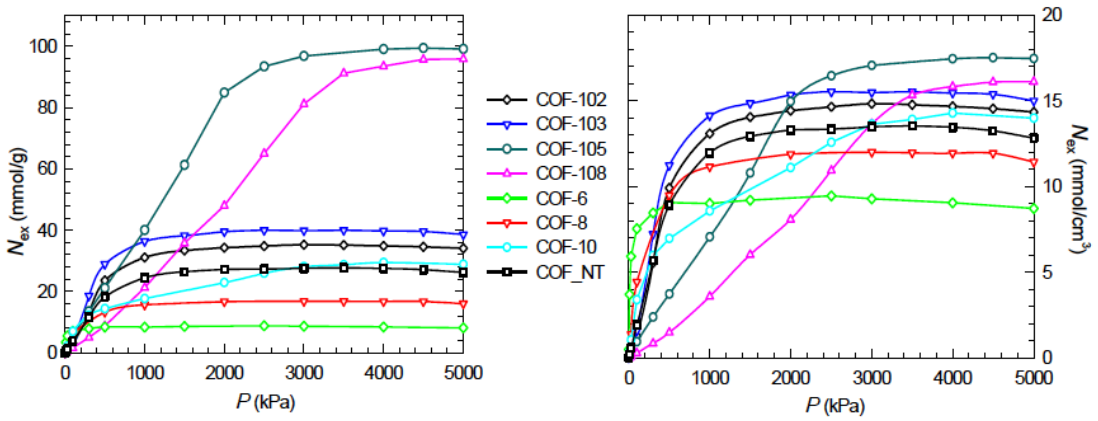

Figure 5.9. Gravimetric (left) and volumetric (right) isotherms of CO_2 adsorption in COF-102, COF-103, COF-105, COF-108, COF-6, COF-8, COF-10 and COF_NT at 300 K. Symbols are from simulation and the lines are to guide the eye.

As a consequence, COF-105 and COF-108 have the largest capacity for CO_2 adsorption at high pressures compared to other COFs, although the adsorption is lower at low pressures. Since the pores are almost fully filled at high pressures and adsorption approaches saturation, adsorbent with a larger free volume has more space to accommodate sorbate molecules and hence exhibits a higher capacity. At 30 bar, the capacities in COF-105 and COF-108 are 82 and 96 mmol/g, respectively. These values are two to three fold greater than in MOF-177, which was reported experimentally to be the highest as of 33 mmol/g [98] and also greater than in other MOFs discussed earlier. Using the framework density shown in Table 5.3, the gravimetric capacity is converted in to the volumetric capacity. While COF-105 and COF-108 have significantly higher gravimetric capacities than other COFs, in volumetric basis the capacities are close due to the cancelling effect of the framework density.

In order to identify the favorable locations of CO_2 adsorption in COFs, the density distribution contours in the *xy* plane of COF-108, COF-6 and COF_NT at 1000 kPa are shown in Figure 5.10. In COF-108, CO_2 adsorption occurs preferentially around

the carbon-oxygen-boron rings where CO_2 interacts strongly with the framework. At higher pressures (not shown), adsorption also occurs in the central cavity. As the inter-layer distance in COF-6 is short, CO_2 molecules predominantly intercalate the constricted central pores. In COF-_NT, CO_2 is adsorbed at the annular layer and the center inside nanotube as well as into the interstitial channels among nanotubes. This observation found here is similar to gas adsorption in carbon nanotubes at high pressures [351].

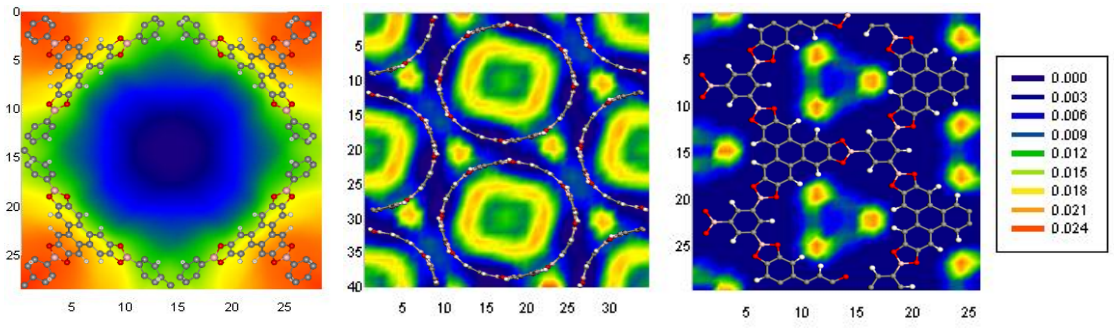

Figure 5.10. Density distribution contours for the center-of-mass of CO_2 molecules in COF-108, COF_NT and COF-6 at 1000 kPa.

5.4.3 Quantitative Assessment of CO_2 Storage in MOFs and COFs

To quantitatively assess the ability of various MOFs and COFs for CO_2 storage, the capacities at 30 bar are shown in Figure 5.11 as a function of the framework density ρ_f, free volume V_{free}, porosity ϕ and accessible surface area A_{suf}. All these factors affect the adsorption capacity of adsorbent. In Figure 5.10a, the gravimetric capacity N_{ex}^{gra} drops inversely proportional to the framework density ρ_f and the volumetric capacity N_{ex}^{vol} drops linearly, both can be well described by

$$N_{ex}^{gra} = -6.48 + 17.00/\rho_f \tag{5.7}$$

$$N_{ex}^{vol} = 16.95 - 6.47\rho_f \tag{5.8}$$

In Figure 5.10b, while N_{ex}^{gra} rises with free volume V, N_{ex}^{vol} first rises and then tends to drop slightly. The relations of N_{ex}^{gra} and N_{ex}^{vol} with V_{free} are

$$N_{ex}^{gra} = -0.34 + 17.41V_{free} - 0.12V_{free}^2 \quad (5.9)$$

$$N_{ex}^{vol} = 3.82 + 11.28V_{free} - 3.66V_{free}^2 + 0.36V_{free}^3 \quad (5.10)$$

In Figure 5.10c, both N_{ex}^{gra} and N_{ex}^{vol} rise with porosity ϕ following

$$N_{ex}^{gra} = 8.29 + 0.002\exp(11.36\phi) \quad (5.11)$$

$$N_{ex}^{vol} = -0.82 + 17.84\phi \quad (5.12)$$

N_{ex}^{gra} in Figure 5.10d rises with the accessible surface area A_{surf}, whereas N_{ex}^{vol} rises and then tends to be constant. As a function of A_{surf}, N_{ex}^{gra} and N_{ex}^{vol} can be correlated as

$$N_{ex}^{gra} = -17.86 + 0.04A_{surf} - 1.21E-6A_{surf}^2 + 1.39E-9A_{surf}^3 \quad (5.13)$$

$$N_{ex}^{vol} = 6.80 + 0.002A_{surf} \quad (5.14)$$

Good correlations are found between N_{ex}^{gra} and N_{ex}^{vol} with the framework density, free volume, porosity and accessible surface area. It appears that N_{ex}^{gra} and N_{ex}^{vol} can be enhanced by decreasing framework density, increasing free volume, porosity or accessible surface area. Nevertheless, not all these options are practically feasible and they actually interplay with one another. These correlations are useful for *a prior* prediction of CO_2 adsorption capacities in to-be-synthesized adsorbents, which can then be screened before experimental tests.

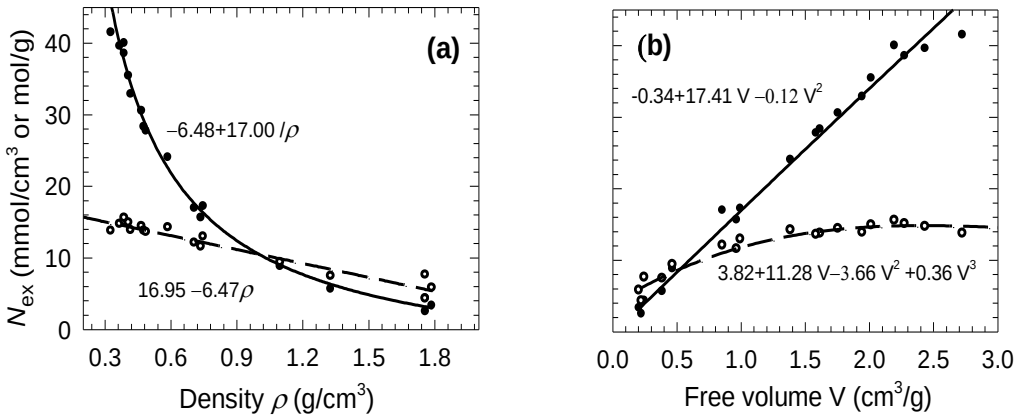

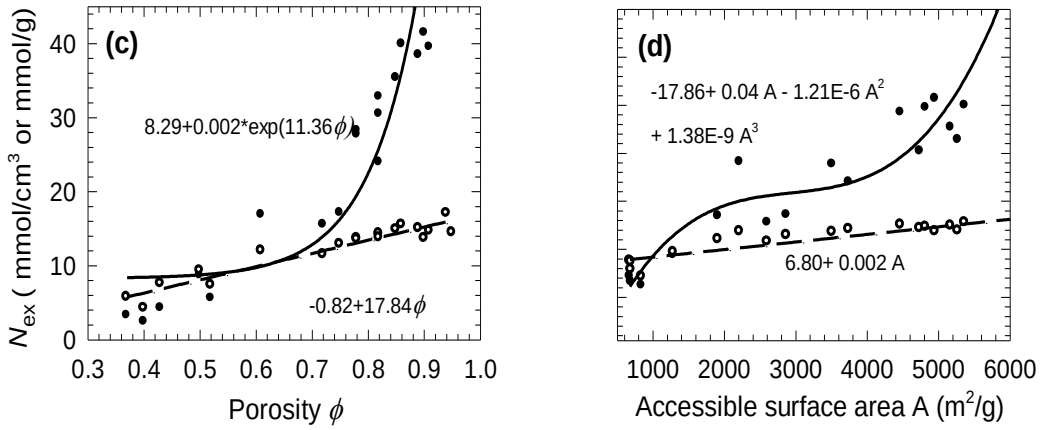

Figure 5.11. CO_2 capacities at 30 bar as a function of (a) framework density (b) free volume (c) porosity (d) accessible surface area. Solid circles and curves: gravimetric capacity, open circles and dashed curves: volumetric capacity.

5.5 Summary

A wide variety of nanoporous materials have been investigated for CO_2 storage from molecular simulations. Unlike most simulation studies for adsorption using GCMC method, GEMC method was employed in this work and there was no need to convert the chemical potential of adsorbate to pressure. GEMC simulation gives adsorption directly at a given pressure, as well as the density and enthalpy of bulk adsorbate.

Good agreement was found between the simulated and experimental isotherms for CO_2 in MFI and IRMOF1. Upon comparison, IRMOF1 shows far higher capacity than MFI and SWNT bundle. As loading increase, the isosteric heat in IRMOF1 continues rising, but it first rises and then drops in MFI and SWNT. While the incorporation of nonframework Na^+ cations into MFI has a marked effect on CO_2 capacity at low pressures, it is insignificant at high pressures. By varying the metal oxide, organic linker, functional group or interpenetrating framework, Mg-IRMOF1, Be-IRMOF1, IRMOF3-$(NH_2)_4$, IRMOF10, IRMOF13, IRMOF14, UMCM-1 have been examined as variations of the prototype IRMOF1. Compared to IRMOF1, the

isosteric heat and Henry constant at infinite dilution is larger in IRMOF3-$(NH_2)_4$ and IRMOF13. This is attributed to the higher affinity with adsorbate by adding functional groups and the formation of constricted pore by interpenetrating framework. Consequently, adsorption in IRMOF3-$(NH_2)_4$ and IRMOF13 is higher than in IRMOF1 at low pressures. However, the reverse is true at high pressures because of the reduced free volume and accessible surface area, which are the primary controlling factors at high pressures. Substitution of the metal oxide or organic linker does not appreciably affect the isosteric heat and Henry constant. The gravimetric adsorption in Mg-IRMOF1 and Be-IRMOF1 increases compared to IRMOF1 over all pressure range due to the reduced framework density. The organic linkers in IRMOF10 are IRMOF14 are longer and bigger than in IRMOF1, thus significantly increase the free volume and accessible surface area. Similarly, using two different linkers, an increase in surface area and free volume is observed in UMCM-1. In COFs, the 3D COFs possess larger free volume, porosity and surface area than the 2D and 1D COFs. COF-105 and COF-108 show exceptionally high storage capacity and even surpass the experimentally reported highest capacity in MOF-177. The compact atomic packing in COF-102 and COF-103 enhances isosteric heat and subsequently strong adsorption at low pressures. COF-6 exhibits the largest isosteric heat and Henry constant due to the constricted pores within the layered framework. Adsorption in 1D COF_NT is similar to that in a carbon nanotube. From this study, COF-105 and COF-108 appear to be the best for CO_2 storage as a counterbalance of high capacity and low density compared to other MOFs reported to date.

The adsorption capacity is a complex interplay of many factors including the framework density, free volume, porosity and accessible surface area. Varying one of them might simultaneously change the other. Molecular–based correlations are

developed for the gravimetric and volumetric capacities of CO_2 at 30 bar with these factors. From the correlations, CO_2 capacity can be estimated without time-consuming simulation or expensive experiment and more importantly, unknown materials can be rapidly screened for CO_2 these structure-function relations.

Chapter 6

Adsorption Separation of CO_2/CH_4 Mixture in Metal-Organic Frameworks with Unique Characteristics

6.1 Introduction

As discussed earlier in Chapter 4, the adsorption selectivity of CO_2/CH_4 in a prototype IRMOF-1 is found to be marginal and not suitable for practical application. Unlike zeolitic and carbonaceous structures, the controllable length of organic linkers and the variation of metal oxides in MOFs allow for rationally tailoring their pore size, volume and functionality. A large number of MOFs have been synthesized to date as discussed in detail in Chapter 1. Nevertheless, experimentally synthesizing and screening MOFs for a particular application can be a difficult and time-consuming task. The aim of this study is to find whether MOFs with different characteristics features can enhance the adsorption separation of CO_2/CH_4.

In this chapter, a systematical simulation study is reported on the separation of CO_2/CH_4 mixture in a series of MOFs with unique characteristics such as open metal sites, interpenetration and extraframework ions. The presence of exposed metal sites and catenation can enhance both adsorption and selectivity; therefore, MOFs with exposed metal sites (Cu-BTC, PCN-6′ and PCN-6) and catenated frameworks (IRMOF-13 and PCN-6) were chosen. In addition, a charged MOF with extraframework ions was considered, for the first time, for CO_2/CH_4 separation and compared with other non-catenated MOFs. In Section 6.2, the models for CO_2, CH_4 and the MOFs are described. The simulation methods are briefly introduced in Section 6.3. Specifically, GCMC simulations were used to calculate the adsorption of

an equimolar CO_2/CH_4 mixture at room temperature. The adsorption isotherms, simulation snapshots, adsorption selectivity and the effect of electrostatic interactions on selectivity are presented and discussed in Section 6.4, with summary in Section 6.5.

6.2 Models

Figure 6.1 shows the atomic structures of the seven MOFs considered in this study constructed from experimental crystallographic data [2,138,355-357]. As a prototype of isoreticular MOFs, IRMOF-1 consists of Zn_4O as the metal-oxide cluster and 1, 4-benzenedicarboxylate (BDC) as the organic linker [2]. It has straight pores with alternating diameters of 15 and 12 Å along the pores. IRMOF-14 is formed by substituting BDC in IRMOF-1 with pyrene dicarboxylate (PDC), which is longer in length and leads to a larger pore size. The pore diameters in IRMOF-14 are approximately 20.1 and 14.7 Å [2]. Despite identical metal oxide and organic linker in IRMOF-13 and IRMOF-14, IRMOF-13 has a catenated framework and differs in the topology from IRMOF-14. The pore diameters in IRMOF-13 are only 12.4 and 8.7 Å as a result of catenation [2]. Cu-BTC (BTC: benzene-1, 3, 5–tri-carboxylate) is a face-centered cubic crystal composed of paddle-wheel building blocks of dimeric cupric tetracarboxylate. There are square-shaped pores of 9.0 × 9.0 Å and octahedral side-pockets of diameter 5 Å connected by 3.5 Å windows [138].

PCN-6 consists of dimeric coppers linked with TATB (4,4′,4′′-s-triazine-2,4,6-triyl-tribenzoate) to form paddle-wheel secondary building unit resulting in a catenated framework [355]. It has triangular channels of 9.2 Å along an edge connected by 5 Å windows. With boracite net topology, PCN-6′ is considered to be a non-catenated counterpart of PCN-6, and isostrucutral with Cu-BTC [356]. Similar to Cu-BTC, PCN-6′ has open square pores along the diagonals, but with a larger size of

21.44 × 21.44 Å. The experimentally determined surface area is 3800 m^2/g in PCN-6, whereas it is only 2700 m^2/g in PCN-6′. Unlike neutral MOFs, *soc*-MOF has a cationic framework with charge balancing extraframework NO_3^- ions [357]. As the assembly of trimer building block with square-octahedral connectivity nets, *soc*-MOF contains nanometer-scale pores and carcerand capsules.

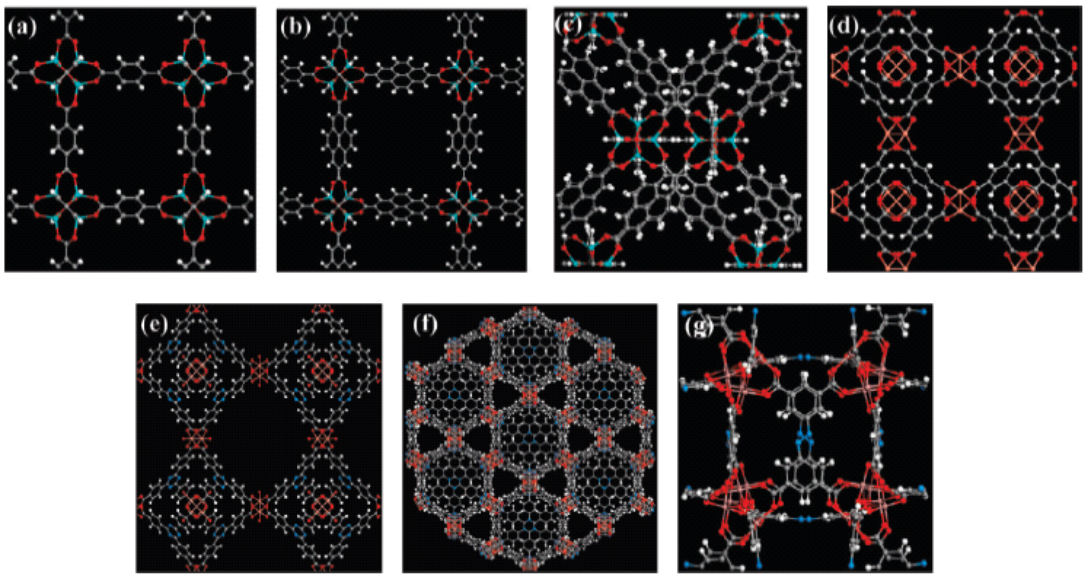

Figure 6.1. Atomic structes of (a) IRMOF-1 (b) IRMOF-14 (c) IRMOF-13 (d) Cu-BTC (e) PCN-6′ (f) PCN-6 (g) *soc*-MOF. N: Blue, C: grey, O: red, Zn: cyan, H: white, Cu and In: orange. The structures are scaled to the actual sizes.

The models for CO_2 and CH_4 are the same as mentioned earlier in Chapter 4. The atomic charges of the atoms in various MOFs were estimated using cluster model approach and the ESP method described earlier. The different cluster models for the MOFs studied are shown in Figure 6.2. The estimated partial charges of the framework atoms are shown in Table 6.1. The atomic charges of extra-framework NO_3^- in *soc*-MOF were adopted from *ab initio* calculations with 0.197*e* for N atom and –0.399*e* for O atom [358]. NO_3^- ion was mimicked as rigid with bond length of 1.302 Å and bond angle ∠ONO of 120°. The dispersion interactions of the framework atoms in MOFs were modeled using the Universal Force Field (UFF) [174]. A

number of simulation studies have shown that UFF leads to accurate predictions of gas adsorption in MOFs [173,334]. The interactions between CO_2 and framework atoms were modeled using LJ and Coulombic potentials, while only LJ potential was used between CH_4 and the framework atoms. The Lorentz-Berthelot combining rules [296] were used to calculate the cross LJ interaction parameters.

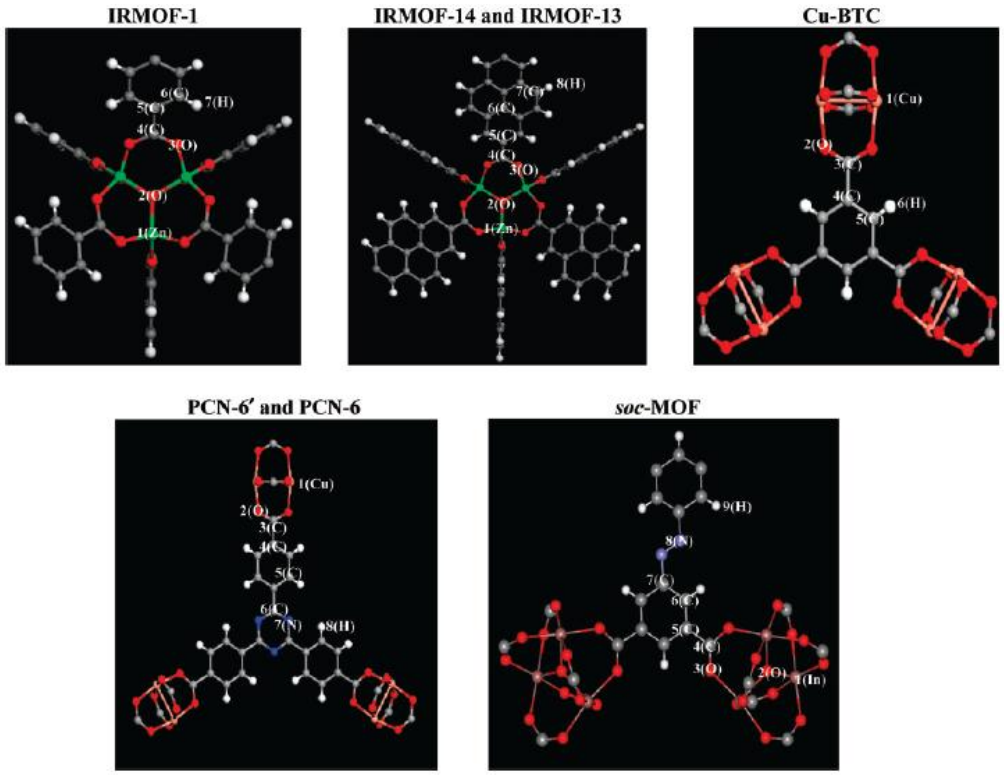

Figure 6.2. Fragmental clusters used in the B3LYP/6-31g(d) calculations for IRMOF-1, IRMOF-14, IRMOF-13, Cu-BTC, PCN-6′, PCN-6 and *soc*-MOF. To maintain the correct hybridization, the dangling bonds on all the fragmental clusters were terminated by $-CH_3$.

Table 6.1. Atomic charges on the fragmental clusters shown in Figure 6.2

Atom No.	1	2	3	4	5	6	7	8	9
IRMOF-1	1.514 (Zn)	-1.798 (O)	-0.715 (O)	0.698 (C)	0.203 (C)	-0.252 (C)	0.162 (H)		
IRMOF-13 & -14	1.463 (Zn)	-1.753 (O)	-0.770 (O)	0.848 (C)	-0.047 (C)	0.144 (C)	-0.204 (C)	0.110 (H)	
Cu-BTC	1.026 (Cu)	-0.671 (O)	0.875 (C)	-0.197 (C)	0.028 (C)	0.123 (H)			
PCN-6 & PCN-6′	0.937 (Cu)	-0.636 (O)	0.840 (C)	-0.084 (C)	-0.107 (C)	0.762 (C)	-0.724 (N)	0.130 (H)	
soc-MOF	2.173 (In)	-1.549 (O)	-0.725 (O)	0.996 (C)	-0.184 (C)	-0.260 (C)	0.314 (C)	-0.147 (N)	0.189 (H)

6.3 Methodology

GCMC simulations were carried out for the adsorption of CO_2/CH_4 mixture at 300 K. The simulation boxes representing MOF adsorbents varied from $(1 \times 1 \times 1)$ to $(2 \times 2 \times 2)$ unit cells and the periodic boundary conditions were used in three directions. The MOF frameworks were assumed to be rigid, and the potential energy between adsorbate atoms and frameworks were pre-tabulated. This is because low-energy equilibrium configurations are involved in adsorption and framework flexibility has only a marginal effect [359]. The LJ interactions were evaluated with a spherical cutoff equal to half of the simulation box with long-range corrections added; the Coulombic interactions were calculated using the Ewald sum method [252]. To investigate the effect of framework charges, additional simulations were also performed in the absence of framework charges, i.e., the electrostatic interactions between adsorbate and framework were switched off.

The number of trial moves in a typical GCMC simulation was 2×10^7, though additional trial moves were used at high loadings. The first 10^7 moves were used for equilibration, and the following 10^7 moves to obtain ensemble averages. Six types of trial moves were randomly attempted in the GCMC simulation, displacement, rotation, and partial regrowth at a neighboring position; complete regrowth at a new position; and exchange with the reservoir including creation and deletion with equal probability, exchange of molecular identity, i.e., CO_2 to CH_4 and vice versa, with equal probability. While the last trial move is usually not required in GCMC simulation, its use allows faster equilibration and reduces fluctuation after equilibration. In *soc*-MOF, NO_3^- ions were allowed to move during the adsorption of adsorbate molecules. Unless otherwise mentioned, the simulation uncertainties were smaller than the symbol sizes presented in the figures.

6.4 Results and Discussion

The adsorption isotherms are presented for CO_2/CH_4 mixture in the six neutral MOFs: IRMOF-1, IRMOF-13, IRMOF-14, Cu-BTC, PCN-6′ and PCN-6 and in charged *soc*-MOF. Typical simulation snapshots are illustrated in Cu-BTC and PCN-6′, and the separation of CO_2 and CH_4 is characterized in terms of adsorption selectivity. The effect of electrostatic interactions between CO_2 and framework is also examined on adsorption and selectivity.

6.4.1 Adsorption Isotherms

Figure 6.3 shows the adsorption isotherms of the CO_2/CH_4 mixture in IRMOF-1, IRMOF-13, IRMOF-14, Cu-BTC, PCN-6′ and PCN-6. CO_2 is preferentially adsorbed over CH_4 in all the MOFs due to its stronger interaction with the framework atoms as CO_2 is a three-site and quadrupolar molecule. Substituting the organic linker BDC in IRMOF-1 with PDC leads to a larger pore in IRMOF-14, consequently, a greater uptake of both CO_2 and CH_4. Catenated IRMOF-13 consists of small pores and additional adsorption sites. This enhances the interaction of adsorbate molecules with framework, and a higher uptake at low pressures, particularly for CO_2. Nevertheless, IRMOF-14 has a larger free volume than IRMOF-13 and can accommodate more molecules; consequently, adsorption of both CO_2 and CH_4 is greater in IRMOF-14 at high pressures. PCN-6 exhibits similar behavior to that observed in IRMOF-13 compared to the non-catenated PCN-6′. In IRMOF-1, IRMOF-13, IRMOF-14, Cu-BTC and PCN-6, CH_4 reaches saturation at approximately 2000 - 3000 kPa, and CO_2 tends to be saturated at the highest pressure considered. In contrast, the adsorption behavior appears to be different in PCN-6′, which is isostructural with Cu-BTC. Both CO_2 and CH_4 exhibit a linear isotherm in PCN-6′ with increasing pressure due to the

substantially larger pore size compared to Cu-BTC. The linear adsorption increase in PCN-6′ indicates that a large space is available to accommodate adsorbate molecules even at high pressures. This observation is further elucidated from the simulation snapshots in Cu-BTC and PCN-6′, discussed later in the section.

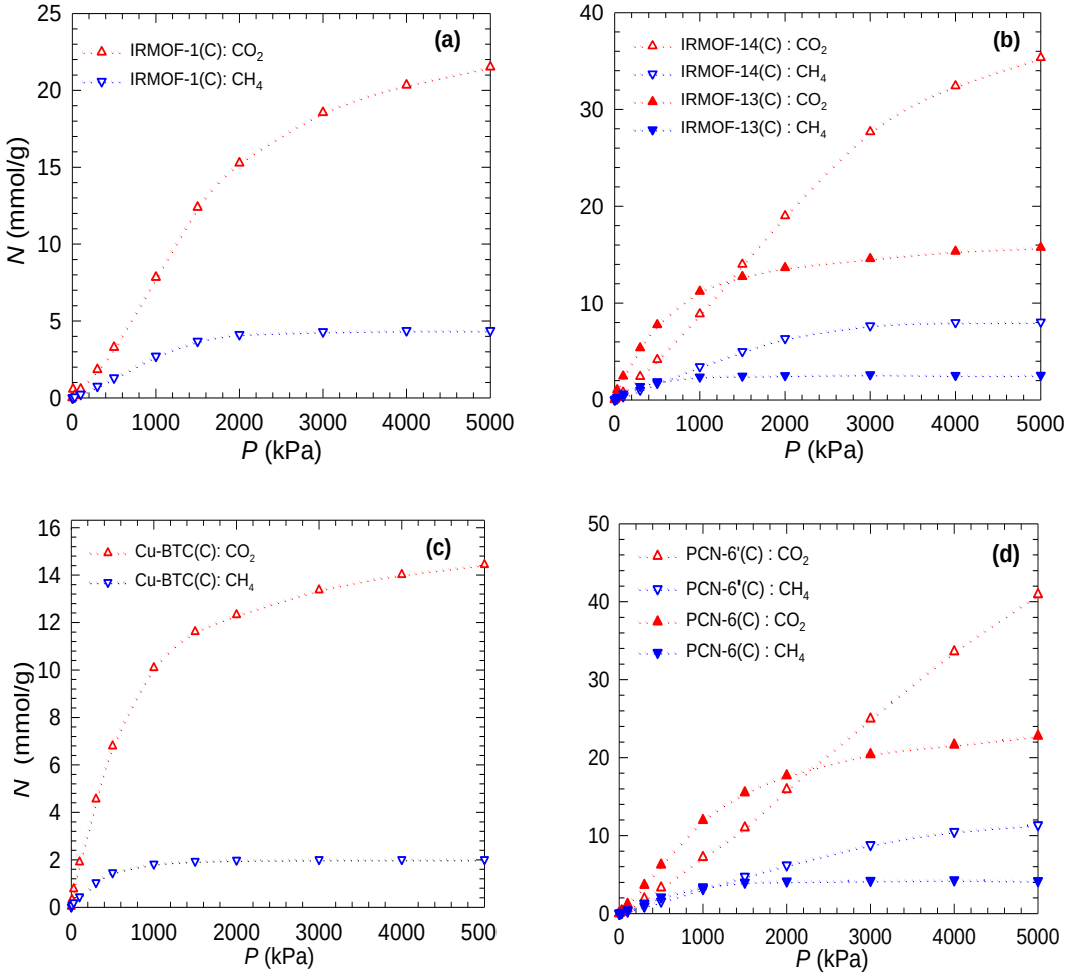

Figure 6.3. Adsorption isotherms of the CO_2/CH_4 mixture in (a) IRMOF-1 (b) IRMOF-14 and IRMOF-13 (c) Cu-BTC (d) PCN-6′ and PCN-6. Upward triangles: CO_2 and downward triangles: CH_4. In the legend, "C" denotes that framework charges were used in the simulations.

Figure 6.4 shows the simulation snapshots of the CO_2/CH_4 mixture in Cu-BTC and PCN-6′ at various pressures. At a low pressure (100 kPa in Figure 6.4a), CO_2 molecules in Cu-BTC are preferentially adsorbed within the octahedral side-pockets, and CH_4 molecules are a bit away from the pockets. With an increase in pressure (300 kPa in Figure 6.4b), the side-pockets are first saturated with CO_2 molecules, followed

by adsorption around the exposed metal sites and organic linkers. At a high pressure (1000 kPa in Figure 6.4c), the open square pores become filled with adsorbed molecules. The order of occupation with increasing pressure is a result of the strength of the interactions at the different adsorption sites. Isostructural to Cu-BTC, PCN-6′ consists of octahedral pockets and square pores, but of larger dimensions. Similar to that observed in Cu-BTC, CO_2 molecules in PCN-6′ are adsorbed within the side-pockets at a low pressure (300 kPa in Figure 6.4d), while CH_4 molecules are dispersed throughout the framework. As pressure increases (1000 kPa in Figure 6.4e), the pockets are fully saturated, and adsorption occurs near the exposed metal sites and organic linkers. With a further increase in pressure (3000 kPa in Figure 6.4f), CO_2 molecules are bound onto the square pore surfaces, but the pores are not completely occupied. This observation is consistent with the adsorption behavior in Figure 6.3d, which shows a linear increase as a function of pressure, indicating that sufficient space is available to accommodate adsorbate molecules at high pressures.

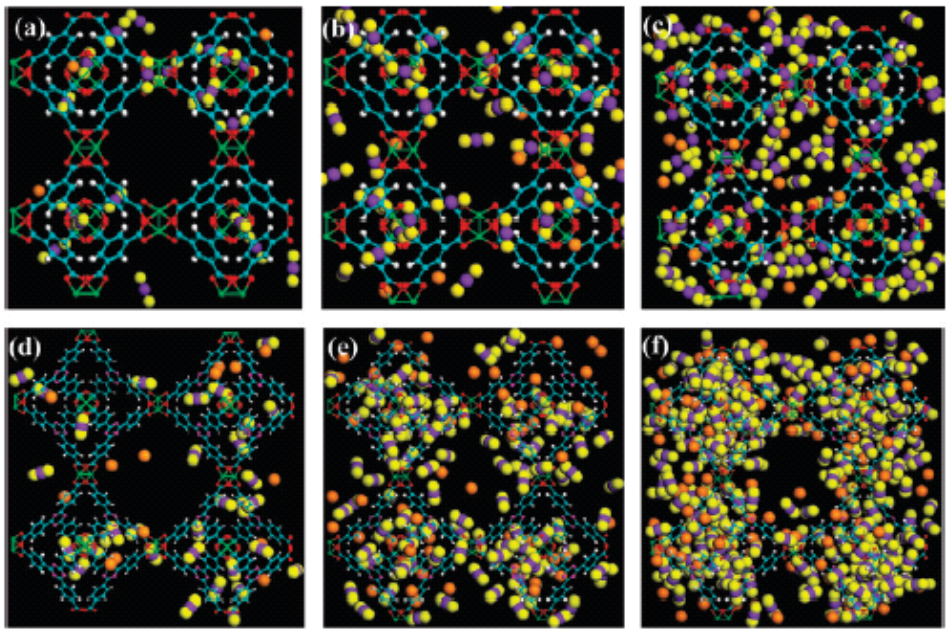

Figure 6.4. Simulation snapshots of the CO_2/CH_4 mixture at pressures (a) 100 kPa (b) 300 kPa (c) 1000 kPa in Cu-BTC (top) and (d) 300 kPa (e) 1000 kPa (f) 3000 kPa in PCN-6′ (bottom). Cu: green, O: red, C: cyan, N: pink, H: white; CH_4: orange; CO_2: purple for C and yellow for O.

6.4.2 Adsorption Selectivity

Adsorptive separation in a binary mixture of component *i* and *j* is characterized by the selectivity $S_{i/j} = (x_i / x_j)(y_j / y_i)$, where x_i and y_i are the mole fractions of component *i* in the adsorbed and bulk phases respectively. Figure 6.5 shows the simulated selectivity of the CO_2/CH_4 mixture in IRMOF-1, IRMOF-13, IRMOF-14, Cu-BTC, PCN-6, and PCN-6′, respectively. The selectivity in IRMOF-1 remains nearly constant at low pressures and increases with pressure due to the preferential interaction of CO_2 with framework. The selectivity in IRMOF-14 follows a similar trend, but is slightly reduced because the pore size in IRMOF-14 is approximately one-fourth greater than in IRMOF-1. As a result of catenation, the pore size in IRMOF-13 is constricted and the selectivity is increased compared to its non-catenated counterpart. With increasing pressure, the selectivity in IRMOF-13 initially decreases slightly, then increases as pressure increases, and finally approaches a plateau. This behavior is due to the counterbalance between energetic and entropic (packing) effects. At low pressures, CO_2 molecules in IRMOF-13 are preferentially adsorbed in the constricted pores. The volume of these constricted pores is small and gets saturated rapidly; in addition, the adsorption sites are heterogeneous. Consequently, CO_2 molecules tend to occupy less adsorptive sites with increasing pressure and the selectivity decreases slightly. With a further increase in pressure, CO_2 molecules intercalate the large pores, and the cooperative attraction between adsorbed CO_2 molecules further promotes CO_2 adsorption so that the selectivity increases. Finally, the selectivity becomes almost independent of pressure as both CO_2 and CH_4 reach saturation at high pressures.

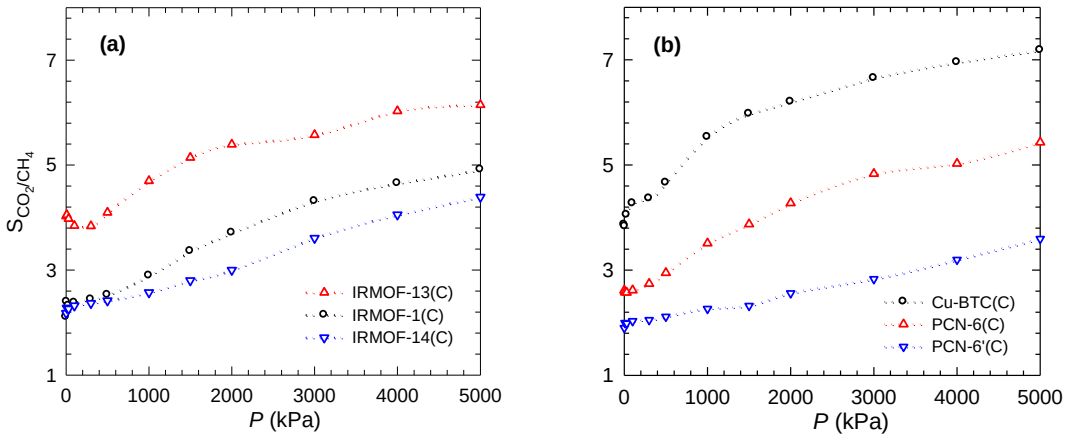

Figure 6.5. Adsorption selectivity of the CO_2/CH_4 mixture in (a) IRMOF-1, IRMOF-13 and IRMOF-14 (b) Cu-BTC, PCN-6 and PCN-6′. In the legend, "C" denotes that framework charges were used in the simulations.

In Cu-BTC and PCN-6, the selectivity increases with increasing pressure and approaches a constant at high pressures, as in IRMOF-1 and IRMOF-14. In PCN-6′, the selectivity rises linearly with pressure, consistent with the isotherm in Figure 6.3d. As mentioned above, because of the large pores, adsorption in PCN-6′ is not saturated at the pressures considered here. Nevertheless, it is expected that the adsorption isotherm and selectivity in PCN-6′ will approach saturation at still higher pressures. The catenated framework in PCN-6 shows a higher selectivity than PCN-6′, which is due to the presence of additional adsorption sites and constricted pores that enhance the interaction with CO_2.

To investigate the effect of electrostatic interactions between CO_2 and framework, simulations were also carried out for the adsorption of CO_2/CH_4 mixture in the absence of framework charges. Figure 6.6 shows the adsorption isotherms in IRMOF-1, IRMOF-13, IRMOF-14, Cu-BTC, PCN-6 and PCN-6′ in the presence and absence of framework charges. In all the MOFs, the presence of framework charges and thus electrostatic interactions with CO_2 lead to a slight increase in CO_2 adsorption. CH_4 is neutral and in principle its adsorption is not influenced by framework charges.

However, there is a competitive adsorption between CO_2 and CH_4. While CO_2 adsorption is enhanced by the electrostatic interactions with framework and more adsorption sites are thus occupied by CO_2 molecules, CH_4 adsorption is slightly reduced. Compared to other MOFs, Cu-BTC exhibits a larger effect of framework charges on both CO_2 and CH_4 adsorption due to the exposed metal sites. PCN-6′ and PCN-6 also have exposed metal sites, however, the effect of their framework charges on adsorption is smaller than with Cu-BTC. The reason is PCN-6′ contains larger octahedral side-pockets and wider square pores, and in the case of PCN-6 most of the exposed metal sites are blocked due to catenation.

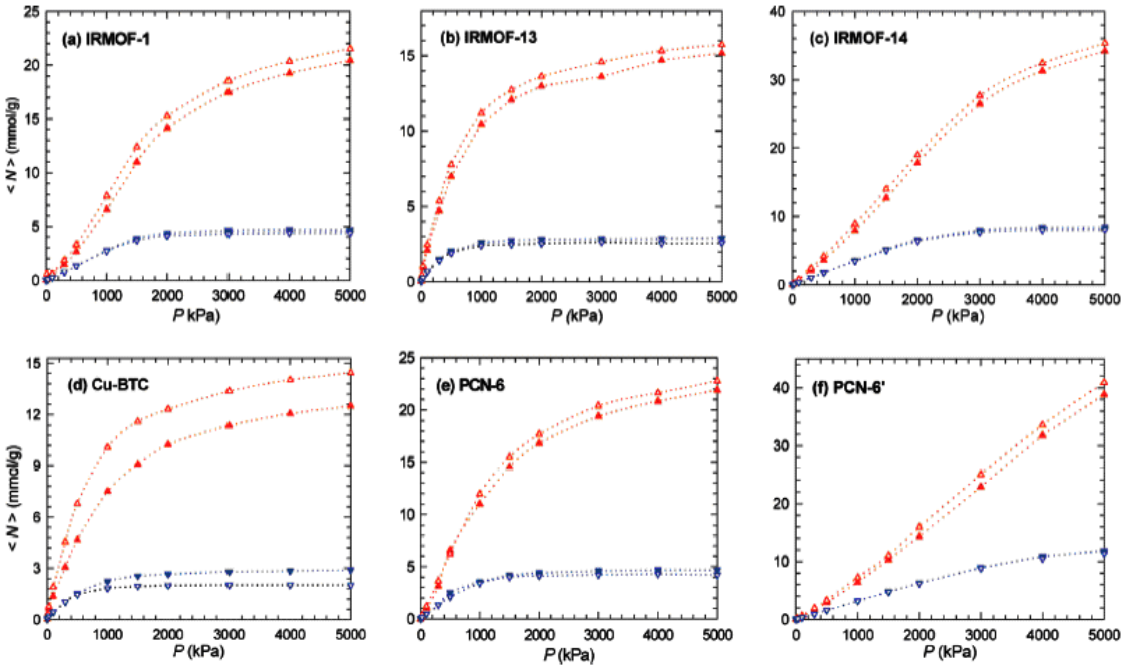

Figure 6.6. Effect of framework charges on the adsorption isotherms of the CO_2/CH_4 mixture in (a) IRMOF-1 (b) IRMOF-13 (c) IRMOF-14 (d) Cu-BTC (e) PCN-6 (f) PCN-6′. The open (closed) symbols indicate the isotherms in the presence (absence) of framework charges. Upward triangles: CO_2 and downward triangles: CH_4.

6.4.3 Effect of Electrostatic Interactions on Adsorption Selectivity

Figure 6.7 shows the effect of the electrostatic interactions on the selectivity in IRMOF-1, IRMOF-13, IRMOF-14, Cu-BTC, PCN-6′ and PCN-6. As mentioned

above, the electrostatic interactions between CO_2 and framework cause a slight increase in CO_2 adsorption and a marginal decrease in CH_4 adsorption. This leads to a higher selectivity for CO_2/CH_4 mixture in all the MOFs with framework charges. In IRMOF-1 and IRMOF-14, the selectivity is almost constant at low pressures and then increases as the pressure increases. The selectivity in IRMOF-13 first decreases slightly, then increases with increasing pressure, and finally remains almost constant with further increase in pressure. The effect of electrostatic interactions on the selectivity is weaker in non-catenated IRMOF-14 due to its larger pore size compared to IRMOF-13.

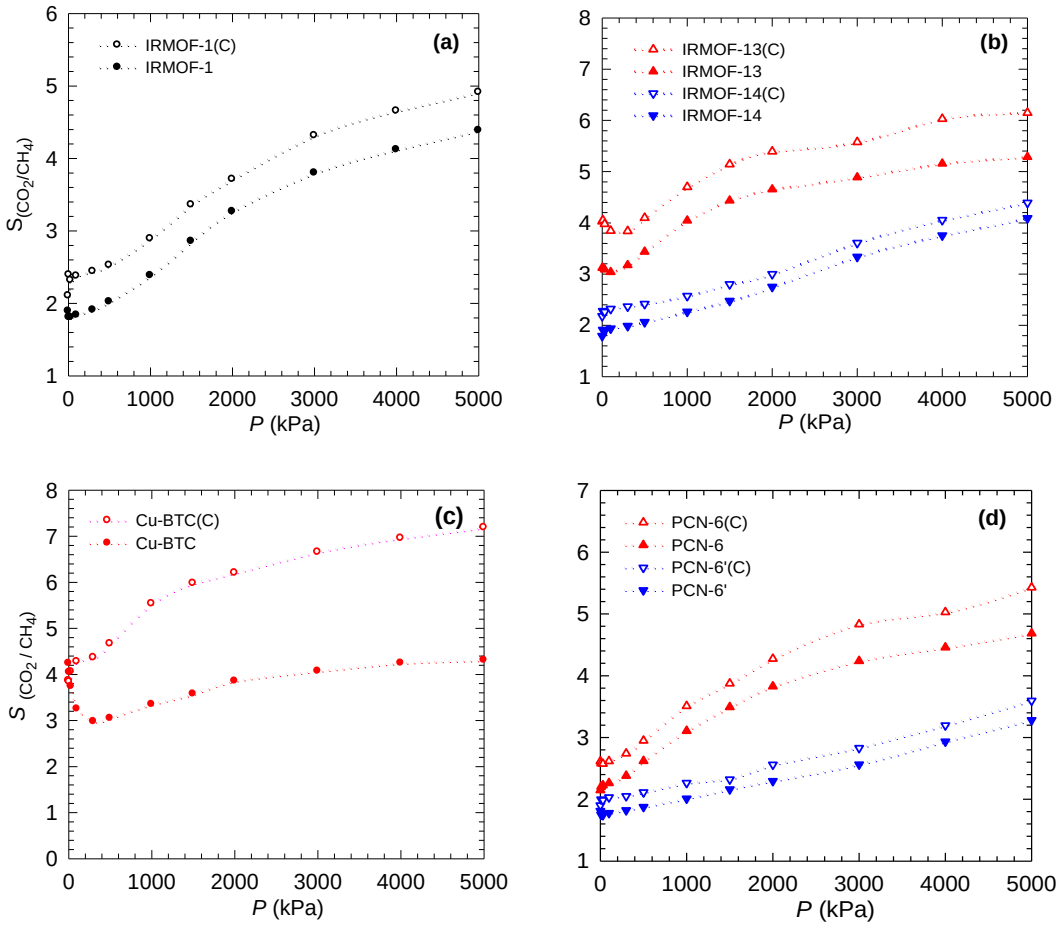

Figure 6.7. Effect of framework charges on the adsorption selectivity of the CO_2/CH_4 mixture in (a) IRMOF-1 (b) IRMOF-13 and IRMOF-14 (c) Cu-BTC (d) PCN-6′ and PCN-6. The open (closed) symbols indicate the selectivity in the presence (absence) of framework charges.

In Cu-BTC, the presence of framework charges as well as the exposed metal sites enhances the interaction with CO_2, which leads to a selectivity that increases over the whole pressure range. In the absence of framework charges, however, the selectivity decreases at low pressures, then increases with pressure and finally becomes a constant. This behavior is similar to that observed in Figure 6.5a for IRMOF-13. Increased selectivity in PCN-6 and PCN-6′ is seen over the whole pressure range as found in IRMOFs, and the effect of electrostatic interactions is more pronounced in the catenated framework. PCN-6′ is considered to be isostructural with Cu-BTC, however, the charges in PCN-6′ framework do not significantly affect the selectivity compared to that in Cu-BTC. This is because PCN-6′ consists of larger octahedral side-pockets and wider square pores. The exposed metal sites are largely blocked in catenated PCN-6, therefore, the effect of electrostatic interactions on selectivity is also weaker in PCN-6 than in Cu-BTC. In our recent study, we showed that the effect of the electrostatic interactions between CO_2 and the framework was insignificant for the adsorption of pure CO_2, and the main contribution to adsorption was from the LJ interactions [360]. This was also observed for CO_2 adsorption in IRMOF-1, IRMOF-3 and MOF-177 [199]. These simulation findings show that, except for Cu-BTC, the electrostatic interactions have only a small effect on the adsorption of CO_2 and on the separation of CO_2/CH_4 mixture.

6.4.4 Adsorption Isotherm and Selectivity in Charged *soc*-MOF

The presence of extra-framework ions has a significant impact on adsorption and selectivity. Figure 6.8a shows the adsorption isotherms of CO_2/CH_4 mixture in *soc*-MOF. CO_2 is strongly adsorbed, whereas CH_4 adsorption is vanishingly small. The extra-framework NO_3^- ions in *soc*-MOF act as additional sites, particularly for

quadrupolar CO_2 molecules, and thus substantially enhance the selectivity of CO_2 over CH_4. Figure 6.8b shows that the selectivity in *soc*-MOF increases from 22 to 36 as pressure rises. The predicted selectivity in *soc*-MOF is the *highest* yet reported in MOFs at the time when the results were reported, and higher than the selectivity in IRMOF-1 (2 - 3) [172,334], Cu-BTC (6 - 9) [172], mixed-ligand MOFs (~ 30) [361] and carborane-based MOFs (~17) [146], MOF-508b (3 - 6) [362]. The high selectivity in *soc*-MOF is achievable at a pressure of about 300 kPa, which is the typical operating condition for pressure-swing adsorption. Currently no experimental study is available for the adsorption of gas mixture in a charged MOF; consequently, we cannot make a comparison.

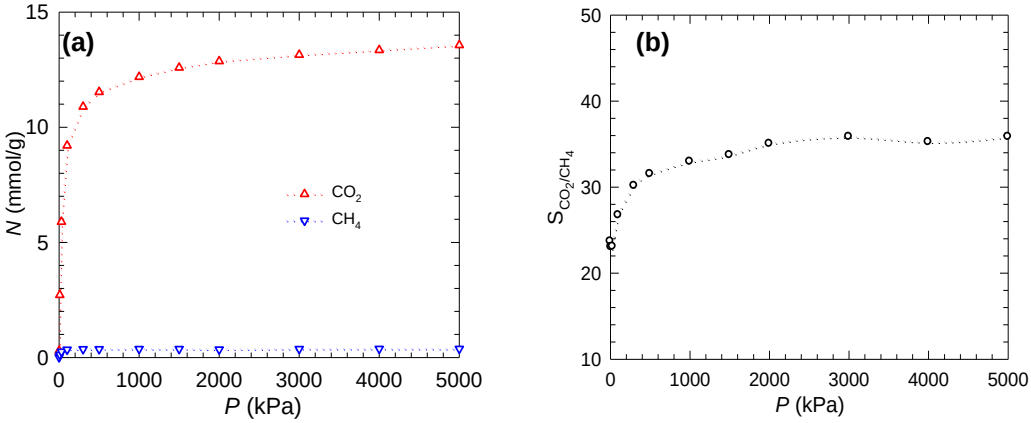

Figure 6.8. (a) Adsorption isotherms (b) Selectivity of the CO_2 /CH_4 mixture in *soc*-MOF.

6.5 Summary

The adsorptive separation of CO_2/CH_4 mixture was studied systematically in seven MOFs, including the prototype IRMOF-1, metal-exposed Cu-BTC, PCN-6′ and PCN-6, catenated IRMOF-13, non-catenated IRMOF-14 and charged *soc*-MOF. There is a greater uptake of both CO_2 and CH_4 in IRMOF-14 than in IRMOF-1 since substituting the organic linker BDC with PDC leads to a larger pore size. Due to catenation, constricted small pores and additional adsorption sites are formed in

IRMOF-13 and PCN-6. Consequently, adsorption increases at low pressures in IRMOF-13 and PCN-6, but decreases at high pressures as compared to the non-catenated IRMOF-14 and PCN-6′. This behavior is more pronounced for CO_2, which has a stronger affinity than CH_4 with the framework. Over the pressure range in this study, CH_4 adsorption reaches saturation at approximately 2000 - 3000 kPa in all MOFs, and CO_2 tends towards saturation except in PCN-6′ with a large pore volume. The selectivity in IRMOF-1 and IRMOF-14 remains nearly constant at low pressures and increases as pressure rises. The selectivity in IRMOF-13 initially decreases slightly, then increases with pressure, and finally approaches a constant. This is a consequence of the counterbalance between energetic and entropic effects in the constricted pores at low pressures, and in the large pores at high pressures. Framework catenation enhances interaction with CO_2, therefore, catenated IRMOF-13 and PCN-6 exhibit a higher selectivity than IRMOF-14 and PCN-6′.

The electrostatic interactions between CO_2 and framework atoms lead to a slight increase in CO_2 adsorption and a marginal decrease in CH_4 adsorption, and a higher selectivity in the CO_2/CH_4 mixture in all the MOFs. Compared to the other MOFs, there is a larger effect of framework charges on both CO_2 and CH_4 adsorption in Cu-BTC due to the exposed metal sites, small side-pockets and narrow pores. The effect of electrostatic interactions on selectivity is stronger in IRMOF-13 and PCN-6 compared to their non-catenated counterparts. The presence of extra-framework ions can augment the interactions with guest molecules and act as additional adsorption sites. The adsorption selectivity of CO_2 over CH_4 in charged *soc*-MOFs is predicted to be one order of magnitude greater than in IRMOFs and PCNs structures considered in this study. Therefore, charged MOFs are promising for the separation of qudra (polar)

from non-polar gas. In the next chapter, separation of CO_2 from various binary mixtures in a charged MOF will be discussed in detail.

Chapter 7

Separation of Gas Mixtures in Zeolite-like Metal-Organic Framework

7.1 Introduction

In chemical industry, the separation of CO_2 from mixtures such as syngas, natural gas, and flue gas is tremendously important. Syngas is produced through steam-methane reformation and composed primarily of H_2 and CO_2. To purify the H_2, which is regarded as an ideal energy carrier and pollution-free fuel, CO_2 separation from syngas is a prerequisite [363]. Natural gas is an alternative substitute for environmentally unfriendly fossil fuels. Impurities such as CO_2 in natural gas must be removed for the improvement of calorie content [282]. A vast amount of flue gas is emitted by power plants and a pressing issue in environmental protection is the need to sequester greenhouse gas CO_2. Prior to sequestration, however, CO_2 must be separated from flue gas [364].

Techniques proposed to separate CO_2 from gas mixtures include amine absorption, cryogenic distillation, adsorption and enzymatic conversion. Among these, adsorption in porous materials is energetically efficient and economically competitive. In past years, a number of experimental and simulation studies have been reported for the adsorptive separation of CO_2/H_2, CO_2/N_2, and CO_2/CH_4 mixtures in a variety of nanoporous materials such as carbons, zeolites and emerging MOFs. In regard to removal of CO_2 from syngas, for example, the separation of CO_2/H_2 mixture was studied in silicalite and ETS-10 (Engelhard TitanoSilicate No. 10) and a larger selectivity for CO_2 over H_2 was found in ETS-10 [365]. CO_2/H_2 mixture in a

microporous silica was simulated and the CO_2 selectivity was compared with experimental data [366]. Activated carbons mimicked by slit pores were investigated by simulation for CO_2/H_2 separation and the CO_2 selectivity reached a maximum of 90 but decreased monotonically with increasing pore size [367]. In a dehydrated Na-4A zeolite, the CO_2 selectivity of CO_2/H_2 and CO_2/N_2 mixtures was predicted to decrease with increasing pressure at room temperature [368]. A simulation study for syngas in IRMOF-1 and Cu-BTC showed that separation efficiency was affected by geometry, pore size, and electrostatic interaction [172].

Numerous studies of the separation of CO_2 from flue gas have also been reported. Adsorption of CO_2, CH_4, N_2, and their mixtures was measured in activated carbon Norit R1 at room temperature using volume-gravimetric method [369]. CO_2 and N_2, as single components and as a binary mixture, were simulated in three zeolites with identical chemical composition but different pore structures [370]. The effects of various operating conditions on CO_2/N_2 separation in MFI and FAU membranes were investigated [371,372]. A multiscale approach from quantum mechanics to molecular simulation was employed to CO_2/N_2 separation in a nanoporous carbon (C_{168} schwarzite) and compared with cation-exchanged ZSM-5 [288]. A simulation study was reported for separation of CO_2 from $CO_2/N_2/O_2$ mixture in Cu-BTC and the selectivity was ~ 35 [208]. From fixed-bed adsorption, the separation of CO_2/N_2 was examined experimentally in microporous MOF-508b [362].

In connection with natural gas purification, the separation of CO_2/CH_4 mixture was simulated in MFI with intersecting channels and in CHA and DDR with cages connected by narrow windows,[323,373] and in IRMOF-1 and Cu-BTC [374]. Adsorption of CO_2 and CH_4 in three types of nanostructures, namely IRMOF-1, silicalite, and nanoporous carbon were investigated. IRMOF-1 was found to have the

largest capacity for adsorption of CO_2 and CH_4, but to be unsatisfactory for separation [334]. Atomistic simulations were reported for separation of CO_2/CH_4 and other mixtures in IRMOF-1; mixture effects were found to play a crucial role in determining the performance [236,237]. CO_2/CH_4 mixtures in carborane-based MOFs were studied and a higher selectivity was reported in MOF possessing exposed metal sites [146]. Mixed-ligand MOFs were examined for separation of CO_2 from CH_4, where mixture adsorption was predicted from the ideal-adsorption-solution theory and subsequently verified by simulation [361]. A simulation study of the separation of CO_2/CH_4 and CO_2/N_2 mixtures in IRMOF-1 and Cu-BTC reported that a higher selectivity was observed in Cu-BTC [216].

MOFs are considered as promising candidates for gas storage and separation. However, the reported selectivities for gas mixtures to date are not sufficiently high for practical applications. Recently, a unique subset of MOFs, zeolite-like MOFs (ZMOFs) have been developed [61,71,72,375,376]. They are topologically relevant to inorganic zeolites and exhibit similar structural properties. The substitution of oxygen atoms in zeolites by organic linkers leads to extra-large cavities and pores. This edge expansion approach offers great potential toward the design and synthesis of very open materials. A number of ZMOFs contain charged frameworks and charge-balancing extraframework ions, e.g., *rho*-ZMOF synthesized by the assembly of tetrahedral building units with a long ditopic organic linker [71,377]. The presence of extraframework ions in the pores of molecular dimensions increases the interactions with guest molecules; consequently enhances storage, separation and ion-exchange capability. For example, the exchangeable ions in natural and synthetic zeolites were found to play a key role in CO_2 adsorption [378]. Li- and Ca-exchanged faujasites are

practically used in air separation by pressure swing adsorption process [379], and Ba-exchanged form is used in the selective separation of aromatic molecules [380].

To the best of our knowledge, all previous studies on gas separation in MOFs were conducted exclusively in neutral frameworks. As discussed earlier in Section 6.4.4, for the first time, the separation of gas mixtures in a charged MOF, namely, *soc*-MOF with cationic framework were reported [381]. The selectivity was found to enhance significantly in *soc*-MOF. In the present study, the separation of gas mixtures is investigated in *rho*-ZMOF with anionic framework. First, the static and dynamic properties of extraframework ions in *rho*-ZMOF are examined in detail. Then, separation of CO_2 from CO_2/N_2, CO_2/CH_4 and CO_2/CH_2 binary mixtures is investigated. Finally, the effect of H_2O on CO_2/CH_4 mixture is studied.

Following this Section, the molecular models for the adsorbent and adsorbates are described in Section 7.2. The simulation methods are briefly introduced in Section 7.3, including MC and MD simulations in canonical ensemble to characterize ions and GCMC simulations to predict the adsorption of gas mixtures. In Section 7.4, the results are discussed in detail and the predicted selectivities in *rho*-ZMOF are compared with reported data in many other nano-materials. Finally, the concluding remarks are summarized in Section 7.5.

7.2 Models

Rho-ZMOF represents the first example of a 4-connected MOF with a topology of *rho*-zeolite. It was synthesized by metal-ligand-directed assembly of In atoms and 4,5-imidazoledicarboxylic acid (H_3ImDC). The space group in *rho*-ZMOF is *Im-3m* and the lattice constants are $a = b = c = 31.062$ Å (Figure 7.1). In the crystal structure, each In atom is coordinated to four N and four O atoms of four separate doubly

deprotonated H_3ImDC (HImDC) to form an eight-coordinated dodecahedron. Each independent HImDC is coordinated to two In atoms resulting in two rigid five-membered rings via N-, O-hetero-chelation. The structure is truncated cuboctahedra (α-cages) containing 48 In atoms, which link together through double eight-membered rings (D8MR). The substitution of oxygen in *rho*-zeolite with HImDCs generates a very open-framework with extra-large cavity of 18.2 Å in diameter. Unlike *rho*-zeolite and other *rho*-aluminosilicate or aluminophosphate, *rho*-ZMOF contains twice as many positive charges (48 vs. 24) in a unit cell to neutralize the anionic framework. The elevated concentration of charge present in *rho*-ZMOF could augment ionic conductivity [71].

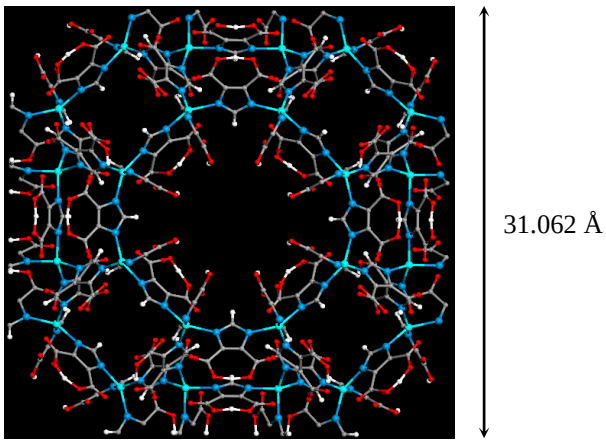

Figure 7.1. A unit cell of *rho*-ZMOF constructed from the experimental crystallographic data. The extraframework ions are not shown. Color code: In, cyan; N, blue; C, grey; O, red; and H, white.

The dispersion interactions of framework atoms were presented by Lennard-Jones (LJ) potential with parameters adopted from the Universal force field (UFF) [174]. The cross LJ parameters were estimated by the Lorentz-Berthelot combining rules [296]. The atomic charges of *rho*-ZMOF framework atoms were calculated from density-functional theory (DFT) based on a fragmental cluster as shown in Figure 7.2.

Similar approach was employed to calculate the atomic partial charge as described in Chapter 4. The extraframework Na^+ ion in *rho*-ZMOF carried a positive unit charge.

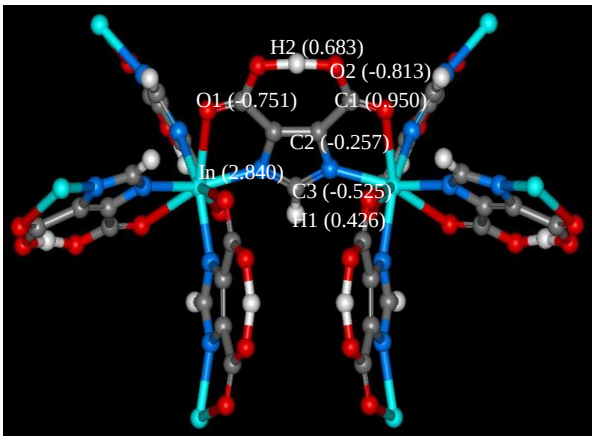

Figure 7.2. Atomic charges in a fragmental cluster of *rho*-ZMOF calculated using density functional theory.

CO_2 was represented as a three-site rigid molecule and its intrinsic quadrupole moment was described by a partial-charge model [287]. The partial charges on C and O atoms were q_C = 0.576*e* and q_O = –0.288*e* (*e* = 1.6022 ×10^{-19} is the elementary charge), respectively. The C–O bond length was 1.18 Å and the bond angle ∠OCO was 180°. The CO_2-CO_2 interaction was modeled as a combination of LJ and Coulombic potentials. CH_4 was represented by a united-atom model interacting with the LJ potential. The potential parameters were adopted from the TraPPE force field, which was developed to reproduce the critical parameters and liquid densities of alkanes [295]. H_2 was mimicked by a two-site model with the LJ potential parameters fitted to the isosteric heat of H_2 adsorption on a graphite surface [382]. Similar to H_2, N_2 was also considered as a two-site model with the LJ potential parameters fitted to the experimental bulk properties [383]. The electrostatic interaction between N_2 molecules was not considered, as reported in earlier study that the incorporation of quadrupole moment was found to have an insignificant effect on N_2 adsorption [288].

H_2O was represented by TIP3P (three-point transferable interaction potential) model [384]. Table 7.1 lists the potential parameters for extraframework ions and adsorbates.

Table 7.1. Force field parameters for extraframework ions and adsorbates [174, 287, 382-384].

Species	Site	σ (Å)	ε / k_B (K)	q (e)
Na^+	Na^+	2.658	15.09	+1
CO_2	C	2.789	29.66	+0.576
	O	3.011	82.96	–0.288
CH_4	CH_4	3.73	148.0	0
H_2	H	2.59	12.5	0
N_2	N	3.32	36.4	0
H_2O	OW	3.151	76.42	- 0.834
	HW	–	–	+0.417

7.3 Methodology

To examine the locations of extraframework ions, canonical MC simulation was performed at 298 K. The simulation box contained a unit cell of *rho*-ZMOF with 48 Na^+ ions and the periodic boundary conditions were applied. The framework was assumed as being rigid and the framework atoms were fixed during simulation. As a consequence, the unit cell was divided into three dimensional grids with the potential energy tabulated in advance and then used by interpolation during simulation. Such a treatment accelerated the simulation by approximately two orders of magnitude. A spherical cutoff of 15.0 Å was used to evaluate the LJ interactions. Beyond the cutoff, the usual long-range corrections for homogeneous system were used [253]. The use of the usual long-range corrections was an appropriate approximation because the error introduced by assuming homogeneity was small compared with the magnitude of the

long-range corrections [385]. For the Coulombic interactions, a simple spherical truncation could result in significant errors; consequently, Ewald sum with a tin-foil boundary condition was used instead [252]. The real/reciprocal space partition parameter and the cutoff for reciprocal lattice vectors were chosen to be 0.2 $Å^{-1}$ and 8, respectively, to ensure the convergence of Ewald sum. These methods to evaluate the LJ and Coulombic interactions were also used in the simulations for the adsorption of pure gas and mixtures. A total of 10^7 trial moves were carried out to sample the configurational space of extraframework ions. In *rho*-ZMOF, 48 Na^+ ions were introduced randomly into the system and followed by 10^7 trial moves. Two types of trial moves, translation and rotation, were used with equal probability.

To quantitatively characterize the dynamics of Na^+ ions, MD simulation was performed using DL_POLY program [386]. The starting configuration for MD was generated directly from the MC simulation mentioned above. The Nosé-Hoover thermostat was used to maintain a constant temperature. The MD simulation was performed for 3 ns, including 1 ns equilibration and 2 ns production. The potential and kinetic energies were monitored during the MD simulation to ensure equilibration. The time step was 1 fs for good energy conservation and history file was saved every 1 ps for analysis.

The isosteric heat and Henry constant of each gas in *rho*-ZMOF were calculated at infinite dilution using MC simulations at 298 K. A single gas molecule was added into the adsorbent and subjected to three types of trial moves, namely, translation, rotation and regrowth. The isosteric heat was evaluated by

$$Q_{\mathrm{st}}^{\mathrm{o}} = RT - \left\langle U_{\mathrm{a}}^{\mathrm{o}} \right\rangle \tag{7.1}$$

where $\left\langle U_{\mathrm{a}}^{\mathrm{o}} \right\rangle$ is the ensemble averaged adsorption energy of a gas molecule with adsorbent. The Henry constant K_{H} was evaluated by

$$K_{\mathrm{H}} = \beta \int \exp[-\beta u_{\mathrm{a}}(\mathbf{r}, \varpi)]\, \mathrm{d}\mathbf{r}\mathrm{d}\varpi \tag{7.2}$$

where $\beta = k_{\mathrm{B}}T$ and k_{B} is the Boltzmann constant, $u_{\mathrm{a}}(\mathbf{r}, \varpi)$ is the adsorption energy for a gas molecule at position r with orientation ϖ . The integral yields the excess chemical potential of a single gas molecule upon adsorption. From the regrowth move, which is equivalent to the test−particle insertion method [352], the excess chemical potential was evaluated.

GCMC simulations were carried out for the adsorption of various gas mixtures at 298 K. The simulation boxes contained one unit cell of MOF adsorbents and the periodic boundary conditions were used in three directions. The MOF frameworks were assumed to be rigid, and the potential energy between adsorbate atoms and frameworks were pre-tabulated. This is because low-energy equilibrium configurations are involved in adsorption and framework flexibility has only a marginal effect [359]. The bulk composition was 50:50 for CO_2/CH_4 and 15:85 for both CO_2/H_2 and CO_2/N_2 mixtures. The compositions chosen for these mixtures are found practically in chemical industry. To examine the effect of H_2O, 0.1 wt% of H_2O was added into CO_2/CH_4 mixture. As in canonical MC simulation described above, the LJ interactions were evaluated with a spherical cutoff equal to half of the simulation box, with long-range corrections added; the Coulombic interactions were calculated using the Ewald sum method. The extraframework ions were allowed to move during simulation. As we shall observe, the positions of ions were indeed shifted upon adsorption. To examine the effect of charged framework and extraframework ions on separation, additional simulations were performed for gas mixtures in a neutral structure, in which the charges on the framework and extraframework ions were switched off.

The number of trial moves in a typical GCMC simulation was 2×10^8, though additional trial moves were used at high loadings. The first 10^8 moves were used for equilibration, and the following 10^8 moves to obtain ensemble averages. Six types of trial moves were randomly attempted in the GCMC simulation, displacement, rotation, and partial regrowth at a neighboring position; complete regrowth at a new position; and exchange with the reservoir including creation and deletion with equal probability, exchange of molecular identity, i.e., CO_2 to CH_4 and vice versa, with equal probability. While the last trial move is usually not required in GCMC simulation, its use allows faster equilibration and reduces fluctuation after equilibration. Unless otherwise mentioned, the simulation uncertainties were smaller than the symbol sizes presented in the figures.

7.4 Results and Discussion

First, the extraframework Na^+ ions in *rho*-ZMOF are characterized in terms of static locations, radial distribution functions, and dynamic displacements. The locations are compared with those in the inorganic counterpart *rho*-zeolite. Then, the isosteric heats and Henry constants for pure CO_2, CH_4, H_2, and N_2 at infinite dilution are presented. The separation of syngas, natural gas, and flue gas are reported in *rho*-ZMOF. The adsorption isotherms, selectivities, density contours, and structural properties are specifically discussed in detail. The capability of *rho*-ZMOF for gas separation is compared with other MOFs and porous materials available in the literature. Finally, the effect of H_2O is examined on the separation of CO_2/CH_4 mixture.

7.4.1 Characterization of Na^+ ions

Based on the coordination environment and binding energy, two types of binding sites were identified for Na^+ ions in *rho*-ZMOF as shown in Figure 7.3a. Site I is in the single eight-membered ring (S8R) and at the entrance to the α-cage. Two S8Rs in neighboring unit cells form a double eight-membered ring (D8R). The distance from site I to the nearest In atoms in S8R is 5.0 - 5.3 Å (Figure 7.3b), and is approximately 7.8 Å to the next-to-nearest In atoms in the D8R (not shown). Site II is in the α-cage and proximal to the moiety of organic link. In one unit cell, twenty six Na^+ ions are located at site I and the remaining at site II. Compared with site II, site I has a larger coordination number with neighboring atoms in the S8R and thus a stronger interaction with framework. Intriguingly, the two types of binding sites in *rho*-ZMOF resemble those in its inorganic counterpart *rho*-zeolite [387]. In the latter, however, an additional type of site is located at the center of the D8R and equally distanced from both S8R.

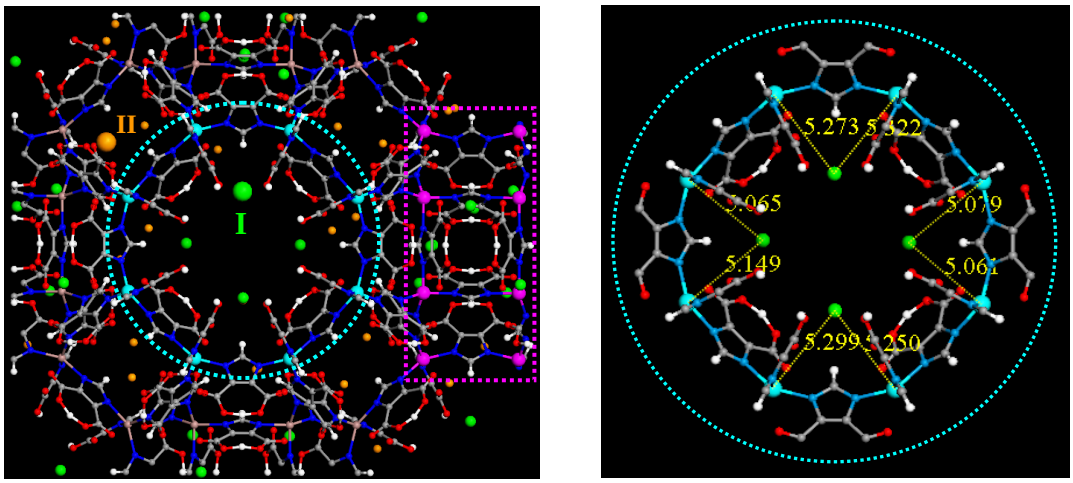

Figure 7.3. (a) Binding sites of Na^+ ions in *rho*-ZMOF. Site I (green) is in the single eight-membered ring (S8R), while site II (orange) is in the α-cage. (b) The central S8R is enlarged for clarity. Color code: In, cyan (S8R); In, pink (D8R); N, blue; C, grey; O, red; and H, white.

To quantitatively identify the locations of Na^+ ions, the radial distribution functions were calculated by

$$g_{ij}(r) = \frac{\Delta N(r, r+\Delta r)V}{4\pi r^2 \Delta r\, N_i N_j} \tag{7.3}$$

where r is the distance from species i to j, $\Delta N(r, r+\Delta r)$ is the coordination number of species j around i within a shell from r and $r + \Delta r$, V is the system volume, and N_i and N_j are the numbers of species i and j.

Figure 7.4a shows $g(r)$ between Na^+ ions and In atoms of *rho*-ZMOF. At site I, $g(r)$ exhibits two distinct peaks at $r \approx 5.2$ and 7.8 Å, respectively. These are attributed to Na^+ ions around the nearest In atoms in S8R and the next-to-nearest In atoms in D8R. Na^+ ions at site I have a stronger affinity with framework; consequently, the peak at site I is higher than at site II. Figure 7.4b shows $g(r)$ between Na^+ ions and oxygen atoms of *rho*-ZMOF. A pronounced peak is observed at $r \approx 2.1$ Å, which indicates that Na^+ ions are located very close to the carboxylic groups because of the strong electrostatic attractions. Na^+ ions at site II have a smaller peak in $g(r)$ than at site I, implying a relatively scattered distribution of Na^+ ions at site II.

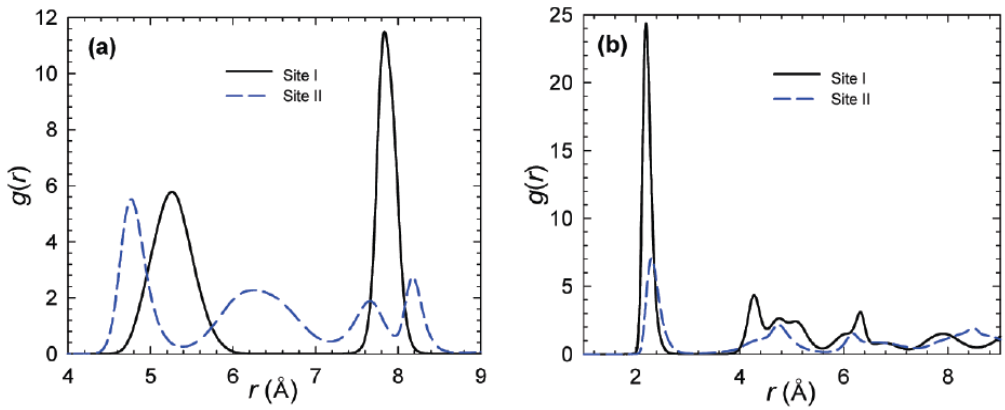

Figure 7.4. Radial distribution functions (a) between Na^+ ions and indium atoms (b) between Na^+ ions and oxygen atoms.

The mobility of Na^+ ions was examined by the mean-squared displacements (MSDs). The MSD was estimated from MD simulation by

$$\text{MSD}\,(t) = \frac{1}{N}\sum_{i=1}^{N}\left|\Delta \mathbf{r}_i(t)\right|^2 \tag{7.4}$$

Figure 7.5 shows the MSDs of Na^+ ions at site I and II, respectively. MSD at site I is nearly flat with negligible value of 0.15 $Å^2$. In contrast, MSD at site II initially increases and then approaches a constant about 1.3 $Å^2$. The mobility of Na^+ at site II is greater than at site I due to the relatively weaker interaction with framework and the larger void space available around site II. In general, the mobility of extraframework ions in *rho*-ZMOF is small. This could be attributed to the degenerated favorable sites away from each other, which largely prohibits ion hopping from one site to other. In addition, the steric hindrance of metal atoms and organic linkers also reduces ion mobility. Consequently, the dynamics of extraframework ions can be regarded as local vibration at their favorable binding sites.

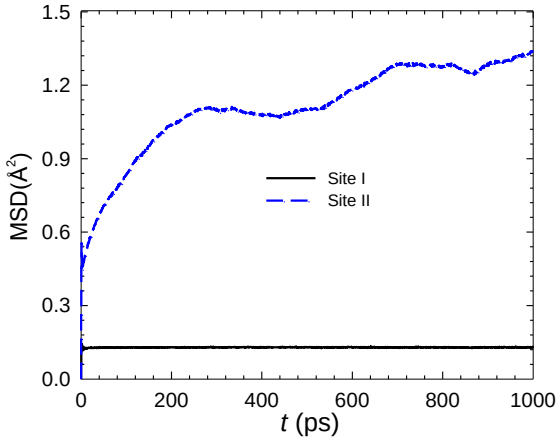

Figure 7.5. Mean-squared displacements of Na^+ ions in *rho*-ZMOF.

7.4.2 Pure Gas

The interaction strength between adsorbate and adsorbent is directly reflected by isosteric heat Q_{st}^{o} and Henry constant K_H at infinite dilution. As listed in Table 7.2, CO_2 exhibits significantly larger Q_{st}^{o} and K_H compared to that of other gases. This is due to the extremely strong electrostatic interactions of quadrupolar CO_2 molecules with the highly charged framework and the concentrated Na^+ ions in *rho*-ZMOF. In silicalite, carbon and neutral MOFs, Q_{st}^{o} of CO_2 is in the range 13 - 33 kJ/mol and K_H

is in the range 0.004 - 0.5 mmol/cm^3/kPa [288,315,334,360] substantially smaller than in *rho*-ZMOF. The predicted Q_{st}^{o} of CO_2 in *rho*-ZMOF is comparable to experimentally measured Q_{st}^{o} in Na-ZSM5 (50 kJ/mol) [315] and Na-MOR (65 kJ/mol) [388]. For CH_4, N_2 and H_2, the predicted Q_{st}^{o} and K_H in *rho*-ZMOF are close to measured and simulated values in various nanostructures [208,288,334,389]. Among the four gases, H_2 has the smallest Q_{st}^{o} and K_H, indicating the weakest affinity with *rho*-ZMOF.

Table 7.2. Isosteric Heats and Henry Constants for CO_2, CH_4, H_2, and N_2 in *rho*-ZMOF

Species	Q_{st}^{o} (kJ/mol)	K_H (mmol/g/kPa)
CO_2	58.25	50.37
CH_4	20.73	0.0133
H_2	6.02	0.0003
N_2	15.18	0.0026

7.4.3 CO_2/H_2 mixture

Figure 7.6 shows the adsorption isotherm for CO_2/H_2 mixture (bulk composition 15:85). A separate simulation in a larger box with 2 × 2 × 2 unit cells gave very close results within statistical error, implying negligible finite-size effect. The isotherm belongs to type I (Langmuirian), the characteristic feature of adsorption in microporous adsorbents. Over the entire range of pressure, CO_2 is more predominantly adsorbed than H_2 due to three reasons. First, CO_2 is a three-site molecule and has a much stronger interaction than H_2 with the framework. Second, the temperature 298 K considered is subcritical for CO_2 (T_c = 304.4 K), but supercritical for H_2 (T_c = 33.2 K); that is, CO_2 is more condensable than H_2 at 298 K. It was observed in many studies that H_2 adsorption at room temperature is quite small in various MOFs, though the adsorption could be rather high at cryogenic

temperatures [121,178]. Third, the highly ionic framework and the presence of extraframework ions induce strong electrostatic interactions with quadrupolar CO_2 molecules, and thus enhance CO_2 adsorption.

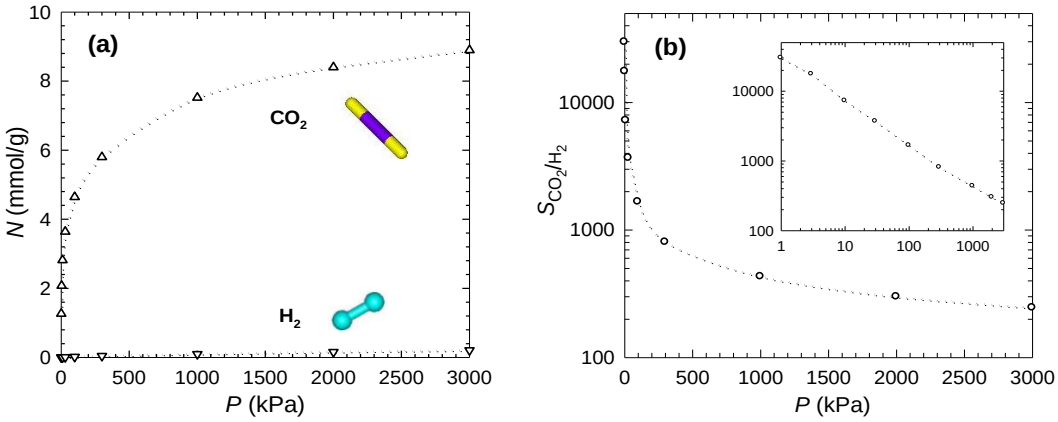

Figure 7.6. (a) Adsorption isotherm (b) selectivity for CO_2/H_2 mixture (15:85).

The separation of CO_2/H_2 mixture is quantified by selectivity $S_{i/j} = (x_i / x_j)(y_j / y_i)$, where x_i and y_i are the mole fractions of component i in adsorbed and bulk phases, respectively. Figure 7.6b shows the selectivity for CO_2/H_2 mixture in *rho*-ZMOF. At infinite dilution the selectivity is $K_H(CO_2)/K_H(H_2) \approx 1.6 \times 10^5$. With increasing pressure, it decreases sharply as a consequence of two factors. First, the adsorption sites in *rho*-ZMOF are heterogeneous and adsorbate molecules occupy less favorable sites at high pressures. Second, H_2 is much smaller than CO_2 and can pack into the partially filled pores more easily with increasing pressure. At 298 K and 1 atm, the selectivity is about 1800. Separation of CO_2 from syngas has been studied in other porous materials by experiments and simulations. For example, the selectivity is 5 in MFI and 3.5 in ETS-10 for an equimolar CO_2/H_2 mixture [365]. In an activated carbon the selectivity ranges 60 ~ 90 for CO_2/H_2 mixture with different mole fractions [367]. In zeolite Na-4A the selectivity is 70 for a mixture with 98.6% H_2 and 1.4% CO_2 [368]. The selectivity is 40 in IRMOF-1 and 90 in Cu-BTC at 298 K and 1 atm [172]. In charged *soc*-MOF, the selectivity is in the range of 300 -

600 [390]. In this study, the selectivity in *rho*-ZMOF is 1.6×10^5 at infinite dilution and 1800 at ambient condition, the *highest* among all reported values to date.

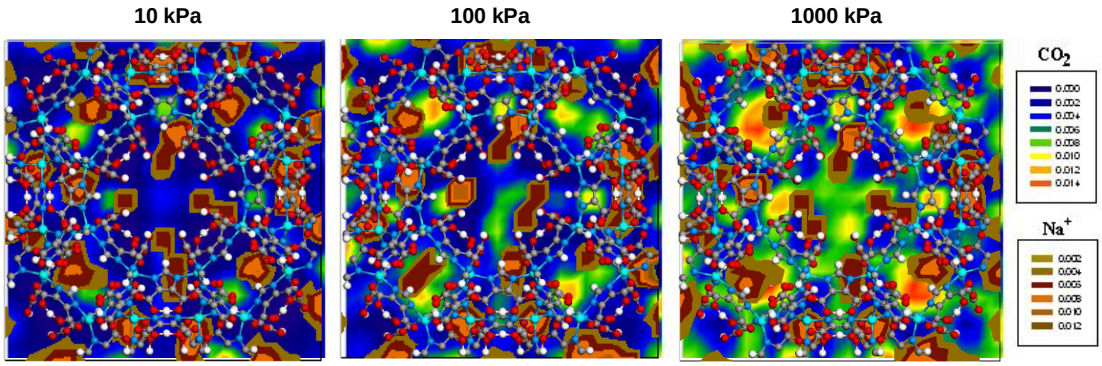

Figure 7.7. Density distribution contours of CO_2 molecules and Na^+ ions for CO_2/H_2 mixture (15:85) at 10, 100 and 1000 kPa, respectively.

Figure 7.7 shows the density distribution contours of CO_2 molecules and Na^+ ions for CO_2/H_2 mixture in *rho*-ZMOF at 10, 100 and 1000 kPa, respectively. At low and moderate pressures (10 and 100 kPa), CO_2 molecules are adsorbed closely to Na^+ ions. Therefore, Na^+ ions act as additional sites for CO_2 adsorption due to the strong electrostatic interactions. At high pressure (1000 kPa), Na^+ ions are solvated by surrounding CO_2 and the void space between Na^+ ions is also occupied by CO_2. This suggests that further adsorbed CO_2 molecules have relatively weaker interactions with Na^+ ions. Interestingly, the locations of Na^+ ions are observed to shift, to some extent, upon adsorption at different pressures.

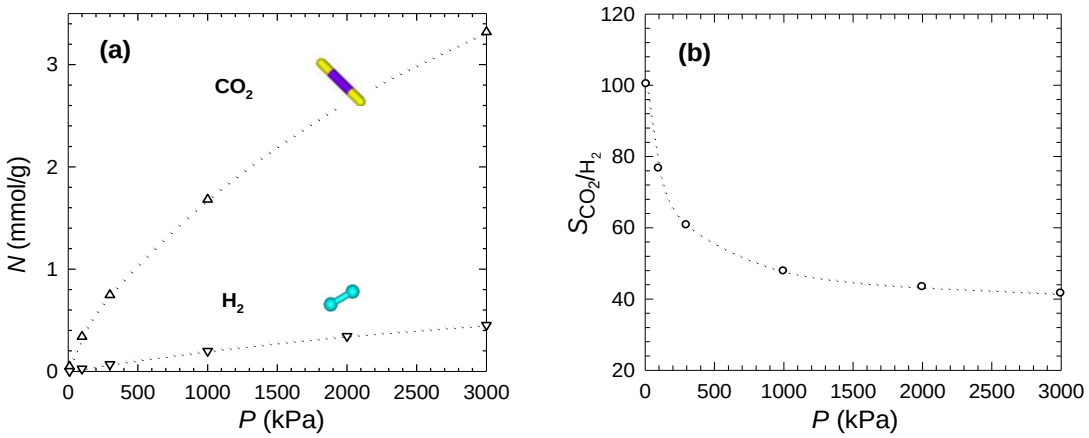

Figure 7.8. (a) Adsorption isotherm (b) Selectivity for CO_2/H_2 mixture (15:85). The charges on framework and extraframework ions were switched off.

The adsorption of CO_2/H_2 mixture was also simulated in a neutral structure by switching off the charges on framework and Na^+ ions. The isotherm and selectivity in the neutral structure are presented in Figures 7.8. Compared with Figure 7.6a, CO_2 adsorption in the neutral structure decreases by three-fold at high pressures, whereas H_2 adsorption increases by two-fold. With increasing pressure, the selectivity in the neutral structure exhibits a trend similar to Figure 7.6b. However, it decreases three orders of magnitude at low pressures from that in the charged framework, though less drastically at high pressures. This clearly demonstrates the important role of the charged framework and Na^+ ions in the selective adsorption of CO_2 over H_2.

7.4.4 CO_2/N_2 Mixture

Figure 7.9 shows the adsorption isotherm and selectivity for CO_2/N_2 mixture (bulk composition 15:85) in *rho*-ZMOF. The trend is similar to CO_2/H_2 mixtures discussed above. CO_2 is more preferentially adsorbed than N_2 and the selectivity decreases monotonically with pressure. At infinite dilution the selectivity is K_H (CO_2)/K_H (N_2) ≈ 1.9×10^4 and 500 at ambient condition. CO_2/N_2 separation has been investigated in other nanoporous materials. The selectivity are approximately 18.8 in zeolites Na-4A [368], 15.3 in activated carbon Norit R1 [369], 30 in silicalite [370], 100 in ITQ-3 [370], 14 in MFI [371], 20 in FAU [372], 35 in Cu-BTC [208,216], 3 - 6 in MOF-508b [362]. In Na-ZSM-5, the selectivity ranges from 4000 to 200 depending on Si/Al ratio [288]. The simulated selectivity in *rho*-ZMOF is the *highest* yet reported in MOFs to date and also substantially higher than in other materials.

To explore the structural information for CO_2 and N_2 in *rho*-ZMOF, the radial distribution functions $g(r)$ between Na^+ ions and adsorbates at 10, 100, and 1000 kPa are shown in Figure 7.10. A pronounced peak in $g(r)$ for Na^+-CO_2 is observed at r = 3.6 Å at all the three pressures, but no such peak exists for Na^+-N_2. This confirms that

CO_2 interacts with Na+ ions more strongly than does N_2 because of the large quadrupole moment. As the pressure is increased from 10 to 100 and then to 1000 kPa, the peak height in $g(r)$ for Na^+-CO_2 drops, whereas the coordination number of CO_2 molecules surrounding Na^+ ions increases (data not shown). This indicates that Na+ ions are solvated by more CO_2 molecules.

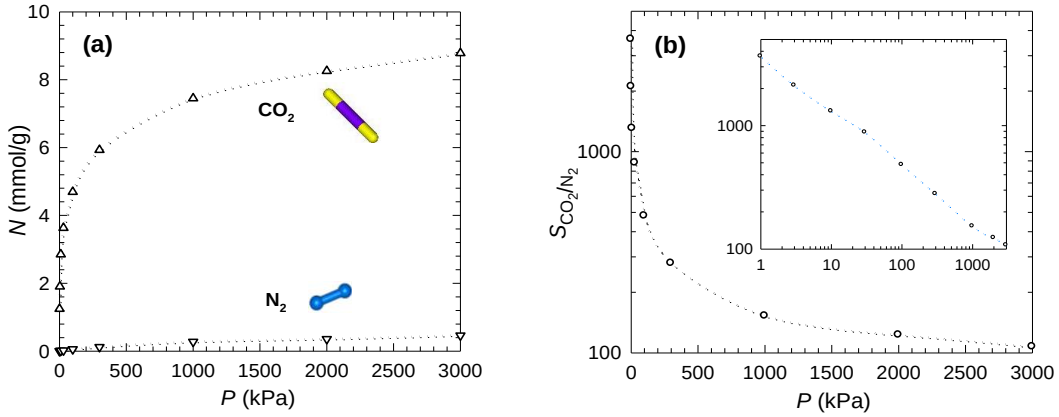

Figure 7.9. (a) Adsorption isotherm (b) Selectivity for CO_2/N_2 mixture (15:85).

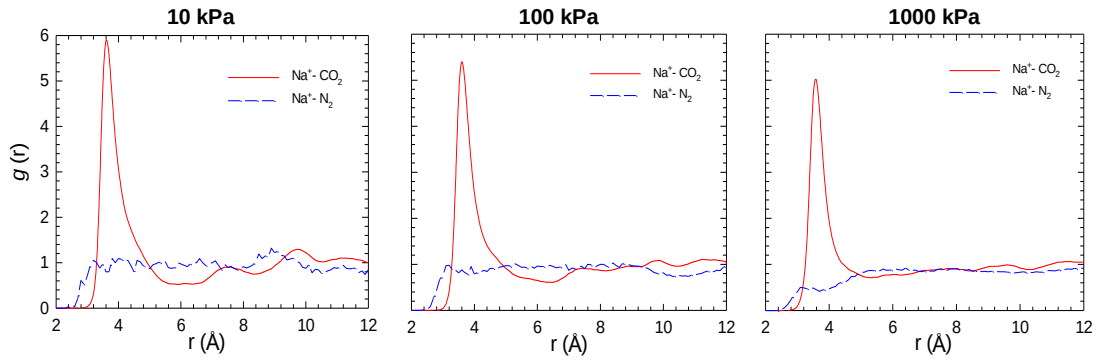

Figure 7.10. Radial distribution functions between Na^+ ions and adsorbate molecules for CO_2/N_2 mixture (15:85) at 10, 100 and 1000 kPa.

7.4.5 CO_2/CH_4 Mixture and Effect of H_2O

For the adsorption of equimolar CO_2/CH_4 mixture in *rho*-ZMOF, Figure 7.11 illustrates the typical locations of CO_2 molecules in the S8R. At 10 kPa, CO_2 molecules are observed to bind preferentially with Na^+ ions. This is because CO_2 has a quadrapolar moment and can strongly interact with Na^+ ions, which act as additional adsorption sites for CO_2. With increasing pressure to 500 and 3000 kPa, Na^+ ions are

coordinated by more CO_2 molecules, i.e., increasingly solvated by surrounding CO_2 molecules. The distance between CO_2 molecules (C_{CO2}-C_{CO2}) becomes shorter with increasing pressure, while the distance between Na^+ and CO_2 (Na^+-O_{CO2}) remains more or less constant. This implies an enhancement in the cooperative interactions between CO_2 molecules. As pressure rises, however, more CO_2 molecules are adsorbed in the *a*-cages (figures are not shown) and the electrostatic interactions between CO_2 and Na^+ ions are largely reduced. Upon comparison, the enhanced cooperative interactions of CO_2 molecules are negligible.

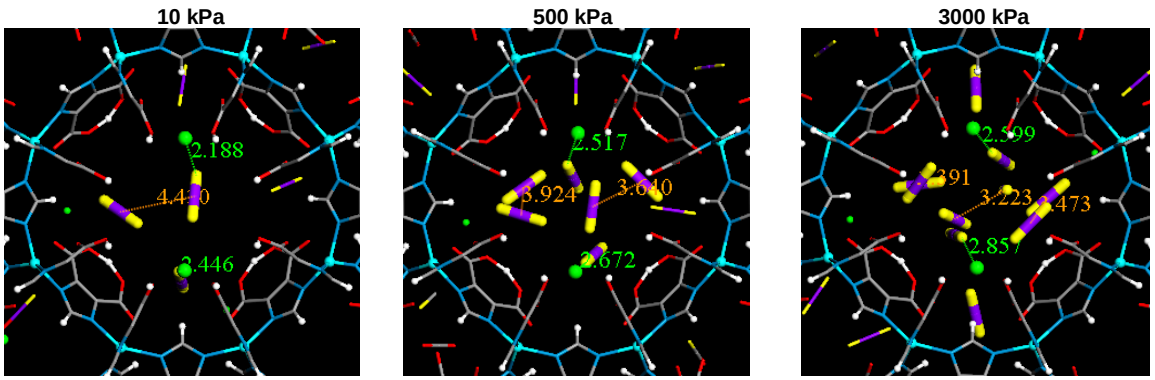

Figure 7.11. Locations of CO_2 molecules for CO_2/CH_4 mixture (50:50) in the S8MR at 10, 500 and 3000 kPa, respectively. Na^+ ions and CO_2 molecules are represented by balls and sticks. The distances of C_{CO2}-C_{CO2} (orange) and Na^+-O_{CO2} (green) are in angstroms.

To explore the structural information of CO_2 and CH_4 in *rho*-ZMOF, the radial distribution functions $g(r)$ between Na^+ ions and adsorbates are shown in Figure 7.12 at 10, 500, and 3000 kPa. A pronounced peak in $g(r)$ for Na^+-CO_2 is observed at r = 3.6 Å at all the three pressures, nevertheless, no such peak exists for CH_4. This confirms that CO_2 interacts with Na^+ ions more strongly than CH_4. With increasing pressure from 10, 500 to 3000 kPa, the peak height in $g(r)$ for Na^+-CO_2 drops and the coordination number of CO_2 molecules around Na^+ ions increases (not shown). This indicates that Na^+ ions are coordinated and solvated gradually by CO_2 molecules. For

Na^+-CH_4, $g(r)$ does not change much because the adsorption of CH_4 is vanishingly small.

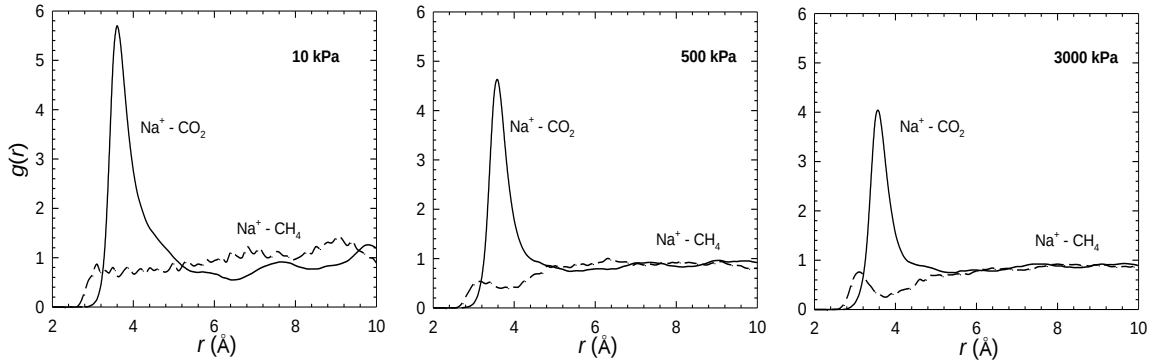

Figure 7.12. Radial distribution functions between Na^+ ions and adsorbates for CO_2/CH_4 mixture at 10, 500 and 3000 kPa.

Figure 7.13 shows the adsorption isotherms and selectivity for CO_2/CH_4 and $CO_2/CH_4/H_2O$ mixtures in *rho*-ZMOF. For CO_2/CH_4 mixture, there is a sharp increase in CO_2 adsorption at low pressures. With increasing pressure, CO_2 adsorption tends to approach saturation. Over the entire range of pressure, CO_2 is predominantly more adsorbed than CH_4 due to two reasons. First, CO_2 is a three-site molecule and has a much stronger interaction with the framework than CH_4. Second, the charged framework and the presence of Na^+ ions induce strong electrostatic interactions with CO_2 molecules. Interestingly, with 0.1% of H_2O added in CO_2/CH_4 mixture, CO_2 adsorption drops significantly while CH_4 adsorption is not discernibly affected. Although not shown, the extent of H_2O adsorption is much larger than CO_2 despite its negligible composition. This is because H_2O is highly polar, interacts with charged framework and ions substantially more strongly than CO_2, and therefore has a significant effect on CO_2 adsorption.

The selectivity $S_{CO2/CH4}$ at infinite dilution is equal to $K_H(CO_2)/K_H(CH_4) \approx 3800$ for CO_2/CH_4 mixture in *rho*-ZMOF. With increasing pressure, the selectivity for both CO_2/CH_4 and $CO_2/CH_4/H_2O$ mixtures reduce and level off. The reason is that the

interactions of CO_2 with framework and ions become less strong at high pressures. With a trace amount of H_2O, the selectivity of CO_2/CH_4 mixture reduces by one order of magnitude. For CO_2/CH_4 mixture, the selectivity reaches 80 at 298 K and 1 atm. This selectivity is unprecedentedly high in MOFs and higher than reported data in IRMOF-1 (2 - 3) [172,334,391], carborane-based MOFs (17) [146], mixed-ligand MOFs (30) [361], and Cu-BTC (6 - 9) [172,391]. At pressures less than 5 atm, the selectivity in *rho*-ZMOF is also higher than that in charged *soc*-MOF [381].

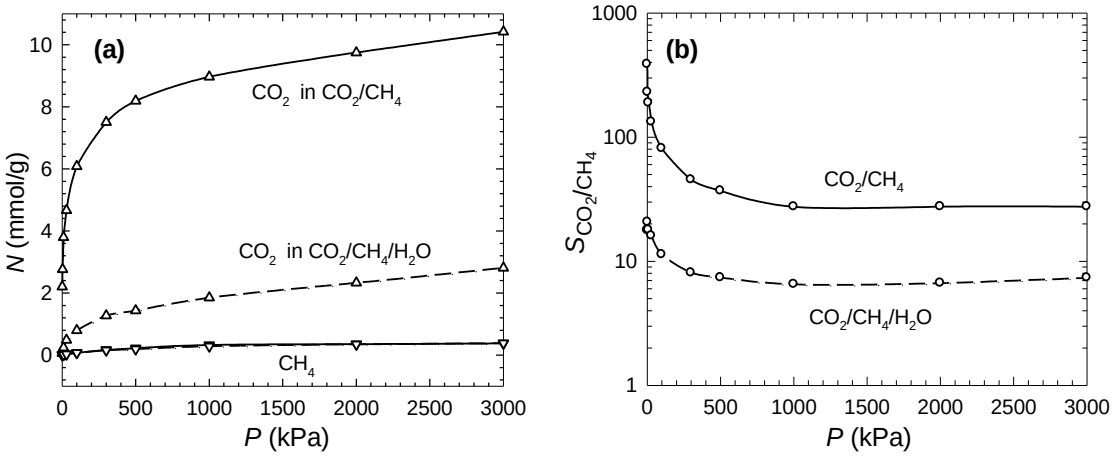

Figure 7.13. (a) Isotherms and (b) selectivity for CO_2/CH_4 and $CO_2/CH_4/H_2O$ mixtures in *rho*-ZMOF. The bulk composition is 50:50 for CO_2/CH_4, and 50:50:0.1 for $CO_2/CH_4/H_2O$.

It is instructive to note that the selectivity of gas mixture might behave differently in various MOFs and needs to be analyzed case by case. In Chapter 6 for CO_2/CH_4 mixture in *soc*-MOF, the selectivity increases with pressure and reaches a plateau [381]. The increase is caused by the strong interactions of CO_2 molecules with the multiple binding sites and by the cooperative interactions of adsorbed CO_2 molecules. However, the selectivity for CO_2/CH_4 mixture in *rho*-ZMOF decreases monotonically with increasing pressure. This is a consequence of the significant reduction in the electrostatic interactions between CO_2 and *rho*-ZMOF with increased loading. The different behavior of selectivity in *soc*-MOF and *rho*-ZMOF is attributed to the

different framework topologies and charge densities. More specifically, there exist carcerand-like capsules and narrow channels of approximately 10 Å in *soc*-MOF, whereas *rho*-ZMOF has a very open-framework with extra-large cavity of 18.2 Å. A unit cell of *soc*-MOF contains 8 NO_3^- ions, corresponding to a charge density of 7.1×10^{-4} $e/Å^3$. In contrast, *rho*-ZMOF possesses 48 Na^+ ions in a unit cell and a charge density of 1.6×10^{-3} $e/Å^3$. Therefore, the geometry constrains and surface interactions differ in the two charged MOFs, which leads to different behavior of selectivity.

As seen from Figure 7.13, the adsorption of CO_2/CH_4 mixture is significantly affected by H_2O. With even 0.1% of H_2O, CO_2 adsorption drops significantly, while CH_4 adsorption is not discernibly affected. Upon addition of H_2O, the selectivity of CO_2/CH_4 mixture is reduced approximately by one order of magnitude. To provide a more detailed insight, Figure 7.14 presents the locations of CO_2 and H_2O molecules in the S8R for $CO_2/CH_4/H_2O$ mixture at 500 kPa. There are a large number of H_2O molecules around Na^+ ions, which are considered as being solvated. Compared with Figure 7.11, the number of CO_2 molecules is lesser and the distance from CO_2 and Na^+ is longer, changing from 2.5 - 2.6 Å to 4.0 - 4.4 Å. Figure 7.15 shows $g(r)$ between Na^+ and adsorbates. A very high peak is observed in $g(r)$ of Na^+-H_2O, indicating a strong affinity of Na^+ toward H_2O. However, no peak is observed here for Na^+-CO_2, which is in remarkable contrast to Figure 7.12. These further suggest that H_2O competes with CO_2 and has a significant effect on CO_2 adsorption. Therefore, it is important to remove moisture before the separation of CO_2/CH_4 mixture.

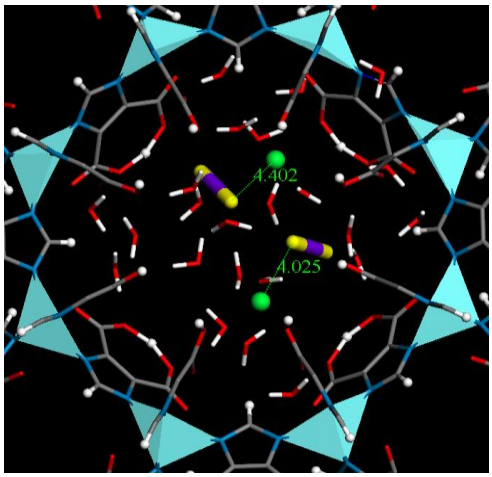

Figure 7.14. Locations of CO_2 and H_2O molecules in the S8R for $CO_2/CH_4/H_2O$ mixture at 500 kPa. Na^+ ions are represented by balls, CO_2 and H_2O molecules are represented by sticks. The distances of Na^+-O_{CO2} are in angstroms.

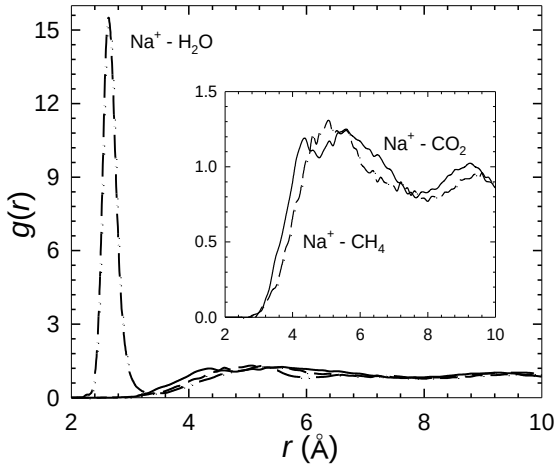

Figure 7.15. Radial distribution functions between Na^+ ions and adsorbates for $CO_2/CH_4/H_2O$ mixture at 500 kPa.

7.5 Summary

The extraframework Na^+ ions are characterized and the separation of CO_2/H_2, CO_2/N_2, and CO_2/CH_4 mixtures are examined in novel *rho*-ZMOF. With a topology similar to the inorganic counterpart, *rho*-ZMOF contains twice as many positive charges and extra-large cavities. Two types of binding sites were identified for Na^+ ions. Site I is in the single eight-membered ring and site II is in the α-cage. The locations of Na^+ ions in *rho*-ZMOF are similar to *rho*-zeolite. The mobility of Na^+

ions was estimated by mean-squared displacements. Because of the strong affinity with the charged framework, Na^+ ions essentially vibrate around the binding sites, though ions at site II have a slightly greater mobility than at site I.

An ideal adsorbent for CO_2 separation from gas mixture is to have the maximum capacity of CO_2, while minimizing the capacities of other species. For CO_2/H_2, CO_2/CH_4, and CO_2/N_2 mixtures in *rho*-ZMOF, CO_2 is preferentially more adsorbed over other gases. This is attributed to the highly charged framework and the large density of extraframework Na^+ ions; both exert the strong electrostatic interactions with quadrupolar CO_2 molecules. Furthermore, Na^+ ions act as additional adsorption sites and augment the interactions with CO_2 molecules. At low pressures, CO_2 is adsorbed proximally to Na^+ ions. With increasing pressure, Na^+ ions are coordinated and solvated by CO_2 molecules. The locations of Na^+ ions are shifted slightly upon adsorption. The selectivity of CO_2 over H_2, N_2, and CH_4 are ~ 1800, 500, and 80 at 298 K and 1 atm, the typical condition for pressure swing adsorption. The predicted selectivity in *rho*-ZMOF are the highest reported to date and unprecedentedly higher than other porous materials. *Rho*-ZMOF turns out to be an extremely promising material for the separation of syngas, natural gas, and flue gas. Combined with the study in *soc*-MOF, it can be concluded that charged MOFs are generally well-suited for gas separation.

Chapter 8

Adsorption and Diffusion of Alkane Isomer Mixtures in Metal -Organic Frameworks

8.1 Introduction

Most reported studies for gas adsorption and separation in MOFs have been focused on light gases. In chemical engineering processes and industrial applications, however, separation of alkane mixtures is crucial. For example, it is preferential to have branched alkanes rather than linear ones as ingredients in gasoline, as the former enhance the fuel octane number. Branched alkanes are usually converted from linear alkanes by catalytic cracking and they need to be separated. Numerous experimental and simulation studies have been carried out on alkane adsorption in a wide variety of traditional adsorbents such as zeolites and carbon materials. For instance, the enthalpies, Henry constants, van't Hoff pre-exponential factors, and separation factors of C_5–C_8 alkanes were determined in zeolites at 473–648 K. Both nonselective and selective adsorption were found between linear and branched alkanes depending on zeolite type [392]. The isosteric heats and adsorption isotherms of C_1, C_2, and C_3 alkanes were measured in high-silica zeolites and an inverse relationship was observed between the limiting isosteric heat and pore diameter [393]. Adsorption capacities of linear C_6, C_7, C_8, and C_9 alkanes in microporous silica solids were measured at different temperatures and the limiting adsorption energy was found to be more attractive for longer alkanes [394]. With the advanced configurational-bias Monte Carlo method, adsorption of *n*C_4 to *n*C_{12} was simulated in silicalite and a linear dependence of isosteric heat on chain length was found [395]. The low-coverage sorption of normal alkanes from C_4 to C_{25} in silicalite, temperature-dependent

configurations and locations were examined [396]. The adsorption isotherms of C_1 to nC_5 were calculated in aluminophosphate $AlPO_4$–5 and surprisingly a low density–high density transition was observed resembling a capillary condensation [397]. Subtle entropy effects were investigated in the adsorption of multi-component mixtures of linear and branched alkanes in silicalite and the development of novel separation processes was demonstrated [398,399]. Adsorption of C_5 isomers in carbon nanotubes and nanoslits was studied by simulations. The length and area entropy effects were found to play a key role and the pore size rather than pore geometry determines the shape and inverse-shape selective adsorption [400-402].

Few simulation and experimental studies were recently reported for alkanes in MOFs. The adsorption of C_1 and nC_4 and their mixtures in IRMOFs was simulated and the influences of organic-linkers on adsorption and selectivity were analyzed [211]. A simulation study of pure and mixed linear and branched alkanes suggested that IRMOF-1 might be a good candidate for the storage and separation of hydrocarbons [212]. From fixed-bed adsorption experiment, a microporous MOF with two types of intersecting pores was found to discriminate *n*-hexane from branched isomers [403]. The chromatographic separation of alkane isomers based on size- and shape-selectivity was investigated in a microporous MOF-508 [132]. Unique gas and hydrocarbon adsorption was measured experimentally in a highly porous MOF composed of extended aliphatic ligands and a transition from monolayer adsorption to pore filling was observed upon increasing temperature [404]. The siting and segregation of complex alkane mixtures were simulated in MOF-1, which suggested new possibilities for the design and creation of highly selective adsorption sites in MOFs [217]. Alkanes in Cu-BTC were studied by infrared microscopy and simulation,

and strong inflection characteristics were found in the isotherms due to the preferential locations close to the mouths of tetrahedral pockets [218].

Currently, the intriguing properties of alkane isomers confined in MOFs remain elusive. For example, where are the preferential binding sites located in a framework? Why does competitive adsorption occur between isomers? How does framework topology come into play? In this work, these important issues are addressed by investigating the adsorption and diffusion of C_4 and C_5 isomer mixtures in two types of MOFs, noncatenated (IRMOF-14 and PCN-6′) and catenated (IRMOF-13 and PCN-6). Catenation results in constricted pores and has the benefit of increasing surface-to-volume ratio and framework stability. H_2 sorption in PCN-6 and PCN-6′ revealed that catenation leads to 41% improvement in surface area and 133% increase in volumetric uptake (29% increase in gravimetric unit) [356]. However, knowledge on the microscopic behavior of alkane isomers and their mixtures in catenated MOFs is lacking. In Section 8.2, the models for alkanes and MOFs are described briefly. The simulation methods for adsorption and diffusion are given in Section 8.3, including MC and MD simulations. In Section 8.4, the adsorption isotherms and selectivities of C_4 and C_5 isomer mixtures in IRMOF-14, IRMOF-13, PCN-6′ and PCN-6 are presented. The adsorption properties in MOFs are compared with those in carbon nanotube and silicalite. The diffusivities of C_4 and C_5 isomer mixtures in IRMOF-14, IRMOF-13, PCN-6′ and PCN-6 are reported along with the corresponding mechanisms. Finally, the concluding remarks are summarized in Section 8.5.

8.2 Models

Figure 8.1 shows the atomic structures of four MOFs (IRMOF-14, IRMOF-13, PCN-6′ and PCN-6) examined under this study. IRMOF-14 has a cubic structure with a lattice constant of 34.38 Å [2]. It is formed by substituting 1, 4-

benzenedicarboxylate (BDC) in the prototype IRMOF-1 with pyrene-dicarboxylate (PDC), which is longer in length and leads to larger pores. The pore diameters in IRMOF-14 are approximately 20.1 and 14.7 Å. IRMOF-13 has a trigonal space group with unit cell lengths of $a = b = 24.82$ Å and $c = 56.73$ Å [2]. Despite the identical metal oxide and organic linker in IRMOF-13 and IRMOF-14, IRMOF-13 has a catenated framework and differs in the topology from IRMOF-14. The pore diameters in IRMOF-13 are 12.4 and 8.7 Å, smaller than in IRMOF-14 due to catenation. PCN-6′ is a noncatenated structure with boracite net topology similar to Cu-BTC. The primary building block is 4,4′,4′′-s-triazine-2,4,6-triyl-tribenzoate (TATB) instead of benzene-1,3,5-tricarboxylate (BTC) in Cu-BTC. It has a cubic structure with unit cell length of 46.64 Å and a void cuboctahedron with diameter 30.32 Å. The open square pores in PCN-6′ are 15.16 × 15.16 Å or 21.44 × 21.44 Å along the edges or diagonals. PCN-6 is a catenated counterpart of PCN-6′ and can be reproduced by two identical catenated nets of PCN-6′ [355]. It exists in R-3m space group with cell dimensions of $a = b = 32.97$ Å and $c = 80.78$ Å. In PCN-6 there are triangular channels of 9.2 Å along the edge connected by 5 Å windows. The experimentally determined Langmuir surface area and pore volume are 2700 m^2/g and 1.045 mL/g in PCN-6′, which rise to 3800 m^2/g and 1.453 mL/g in PCN-6. Apparently, catenation leads to an increase of 41% in surface area and of 39% in pore volume [356].

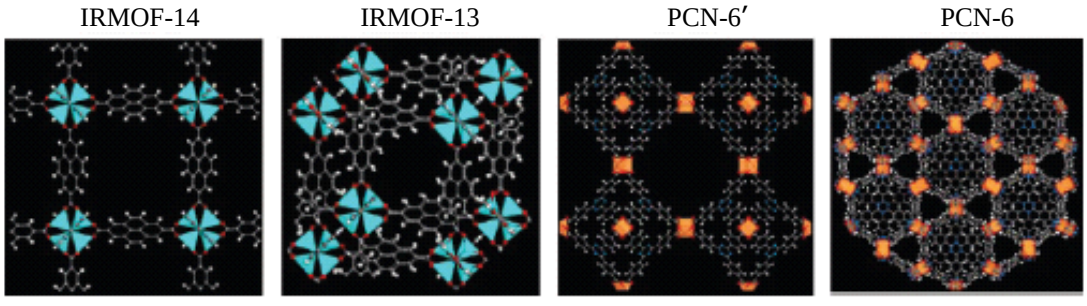

Figure 8.1. Atomic structures of IRMOF-14, IRMOF-13, PCN-6’ and PCN-6. Zn: cyan polyhedra, O: red, N: blue, C: grey, H: white, Cu: orange polyhedra.

Two types of models are commonly used to mimic alkane molecules, the united-atom model and the all-atom model [405]. Both models were found to give comparable adsorption isotherms for alkanes in silicalite; however, computation was faster with the united-atom model [406]. Consequently, in this work the united-atom model was used with every CH_x group model as a single interaction site. The C–C bonds were assumed to be rigid and fixed at 1.54 Å . The nonbonded dispersive interaction between sites of different molecules or four sites apart within a molecule was modeled by the Lennard-Jones (LJ) potential

$$u_{\mathrm{LJ}}(r) = 4\varepsilon[(\sigma/r)^{12} - (\sigma/r)^{6}]. \tag{8.1}$$

The bond bending between three successive sites was modeled using a harmonic potential

$$u_{\mathrm{bending}}(\theta) = 0.5k_{\theta}(\theta - \theta_0)^2. \tag{8.2}$$

The dihedral torsion between four successive sites was modeled using a cosine potential

$$u_{\mathrm{torsion}}(\phi) = c_0 + c_1[1+\cos\phi] + c_2[1-\cos(2\phi)] + c_3[1+\cos(3\phi)]. \tag{8.3}$$

Table 8.1 gives the force field parameters for alkanes, which were optimized to reproduce the experimental vapor-liquid coexistence curves and critical properties of pure alkanes [295,407]. It is noteworthy that the development of more accurate force fields for alkanes should take into account adjacent gauche stabilization [408,409].

The interactions between alkanes and MOFs were modeled by LJ potentials. The LJ parameters for MOFs were adopted from the universal force field (UFF) [174]. The cross LJ parameters were obtained using the Lorentz-Berthelot combining rules. A number of simulation studies have shown that UFF can accurately predict gas adsorption and diffusion in various MOFs [173,205,222,234,334,360]. For instance,

good agreement between simulation and experiment was obtained for Ar adsorption in Cu-BTC [205]. Simulated isotherms and diffusivities of CO_2 and CH_4 in IRMOF-1 matched well with experimental data [234,334,360].

Table 8.1. Force field parameters for alkanes

	Site	σ (Å)	ε/k_B (K)
Nonbonded LJ	CH_3	3.75	98.0
	CH_2	3.95	46.0
	CH	4.68	10.0
	C	6.40	0.5
Bond	$CH_x - CH_y$	r_0 = 1.54 Å	
Bending	$CH_x - CH_2 - CH_y$ $CH_x - CH - CH_y$ $CH_x - C - CH_y$	k_θ / k_B = 62500 K $\theta_0 = 113.0^o$	
Torsion	$CH_x - CH_2 - CH_2 - CH_y$	c_0 / k_B = 0, c_1 / k_B = 355.03, c_2 / k_B = - 68.19, c_3 / k_B = 791.32	
	$CH_x - CH_2 - CH - CH_y$	c_0 / k_B = - 251.06, c_1 / k_B = 428.73, c_2 / k_B = - 111.85, c_3 / k_B = 441.27	

8.3 Methodology

Adsorption of C_4 and C_5 alkane isomer mixtures in the four MOFs was simulated by GCMC method at T = 300 K. The conventional Metropolis techniques in MC simulation are prohibitively expensive in sampling the conformation of alkane molecules. To improve the efficiency, the advanced configurational-bias technique was adopted in which a molecule was grown atom-by-atom biasing energetically favorable configurations while avoiding overlap with other atoms [410-412]. First, eight trial positions were generated with a probability proportional to $\exp(-\beta U^i_{\text{internal}})$, where $\beta = 1/k_B T$ and U^i_{internal} is the internal energy at a position i including the

intramolecular bond bending and dihedral torsion interactions. Then, one of the trial positions was chosen for growing an atom with a probability proportional to $\exp(-\beta U^{i}_{\text{external}}) / \sum_{i} \exp(-\beta U^{i}_{\text{external}})$, where U^{i}_{external} is the external energy including all non-bonded intramolecular and intermolecular LJ interactions. In addition, the insertion of molecules was enhanced using the multiple first-bead scheme with fifteen trial positions [413].

All the four MOFs were treated as rigid and the periodic boundary conditions were used in three dimensions to mimic crystalline periodicity. As our study of adsorption was focused on low-energy equilibrium configurations, framework flexibility would not exert significant effect. A recent simulation study for noble gases and hydrogen in IRMOF-1 showed that there was a negligible difference in the adsorption loading between rigid and flexible frameworks [414]. The simulation box contained one unit cell for IRMOF-14 and PCN-6′, and four ($2 \times 2 \times 1$) unit cells for IRMOF-13 and PCN-6. No finite-size effect was found in a larger box with eight ($2 \times 2 \times 2$) unit cells. A spherical cutoff length equal to half of the minimum box length was used to evaluate the LJ interactions with the long-range corrections included.

A typical GCMC simulation was carried out for 20000 cycles, in which the first 10000 cycles were used for equilibration, and the second 10000 cycles for ensemble averages. Each cycle consisted of a number of trial moves: (a) translation: A randomly selected adsorbate molecule was translated with a random displacement in either *x*, *y*, or *z* dimension, and the maximum displacement was adjusted to an overall acceptance ratio of 50%. (b) rotation: A randomly selected adsorbate molecule was rotated around either *x*, *y*, or *z* dimension with a random angle, and the maximum angle was adjusted to an overall acceptance ratio of 50%. (c) partial regrowth: Part of a randomly selected adsorbate molecule was regrown locally. It was decided at

random which part of the molecule was regrown and from which bead the regrowth was started. (d) complete regrowth: A randomly selected adsorbate molecule was regrown completely at a random position. (e) swap with reservoir: A new adsorbate molecule was created at a random position, or a randomly selected adsorbate molecule was deleted. To ensure microscopic reversibility, the creation and deletion were attempted at random with equal probability. (f) exchange of molecular identity: An adsorbate molecule was selected randomly and an attempt was made to change its molecular identity. While this trial move is usually not required in GCMC simulation, its use allows reaching equilibrium faster and reduces fluctuations after equilibration [300]. Within statistical uncertainty, the simulation results were found to be independent of the sequence of the trial moves.

The diffusion of C_4 and C_5 alkane isomers were examined using DL_POLY program [386]. The simulations were carried out in canonical ensemble at T = 300 K. The Nosé-Hoover thermostat was used to maintain temperature with a relaxation constant of 0.8 fs. The equations of motion were integrated using a velocity verlet algorithm and the time step was 1 fs. Similar to the GCMC simulations, the simulation box for IRMOF-14 and PCN-6′ contained one unit cell, while four ($2 \times 2 \times 1$) unit cells were used for IRMOF-13 and PCN-6. Nevertheless, at low loadings the simulation box size was increased to eight ($2 \times 2 \times 2$) unit cells in order to accommodate at least 50 molecules to ensure the desired level of statistical accuracy. All adsorbents were assumed to be rigid and the framework atoms were fixed during MD simulation. However, it should be noted that diffusion might be influenced by framework flexibility. For example, diffusion in zeolites is usually accelerated in a flexible model due to the increased possible pathways for molecular jump [307]. A reduction of diffusion was observed in a flexible carbon nanotube by taking into

account the energy exchange between diffusing molecules and nanotube [308]. The activation energy of benzene in a rigid model of IRMOF-1 was found to be considerably smaller than that in a flexible model and hence a higher diffusivity was observed in the former. This was attributed to the correlation motion of benzene with the phenylene rings of IRMOF-1, leading to an increase of benzene population in the A-cell pockets [225]. In our MD simulations, the initial configurations were taken from the GCMC simulations mentioned above. The MD simulations were performed for a total period of 5 ns, with the first half left out for equilibration and the second half for ensemble average. As we shall see, 2.5 ns were sufficiently long for alkanes molecules to reach normal diffusion. During the production run, the atomic coordinates and velocities were written to disk every 1 ps. The diffusivities were estimated from the mean-squared displacements based on Einstein relation [252]. Unless otherwise mentioned, simulation uncertainties were no larger than the symbol sizes presented in the figures.

8.4 Results and Discussion

8.4.1 Adsorption

Figure 8.2 shows the adsorption isotherms of equimolar mixture of nC$_4$ and iC$_4$ isomers in IRMOF-14, IRMOF-13, PCN-6′ and PCN-6, respectively. At low pressures, both isomers have a similar amount of adsorption, particularly, in the noncatenated IRMOF-14 and PCN-6′ possessing relatively larger pores. Upon increasing pressure, nC$_4$ exhibits a greater increase in adsorption than iC$_4$ and reaches a higher saturation capacity. This implies that a competitive adsorption occurs between nC$_4$ and iC$_4$ at high pressures. The packing efficiency in MOFs is better for a linear isomer with a lower degree of branching, in accordance with the concept of

shape selectivity, i.e., a slender isomer is preferentially adsorbed over a bulky one due to the effect of configurational entropy.

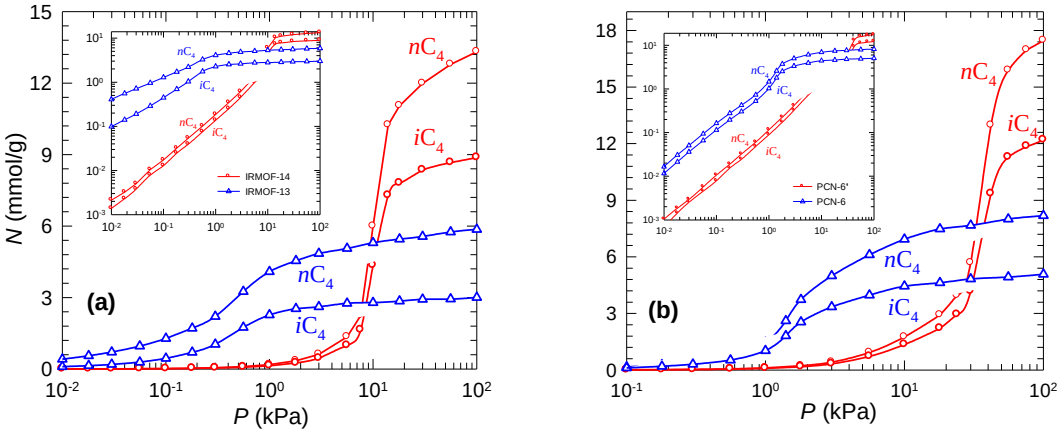

Figure 8.2. Adsorption isotherms of nC$_4$/iC$_4$ mixture in (a) IRMOF-14 and IRMOF-13, and (b) PCN-6′ and PCN-6. The insets are in the log-log scale for the clarity of isotherm inflection. The circles are in IRMOF-14 and PCN-6′; the triangles are in IRMOF-13 and PCN-6.

As shown in the inset, interestingly, the isotherm exhibits an inflection for both isomers. Note that the inflection may result in step-like adsorption, as observed in earlier study for alkanes in IRMOF-1 [212]. The adsorption of nC$_4$ and iC$_4$ starts to increase at almost the same pressure, remarkably different from the adsorption behavior in MFI zeolite. In the latter, iC$_4$ adsorption reaches a maximum and then decreases due to the small pore size of MFI and the strong repulsive interaction between adsorbates, whereas nC$_4$ adsorption increases with increasing pressure until saturation and replaces iC$_4$ [415,416]. Such a trend is not observed here because the pore sizes of the four MOFs are sufficiently larger compared with the critical diameters of C$_4$ isomers, which enables both linear and branched C$_4$ isomers to coexist even at high pressures.

Comparing IRMOF-13 and IRMOF-14, the extent of adsorption for both nC$_4$ and iC$_4$ in IRMOF-13 is greater at low pressures and the reverse is observed at high pressures. This is due to the presence of constricted pores in IRMOF-13 with

catenated framework. Consequently, adsorbate experiences a stronger potential overlap in IRMOF-13 than in IRMOF-14, leading to a greater adsorption at low pressures. With increasing pressure, however, it becomes difficult to accommodate adsorbate molecules in IRMOF-13 due to its smaller pore volume, particularly upon saturation. Similar behavior is observed in the adsorption of C_4 isomers in PCN-6 and PCN-6′. Thus, adsorption capacity at low pressures is higher in catenated MOFs than in the noncatenated counterparts, while the opposite is observed at high pressures.

To identify the favorable adsorption sites in the framework, Figure 8.3 shows the density contours of *n*C_4 in IRMOF-14 at 1, 10, and 100 kPa. The contours were generated on the basis of the locations of the centers-of-mass of *n*C_4 molecules during simulation. At a low pressure (1 kPa), adsorption occurs preferentially close to the metal-oxide clusters. This resembles the adsorption of small gases in IRMOF-1 verified both experimentally and theoretically [206]. The regions surrounding metal-oxide clusters are small and get saturated quickly; consequently, when pressure increases to 10 kPa, adsorption starts to occur near the organic linkers. At a high pressure (100 kPa), adsorbates are further adsorbed into the open pores. Such sequential adsorption at multiple sites leads to the isotherm inflection observed in Figure 8.2. The contours of *i*C_4 are similar; however, its density value at a given pressure is lower than *n*C_4. Figure 8.4 shows the density contours for *n*C_4 in IRMOF-13. Due to framework catenation, the preferential adsorption sites in IRMOF-13 are the narrow pores constricted between pyrene rings. This is remarkably different from IRMOF-14, in which the metal-oxides have the strongest binding affinity. With increasing pressure, the constricted pores are progressively filled by adsorbates and start to enter the larger pore space.

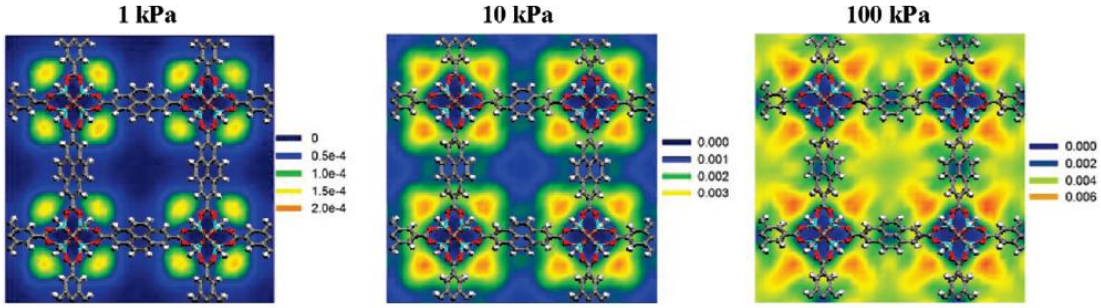

Figure 8.3. Density contours of *n*C_4 isomer in IRMOF-14 at 1, 10, and 100 kPa.

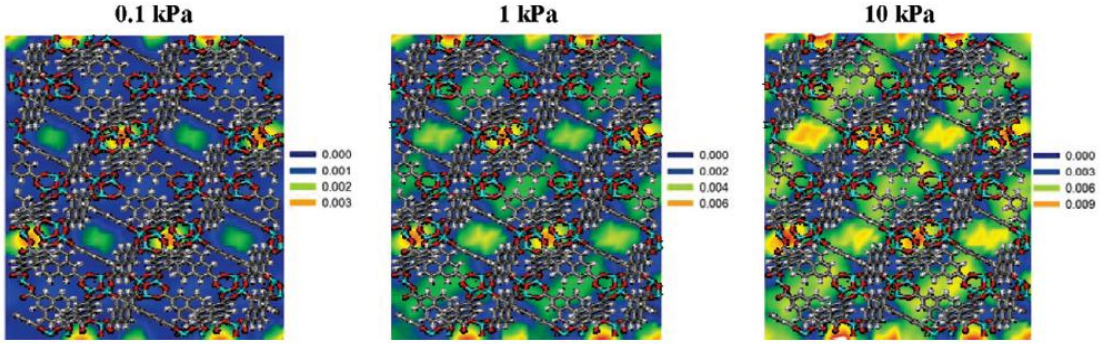

Figure 8.4. Density contours of *n*C_4 isomer in IRMOF-13 at 0.1, 1, and 10 kPa, respectively.

Figure 8.5 shows the density contours of *n*C_4 in PCN-6′ at 10, 50, and 100 kPa. Similar to the observation in our recent work for the adsorption of CO_2 and CH_4 in Cu-BTC and PCN-6′ [381], at a low pressure (10 kPa) adsorbates are preferentially adsorbed inside the octahedral pockets. The pockets are formed by four 4,4′,4′′-s-triazine-2,4,6-triyl-tribenzenes. With increasing pressure to 50 kPa, the pockets get saturated and adsorbates enter the windows connecting the pockets. At a high pressure (100 kPa), adsorption further occurs near the exposed metal-sites and organic linkers, and finally in the open pores. This clearly indicates the presence of different adsorption sites in PCN-6′. The linear and branched C_4 isomers have similar locations but the latter has a lower density. Figure 8.6 shows the density contours of *n*C_4 in PCN-6 at 0.1, 1, and 10 kPa. Similar to the case in PCN-6′, adsorption first occurs in

the octahedral pockets at a low pressure. With increasing pressure, the constricted triangular pores due to catenation are gradually occupied.

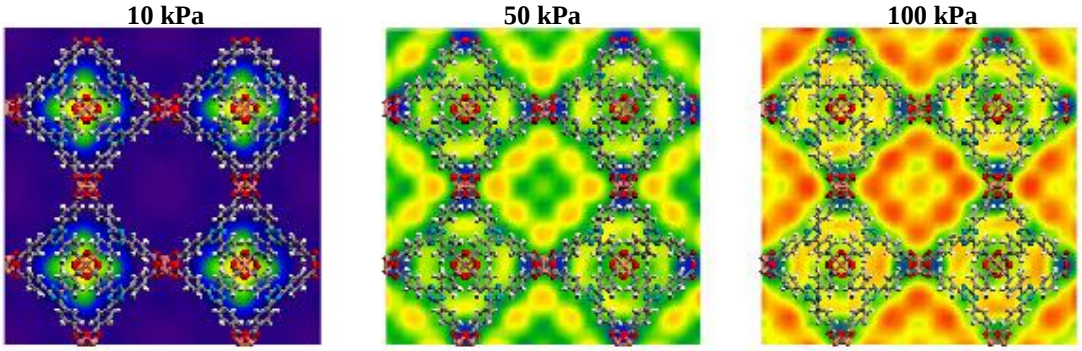

Figure 8.5. Density contours of nC$_4$ in PCN-6' at 10, 50, and 100 kPa. Brighter color indicates a higher density.

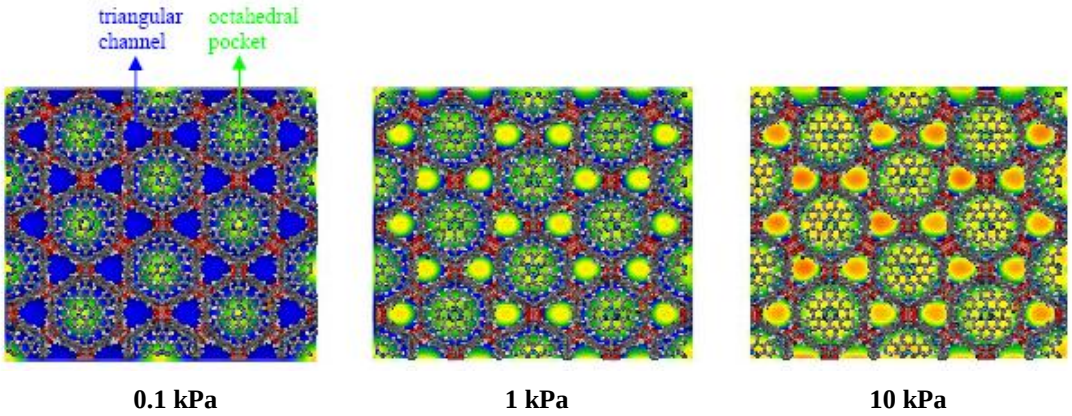

Figure 8.6. Density contours of nC$_4$ in PCN-6 at 0.1, 1, and 10 kPa. Brighter color indicates a higher density.

Figure 8.7 shows the adsorption isotherms of equimolar nC$_5$/iC$_5$/neoC$_5$ mixture in IRMOF-13, IRMOF-14, PCN-6 and PCN-6′. The behavior of the ternary mixture of C$_5$ isomers resembles that of nC$_4$/iC$_4$ mixture described earlier. At low pressures, the linear and branched C$_5$ exhibit similar amount of adsorption. With increasing pressure, adsorption of each isomer increases, whereas nC$_5$ increases the most greatly with the highest saturation capacity. At a given pressure, the loading decreases with increased degree of branching due to the configurational entropy effect. Adsorption of both linear and branched C$_5$ is higher in IRMOF-13 and PCN-6 than in IRMOF-14 and

PCN-6′ at low pressures but lower at high pressures. This is a consequence of the presence of narrower pores in catenated IRMOF-13 and PCN-6, and the availability of larger pore volumes to accommodate more adsorbates at high pressures in the noncatenated counterparts. PCN-6′ and PCN-6 show higher saturation capacity than IRMOF-14 and IRMOF-13 because of the larger surface areas and higher free volumes.

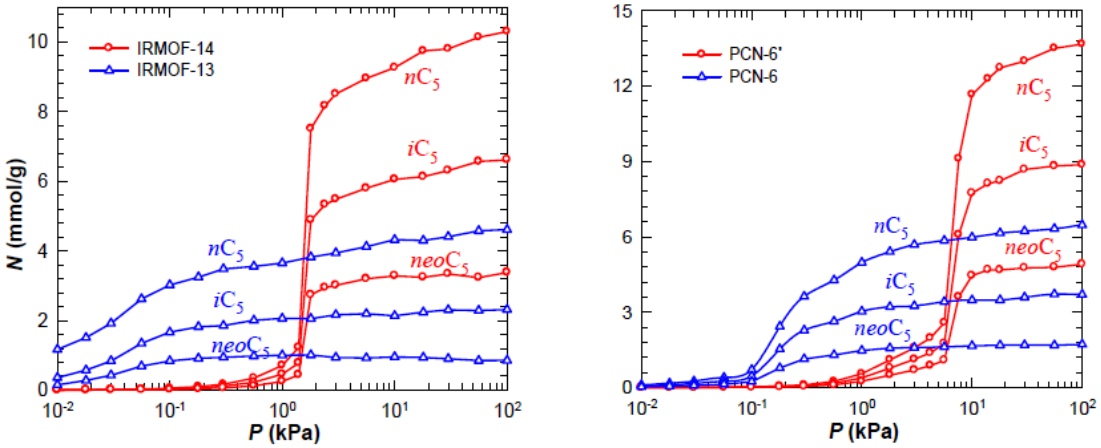

Figure 8.7. Adsorption isotherms of nC$_5$/iC$_5$/neoC$_5$ mixture in IRMOF-14, IRMOF-13, PCN-6' and PCN-6. The circles are in IRMOF-14 and PCN-6'; the triangles are in IRMOF-13 and PCN-6.

8.4.2 Adsorption Selectivity

In separation processes, the most important factor is selectivity among different components. Figure 8.8 shows the adsorption selectivity of nC$_4$ over iC$_4$, nC$_5$ and iC$_5$ over neoC$_5$ as a function of pressure. Due to the large pores existing in the four MOFs, the linear and branched isomers can coexist even at high pressures; therefore, the selectivity is not very high.

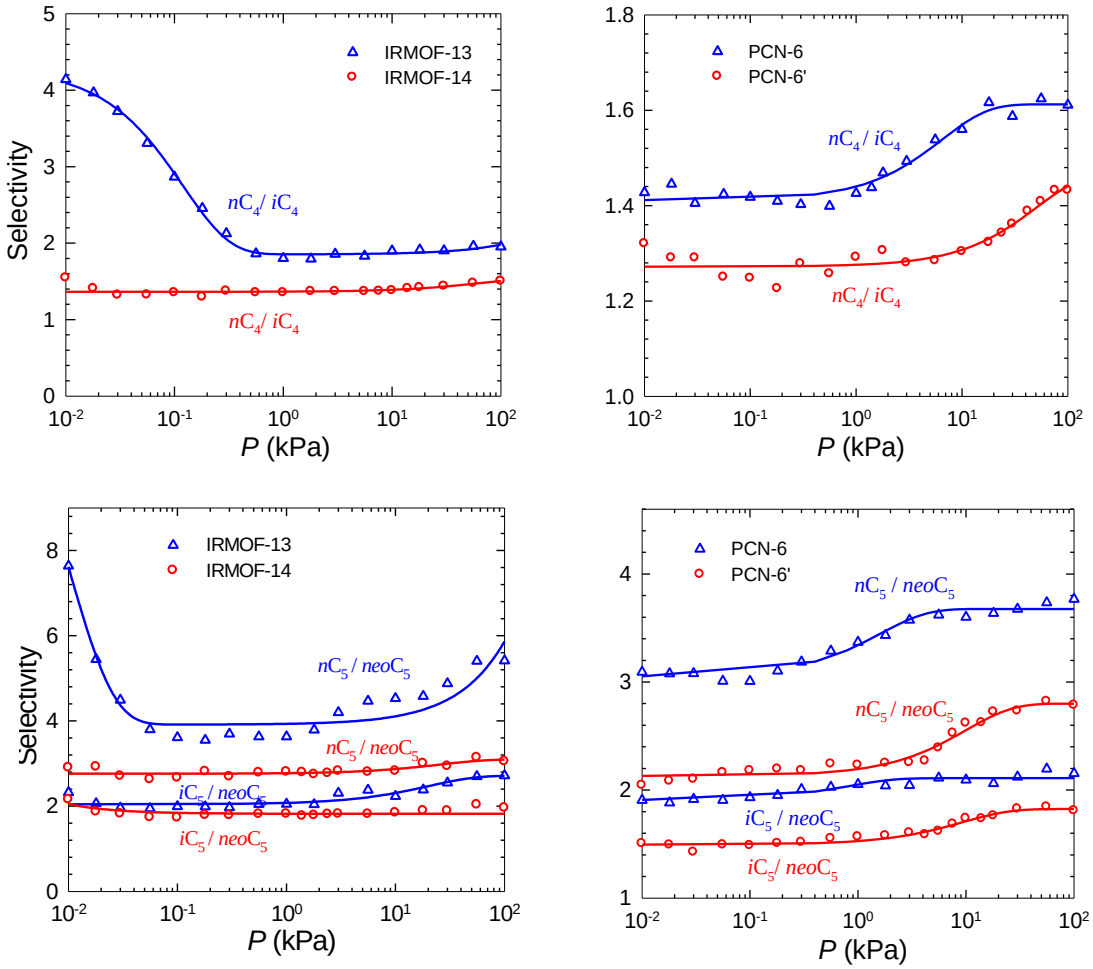

Figure 8.8. Selectivity of nC_4/iC_4 and $nC_5/iC_5/neoC_5$ mixtures in IRMOF-14, IRMOF-13, PCN-6' and PCN-6. The circles are in IRMOF-14 and PCN-6'; the triangles are in IRMOF-13 and PCN-6. The lines are the best fits to the simulation results.

In IRMOF-13 and PCN-6 with constricted pores, the selectivity for both C_4 and C_5 isomer mixtures is generally higher than in the noncatenated counterparts. This implies that adsorptive separation in MOFs could be improved by adjusting the pore size via framework catenation. The selectivity of nC_4/iC_4 in IRMOF-13 decreases as a function of pressure and reaches almost a constant at high pressures; however, it increases slightly in IRMOF-14, PCN-6 and PCN-6′. The decrease of selectivity in IRMOF-13 is due to the reduced interaction between nC_4 and framework upon increasing pressure. The relatively constant selectivity observed in other MOFs is attributed to the large pore size present and consequently the interaction is not

significantly affected over the pressure range under study. PCN-6 has a higher saturation loading for C_4 isomers than IRMOF-13; however, the selectivity is lower in PCN-6 especially at low pressures. The higher saturation loading in PCN-6 is simply because of the larger pore volume and surface area, whereas the lower selectivity is due to the existence of pores in PCN-6 with size range not well suited for the separation of C_4 isomers as compared with IRMOF-13.

Similarly, the selectivity of nC$_5$ or iC$_5$ with respect to *neo*C$_5$ is higher in catenated MOFs than in the noncatenated counterparts. Interestingly, selectivity of nC$_5$/*neo*C$_5$ in IRMOF-13 shows a different trend compared with that of nC$_4$/iC$_4$. The selectivity initially decreases at low pressures, reaches a constant at intermediate pressures, and finally increases with pressure. The initial decrease is similar to the reason mentioned earlier for C_4 isomers in IRMOF-13. The increase at high pressures is because only nC$_5$ continues to be adsorbed beyond a specific pressure (~ 1 kPa), whereas *neo*C$_5$ is depleted to some extent (see Figure 8.7). Again, this is due to the configurational entropy effect, in which the branched isomer is too bulky to intercalate into already packed pores. Nevertheless, the selectivity of nC$_5$/*neo*C$_5$ in IRMOF-14 is nearly a constant. This is because at low pressures the adsorption of both linear and branched C_5 isomers is low and almost the same. With increasing pressure, the degree of increase in adsorption is also similar for both isomers, though nC$_5$ isomer shows a higher capacity due to the configurational entropy. The selectivity of iC$_5$/*neo*C$_5$ in both IRMOF-13 and IRMOF-14 is approximately equal to 2; nevertheless, the selectivity in IRMOF-13 is slightly larger due to catenation effect. Compared with that in IRMOF-13, the selectivity of nC$_5$/*neo*C$_5$ in PCN-6 is different, in which the selectivity remains as constant at low pressures and increases slightly with pressure. The increase at high pressures is similar to the observation in IRMOF-13 and such

behavior also exists in PCN-6′. In PCN-6 and PCN-6′, the selectivity of iC$_5$/neoC$_5$ is about 1.5 ~ 2 over the entire range of pressure. The adsorption capacity of C$_5$ isomer mixtures in MOFs is greater than that in carbon nanotube bundle [400] and silicalite [398,417]; however, the adsorption selectivity is comparable in these different types of materials.

8.4.3 Diffusion

To investigate the intra-crystalline diffusion in noncatenated and catenated MOFs, the diffusivities of isomer mixtures in the four MOFs were calculated from MD simulations. Figure 8.9 and 8.10 show the mean-squared displacements (MSDs) for nC$_4$/iC$_4$ mixture in PCN-6′ and PCN-6, respectively. In the log-log scale, MSD increases linearly with time t after 200 ps. That is, MSD is proportional to t^{α} with $\alpha \approx 1$. This reveals that the MD simulations used were sufficiently long for the sorbate molecules to reach normal diffusion. The diffusivities were estimated in the time range from 200 to 1000 ps by Einstein equation.

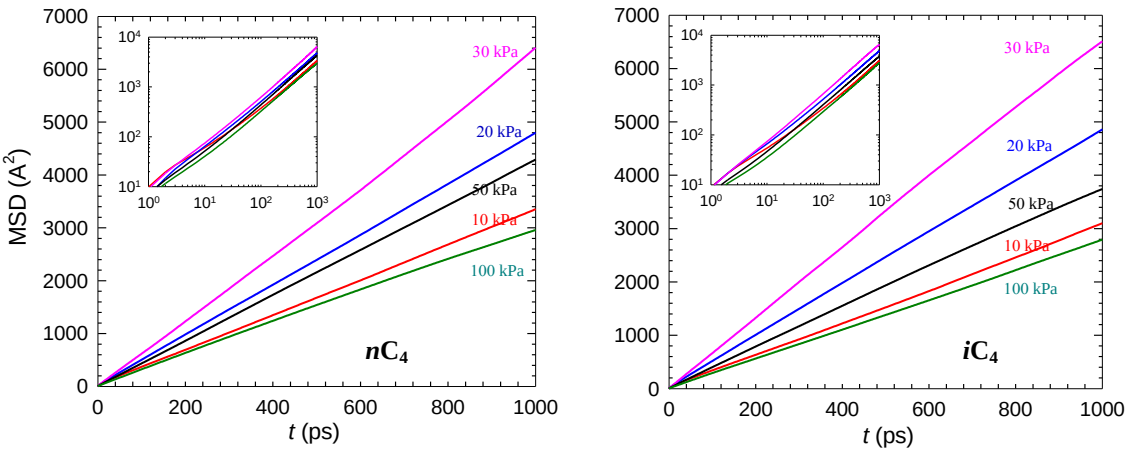

Figure 8.9. Mean-squared displacements of nC$_4$/iC$_4$ mixture in PCN-6'. The insets are log-log plot.

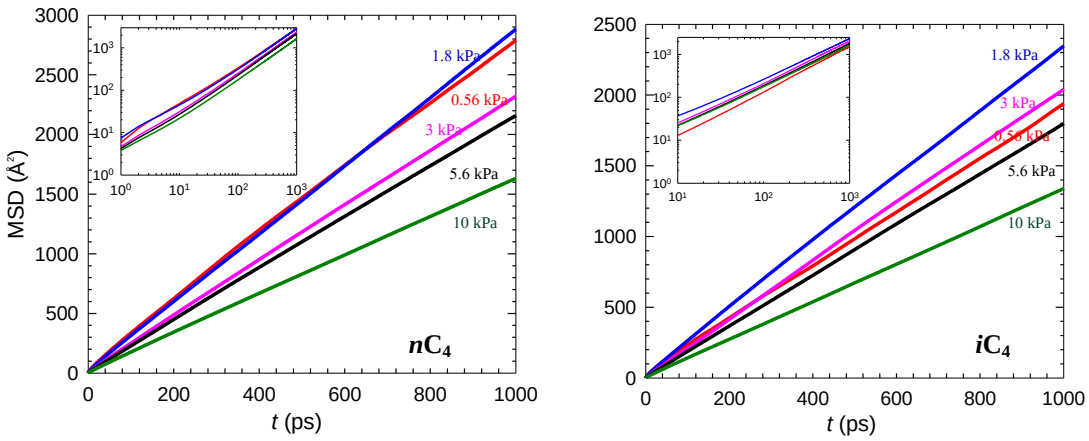

Figure 8.10 Mean-squared displacements of nC_4/iC_4 mixtures in PCN-6. The insets are log-log plot.

Figure 8.11 shows the diffusivities of C_4 isomers in IRMOF-14 and IRMOF-13. They decrease monotonically as a function of pressure. This behavior is commonly observed and attributed to the increasingly important steric effect with loading, which retards diffusion.

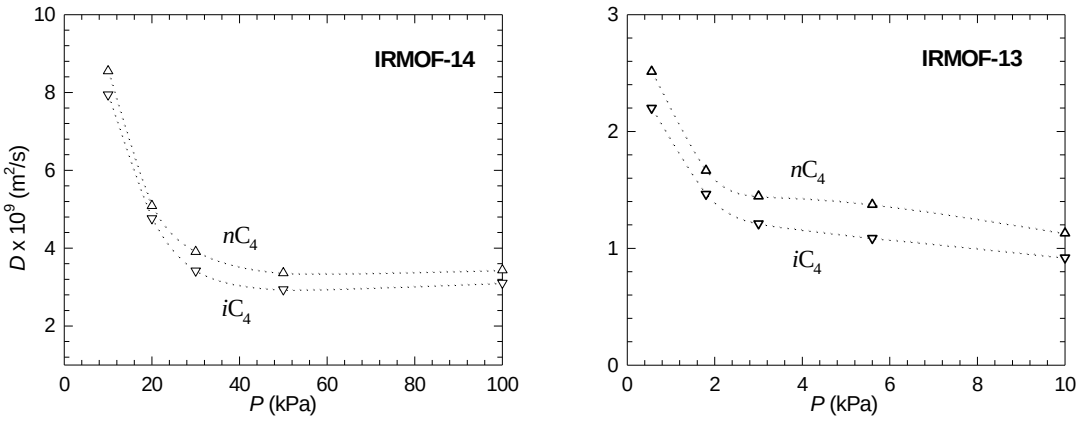

Figure 8.11. Diffusivities of nC_4/iC_4 mixture in IRMOF-14 and IRMOF-13. The dotted lines are for visual clarity.

Interestingly, the diffusivities of C_4 isomers in PCN-6′ and PCN-6 do not behave in such a way. As shown in Figure 8.12, the diffusivities initially increase, reach a maximum, and finally decrease with pressure. This type of behavior has been recently observed for the diffusion of C_4 and C_5 alkanes in Cu-BTC [218], also in the cage-type zeolites with narrow windows such as LTA, CHA, DDR and ERI [323]. The

initial increase can be interpreted in terms of a reduction in the free energy barrier for inter-cage hopping. More specifically, at a low pressure, adsorbates in PCN-6′ are preferentially located inside the octahedral pocket as illustrated in Figure 8.5. The pocket has a limited space and hence the diffusion is largely prohibited. As pressure increases, however, adsorbates populate near the open metal-sites and further in the large open pores; consequently, diffusivity increases till a maximum. With further increasing pressure, the diffusivities decrease simply due to steric hindrance.

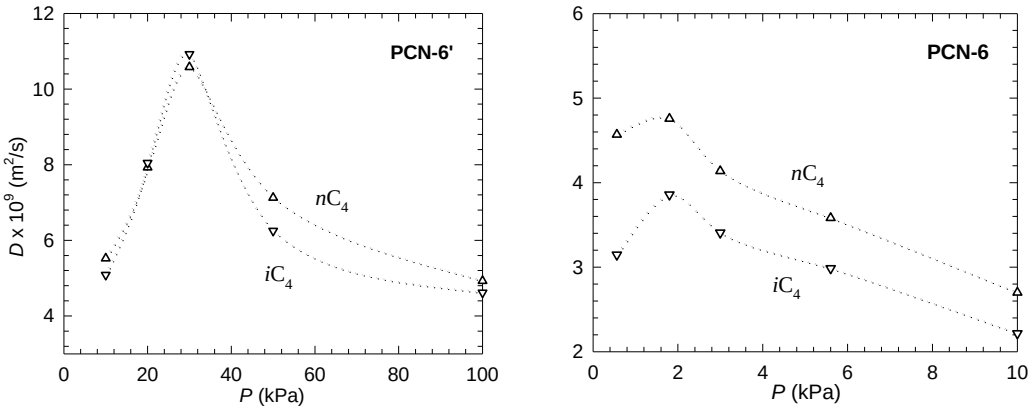

Figure 8.12 Diffusivities of nC$_4$/iC$_4$ mixture in PCN-6' and PCN-6. The dotted lines are for visual clarity.

The diffusivities of nC$_4$ and iC$_4$ in PCN-6 also initially increase and then decrease with increasing pressure. Similar to PCN-6′, at a low pressure adsorbates are located in the octahedral pockets; therefore, diffusivity is small in the limited space. With increasing pressure, nC$_4$ and iC$_4$ can diffuse from the pockets to the triangular pores and hence the diffusivity increases. Nevertheless, the increase in PCN-6 is not so sharp as in PCN-6′ due to the framework catenation in PCN-6, which leads to a higher free energy barrier for hopping. In addition, as expected the diffusivity magnitude in PCN-6 is smaller than in PCN-6′. Comparing nC$_4$ and iC$_4$ isomers, in general nC$_4$ diffuses faster than iC$_4$ in both structures. This is because nC$_4$ has a slender shape and can more easily diffuse through narrow regions than iC$_4$. Interestingly, the diffusivity difference between the two isomers in PCN-6 is larger than in PCN-6′, particularly at

low pressures. In other words, diffusion selectivity is enhanced by catenation, which has not been reported before in the literature.

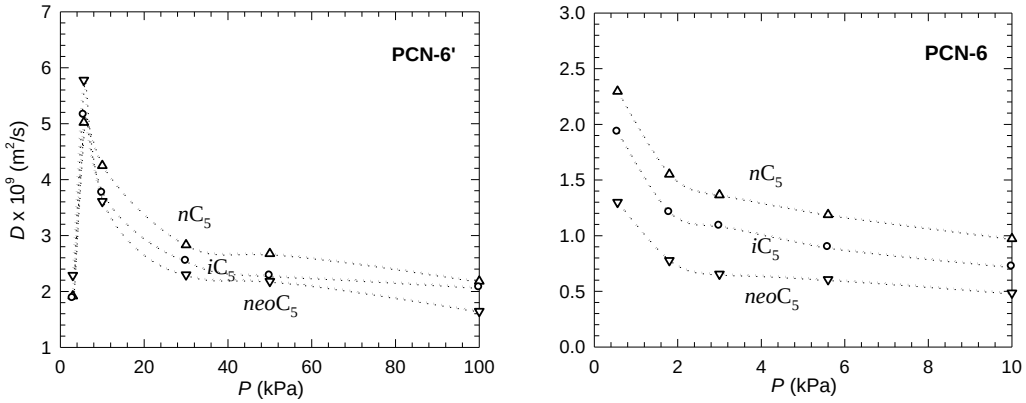

Figure 8.13. Diffusivities of nC$_5$/iC$_5$/*neo*C$_5$ mixture in PCN-6' and PCN-6. The dotted lines are for visual clarity.

Figure 8.13 shows the diffusivities of C_5 isomer mixture in PCN-6′ and PCN-6 as a function of pressure. In PCN-6′, the diffusion characteristics of C_5 isomers resemble that of C_4 isomers, even though the diffusivity values of the former are smaller. Except at very low pressures in PCN-6′, the diffusivities follow the order of nC$_5$ > iC$_5$ > *neo*C$_5$, consistent with the increased degree of branching. That is, a more slender isomer diffuses faster than a bulky one. In PCN-6, the diffusivities drop monotonically with increasing pressure, in contrast to C_4 isomers. While C_4 isomers can diffuse relatively easily in narrow triangular channels of PCN-6, diffusion of C_5 isomers is retarded because of their bulky sizes and also their stronger interactions with the framework compared with the case of C_4 isomers. Consequently, C_5 isomers show a decrease in diffusivity as a function of pressure. The diffusion characteristics of C_5 isomer mixture in PCN-6 are similar to those observed for nC$_6$/iC$_6$ mixture in MFI [399], CH_4/CO_2 mixture in silicalite [234,323], and C_1/C_2, C_1/C_3, C_1/nC$_4$ mixtures in carbon nanotubes [339], where diffusivities also decrease monotonically due to steric hindrance. In general, the diffusivities of C_4 or C_5 isomers in PCN-6 are

smaller than in PCN-6′. However, the diffusion selectivity among isomers is larger in catenated PCN-6.

In separation processes, the efficacy is characterized by permselectivity, which depends on adsorption selectivity – an equilibrium property, and diffusion selectivity – a dynamic property. As shown in Figure 8.8, a linear isomer has a stronger adsorption over a branched isomer. Figures 8.11, 8.12 and 8.13 further demonstrate that a linear isomer diffuses faster. Combining these two factors, a linear isomer has a larger permeability than its branched counterpart; and a mixture of isomers can be separated. Moreover, both adsorption and diffusion selectivities are found to be larger in catenated IRMOF-13 and PCN-6 than in noncatenated IRMOF-14 and PCN-6′. This suggests that framework catenation might be an appropriate way to enhance separation efficacy.

8.5 Summary

Adsorption and diffusion of alkane (C_4 and C_5) isomer mixtures in IRMOF-13, IRMOF-14, PCN-6 and PCN-6′ have been investigated using molecular simulations. The isotherms show a linear isomer has a larger loading than the branched one because the configurational entropy effect favors the packing of linear isomer. Due to catenation, IRMOF-13 and PCN-6 have a stronger adsorption for both linear and branched isomers at low pressures compared with noncatenated IRMOF-14 and PCN-6′. However, the reverse is observed at high pressures due to the smaller pore volume in catenated MOFs. The preferential adsorption sites in IRMOF-14 are near the metal-oxides, in contrast to the constricted pores in IRMOF-13. In PCN-6′, adsorption occurs first in the octahedral pockets, then near the metal-sites and organic linkers, and finally in the open pores. In PCN-6, adsorption first occurs in the octahedral

pockets and then in the constricted triangular pores. The sequential adsorption leads to inflection observed in the isotherms. IRMOF-13 exhibits the highest adsorption selectivity for C_4 and C_5 isomer mixtures in the four MOFs studied. Compared with carbon nanotube bundle and silicalite, MOFs exhibit greater adsorption capacity and comparable adsorption selectivity.

The diffusivities of alkane isomers in IRMOF-13, IRMOF-14, PCN-6 and PCN-6′ decrease in the order of nC$_4$ > iC$_4$ and nC$_5$ > iC$_5$ > neoC$_5$ because a slender molecule can diffuse faster than a bulky one. In IRMOF-14 and IRMOF-13, the diffusivities decrease with pressure simply due to the steric effect. Nevertheless, the diffusivities in PCN-6′ initially increase with pressure, pass a maximum and finally decrease. The reason is that at low pressures adsorbates in PCN-6′ are preferentially located in the octahedral pockets and thus the diffusion is largely prohibited. As pressure increases, however, adsorbates start to reside near the metal-sites and in the center pores; consequently, the diffusivities increase in the relatively large open space. Finally, the decrease is attributed to the steric hindrance at high pressures. While C_4 isomers exhibit similar trend of diffusivity in PCN-6 and PCN-6′, C_5 isomers in PCN-6 behave differently from that in PCN-6′ with monotonically decreasing diffusivity. This is primarily due to the steric effect of bulky C_5 isomers. The diffusivities in IRMOF-13 and PCN-6 are smaller than in IRMOF-14 and PCN-6′ because catenation leads to a higher free energy barrier for hopping. Remarkably, both adsorption and diffusion selectivities are enhanced in catenated IRMOF-13 and PCN-6, implying that separation efficacy can be improved by catenation.

Chapter 9

Drug in Mesoporous Metal-Organic Frameworks

9.1 Introduction

Combining targeted chemistry and computation, Ferey and co-workers developed a mesoporous metal-organic framework, MIL-101 (Materials of Institut Lavoisier) [418]. MIL-101 possesses several salient features such as zeotype architecture with mesoporous and microporous cages, a gaint cell volume, huge surface area and unsaturated chromium sites. MIL-101 is one of the most porous materials to date and many experimental studies have been reported in this material.

Thermal behaviour of MIL-101 reveals that MIL-101 is stable up to 275 ºC and also stable under air and in various organic solvents when treated at elevated temperature. In contrast, MOFs like MOF-177 [35] and MOF-5 [3] easily decompose in the presence of moisture and organic solvent. Because of the considerable interest in MOFs for gas storage, MIL-101 was tested for storing various gases. A record high uptake was determined for CO_2 in MIL-101, which was up to 40 mmol/g at 303 K and 50 bar [127]. Surprisingly, MIL-101 also shows very high uptakes for H_2 at cryogenic temperatures and for organic vapors such as benzene and *n*-hexane [419,420]. Chowdhury et al. [128] reported the adsorption properties of CO_2 and CH_4 along with C_3H_8, SF_6, and Ar in MIL-101 using a standard gravimetric method. Surface functionalization of dehydrated MIL-101 with ethylene-diamine were also reported [158]. Interestingly, MIL-101 allows the introduction of large inorganic species and drugs in the mesoporous cages. For example, MIL-101 incorporated Keggin polyanion in the larger cage and it was confirmed that each cage accepts five

Keggin ions, representing 50% of the volume of the cage [418]. MIL-101 has also been tested for the delivery of ibuprofen (abbr. IBU), an analgesic and anti-inflammatory drug. MIL-101 exhibited a remarkably high dosage capacity of IBU, up to 1.38 g/g MIL-101. This result indicated that each medium and large cage of MIL-101 hosts approximately 56 and 92 IBU molecules, which represent four times the capacity of MCM-41 toward IBU [104,106]. The sorption and *in vitro* delivery of IBU were also examined in MIL-53, and the loading was about 0.22 g IBU/g MIL-53 and independent of metal type (Cr, Fe) [105].

Despite many experimental studies in MIL-101, no theoretical study is reported yet to understand the behavior of drug at a microscopic level in mesoporous MIL-101. Currently, the fundamental mechanisms of drug delivery in MOFs remain elusive. For instance, how would a drug interact with the host structure? Between metal oxide and organic linker, which plays a dominant role in drug adsorption and release? Why is there different behavior for a drug release in various MOFs? To address these important questions for drug delivery, in this work a computational study on the energetics and dynamics of IBU in two host carriers, MIL-101 and UMCM-1 were reported, where UMCM-1, a mesoporous material without unsaturated metal centers is chosen for comparison.

The models of IBU, MIL-101 and UMCM-1 are briefly described in Section 9.2. The simulation methods are introduced in Section 9.3. More specifically, configurational-bias MC and MD simulations were employed to calculate the loading and mobility of IBU in MOFs. The favorable conformations of IBU were identified using simulated annealing technique and followed by first-principle density functional theory calculations. In Section 9.4, the loading capacity, lowest-energy conformation, binding energy and diffusion of IBU are reported. In addition, the highest-occupied

molecular orbital (HOMO) and band gap are presented to identify the possible bond formation between IBU and MOF cluster. Finally, the concluding remarks are summarized in Section 9.5.

9.2 Models

IBU was chosen as a model drug because it is a worldwide used pharmaceutical compound with analgesic and antipyretic features [421]. It was first launched in late 1960's for the treatment of rheumatoid arthritis. Nowadays, it has become a core non-steroidal anti-inflammatory drug and is commonly used for relief of arthritis, dysmenorrhea, acne and fever. IBU exists with two enantiomers, in which (S)-IBU is active both *in vitro* and *in vivo*; consequently, (S)-IBU is considered in this study.

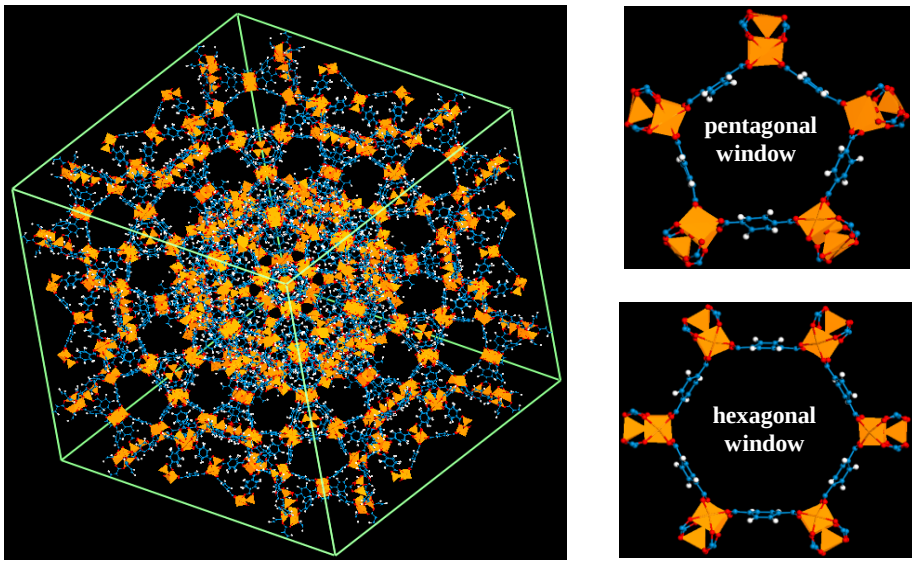

Figure 9.1. Unit cell of MIL-101 constructed from experimental crystallographic data [418]. The pentagonal and hexagonal windows are enlarged for clarity. Color code: Cr, orange polyhedra; C, blue; O, red; H, white.

Figure 9.1 shows the unit cell of MIL-101 constructed from experimental crystallographic data [418]. The pentagonal and hexagonal windows in the cages are enlarged for clarity. MIL-101 is assembled by computationally designed hybrid

supertetrahedra consisting of Cr_3O trimers and 1,4-benzenedicarboxylic acids. Two types of mesoporous quasi-spherical cages exist in MIL-101. The smaller one has 20 supertetrahedra and a free diameter of 29 Å accessible through a pentagonal windows with 12 Å aperture, while the larger one has 28 supertetrahedra and a free diameter of 34 Å accessible through both hexagonal and pentagonal windows with 14.7 × 16 Å aperture. Unsaturated Lewis acidic Cr sites are formed by removing terminal waters in octahedral Cr_3O trimers. The cell volume of MIL-101 is very huge (~ 702,000 $Å^3$) with a porosity of 0.833, one of the most porous materials to date.

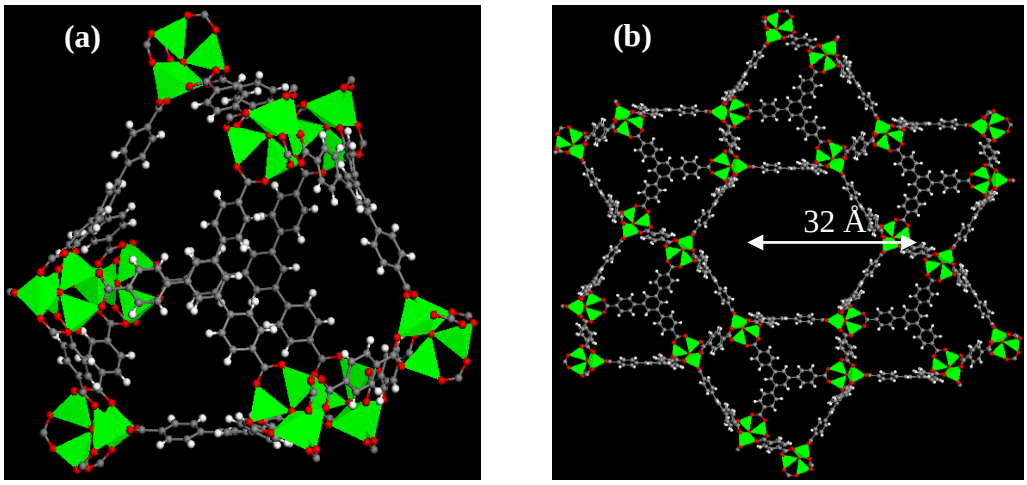

Figure 9.2. (a) A microporous cage in UMCM-1 constructed from six BDC linkers, five BTB linkers, and nine Zn_4O clusters. (b) Supercell of UMCM-1 viewed along the c axis showing the one-dimensional mesopore. Color code: Zn, green polyhedra; C, ash; O, red; H, white.

UMCM-1 contains two organic linkers of different topologies, namely, terephthalic acid (H_2BDC) and 1,3,5-tris(4-carboxyphenyl)benzene (H_3BTB) [38]. The structure differs dramatically from those based on pure linkers. The metal clusters ZnO_4 in UMCM-1 are connected with two BDC and four BTB linkers. The octahedral geometry of UMCM-1 leads to two types of pore, one is micropore with a dimension of 14 × 17 Å and the other is mesopore with a 1D hexagonal channel of 27 × 32 Å.

The microporous cage and one-dimensional mesoporous channel in UMCM-1 are shown in Figure 9.2. Unlike MIL-101, no exposed metal sites exist in UMCM-1.

The interactions of IBU with MIL-101 and UMCM-1 in MC and MD simulations were modeled using Lennard-Jones (LJ) and Coulombic potentials. The LJ parameters were adopted from the Universal Force Field (UFF) [174]. The Lorentz-Berthelot combining rules were used to calculate the cross LJ interaction parameters. For the Coulombic interactions, the atomic charges of IBU, MIL-101 and UMCM-1 were calculated from density-functional theory (DFT) using the similar approach as discussed earlier. The fragmental clusters of MIL-101 and UMCM-1 used in the DFT calculations are shown in Figure 9.3. The cleaved bonds (indicated by circles) were terminated by methyl groups to maintain the original hybridization.

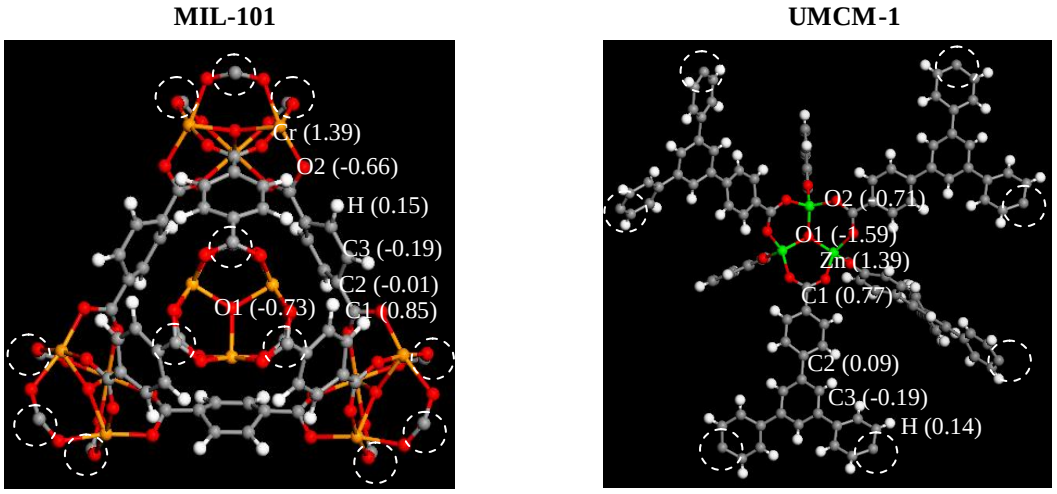

Figure 9.3. Atomic charges in the fragmental clusters of MIL-101 and UMCM-1 calculated from density-functional theory. The cleaved bonds (indicated by circles) were terminated by methyl groups to maintain the original hybridization.

To characterize MIL-101 and UMCM-1, their pore volumes and surface areas were estimated from MC methods. Specifically, a single helium atom was attempted to insert into the host structure and the integration of energetic Boltzmann contribution gave free volume [303]. The surface area was calculated by rolling over a

probe along adsorbent surface [422]. The probe had a diameter of 3.68 Å, corresponding to a nitrogen molecule.

9.3 Methodology

The maximum loadings of IBU in MIL-101 and UMCM-1 were determined by the configurational-bias GCMC simulations at 298 K. Conventional Metropolis technique in MC simulation is prohibitively expensive in sampling the phase space of big molecules. In configurational-bias algorithm, molecule is grown atom-by-atom biasing energetically favorable configurations while avoiding overlap with other atoms [410-412]. The simulation box contained one unit cell for MIL-101 and two $(1\times1\times2)$ unit cells for UMCM-1, and the periodic boundary conditions were exerted in all three dimensions.

To examine the mobility of IBU in MIL-101 and UMCM-1, MD simulations were conducted in canonical ensemble at 298 K. The frameworks of MIL-101 and UMCM-1 were considered to be flexible. It has been demonstrated that the diffusion of big molecules could be substantially influenced by framework flexibility. For instance, diffusion in zeolites is usually accelerated in a flexible model due to the increased possible pathways for molecular jump [307]. Nevertheless, the diffusion of benzene in IRMOF-1 was found to be considerably slower in a flexible framework compared to rigid one, and attributed to the correlation motion of benzene with organic linker [225]. The temperature in MD simulations was maintained by Nosé-Hoover thermostat and the velocity-verlet algorithm was used to integrate the equations of motion. The time step was 1 fs and the total simulation time was 250 ps. The total energy was monitored during simulation to ensure proper energy convergence.

Simulated annealing and steepest descent algorithm were used to identify the favorable conformations of IBU in MIL-101 and UMCM-1. Temperature was gradually reduced from 500 K to 50 K. At a high temperature, IBU molecule was capable of probing most configurational positions. With decreasing temperature, IBU molecule tended to reside in positions with lower energy. A handful of energy minima were found on the energy landscape due to the presence of multiple binding sites in the host structure. Thereafter, the lowest-energy conformation was selected and further optimized using DFT. Small cleaved clusters of MIL-101 and UMCM-1 were used in the optimization, which contained one metal oxide with the dangling bonds saturated by hydrogen atoms. The binding energies of IBU with clusters were estimated as the energy difference between adduct (IBU and cluster) and its constituents.

9.4 Results and Discussion

9.4.1 Maximum Loading and Lowest Energy Conformation

Microscopic behavior of drug in a host matrix is largely governed by the intrinsic host structure. From our calculations, MIL-101 has a free volume 1.96 cm^3/g and a surface area 3451 m^2/g, close to experimentally measured 1.74 cm^3/g and 3780 m^2/g [127]. UMCM-1 has a free volume 2.28 cm^3/g and a surface area 4764 m^2/g; the latter is in accord with experimental value 4730 m^2/g [38]. Based on these characteristics, UMCM-1 is apparently more porous than MIL-101. The maximum loading of IBU in MIL-101 is predicted to be 1.11 g IBU/g MIL-101, slightly lesser than the experimentally measured 1.37 [106]. The classical force field was used in this work and a better force field might improve the prediction. The loading in UMCM-1 is 1.36 g IBU/g UMCM-1, however, no experimental result is available for comparison.

Overall, MIL-101 and UMCM-1 exhibit four times greater of IBU loading than mesoporous silica MCM-41 [104]. A crucial factor in drug delivery is the desired loading, the substantially high loadings in MIL-101 and UMCM-1 suggest that they might be useful for drug delivery as very small amount of carrier is need for high dosage.

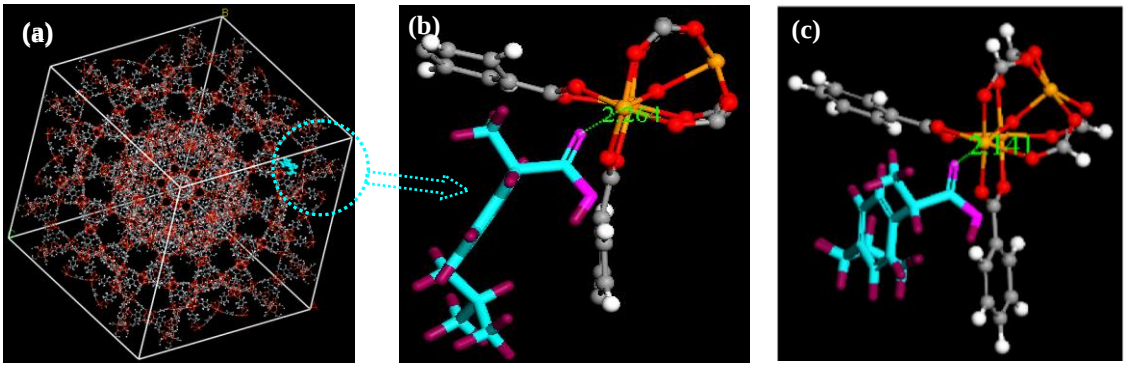

Figure 9.4. (a) Lowest-energy conformation of IBU in MIL-101 from simulated annealing (b) Enlarged view for the location of IBU near the Cr_3O metal-oxide in MIL-101. (c) Optimized conformation of IBU near the Cr_3O metal-oxide in MIL-101. The distances are represented in angstroms. MIL-101: Cr, orange; C, grey; O, red; H, white. IBU: C, cyan; O, pink; H, purple.

From simulated annealing, the favorable conformations of IBU in host structure were identified. Figure 9.4a shows the lowest-energy conformation in a unit cell of MIL-101, which is enlarged in Figure 9.4b. Interestingly, the carboxylic group of IBU points toward the Cr atom of MIL-101 and the distance from the carboxylic O atom to the Cr atom is 2.261 Å. This remarkably supports the commonly recognized factor that metal oxides in MOFs are the preferential adsorption sites, which has been confirmed by numerous experimental and simulations studies for gas adsorption in various MOFs [206]. The conformation in Figure 9.4b was further optimized using DFT and the binding energy was subsequently estimated between IBU and MIL-101 cluster. After DFT optimization, the distance between the carboxylic O atom of IBU and the Cr atom is 2.141 Å as shown in Figure 9.4c, slightly decreased from 2.261 Å

obtained using simulated annealing. The Cr-O distance is very close to experimentally determined 1.9 ~ 2.0 Å between Cr and terminal water [418]. This suggests that a coordination bond is formed between IBU and MIL-101, consistent with the broadening NMR signals of IBU observed in experiment [106]. Upon removal of terminal water, Cr site in MIL-101 possesses Lewis acidic character and forms a complex with IBU. The binding energy between IBU and MIL-101 is -73.17 kJ/mol, larger than -57 kJ/mol in MIL-53(Cr) [105] and close to those in natural zeolites [423]. It is expected that the surrounding region of the metal oxide will get saturated as loading increases. Subsequently adsorbed IBU will experience weaker interaction and reside a bit away from the metal oxide.

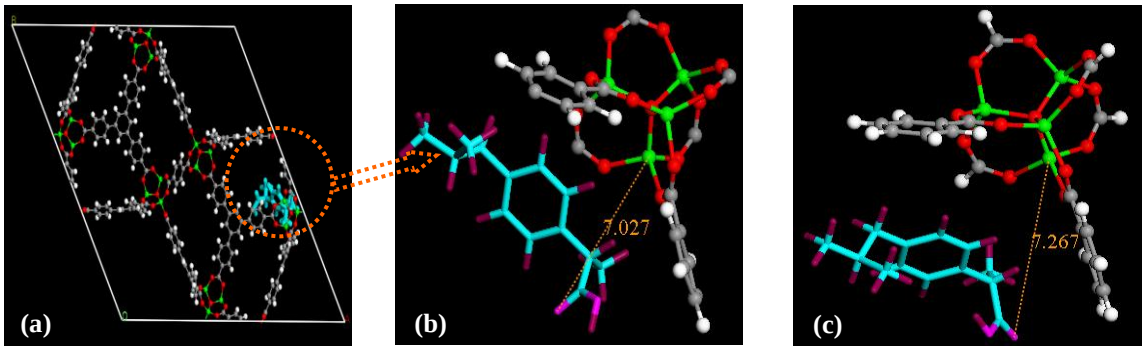

Figure 9.5. (a) Lowest-energy conformation of IBU in UMCM-1 from simulated annealing (b) Enlarged view for location of IBU near the metal oxide in UMCM-1. (c) Optimized conformation of IBU near the metal oxide in UMCM-1. The distances are represented in angstroms. Color codes: UCMC-1: Zn, green; C, grey; O, red; H, white; and Ibuprofen: C, cyan; O, pink; H, purple.

Figure 9.5 shows the lowest-energy conformation in UMCM-1 from simulated annealing and DFT optimization. Compared with the distance between IBU and Cr atom in MIL-101, the location of IBU in UMCM-1 is far away from the metal oxide. The distance from carboxyl O atom to Zn atom is 7.027 Å, which increases to 7.267 Å after DFT optimization. The binding energy of IBU in UMCM-1 is -34.97 kJ/mol,

only half of that in MIL-101. As will be confirmed below, no chemical bond is formed between IBU and UMCM-1. Most likely, weak disperse and π-π interactions exist between the aromatic linker of IBU and UMCM-1.

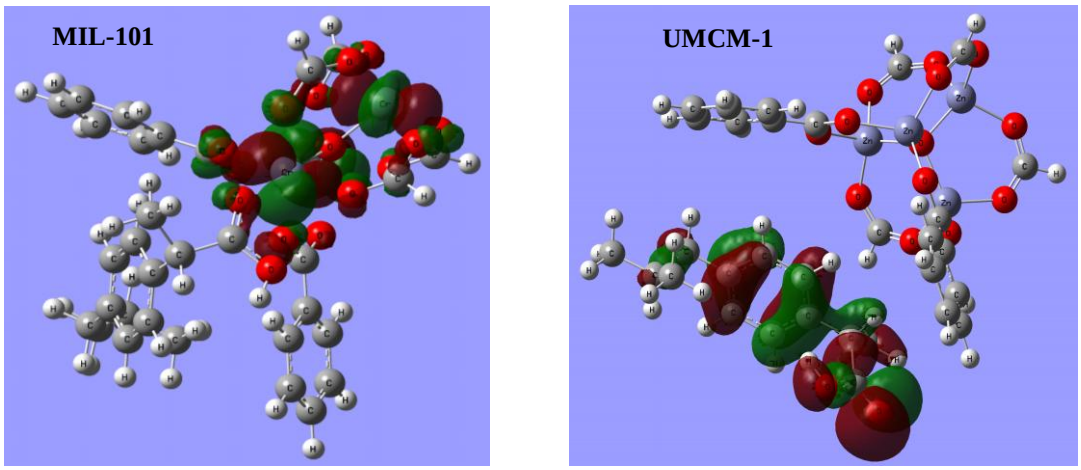

Figure 9.6. Highest-occupied molecular orbitals (HOMOs) in IBU/MIL-101 and IBU/UMCM-1 complexes. A coordination bond is formed between the carboxylic group in IBU and the Cr_3O metal oxide in MIL-101.

Figure 9.6 shows the highest-occupied molecular orbitals (HOMOs) in order to provide further information about the possible bond formation between IBU and host structure. The HOMOs are distinctly different in MIL-101 and UMCM-1. From the frontier HOMOs, a coordination bond is observed to form between the carboxylic group in IBU and the Cr_3O metal oxide in MIL-101. The band gap, which quantifies the excitability to form a chemical bond, is only 0.064 eV in IBU/MIL-101. However, the band gap in IBU/UMCM-1 is prohibitively large as of 3.146 eV. This suggests it is difficult for IBU and UMCM-1 to form a bond as there are no frontier HOMOs between IBU and UMCM-1.

Guest molecule confined in a nanoporous material behaves differently from that in bulk phase. Figure 9.7 shows the conformations of geometrically optimized IBU in vacuum, MIL-101 and UMCM-1, respectively. The spatial arrangement of IBU in

UMCM-1 is very similar to that in vacuum, demonstrating IBU structure is not discernibly perturbed in UMCM-1. Similar behavior was observed for IBU in MIL-53 [105]. However, a rearrangement of carboxyl of IBU is observed in MIL-101 as a consequence of the bond formation between IBU and MIL-101 and the small pore volume available in MIL-101.

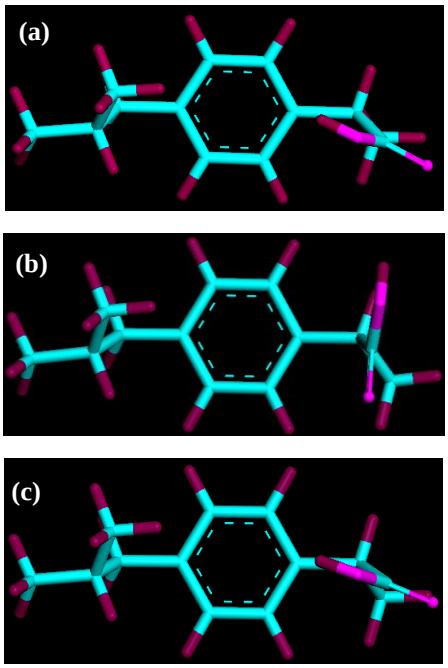

Figure 9.7. Optimized conformations of IBU in (a) vacuum (b) MIL-101 (c) UMCM-1. Color code: C, cyan; O, pink; H, purple.

9.4.2 Mobility of Ibuprofen

The mobility of IBU in host structure was quantified by the mean-squared displacement (MSD) of a single IBU molecule in MIL-101 and UMCM-1. As shown in Figure 9.8, MSD in MIL-101 is substantially smaller than in UCMC-1. This is attributed to the coordination bond formation between the electronegative carboxylic O of IBU and the Cr site of MIL-101, in addition to the small pore volume. These two factors strongly restrain the motion of IBU in MIL-101. A delayed release of IBU in MIL-101 was indeed observed by experiment [106]. However, a direct comparison is not possible because the drug release was experimentally conducted in a physiological

serum medium. From Figure 9.8, it is expected that the release of IBU would be relatively faster in UMCM-1. Using this fundamental information on the interactions between drug and framework, one can understand the release rate taking place in mesoporous materials from the microscopic level.

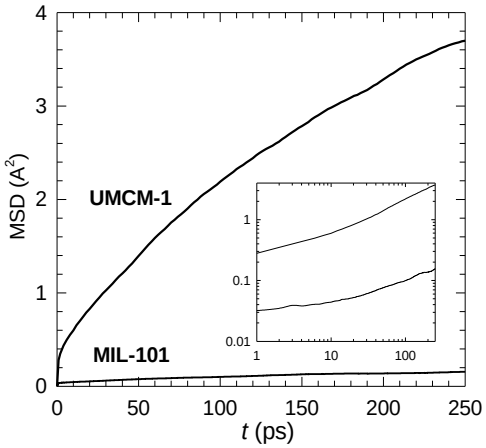

Figure 9.8. Mean-squared displacements of IBU in MIL-101 and UMCM-1. The inset is in the logarithmic scale.

9.5 Summary

The energetic and dynamic properties of IBU have been studied in mesoporous MIL-101 and UMCM-1 using molecular simulations and first-principles calculations. The loading of IBU in MIL-101 predicted matches well with experimental result and about four times greater than in MCM-41. Such a high loading suggests that only a very small amount of carrier is needed for drug dosage. Geometry optimization demonstrated that the lowest-energy conformation of IBU in MIL-101 is preferentially located in proximal to the metal-oxide. This is similar to that observed for gas sorption in various MOFs, which has been verified both theoretically and experimentally. The binding energy between IBU and MIL-101 is two times as that in UMCM-1 due to the strong coordination between the carboxylic O atom of IBU and

the exposed Cr atom of MIL-101. As a consequence, the spatial arrangement of IBU in MIL-101 is different from those in vacuum and UMCM-1; the mobility of IBU is smaller in MIL-101 than in UMCM-1. This work underscores the fact that molecular behavior of drug in porous materials plays a key role in drug loading and release. Thus, a clear molecular-level understanding is important for the development of novel drug delivery systems with better control of drug administration.

Chapter 10

Conclusions and Future Work

10.1 Conclusions

In this thesis, the underlying mechanisms of adsorption and diffusion in various MOFs have been studied using molecular simulations in conjunction with first-principle calculations. The main body of the thesis is summarized below.

In Chapter 4, the storage of pure CO_2 and CH_4 and separation of CO_2/CH_4 mixture were studied in three different nanoporous materials (silicalite, C_{168} schwarzite, and IRMOF-1). CH_4 was represented as a spherical Lennard-Jones molecule, and CO_2 as a rigid linear molecule with a quadrupole moment. The three nanoporous materials were modeled fully atomistically and considered as rigid. CO_2 was preferentially adsorbed than CH_4 in all the three adsorbents, except in C_{168} schwarzite at high pressures. The simulated adsorption isotherms and isosteric heats match closely with available experimental data. Compared to silicalite and C_{168} schwarzite, the adsorption capacities of pure CH_4 and CO_2 in IRMOF-1 are substantially larger. This implies that IRMOF-1 might be a potential storage medium for CH_4 and CO_2. For equimolar CO_2/CH_4 mixture, CO_2 is preferentially adsorbed in all the three adsorbents. Predictions of mixture adsorption with the ideal-adsorbed-solution theory based on pure component adsorption agree well with the simulation results. Though IRMOF-1 has a significantly higher adsorption capacity than silicalite and C_{168} schwarzite, the adsorption selectivity of CO_2 over CH_4 was found to be similar in all three adsorbents. The self-, corrected- and transport diffusivities of CO_2 and CH_4 were examined in these three materials. The activation energies at infinite dilution were evaluated from

the Arrhenius fits to the diffusivities at various temperatures. As loading increases, the self-diffusivities in the three frameworks decrease due to the steric hindrance; the corrected diffusivities remain nearly constant or decrease approximately linearly depending on adsorbate and framework; the transport diffusivities generally increase except for CO_2 in IRMOF-1. The correlation effects were identified to reduce from MFI, C_{168} to IRMOF-1, in accordance with increased porosity in the three frameworks. Predicted self-, corrected- and transport diffusivities for pure CO_2 and CH_4 from the Maxwell-Stefan formulation are consistent with the simulation results. In CO_2/CH_4 mixture, the self-diffusivities also decrease with loading, and good agreement is found between simulated and predicted results. Based on the adsorption and self-diffusivity in the mixture, the permselectivity was found to be marginal in IRMOF-1, slightly enhanced in MFI, and greatest in C_{168} schwarzite. Although IRMOF-1 has the largest storage capacity for CH_4 and CO_2, its selectivity is not satisfactory.

In Chapter 5, a series of MOFs and COFs with various metal centers, organic linkers, functional groups and framework topologies were investigated to assess the storage capacity of CO_2. The affinity with CO_2 is enhanced by adding functional group and constricted pore formed by interpenetrating framework, both leading to a larger isosteric heat and Henry constant and subsequently a stronger adsorption was observed at low pressures. The organic linker plays a critical role in tuning the free volume and accessible surface area, and largely determines CO_2 adsorption at high pressures. As a combination of high capacity and low framework density, IRMOF10, IRMOF14 and UMCM-1 exhibit higher storage capacity than other MOFs considered in this study. Compared to 1D and 2D COFs, 3D COFs have substantially larger free volume, porosity and surface area. COF-6 exhibits the largest isosteric heat and Henry constant due to the presence of constricted pores, but the lowest saturation capacity.

COF_NT has adsorption behavior similar to a carbon nanotube. As a counterbalance of low framework density and large porosity, COF-105 and COF-108 show exceptionally high storage capacity larger than IRMOF10, IRMOF14 and UMCM-1, even surpass the experimentally reported highest capacity in MOF-177. Different adsorption capacities in MOFs and COFs are attributed to the interplay of various complex factors such as framework density, free volume, porosity and surface area. Both gravimetric and volumetric capacities at 300 K and 30 bar correlate well with these factors. These molecular-based structure-function correlations are useful for *a priori* prediction of CO_2 capacities in to-be-synthesized MOFs and COFs toward high-performance CO_2 storage with minimal structural information.

In Chapter 6, the effects of open metal sites, catenation, and extraframework ions on adsorptive separation of CO_2/CH_4 mixtures were investigated. A series of MOFs such as Cu-BTC, PCN-6′ and PCN-6 with exposed metal sites, catenated framework, IRMOF-13 and PCN-6 and charged *soc*-MOF were chosen for study. Because of the strong affinity with framework, CO_2 is preferentially adsorbed over CH_4 in all the MOFs. The framework catenation leads to constricted pores and additional adsorption sites, and enhances the interaction with the adsorbate. Therefore, catenated IRMOF-13 and PCN-6 exhibit a greater extent of adsorption, particularly for CO_2 at low pressures; however, the opposite was observed to be true at high pressures. The adsorption selectivity in IRMOF-1 and IRMOF-14 is nearly constant at low pressures and increases with increasing pressure. As a result of a counterbalance between energetic and entropic effects, the selectivity in IRMOF-13 initially decreases at low pressures, then increases with pressure and finally approaches constant. Catenated MOFs have a higher selectivity than their non-catenated counterparts. The presence of electrostatic interactions between CO_2 and framework leads to an increase in CO_2

adsorption and a corresponding decrease in CH_4 adsorption, and consequently enhances selectivity. In charged *soc*-MOF, the selectivity is substantially higher than in the other IRMOFs and PCNs structures. The simulation results reveal that the selectivity of CO_2 over CH_4 in MOFs is enhanced by exposed metals, catenation, and extraframework ions; and that charged MOF is a promising candidate for the separation of CO_2/CH_4 mixture.

In Chapter 7, the distribution and dynamics of extraframework ions, as well as the adsorption selectivity of CO_2 over other gases were investigated in charged *rho*-ZMOF. Canonical MC and GCMC simulations were used to identify the distribution of extraframework ions and adsorption isotherms of mixtures. In addition, MD simulations were performed to calculate the mobility of ions. Two types of binding sites for Na^+ ions were identified in the framework. Site I is in the single 8-membered ring, whereas site II is in the α-cage. Na^+ ions at site I have a stronger affinity with the framework and thus a smaller mobility. The binding sites in *rho*-ZMOF are in resemblance to its inorganic counterpart *rho*-zeolite. CO_2 was found to be adsorbed predominantly over other gases due to its strong electrostatic interactions with the charged framework, and the presence of Na^+ ions acting as additional adsorption sites. At ambient temperature and pressure, the selectivity is ~ 1800 for CO_2/H_2 mixture, 80 for CO_2/CH_4 mixture, and 500 for CO_2/N_2 mixture. However, with a small trace of H_2O added into CO_2/CH_4 mixture, CO_2 adsorption drops significantly and the selectivity decreases by one order of magnitude. Compared with other MOFs and nanoporous materials reported to date, *rho*-ZMOF exhibits unprecedentedly high selective adsorption for gas mixtures. This work represents the first simulation study to characterize extraframework ions and examine gas separation in a charged ZMOF.

The simulation results reveal that *rho*-ZMOF is a promising candidate for the separation of syngas, natural gas, and flue gas.

In Chapter 8, the separation of C_4 and C_5 alkane isomers mixture in catenated (IRMOF-13 and PCN-6) and non-catenated frameworks (IRMOF-14 and PCN-6') were investigated. Configurational-bias GCMC simulations were used to calculate the adsorption and MD simulations to calculate the diffusivity. Competitive adsorption between isomers was observed, particularly at high pressures, in which a linear isomer shows a larger extent of adsorption due to configurational entropy. An inflection was found in the isotherm as a consequence of sequential adsorption in multiple favorable sites. Compared with the noncatenated counterparts, IRMOF-13 and PCN-6 have a greater loading at low pressures because of the constricted pores and stronger affinity with adsorbate. However, the reverse was true at high pressures due to the smaller pore volume. Catenated MOFs exhibit larger adsorption selectivity for alkane mixtures than the noncatenated. The adsorption selectivity in the four MOFs is comparable to that in carbon nanotube and silicalite, though adsorption capacity is lower in the latter. The diffusivity of alkane in the MOFs decreases with the degree of branching because a slender isomer diffuses faster. In catenated MOFs, the diffusivity is smaller compared with noncatenated MOFs. In IRMOF-14 and IRMOF-13, diffusivity decreases monotonically, while it initially increases and then decreases in PCN-6′. The diffusion selectivity in catenated IRMOF-13 and PCN-6 is larger than in noncatenated IRMOF-14 and PCN-6′. This work provides insightful microscopic mechanisms for the adsorption and diffusion of alkane isomers in MOFs and reveals that both adsorption and diffusion selectivities can be enhanced by catenation, particularly at low pressures.

The underlying mechanism of adsorption and diffusion of small gas molecules in different MOFs were discussed in chapters 4 through 8. In addition to small gas molecules, behavior of larger molecules including drug were further explored. In Chapter 9, the adsorption and dynamics of ibuprofen in mesoporous MIL-101 and UMCM-1 were studied. Configurational-bias GCMC and MD simulations were used to calculate the loading and mobility of ibuprofen. The predicted maximum loading is in good agreement with experimental measurement and approximately four times greater than in silica MCM-41. The lowest-energy conformation of ibuprofen in MIL-101 is preferentially located near the metal-oxide. From the highest-occupied molecular orbitals and band gap, a coordination bond is found to form between the carboxylic group of ibuprofen and the exposed metal site of MIL-101. In addition, ibuprofen exhibits a stronger binding energy and hence a smaller mobility in MIL-101 than in UMCM-1. These factors were crucial for the delayed release of ibuprofen from MIL-101, which was observed experimentally. This work unravels the energetics and dynamics of ibuprofen in MOFs at the molecular level and provides fundamental insight into the interactions of drug with host materials.

The main conclusions from this thesis are that molecular modeling can assist in screening MOFs for storage and separation applications. MOFs exhibit considerably high storage capacity for CO_2 compared to other nanoporous materials. Although the separation efficacy for gas mixtures is marginal in neutral MOFs, the selectivity increases by almost 2-3 orders of magnitude in charged MOFs, substantially higher than any other porous materials to date. Thus charged MOFs can be well-suited for separating gas mixtures, particularly, (quadru) polar from non-polar gas. In addition, the presence of catenation in MOFs increases both the adsorption and diffusion selectivity for alkane isomer mixtures.

10.2 Future Work

MOFs are regarded to be highly useful in various applications such as gas storage, separation, catalysis, drug delivery, and chiral separation. Due to the infinite number of possible MOFs, experimental synthesis and testing are tedious and time-consuming. In this regard, molecular modeling can be a powerful tool to unravel the underlying mechanism at the microscopic level and assist in the rational design of MOFs for a particular application. Currently, most experimental and modeling studies in MOFs have been reported on gas storage and separation. Further investigations are recommended in the following areas.

- In practical separation of mixtures, both adsorption and diffusion play a crucial role in determining the selectivity. A limited number of studies were reported on the diffusion of mixtures. To better understand diffusion phenomena at a microscopic level and screen high-performance MOFs for separation, the diffusion of mixtures in MOFs needs further study.

- Framework flexibility can substantially influence diffusion in MOFs. However, most simulations considered rigid frameworks, except few in which framework flexibility was accounted for with empirical force fields [225,229,424,425]. To accurately describe the flexibility in MOFs, suitable force fields need to be developed to explore framework flexibility.

- A number of MOFs show a structural change upon gas adsorption at different pressures and temperatures. Only few modeling studies were reported attempting to elucidate the phenomenon [426-428]; however, the underlying mechanisms remain elusive. More sophisticated modeling is desired to provide atomic-resolution and time-resolved insights.

- Several MOFs are chiral in nature and can be useful for enantioselective separation [150,429-432]. The advantage of using chiral MOFs is their extraordinary surface areas, which may enhance separation rates. To better elucidate the interactions of enantiomers with chiral MOFs and to improve the selectivity, detailed modeling studies are necessary.

- With the metal-oxides as building block in the frameworks, MOFs have been experimentally demonstrated being useful for catalytic reactions. Molecular modeling for MOFs in this area is rare and at the early stage [433]. First-principles quantum chemical calculations are required to provide the fundamental mechanism of MOFs in catalysis.

References

[1] M. E. Davis, *Nature*, **2002**, 417, 813.

[2] M. Eddaoudi, J. Kim, N. Rosi, D. Vodak, J. Wachter, M. O'Keefe, and O. M. Yaghi, *Science*, **2002**, 295, 469.

[3] H. Li, M. Eddaoudi, M. O'Keeffe, and O. M. Yaghi, *Nature*, **1999**, 402, 276.

[4] S. Kitagawa, R. Kitaura, and S. Noro, *Angew. Chem. Inter. Ed.*, **2004**, 43, 2334.

[5] J. L. C. Rowsell and O. M. Yaghi, *Microporous Mesoporous Mater.*, **2004**, 73, 3.

[6] T. J. Barton, L. M. Bull, W. G. Klemperer, D. A. Loy, B. McEnaney, M. Misono, P. A. Monson, G. Pez, G. W. Scherer, J. C. Vartuli, and O. M. Yaghi, *Chem. Mater.*, **1999**, 11, 2633.

[7] O. M. Yaghi, M. O'Keeffe, N. W. Ockwig, H. K. Chae, M. Eddaoudi, and J. Kim, *Nature*, **2003**, 423, 705.

[8] M. Eddaoudi, D. B. Moler, H. L. Li, B. L. Chen, T. M. Reineke, M. O'Keeffe, and O. M. Yaghi, *Acc. Chem. Res.*, **2001**, 34, 319.

[9] B. L. Chen, M. Eddaoudi, T. M. Reineke, J. W. Kampf, M. O'Keeffe, and O. M. Yaghi, *J. Am. Chem. Soc*, **2000**, 122, 11559.

[10] J. C. G. Bunzli and C. Piguet, *Chemi. Rev.*, **2002**, 102, 1897.

[11] L. Pan, X. Y. Huang, J. Li, Y. G. Wu, and N. W. Zheng, *Angew. Chem. Inter. Ed.*, **2000**, 39, 527.

[12] C. D. Wu, C. Z. Lu, H. H. Zhuang, and J. S. Huang, *J. Am. Chem. Soc.*, **2002**, 124, 3836.

[13] S. Neogi and P. K. Bharadwaj, *Polyhedron*, **2006**, 25, 1491.

[14] S. Neogi and P. K. Bharadwaj, *Cryst. Growth Des.*, **2006**, 6, 433.

[15] S. Neogi and P. K. Bharadwaj, *Synthesis and Reactivity in Inorganic Metal-Organic and Nano-Metal Chemistry*, **2008**, 38, 40.

[16] S. K. Ghosh and P. K. Bharadwaj, *Inorg. Chem.*, **2004**, 43, 6887.

[17] S. K. Ghosh and P. K. Bharadwaj, *Inorg. Chem.*, **2003**, 42, 8250.

[18] S. K. Ghosh and P. K. Bharadwaj, *Inorg. Chem.*, **2004**, 43, 5180.

[19] S. K. Ghosh and P. K. Bharadwaj, *Eur. J. Inorg. Chem.*, **2005**, 4880.

[20] S. K. Ghosh and P. K. Bharadwaj, *Eur. J. Inorg. Chem.*, **2005**, 4886.

[21] S. K. Ghosh and P. K. Bharadwaj, *Inorg. Chem.*, **2005**, 44, 5553.

[22] J. R. Long and O. M. Yaghi, *Chem. Soc. Rev*, **2009**, 38, 1213. http://dx.doi.org/10.1039/b903811f.

[23] D. Riou and G. Ferey, *J. Mater. Chem.*, **1998**, 8, 2733.

[24] D. Riou, O. Roubeau, and G. Ferey, *Microporous Mesoporous Mater.*, **1998**, 23, 23.

[25] D. Riou, C. Serre, and G. Ferey, *J. Solid State Chem.*, **1998**, 141, 89.

[26] F. Serpaggi and G. Ferey, *J. Mater. Chem.*, **1998**, 8, 2737.

[27] F. Serpaggi and G. Ferey, *J. Mater. Chem.*, **1998**, 8, 2749.

[28] F. Serpaggi and G. Ferey, *Microporous Mesoporous Mater.*, **1999**, 32, 311.

[29] C. Serre, F. Millange, C. Thouvenot, M. Nogues, G. Marsolier, D. Louer, and G. Ferey, *J. Am. Chem. Soc*, **2002**, 124, 13519.

[30] T. Loiseau, C. Serre, C. Huguenard, G. Fink, F. Taulelle, M. Henry, T. Bataille, and G. Ferey, *Chem.- Eur. J.*, **2004**, 10, 1373.

[31] F. Millange, N. Guillou, R. I. Walton, J. M. Greneche, I. Margiolaki, and G. Fereya, *Chem. Commu.*, **2008**, 4732.

[32] C. Volkringer, T. Loiseau, N. Guillou, G. Ferey, E. Elkaim, and A. Vimont, *Dalton Transactions*, **2009**, 2241.

[33] K. Barthelet, J. Marrot, D. Riou, and G. Ferey, *Angew. Chem. Inter. Ed.*, **2002**, 41, 281.

[34] G. Ferey, C. Serre, C. Mellot-Draznieks, F. Millange, S. Surble, J. Dutour, and I. Margiolaki, *Angew. Chem. Inter. Ed.*, **2004**, 43, 6296.

[35] H. K. Chae, D. Y. Siberio-Perez, J. Kim, Y. Go, M. Eddaoudi, A. J. Matzger, M. O'Keeffe, and O. M. Yaghi, *Nature*, **2004**, 427, 523.

[36] M. G. Nijkamp, J. Raaymakers, A. J. van Dillen, and K. P. de Jong, *Appl. Phys.*, **2001**, 72, 619.

[37] A. W. Chester, P. Clement, and S. Han, in 'Faujasite zeolitic materials', US patent, 2000.

[38] K. Koh, A. G. Wong-Foy, and A. J. Matzger, *Angew. Chem. Inter. Ed.*, **2008**, 47, 677.

[39] K. Koh, A. G. Wong-Foy, and A. J. Matzger, *J. Am. Chem. Soc*, **2009**, 131, 4184.

[40] A. J. Fletcher, E. J. Cussen, T. J. Prior, M. J. Rosseinsky, C. J. Kepert, and K. M. Thomas, *J. Am. Chem. Soc*, **2001**, 123, 10001.

[41] A. J. Fletcher, E. J. Cussen, D. Bradshaw, M. J. Rosseinsky, and K. M. Thomas, *J. Am. Chem. Soc*, **2004**, 126, 9750.

[42] A. P. Malanoski and F. van Swol, *Phys. Rev. E*, **2002**, 66.

[43] O. M. Yaghi, H. L. Li, C. Davis, D. Richardson, and T. L. Groy, *Acc. Chem. Res.*, **1998**, 31, 474.

[44] S. Kitagawa and K. Uemura, *Chem. Soc. Rev*, **2005**, 34, 109.

[45] S. Kitagawa and M. Kondo, *Bulletin of the Chemical Society of Japan*, **1998**, 71, 1739.

[46] A. J. Fletcher, K. M. Thomas, and M. J. Rosseinsky, *J. Solid State Chem.*, **2005**, 178, 2491.

[47] R. Kitaura, K. Fujimoto, S. Noro, M. Kondo, and S. Kitagawa, *Angew. Chem. Inter. Ed.*, **2002**, 41, 133.

[48] R. Kitaura, K. Seki, G. Akiyama, and S. Kitagawa, *Angew. Chem. Inter. Ed.*, **2003**, 42, 428.

[49] X. B. Zhao, B. Xiao, A. J. Fletcher, K. M. Thomas, D. Bradshaw, and M. J. Rosseinsky, *Science*, **2004**, 306, 1012.

[50] A. P. Cote, A. I. Benin, N. W. Ockwig, M. O'Keeffe, A. J. Matzger, and O. M. Yaghi, *Science*, **2005**, 310, 1166.

[51] A. P. Cote, H. M. El-Kaderi, H. Furukawa, J. R. Hunt, and O. M. Yaghi, *J. Am. Chem. Soc.*, **2007**, 129, 12914.

[52] H. M. El-Kaderi, J. R. Hunt, J. L. Mendoza-Cortes, A. P. Cote, R. E. Taylor, M. O'Keeffe, and O. M. Yaghi, *Science*, **2007**, 316, 268.

[53] M. A. Lino, A. A. Lino, and M. S. C. Mazzoni, *Chem. Phys. Lett.*, **2007**, 449, 171.

[54] J. R. Hunt, C. J. Doonan, J. D. LeVangie, A. P. Cote, and O. M. Yaghi, *J. Am. Chem. Soc*, **2008**, 130, 11872.

[55] F. J. Uribe-Romo, J. R. Hunt, H. Furukawa, C. Klock, M. O'Keeffe, and O. M. Yaghi, *J. Am. Chem. Soc*, **2009**, 131, 4570.

[56] S. Wan, J. Guo, J. Kim, H. Ihee, and D. L. Jiang, *Angew. Chem. Inter. Ed.*, **2008**, 47, 8826.

[57] Y. Q. Tian, C. X. Cai, Y. Ji, X. Z. You, S. M. Peng, and G. H. Lee, *Angew. Chem. Inter. Ed.*, **2002**, 41, 1384.

[58] Y. Q. Tian, C. X. Cai, X. M. Ren, C. Y. Duan, Y. Xu, S. Gao, and X. Z. You, *Chem.- Eur. J.*, **2003**, 9, 5673.

[59] Y. Q. Tian, Z. X. Chen, L. H. Weng, H. B. Guo, S. Gao, and D. Y. Zhao, *Inorg. Chem.*, **2004**, 43, 4631.

[60] Y. Q. Tian, H. J. Xu, L. H. Weng, Z. X. Chen, D. Y. Zhao, and X. Z. You, *Eur. J. Inorg. Chem.*, **2004**, 1813.

[61] Y. Q. Tian, Y. M. Zhao, Z. X. Chen, G. N. Zhang, L. H. Weng, and D. Y. Zhao, *Chem.- Eur. J.*, **2007**, 13, 4146.

[62] X. C. Huang, Y. Y. Lin, J. P. Zhang, and X. M. Chen, *Angew. Chem. Inter. Ed.*, **2006**, 45, 1557.

[63] D. W. Breck, Zeolite Molecular Sieves, Wiley, New York, 1974.

[64] X. C. Huang, J. P. Zhang, and X. M. Chen, *Chinese Science Bulletin*, **2003**, 48, 1531.

[65] K. S. Park, Z. Ni, A. P. Cote, J. Y. Choi, R. D. Huang, F. J. Uribe-Romo, H. K. Chae, M. O'Keeffe, and O. M. Yaghi, *Proc. Nat. Acad. Sci. U.S.A.*, **2006**, 103, 10186.

[66] H. Hayashi, A. P. Cote, H. Furukawa, M. O'Keeffe, and O. M. Yaghi, *Nature Materials*, **2007**, 6, 501.

[67] R. Banerjee, A. Phan, B. Wang, C. Knobler, H. Furukawa, M. O'Keeffe, and O. M. Yaghi, *Science*, **2008**, 319, 939.

[68] B. Wang, A. P. Cote, H. Furukawa, M. O'Keeffe, and O. M. Yaghi, *Nature*, **2008**, 453, 207.

[69] H. Zhang, T. Wu, C. Zhou, S. M. Chen, P. Y. Feng, and X. H. Bu, *Angew. Chem. Inter. Ed.*, **2009**, 48, 2542.

[70] T. Wu, X. H. Bu, J. Zhang, and P. Y. Feng, *Chem. Mater.*, **2008**, 20, 7377.

[71] Y. L. Liu, V. C. Kravtsov, R. Larsen, and M. Eddaoudi, *Chem. Commu.*, **2006**, 14, 1488.

[72] D. F. Sava, V. C. Kravtsov, F. Nouar, L. Wojtas, J. F. Eubank, and M. Eddaoudi, *J. Am. Chem. Soc.*, **2008**, 130, 3768.

[73] E. Dugan, Z. Q. Wang, M. Okamura, A. Medina, and S. M. Cohen, *Chem. Commu.*, **2008**, 3366.

[74] K. K. Tanabe, Z. Q. Wang, and S. M. Cohen, *J. Am. Chem. Soc*, **2008**, 130, 8508.

[75] Z. Q. Wang and S. M. Cohen, *Angew. Chem. Inter. Ed.*, **2008**, 47, 4699.

[76] Z. Q. Wang and S. M. Cohen, *J. Am. Chem. Soc*, **2007**, 129, 12368.

[77] Z. Q. Wang, K. K. Tanabe, and S. M. Cohen, *Inorg. Chem.*, **2009**, 48, 296.

[78] Z. Q. Wang and S. M. Cohen, *Chem. Soc. Rev*, **2009**, 38, 1315.

[79] B. D. Chandler, D. T. Cramb, and G. K. H. Shimizu, *J. Am. Chem. Soc*, **2006**, 128, 10403.

[80] E. Y. Lee, S. Y. Jang, and M. P. Suh, *J. Am. Chem. Soc*, **2005**, 127, 6374.

[81] J. R. Li, Y. Tao, Q. Yu, and X. H. Bu, *Chem. Commu.*, **2007**, 1527.

[82] G. J. Halder, C. J. Kepert, B. Moubaraki, K. S. Murray, and J. D. Cashion, *Science*, **2002**, 298, 1762.

[83] P. D. C. Dietzel, Y. Morita, R. Blom, and H. Fjellvag, *Angew. Chem. Inter. Ed.*, **2005**, 44, 6354.

[84] Z. M. Wang, Y. J. Zhang, T. Liu, M. Kurmoo, and S. Gao, *Adv. Funct. Mater.*, **2007**, 17, 1523.

[85] M. Alvaro, E. Carbonell, B. Ferrer, F. Xamena, and H. Garcia, *Chem.- Eur. J.*, **2007**, 13, 5106.

[86] A. Kuc, A. Enyashin, and G. Seifert, *J. Phys. Chem. B.*, **2007**, 111, 8179.

[87] Q. Ye, Y. M. Song, G. X. Wang, K. Chen, D. W. Fu, P. W. H. Chan, J. S. Zhu, S. D. Huang, and R. G. Xiong, *J. Am. Chem. Soc*, **2006**, 128, 6554.

[88] T. Okubo, R. Kawajiri, T. Mitani, and T. Shimoda, *J. Am. Chem. Soc*, **2005**, 127, 17598.

[89] S. Horike, M. Dinca, K. Tamaki, and J. R. Long, *J. Am. Chem. Soc*, **2008**, 130, 5854.

[90] T. Mueller, M. M. Schubert, and A. O. Yazaydin, in Handbook of Heterogeneous catalysis, Weinheim, 2008.

[91] F. Xamena, O. Casanova, R. G. Tailleur, H. Garcia, and A. Corma, *J. Catal.*, **2008**, 255, 220.

[92] R. Q. Zou, H. Sakurai, S. Han, R. Q. Zhong, and Q. Xu, *J. Am. Chem. Soc*, **2007**, 129, 8402.

[93] B. F. Hoskins and R. Robson, *J. Am. Chem. Soc.*, **1990**, 112, 1546.

[94] G. B. Gardner, D. Venkataraman, J. S. Moore, and S. Lee, *Nature*, **1995**, 374, 792.

[95] E. Lee, J. Kim, J. Heo, D. Whang, and K. Kim, *Angew. Chem. Inter. Ed.*, **2001**, 40, 399.

[96] J. R. Li, R. J. Kuppler, and H. C. Zhou, *Chem. Soc. Rev*, **2009**, 38, 1477.

[97] H. Furukawa and O. M. Yaghi, *J. Am. Chem. Soc.*, **2009**, in press.

[98] A. R. Millward and O. M. Yaghi, *J. Am. Chem. Soc.*, **2005**, 127, 17998.

[99] B. L. Chen, L. B. Wang, F. Zapata, G. D. Qian, and E. B. Lobkovsky, *J. Am. Chem. Soc.*, **2008**, 130, 6718.

[100] B. L. Chen, Y. Yang, F. Zapata, G. N. Lin, G. D. Qian, and E. B. Lobkovsky, *Advan. Mater.*, **2007**, 19, 1693.

[101] B. V. Harbuzaru, A. Corma, F. Rey, P. Atienzar, J. L. Jorda, H. Garcia, D. Ananias, L. D. Carlos, and J. Rocha, *Angew. Chem. Inter. Ed.*, **2008**, 47, 1080.

[102] T. Uemura, D. Hiramatsu, Y. Kubota, M. Takata, and S. Kitagawa, *Angew. Chem. Inter. Ed.*, **2007**, 46, 4987.

[103] T. Uemura, R. Kitaura, Y. Ohta, M. Nagaoka, and S. Kitagawa, *Angew. Chem. Inter. Ed.*, **2006**, 45, 4112.

[104] M. Vallet-Regi, F. Balas, and D. Arcos, *Angew. Chem. Inter. Ed.*, **2007**, 46, 7548.

[105] P. Horcajada, C. Serre, G. Maurin, N. A. Ramsahye, F. Balas, M. Vallet-Regi, M. Sebban, F. Taulelle, and G. Ferey, *J. Am. Chem. Soc.*, **2008**, 130, 6774.

[106] P. Horcajada, C. Serre, M. Vallet-Regi, M. Sebban, F. Taulelle, and G. Ferey, *Angew. Chem. Inter. Ed.*, **2006**, 45, 5974.

[107] 'Hydrogen, Fuel Cells and Infrastructure Technologies Program: Multi-year Research, Development and Demonstration Plan', U.S. Department of Energy, 2005.

[108] J. L. C. Rowsell, A. R. Millward, K. S. Park, and O. M. Yaghi, *J. Am. Chem. Soc.*, **2004**, 126, 5666.

[109] B. L. Chen, N. W. Ockwig, A. R. Millward, D. S. Contreras, and O. M. Yaghi, *Angew. Chem. Inter. Ed.*, **2005**, 44, 4745.

[110] G. Ferey, M. Latroche, C. Serre, F. Millange, T. Loiseau, and A. Percheron-Guegan, *Chem. Commun.*, **2003**, 2976.

[111] L. Pan, M. B. Sander, X. Y. Huang, J. Li, M. Smith, E. Bittner, B. Bockrath, and J. K. Johnson, *J. Am. Chem. Soc.*, **2004**, 126, 1308.

[112] J. L. C. Rowsell and O. M. Yaghi, *Angew. Chem. Int. Ed*, **2005**, 44, 4670.

[113] A. G. Wong-Foy, A. J. Matzger, and O. M. Yaghi, *J. Am. Chem. Soc.*, **2006**, 128, 3494.

[114] M. Dinca, A. Dailly, Y. Liu, C. M. Brown, D. A. Neumann, and J. R. Long, *J. Am. Chem. Soc*, **2006**, 128, 16876.

[115] M. Dinca and J. R. Long, *J. Am. Chem. Soc*, **2007**, 129, 11172.

[116] X. S. Wang, S. Q. Ma, P. M. Forster, D. Q. Yuan, J. Eckert, J. J. Lopez, B. J. Murphy, J. B. Parise, and H. C. Zhou, *Angew. Chem. Inter. Ed.*, **2008**, 47, 7263.

[117] J. G. Vitillo, L. Regli, S. Chavan, G. Ricchiardi, G. Spoto, P. D. C. Dietzel, S. Bordiga, and A. Zecchina, *J. Am. Chem. Soc*, **2008**, 130, 8386.

[118] M. Dinca and J. R. Long, *Angew. Chem. Inter. Ed.*, **2008**, 47, 6766.

[119] Y. W. Li and R. T. Yang, *J. Am. Chem. Soc.*, **2006**, 128, 726.

[120] Y. W. Li and R. T. Yang, *J. Am. Chem. Soc.*, **2006**, 128, 8136.

[121] S. S. Kaye, A. Dailly, O. M. Yaghi, and J. R. Long, *J. Am. Chem. Soc*, **2007**, 129, 14176.

[122] S. H. Yang, X. Lin, A. Dailly, A. J. Blake, P. Hubberstey, N. R. Champness, and M. Schroder, *Chem.- Eur. J.*, **2009**, 15, 4829.

[123] L. J. Murray, M. Dinca, and J. R. Long, *Chem. Soc. Rev*, **2009**, 38, 1294.

[124] T. Duren, L. Sarkisov, O. M. Yaghi, and R. Q. Snurr, *Langmuir*, **2004**, 20, 2683.

[125] S. Q. Ma, D. F. Sun, J. M. Simmons, C. D. Collier, D. Q. Yuan, and H. C. Zhou, *J. Am. Chem. Soc*, **2008**, 130, 1012.

[126] T. Burchell and M. Rogers, *SAE Tech. Pap. Ser.*, **2000**, 2000-01-2205.

[127] P. L. Llewellyn, S. Bourrelly, C. Serre, A. Vimont, M. Daturi, L. Hamon, G. De Weireld, J. S. Chang, D. Y. Hong, Y. K. Hwang, S. H. Jhung, and G. Ferey, *Langmuir*, **2008**, 24, 7245.

[128] P. Chowdhury, C. Bikkina, and S. Gumma, *J. Phys. Chem. C.*, **2009**, 113, 6616.

[129] B. Xiao, P. S. Wheatley, X. B. Zhao, A. J. Fletcher, S. Fox, A. G. Rossi, I. L. Megson, S. Bordiga, L. Regli, K. M. Thomas, and R. E. Morris, *J. Am. Chem. Soc.*, **2007**, 129, 1203.

[130] A. C. McKinlay, B. Xiao, D. S. Wragg, P. S. Wheatley, I. L. Megson, and R. E. Morris, *J. Am. Chem. Soc.*, **2008**, 130, 10440.

[131] S. Sircar, *Ind. Engg. Chem. Res.*, **2006**, 45, 5435.

[132] B. L. Chen, C. D. Liang, J. Yang, D. S. Contreras, Y. L. Clancy, E. B. Lobkovsky, O. M. Yaghi, and S. Dai, *Angew. Chem. Inter. Ed.*, **2006**, 45, 1390.

[133] L. Pan, D. H. Olson, L. R. Ciemnolonski, R. Heddy, and J. Li, *Angew. Chem. Inter. Ed.*, **2006**, 45, 616.

[134] D. N. Dybtsev, H. Chun, S. H. Yoon, D. Kim, and K. Kim, *J. Am. Chem. Soc*, **2004**, 126, 32.

[135] S. Q. Ma, X. S. Wang, C. D. Collier, E. S. Manis, and H. C. Zhou, *Inorg. Chem.*, **2007**, 46, 8499.

[136] M. Dinca and J. R. Long, *J. Am. Chem. Soc*, **2005**, 127, 9376.

[137] J. A. R. Navarro, E. Barea, A. Rodriguez-Dieguez, J. M. Salas, C. O. Ania, J. B. Parra, N. Masciocchi, S. Galli, and A. Sironi, *J. Am. Chem. Soc*, **2008**, 130, 3978.

[138] S. S. Y. Chui, S. M. F. Lo, J. P. H. Charmant, A. G. Orpen, and I. D. Williams, *Science*, **1999**, 283, 1148.

[139] Q. M. Wang, D. M. Shen, M. Bulow, M. L. Lau, S. G. Deng, F. R. Fitch, N. O. Lemcoff, and J. Semanscin, *Microporous Mesoporous Mater.*, **2002**, 55, 217.

[140] S. Q. Ma, X. S. Wang, D. Q. Yuan, and H. C. Zhou, *Angew. Chem. Inter. Ed.*, **2008**, 47, 4130.

[141] R. Matsuda, R. Kitaura, S. Kitagawa, Y. Kubota, R. V. Belosludov, T. C. Kobayashi, H. Sakamoto, T. Chiba, M. Takata, Y. Kawazoe, and Y. Mita, *Nature*, **2005**, 436, 238.

[142] L. Pan, B. Parker, X. Y. Huang, D. H. Olson, J. Lee, and J. Li, *J. Am. Chem. Soc*, **2006**, 128, 4180.

[143] J. Y. Lee, D. H. Olson, L. Pan, T. J. Emge, and J. Li, *Adv. Funct. Mater.*, **2007**, 17, 1255.

[144] S. Horike, D. Tanaka, K. Nakagawa, and S. Kitagawa, *Chem. Commu.*, **2007**, 3395.

[145] H. R. Moon, N. Kobayashi, and M. P. Suh, *Inorg. Chem.*, **2006**, 45, 8672.

[146] Y. S. Bae, O. K. Farha, A. M. Spokoyny, C. A. Mirkin, J. T. Hupp, and R. Q. Snurr, *Chem. Commun.*, **2008**, 4135.

[147] B. Mu, F. Li, and K. S. Walton, *Chem. Commu.*, **2009**, 2493.

[148] M. Fujita, Y. J. Kwon, S. Washizu, and K. Ogura, *J. Am. Chem. Soc*, **1994**, 116, 1151.

[149] O. R. Evans, H. L. Ngo, and W. B. Lin, *J. Am. Chem. Soc*, **2001**, 123, 10395.

[150] J. S. Seo, D. Whang, H. Lee, S. I. Jun, J. Oh, Y. J. Jeon, and K. Kim, *Nature*, **2000**, 404, 982.

[151] C. D. Wu, A. Hu, L. Zhang, and W. B. Lin, *J. Am. Chem. Soc*, **2005**, 127, 8940.

[152] U. Ravon, M. E. Domine, C. Gaudillere, A. Desmartin-Chomel, and D. Farrusseng, *New J. Chem.*, **2008**, 32, 937.

[153] A. Henschel, K. Gedrich, R. Kraehnert, and S. Kaskel, *Chem. Commu.*, **2008**, 4192.

[154] K. Schlichte, T. Kratzke, and S. Kaskel, *Microporous Mesoporous Mater.*, **2004**, 73, 81.

[155] L. Alaerts, E. Seguin, H. Poelman, F. Thibault-Starzyk, P. A. Jacobs, and D. E. De Vos, *Chem.- Eur. J.*, **2006**, 12, 7353.

[156] M. H. Alkordi, Y. L. Liu, R. W. Larsen, J. F. Eubank, and M. Eddaoudi, *J. Am. Chem. Soc*, **2008**, 130, 12639.

[157] S. Hasegawa, S. Horike, R. Matsuda, S. Furukawa, K. Mochizuki, Y. Kinoshita, and S. Kitagawa, *J. Am. Chem. Soc*, **2007**, 129, 2607.

[158] Y. K. Hwang, D. Y. Hong, J. S. Chang, S. H. Jhung, Y. K. Seo, J. Kim, A. Vimont, M. Daturi, C. Serre, and G. Ferey, *Angew. Chem. Inter. Ed.*, **2008**, 47, 4144.

[159] O. Hubner, A. Gloss, M. Fichtner, and W. Klopper, *J. Phys. Chem. A*, **2004**, 108, 3019.

[160] R. Ahlrichs, M. Bar, M. Haser, H. Horn, and C. Kolmel, *Chem. Phys. Lett.*, **1989**, 162, 165.

[161] F. Weigend and M. Haser, *Theor. Chem. Acct.*, **1997**, 97, 331.

[162] F. Weigend, M. Haser, H. Patzelt, and R. Ahlrichs, *Chem. Phys. Lett.*, **1998**, 294, 143.

[163] A. Schafer, C. Huber, and R. Ahlrichs, *J. Chem. Phys.*, **1994**, 100, 5829.

[164] T. Sagara, J. Klassen, J. Ortony, and E. Ganz, *J. Chem. Phys.*, **2005**, 123.

[165] T. Sagara, J. Ortony, and E. Ganz, *J. Chem. Phys.*, **2005**, 123.

[166] S. S. Han, W. Q. Deng, and W. A. Goddard, *Ang. Chem. Inter. Ed.*, **2007**, 46, 6289.

[167] Y. Gao and X. C. Zeng, *J. Phys.-Condensed Matter*, **2007**, 19.

[168] F. Negri and N. Saendig, *Theor. Chem. Acct.*, **2007**, 118, 149.

[169] T. Sagara, J. Klassen, and E. Ganz, *J. Chem. Phys.*, **2004**, 121, 12543.

[170] Q. Y. Yang and C. L. Zhong, *J. Phys. Chem. B*, **2005**, 109, 11862.

[171] W. L. Jorgensen, D. S. Maxwell, and J. TiradoRives, *J. Am. Chem. Soc*, **1996**, 118, 11225.

[172] Q. Y. Yang and C. L. Zhong, *J. Phys. Chem. B*, **2006**, 110, 17776.

[173] G. Garberoglio, A. I. Skoulidas, and J. K. Johnson, *J. Phys. Chem.B*, **2005**, 109, 13094.

[174] A. K. Rappe, C. J. Casewit, K. S. Colwell, W. A. Goddard, and W. M. Skiff, *J. Am. Chem. Soc.*, **1992**, 114, 10024.

[175] S. L. Mayo, B. D. Olafson, and W. A. Goddard, *J. Phys. Chem.*, **1990**, 94, 8897.

[176] H. Frost, T. Duren, and R. Q. Snurr, *J. Phys. Chem. B*, **2006**, 110, 9565.

[177] D. H. Jung, D. Kim, T. B. Lee, S. B. Choi, J. H. Yoon, J. Kim, K. Choi, and S. H. Choi, *J. Phys. Chem. B*, **2006**, 110, 22987.

[178] P. Ryan, L. J. Broadbelt, and R. Q. Snurr, *Chem. Commun.*, **2008**, 4132.

[179] L. Zhang, Q. Wang, and Y. C. Liu, *J. Phys. Chem. B*, **2007**, 111, 4291.

[180] H. Frost and R. Q. Snurr, *J. Phys. Chem.C*, **2007**, 111, 18794.

[181] G. Garberoglio, *Langmuir*, **2007**, 23, 12154.

[182] E. Klontzas, E. Tylianakis, and G. E. Froudakis, *J. Phys. Chem. C*, **2008**, 112, 9095.

[183] W. Q. Deng, X. Xu, and W. A. Goddard, *Phys. Rev. Lett.*, **2004**, 92.

[184] S. S. Han and W. A. Goddard, *J. Phys. Chem. C*, **2008**, 112, 13431.

[185] S. S. Han, H. Furukawa, O. M. Yaghi, and W. A. Goddard, *J. Am. Chem. Soc*, **2008**, 130, 11580.

[186] M. Kosa, M. Krack, A. K. Cheetham, and M. Parrinello, *J. Phys. Chem. C*, **2008**, 112, 16171.

[187] Y. Y. Sun, Y. H. Kim, and S. B. Zhang, *J. Am. Chem. Soc*, **2007**, 129, 12606.

[188] Q. Y. Yang and C. L. Zhong, *J. Phys. Chem. B*, **2006**, 110, 655.

[189] S. S. Han and W. A. Goddard, *J. Am. Chem. Soc*, **2007**, 129, 8422.

[190] A. Blomqvist, C. M. Araujo, P. Srepusharawoot, and R. Ahuja, *Proc. Natl. Acad. Sci. U.S.A*, **2007**, 104, 20173.

[191] A. Mavrandonakis, E. Tylianakis, A. K. Stubos, and G. E. Froudakis, *J. Phys. Chem. C*, **2008**, 112, 7290.

[192] P. Dalach, H. Frost, R. Q. Snurr, and D. E. Ellis, *J. Phys. Chem. C*, **2008**, 112, 9278.

[193] E. Klontzas, A. Mavrandonakis, E. Tylianakis, and G. E. Froudakis, *Nano Letters*, **2008**, 8, 1572.

[194] Y. J. Choi, J. W. Lee, J. H. Choi, and J. K. Kang, *Appl. Phys. Lett.*, **2008**, 92.

[195] D. P. Cao, J. H. Lan, W. C. Wang, and B. Smit, *Ang. Chem. Inter. Ed.*, **2009**, 48, 4730.

[196] S. Y. Wang, *Energy & Fuels*, **2007**, 21, 953.

[197] Y. H. Jhon, M. Cho, H. R. Jeon, I. Park, R. Chang, J. L. C. Rowsell, and J. Kim, *J. Phys. Chem. C*, **2007**, 111, 16618.

[198] T. Kawakami, S. Takamizawa, Y. Kitagawa, T. Maruta, W. Mori, and K. Yamaguchi, *Polyhedron*, **2001**, 20, 1197.

[199] K. S. Walton, A. R. Millward, D. Dubbeldam, H. Frost, J. J. Low, O. M. Yaghi, and R. Q. Snurr, *J. Am. Chem. Soc.*, **2008**, 130, 406.

[200] Q. Y. Yang, C. L. Zhong, and J. F. Chen, *J. Phys. Chem. C*, **2008**, 112, 1562.

[201] N. A. Ramsahye, G. Maurin, S. Bourrelly, P. Llewellyn, T. Loiseau, and G. Ferey, *Phys.Chem. Chem. Phys.*, **2007**, 9, 1059.

[202] N. A. Ramsahye, G. Maurin, S. Bourrelly, P. L. Llewellyn, T. Devic, C. Serre, T. Loiseau, and G. Ferey, *Adsorption*, **2007**, 13, 461.

[203] N. A. Ramsahye, G. Maurin, S. Bourrelly, P. L. Llewellyn, T. Loiseau, C. Serre, and G. Ferey, *Chem. Commu.*, **2007**, 3261.

[204] N. A. Ramsahye, G. Maurin, S. Bourrelly, P. L. Llewellyn, C. Serre, T. Loiseau, T. Devic, and G. Ferey, *J. Phys. Chem. C*, **2008**, 112, 514.

[205] A. Vishnyakov, P. I. Ravikovitch, A. V. Neimark, M. Bulow, and Q. M. Wang, *Nano Letters*, **2003**, 3, 713.

[206] D. Dubbeldam, H. Frost, K. S. Walton, and R. Q. Snurr, *Fluid. Phase. Equilib*, **2007**, 261, 152.

[207] K. S. Walton and R. Q. Snurr, *J. Am. Chem. Soc*, **2007**, 129, 8552.

[208] Q. Y. Yang, C. Y. Xue, C. L. Zhong, and J. F. Chen, *AIChE J.*, **2007**, 53, 2832.

[209] J. C. Liu, J. T. Culp, S. Natesakhawat, B. C. Bockrath, B. Zande, S. G. Sankar, G. Garberoglio, and J. K. Johnson, *J. Phys. Chem. C*, **2007**, 111, 9305.

[210] V. Krungleviciute, K. Lask, L. Heroux, A. D. Migone, J. Y. Lee, J. Li, and A. Skoulidas, *Langmuir*, **2007**, 23, 3106.

[211] T. Duren and R. Q. Snurr, *J. Phys. Chem. B*, **2004**, 108, 15703.

[212] J. W. Jiang and S. I. Sandler, *Langmuir*, **2006**, 22, 5702.

[213] S. Y. Wang, Q. Y. Yang, and C. L. Zhong, *Sep. Purif. Tech.*, **2008**, 60, 30.

[214] S. Y. Wang, Q. Y. Yang, and C. L. Zhong, *J. Phys. Chem. B*, **2006**, 110, 20526.

[215] Q. Y. Yang and C. L. Zhong, *ChemPhysChem*, **2006**, 7, 1417.

[216] A. Martin-Calvo, E. Garcia-Perez, J. M. Castillo, and S. Calero, *Phys.Chem. Chem. Phys.*, **2008**, 10, 7085.

[217] D. Dubbeldam, C. J. Galvin, K. S. Walton, D. E. Ellis, and R. Q. Snurr, *J. Am. Chem. Soc*, **2008**, 130, 10884.

[218] C. Chmelik, J. Karger, M. Wiebckw, J. Caro, J. M. van Baten, and R. Krishna, *Microporous Mesoporous Mater.*, **2009**, 117, 22.

[219] B. Liu, Q. Yang, C. Xue, C. Zhong, B. Chen, and B. Smit, *J. Phys. Chem. C*, **2008**, 112, 9854.

[220] B. Liu and B. Smit, *Langmuir*, **2009**, 25, 5918.

[221] A. I. Skoulidas, *J. Am. Chem. Soc*, **2004**, 126, 1356.

[222] A. I. Skoulidas and D. S. Sholl, *J. Phys. Chem.B*, **2005**, 109, 15760.

[223] L. Sarkisov, T. Duren, and R. Q. Snurr, *Mol. Phys.*, **2004**, 102, 211.

[224] D. S. Sholl, *Accts Chem Res*, **2006**, 39, 403.

[225] S. Amirjalayer, M. Tafipolsky, and R. Schmid, *Angew. Chem. Inter. Ed.*, **2007**, 46, 463.

[226] F. Stallmach, S. Groger, V. Kunzel, J. Karger, O. M. Yaghi, M. Hesse, and U. Muller, *Angew. Chem. Inter. Ed.*, **2006**, 45, 2123.

[227] D. Dubbeldam, K. S. Walton, D. E. Ellis, and R. Q. Snurr, *Ang. Chem. Inter. Ed.*, **2007**, 46, 4496.

[228] J. A. Greathouse and M. D. Allendorf, *J. Am. Chem. Soc*, **2006**, 128, 13312.

[229] J. A. Greathouse and M. D. Allendorf, *J. Phys. Chem. C*, **2008**, 112, 5795.

[230] B. Liu, Q. Y. Yang, C. Y. Xue, C. L. Zhong, and B. Smit, *Phys.Chem. Chem. Phys.*, **2008**, 10, 3244.

[231] J. Liu, J. Y. Lee, L. Pan, R. T. Obermyer, S. Simizu, B. Zande, J. Li, S. G. Sankar, and J. K. Johnson, *J. Phys. Chem. C*, **2008**, 112, 2911.

[232] F. Salles, H. Jobic, G. Maurin, M. M. Koza, P. L. Llewellyn, T. Devic, C. Serre, and G. Ferey, *Phys. Rev. Lett.*, **2008**, 100.

[233] G. Garberoglio and R. Vallauri, *Microporous Mesoporous Mater.*, **2008**, 116, 540.

[234] R. Babarao and J. W. Jiang, *Langmuir*, **2008**, 24, 5474.

[235] S. Keskin, J. C. Liu, J. K. Johnson, and D. S. Sholl, *Langmuir*, **2008**, 24, 8254.

[236] S. Keskin, J. Liu, R. B. Rankin, J. K. Johnson, and D. S. Sholl, *Ind. Engg. Chem. Res.*, **2009**, 48, 2355.

[237] S. Keskin and D. S. Sholl, *J. Phys. Chem. C*, **2007**, 111, 14055.

[238] H. Sun, S. J. Mumby, J. R. Maple, and A. T. Hagler, *J. Am. Chem. Soc*, **1994**, 116, 2978.

[239] E. de Vos Burchart, V. A. Verheij, and H. van Bekkum, *Zeolites*, **1989**, 9, 432.

[240] F. A. Momany, L. M. Carruthers, R. F. McGuire, and H. A. Scheraga, *J. Phys. Chem.*, **1974**, 78, 1595.

[241] N. L. Allinger, *J. Am. Chem. Soc.*, **1977**, 99, 8127.

[242] J. H. Lii and N. L. Allinger, *J. Am. Chem. Soc.*, **1989**, 111, 8566.

[243] J. H. Lii and N. L. Allinger, *J. Am. Chem. Soc*, **1989**, 111, 8576.

[244] J. H. Lii and N. L. Allinger, *J. Comp. Chem.*, **1991**, 12, 186.

[245] N. L. Allinger, Y. H. Yuh, and J. H. Lii, *J. Am. Chem. Soc*, **1989**, 111, 8551.

[246] N. Nevins and N. L. Allinger, *J. Comp. Chem.*, **1996**, 17, 730.

[247] N. Nevins, K. S. Chen, and N. L. Allinger, *J. Comp. Chem.*, **1996**, 17, 669.

[248] N. Nevins, J. H. Lii, and N. L. Allinger, *J. Comp. Chem.*, **1996**, 17, 695.

[249] P. K. Weiner and P. A. Kollman, *J. Comp. Chem.*, **1981**, 2, 287.

[250] A. D. MacKerell, D. Bashford, M. Bellott, R. L. Dunbrack, J. D. Evanseck, M. J. Field, S. Fischer, J. Gao, H. Guo, S. Ha, D. Joseph-McCarthy, L. Kuchnir, K. Kuczera, F. T. K. Lau, C. Mattos, S. Michnick, T. Ngo, D. T. Nguyen, B. Prodhom, W. E. Reiher, B. Roux, M. Schlenkrich, J. C. Smith, R. Stote, J. Straub, M. Watanabe, J. Wiorkiewicz-Kuczera, D. Yin, and M. Karplus, *J. Phys. Chem. B.*, **1998**, 102, 3586.

[251] M. Clark, R. D. Cramer, and N. Vanopdenbosch, *J. Comp. Chem.*, **1989**, 10, 982.

[252] M. P. Allen and D. J. Tildesley, Computer Simulation of Liquids, Oxford University Press, Oxford, 1987.

[253] D. Frenkel and B. Smit, Understanding Molecular Simulations: From algorithms to applications, Academic Press, 2002.

[254] T. J. H. Vlugt, J. P. J. M. van der Eerden, M. Dijkstra, B. Smit, and D. Frenkel, Introduction to Molecular Simulation and Statistical Thermodynamics, http;//www.phys.uu.nl/~vlugt/imsst, 2008.

[255] G. Mooij, D. Frenkel, and B. Smit, *J. Phys.-Condensed Matter*, **1992**, 4, L255.

[256] M. N. Rosenbluth and A. W. Rosenbluth, *J.Chem. Phys*, **1956**, 23, 356.

[257] B. Smit, *J. Phys. Chem.*, **1995**, 99, 5597.

[258] B. Smit, *Mol. Phys.*, **1995**, 85, 153.

[259] T. J. H. Vlugt, R. Krishna, and B. Smit, *J. Phys. Chem. B*, **1999**, 103, 1102.

[260] M. D. Macedonia and E. J. Maginn, *Mol. Phys.*, **1999**, 96, 1375.

[261] M. Mezei, *Mol. Phys.*, **1980**, 40, 901.

[262] M. Mezei, *Mol. Phys.*, **1987**, 61, 565.

[263] R. Q. Snurr, A. T. Bell, and D. N. Theodorou, *J. Phys. Chem.*, **1993**, 97, 13742.

[264] S. Chempath, R. Q. Snurr, and J. J. Low, *AIChE J.*, **2004**, 50, 463.

[265] Y. P. Zeng, S. G. Ju, W. H. Xing, and C. L. Chen, *Sep. Purif. Technol.*, **2007**, 55, 82.

[266] V. Lachet, A. Boutin, R. J. M. Pellenq, D. Nicholson, and A. H. Fuchs, *J. Phys. Chem.*, **1996**, 100, 9006.

[267] V. Lachet, A. Boutin, B. Tavitian, and A. H. Fuchs, *Faraday Discussions*, **1997**, 307.

[268] V. Lachet, A. Boutin, B. Tavitian, and A. H. Fuchs, *J. Phys. Chem. B*, **1998**, 102, 9224.

[269] V. Lachet, S. Buttefey, A. Boutin, and A. H. Fuchs, *Phys. Chem. Chem. Phys.*, **2001**, 3, 80.

[270] S. M. P. Lucena, C. L. Cavalcante, and J. Pereira, *Adsorption*, **2006**, 12, 423.

[271] S. M. P. Lucena, J. Pereira, and C. L. Cavalcante, *Microporous Mesoporous Mater.*, **2006**, 88, 135.

[272] A. Z. Panagiotopoulos, *Mol. Phys.*, **1987**, 61, 813.

[273] B. Smit, P. Desmedt, and D. Frenkel, *Mol. Phys.*, **1989**, 68, 931.

[274] A. Z. Panagiotopoulos, *Mol. Phys.*, **1987**, 62, 701.

[275] S. C. McGrother and K. E. Gubbins, *Mol. Phys.*, **1999**, 97, 955.

[276] A. V. Neimark and A. Vishnyakov, *Phys. Rev. E*, **2000**, 62, 4611.

[277] A. V. Neimark and A. Vishnyakov, *J. Chem. Phys*, **2005**, 122.

[278] D. N. Theodorou, R. Q. Snurr, and A. T. Bell, in Molecular Dynamics and Diffusion in Microporous Materials, ed. T. Bein, 1996.

[279] D. A. McQuarrie, Statistical Mechanics, University Science Books, Sausalito, CA, 2000.

[280] C. M. White, D. H. Smith, K. L. Jones, A. L. Goodman, S. A. Jikich, R. B. LaCount, S. B. DuBose, E. Ozdemir, B. I. Morsi, and K. T. Schroeder, *Energy Fuels*, **2005**, 19, 659.

[281] D. M. Ruthven, S. Farooq and K.Knaebel,, *Pressure Swing Adsorption, VCH Publishers : Newyork ,*, **1994**.

[282] D. Singh, E. Croiset, P. L. Douglas, and M. A. Douglas, *Energy Conversion and Management*, **2003**, 44, 3073.

[283] J. Keller and R. Staudt, Gas Adsorption Equilibria: Experimental Methods and Adsorptive Isotherms, Springer ; New York, 2004.

[284] C. R. A. Catlow, R. A. van Santen, and B. Smit, Computer Modelling of Microporous Materials, Elsevier ; Amsterdam, 2004.

[285] N. L. Rosi, J. Eckert, M. Eddaoudi, D. T. Vodak, J. Kim, M. O'Keeffe, and O. M. Yaghi, *Science*, **2003**, 300, 1127.

[286] R. Q. Snurr, J. T. Hupp, and S. T. Nguyen, *AIChE J.*, **2004**, 50, 1090.

[287] A. Hirotani, K. Mizukami, R. Miura, H. Takaba, T. Miya, A. Fahmi, A. Stirling, M. Kubo, and A. Miyamoto, *Appl. Surf. Sci.*, **1997**, 120, 81.

[288] J. W. Jiang and S. I. Sandler, *J. Am. Chem. Soc*, **2005**, 127, 11989.

[289] R. S. Mulliken, *J. Chem. Phys.*, **1955**, 23.

[290] B. H. Besler, K. M. Merz, and P. A. Kollman, *J. Comp. Chem*, **1990**, 11, 431.

[291] C. I. Bayly, P. Cieplak, W. D. Cornell, and P. A. Kollman, *J. Phys. Chem.*, **1993**, 97, 10269.

[292] C. M. Breneman and K. B. Wiberg, *J. Comp. Chem*, **1990**, 11, 361.

[293] M. J. Frisch, G. W. Trucks, H. B. Schlegel, G. E. Scuseria, M. A. Robb, J. R. Cheeseman, V. G. Zakrzewski, J. A. Montgomery, R. E. Stratmann, J. C. Burant, S. Dapprich, J. M. Millam, A. D. Daniels, K. N. Kudin, M. C. Strain, O. Farkas, J. Tomasi, V. Barone, M. Cossi, R. Cammi, B. Mennucci, C. Pomelli, C. Adamo, S. Clifford, J. Ochterski, G. A. Petersson, P. Y. Ayala, Q. Cui, K. Morokuma, D. K. Malick, A. D. Rabuck, K. Raghavachari, J. B. Foresman, J. Cioslowski, J. V. Ortiz, B. B. Stefanov, G. Liu, A. Liashenko, P. Piskorz, I. Komaromi, R. Gomperts, R. L. Martin, D. J. Fox, T. Keith, M. A. Al-Laham, C. Y. Peng, A. Nanayakkara, C. Gonzalez, M. Challacombe, P. M. W. Gill, B. G. Johnson, W. Chen, M. W. Wong, J. L. Andres, M. Head-Gordon, E. S. Replogle, and J. A. Pople, Gaussian 03, Gaussian, Inc., 2004.

[294] M. D. Macedonia and E. J. Maginn, *Fluid Phase Equilib.*, **1999**, 158, 19.

[295] M. G. Martin and J. I. Siepmann, *J. Phys. Chem. B*, **1998**, 102, 2569.

[296] G. C. Maitland, M. Rigby, E. B. Smith, and W. A. Wakeham, Intermolecular Forces, Claredon Press, 1981.

[297] J. G. Harris and K. H. Yung, *J. Phys. Chem.*, **1995**, 99, 12021.

[298] J. R. Elliott and C. T. Lira, *Introductory Chemical Engineering Thermodynamics; Prentice Hall PTR: London*, **1999**.

[299] D. M. Heyes, *Phys. Rev. B.*, **1994**, 49, 755.

[300] D. A. Kofte, *Mol. Sim.*, **1991**, 7, 285.

[301] J. O. Hirschfelder, C. F. Curtiss, and R. B. Bird, *Molecular Theory of Gases and liquids; John Wiley: New York*, **1964**.

[302] T. Vuong and P. A. Monson, *Langmuir*, **1996**, 12, 5425.

[303] A. L. Myers and P. A. Monson, *Langmuir*, **2002**, 18, 10261.

[304] F. Karavias and A. L. Myers, *Mol. Sim.*, **1991**, 8, 51.

[305] R. L. June, A. T. Bell, and D. N. Theodorou, *J. Phys. Chem.*, **1990**, 94, 8232.

[306] R. L. June, *J. Phys. Chem.*, **1991**, 95, 1014.

[307] F. Leroy, B. Rousseau, and A. H. Fuchs, *Phys. Chem. Chem. Phys.*, **2004**, 6, 775.

[308] H. B. Chen, J. K. Johnson, and D. S. Sholl, *J. Phys. Chem. B*, **2006**, 110, 1971.

[309] M. J. Sanborn and R. Q. Snurr, *Sep. Purif. Technol.*, **2000**, 20, 1.

[310] C. J. Zhang and X. N. Yang, *Fluid Phase Equilib*, **2005**, 231, 1.

[311] E. Buss and M. Heuchel, *J. Chem. Soc. Faraday Transactions*, **1997**, 93, 1621.

[312] T. C. Golden and S. Sircar, *J. Colloid Interface Sci.*, **1994**, 162, 182.

[313] M. S. Sun, D. B. Shah, H. H. Xu, and O. Talu, *J.Phys.Chem.B*, **1998**, 102, 1466.

[314] X. P. Yue and X. N. Yang, *Langmuir*, **2006**, 22, 3138.

[315] J. A. Dunne, R. Mariwals, M. Rao, S. Sircar, R. J. Gorte, and A. L. Myers, *Langmuir*, **1996**, 12, 5888.

[316] F. Rouquerol, J. Rouquerol, and K. Sing, Adsorption: By Powders and Porous Solids, Academic Press, 1999.

[317] D. M. Ruthven, *Principles of Adsorption and Adsorption Processes; Wiley, Newyork*, **1984**.

[318] G. B. Woods and J. S. Rowlinson, *J. Chem. Soc. Faraday Transactions II*, **1989**, 85, 765.

[319] Y. Grillet, P. L. Llewellyn, N. Tosi-Pellenq, and J. Rouquerol, Fundamentals of adsorption: Proceedings of the Fourth International Conference on Fundamentals of Adsorption, Kyoto, Japan, 1992.

[320] W. Rudzinski, in Fundamentals of single-gas and mixed-gas adsorption on heterogenous solid surfaces, ed. J. Fraissard, 1997.

[321] A. L. Myers and J. M. Prausnitz, *AIChE J*, **1965**, 11, 121.

[322] J. W. Jiang and S. I. Sandler, *Langmuir*, **2003**, 19, 5936.

[323] R. Krishna, J. M. van Baten, E. Garcia-Perez, and S. Calero, *Chem. Phys. Lett.*, **2006**, 429, 219.

[324] A. I. Skoulidas and D. S. Sholl, *J. Phys. Chem. B*, **2002**, 106, 5058.

[325] E. J. Maginn, A. T. Bell, and D. N. Theodorou, *J. Phys. Chem.*, **1993**, 97, 4173.

[326] G. K. Papadopoulos, H. Jobic, and D. N. Theodorou, *J. Phys. Chem. B*, **2004**, 108, 12748.

[327] O. Talu, M. S. Sun, and D. B. Shah, *AIChE J*, **1998**, 44, 681.

[328] J. Karger and H. Pfeifer, *Zeolites*, **1987**, 7, 90.

[329] J. Caro, M. Bulow, W. Schirmer, J. Karger, W. Heink, H. Pfeifer, and S. P. Zdanov, *J. Chem. Soc. Faraday Transactions I*, **1985**, 81, 2541.

[330] E. Beerdsen, D. Dubbeldam, and B. Smit, *Phy. Rev. Lett*, **2006**, 96.

[331] E. Beerdsen, D. Dubbeldam, and B. Smit, *Phy. Rev. Lett*, **2005**, 95, 164505.

[332] A. I. Skoulidas and D. S. Sholl, *J. Phys. Chem. A*, **2003**, 107, 10132.

[333] R. Krishna, D. Paschek, and R. Baur, *Microporous Mesoporous Mater.*, **2004**, 76, 233.

[334] R. Babarao, Z. Q. Hu, J. W. Jiang, S. Chempath, and S. I. Sandler, *Langmuir*, **2007**, 23, 659.

[335] R. Krishna and D. Paschek, *Phys. Chem. Chem. Phys.*, **2002**, 4, 1891.

[336] R. Krishna and J. A. Wesselingh, *Chem. Eng. Sci.*, **1997**, 52, 861.

[337] A. I. Skoulidas, D. S. Sholl, and R. Krishna, *Langmuir*, **2003**, 19, 7977.

[338] R. Krishna and J. M. van Baten, *J. Phys. Chem.B*, **2005**, 109, 6386.

[339] R. Krishna and J. M. van Baten, *Ind. Eng. Chem. Res.*, **2006**, 45, 2084.

[340] R. Krishna, J. M. van Baten, E. Garcia-Perez, and S. Calero, *Ind. Eng. Chem. Res.*, **2007**, 46, 2974.

[341] M. O. Coppens and V. Iyengar, *Nanotechnology*, **2005**, 16, S442.

[342] S. Chempath, R. Krishna, and R. Q. Snurr, *J. Phys. Chem. B*, **2004**, 108, 13481.

[343] IPCC Climate Change 2007, Synthesis Report. Contribution of Working Groups I, II and III to the Fourth Assessment Report of the Intergovernmental Panle on Climate Change, ed. A. Reisinger, Geneva, Switzerland, 2007.

[344] E. M. Flanigen, J. M. Bennett, R. W. Grose, J. P. Cohen, R. L. Patton, R. M. Kirchner, and J. V. Smith, *Nature*, **1978**, 271(5645), 512.

[345] S. Iijima, *Nature*, **1991**, 354, 56.

[346] C. Journet, W. K. Maser, P. Bernier, A. Loiseau, M. L. delaChapelle, S. Lefrant, P. Deniard, R. Lee, and J. E. Fischer, *Nature*, **1997**, 388, 756.

[347] A. Thess, R. Lee, P. Nikolaev, H. J. Dai, P. Petit, J. Robert, C. H. Xu, Y. H. Lee, S. G. Kim, A. G. Rinzler, D. T. Colbert, G. E. Scuseria, D. Tomanek, J. E. Fischer, and R. E. Smalley, *Science*, **1996**, 273, 483.

[348] W. Steele, *Chem. Rev.*, **1993**, 93, 2355.

[349] C. Yang, X. P. Wang, and M. A. Omary, *J. Am. Chem. Soc.*, **2007**, 129, 15454.

[350] P. C. Hariharan and J. A. Pople, *Chem. Phys. Lett.*, **1972**, 66, 217.

[351] J. W. Jiang and S. I. Sandler, *Phys. Rev. B*, **2003**, 68, 245412.

[352] B. Widom, *J. Chem. Phys.*, **1963**, 39, 2802.

[353] J. O. C. Hirschfelder, C. F.; Bird, R. B., *Molecular Theory of Gases and liquids; John Wiley: New York*, **1964**.

[354] P. J. E. Harlick and F. H. Tezel, *Microporous Mesoporous Mater.*, **2004**, 76, 71.

[355] D. F. Sun, S. Q. Ma, Y. X. Ke, D. J. Collins, and H. C. Zhou, *J. Am. Chem. Soc*, **2006**, 128, 3896.

[356] S. Q. Ma, D. F. Sun, M. Ambrogio, J. A. Fillinger, S. Parkin, and H. C. Zhou, *J. Am. Chem. Soc*, **2007**, 129, 1858.

[357] Y. L. Liu, J. F. Eubank, A. J. Cairns, J. Eckert, V. C. Kravtsov, R. Luebke, and M. Eddaoudi, *Angew. Chem. Inter. Ed.*, **2007**, 46, 3278.

[358] G. W. Lu, C. X. Li, W. C. Wang, and Z. H. Wang, *Fluid Phase Equilib*, **2004**, 225, 1.

[359] B. Smit, L. Loyens, and G. Verbist, *Faraday Discussions*, **1997**, 93.

[360] R. Babarao and J. W. Jiang, *Langmuir*, **2008**, 24, 6270.

[361] Y. S. Bae, L. K. Mulfort, H. Frost, P. Ryan, S. Punnathanam, L. J. Broadbelt, J. T. Hupp, and R. Q. Snurr, *Langmuir*, **2008**, 24, 8592.

[362] L. Bastin, P. S. Barcia, E. J. Hurtado, J. A. C. Silva, A. E. Rodrigues, and B. Chen, *J. Phys. Chem. C*, **2008**, 112, 1575.

[363] J. R. Hufton, S. Mayorga, and S. Sircar, *AIChE J.*, **1999**, 45, 248.

[364] R. D. Noble and R. Agrawal, *Ind. Eng. Chem. Res.*, **2005**, 44, 2887.

[365] M. Gallo, T. M. Nenoff, and M. C. Mitchell, *Fluid Phase Equilib.*, **2006**, 247, 135.

[366] V. Richard, E. Favre, D. Tondeur, and A. Nijmeijer, *Chem. Eng. J.*, **2001**, 84, 593.

[367] D. P. Cao and J. Z. Wu, *Carbon*, **2005**, 43, 1364.

[368] E. D. Akten, R. Siriwardane, and D. S. Sholl, *Energy & Fuels*, **2003**, 17, 977.

[369] F. Dreisbach, R. Staudt, and J. U. Keller, *Adsorption*, **1999**, 5, 215.

[370] A. Goj, D. S. Sholl, E. D. Akten, and D. Kohen, *J. Phys. Chem. B*, **2002**, 106, 8367.

[371] M. P. Bernal, J. Coronas, M. Menendez, and J. Santamaria, *AIChE J*, **2004**, 50, 127.

[372] T. Seike, M. Matsuda, and M. Miyake, *J. Mater. Chem.*, **2002**, 12, 366.

[373] R. Krishna, J. M. van Baten, E. Garcia-Perez, and S. Calero, *Ind. Eng. Chem. Res.*, **2007**, 46, 2974.

[374] R. Krishna and J. M. van Baten, *Chem. Eng. Sci.*, **2008**, 63, 3120.

[375] M. Dinca, W. S. Han, Y. Liu, A. Dailly, C. M. Brown, and J. R. Long, *Angewandte Chemie-International Edition*, **2007**, 46, 1419.

[376] M. Dinca, A. Dailly, C. Tsay, and J. R. Long, *Inorg. Chem.*, **2008**, 47, 11.

[377] F. Nouar, J. F. Eubank, T. Bousquet, L. Wojtas, M. J. Zaworotko, and M. Eddaoudi, *J. Am. Chem. Soc.*, **2008**, 130, 1833.

[378] D. Bonenfant, M. Kharoune, P. Niquette, M. Mimeault, and R. Hausler, *Science and Technology of Advanced Materials*, **2008**, 9, 013007.

[379] C. G. Coe, *U.S. Patent*, **1992**, 5813815.

[380] R. W. Neuzil, *U.S. Patent*, **1971**, 3558561.

[381] R. Babarao, J. W. Jiang, and S. I. Sandler, *Langmuir*, **2009**, in press.

[382] R. F. Cracknell, *Molecular Physics*, **2002**, 100, 2079.

[383] C. S. Murthy, K. Singer, M. L. Klein, and I. R. McDonald, *Mol. Phys.*, **1980**, 41, 1387.

[384] W. L. Jorgensen, J. Chandrasekhar, J. D. Madura, R. W. Impey, and M. L. Klein, *J. Chem. Phys.*, **1983**, 79, 926.

[385] F. Siperstein, A. L. Myers, and O. Talu, *Molecular Physics*, **2002**, 100, 2025.

[386] W. Smith and T. R. Forester, *J. Mol. Graphics*, **1996**, 14, 136.

[387] Y. Lee, B. A. Reisner, J. C. Hanson, G. A. Jones, J. B. Parise, D. R. Corbin, B. H. Toby, A. Freitag, and J. Z. Larese, *J. Phys. Chem. B*, **2001**, 105, 7188.

[388] J. A. Delgado, M. A. Uguina, J. M. Gomez, and L. Ortega, *Sep. Purif. Tech.*, **2006**, 48, 223.

[389] B. Schmitz, U. Muller, N. Trukhan, M. Schubert, G. Ferey, and M. Hirscher, *Chemphyschem*, **2008**, 9, 2181.

[390] J. W. Jiang, *AIChE J*, **2009**, 55, 2422.

[391] A. Martin-Calvo, E. Garcia-Perez, J. M. Castillo, and S. Calero, *Phys. Chem. Chem. Phys.*, **2008**, 10, 7085.

[392] J. F. Denayer, W. Souverijns, P. A. Jacobs, J. A. Martens, and G. V. Baron, *J. Phys. Chem. B*, **1998**, 102, 4588.

[393] S. Savitz, F. Siperstein, R. J. Gorte, and A. L. Myers, *J. Phys. Chem. B*, **1998**, 102, 6865.

[394] M. A. Hernandez, J. A. Velasco, M. Asomoza, S. Solis, F. Rojas, V. H. Lara, R. Portillo, and M. A. Salgado, *Energy & Fuels*, **2003**, 17, 262.

[395] B. Smit and J. I. Siepmann, *Science*, **1994**, 264, 1118.

[396] E. J. Maginn, A. T. Bell, and D. N. Theodorou, *J. Phys. Chem.*, **1995**, 99, 2057.

[397] T. Maris, T. J. H. Vlugt, and B. Smit, *J. Phys. Chem. B*, **1998**, 102, 7183.

[398] S. Calero, B. Smit, and R. Krishna, *Phys. Chem. Chem. Phys.*, **2001**, 3, 4390.

[399] R. Krishna, B. Smit, and S. Calero, *Chem. Soc. Rev*, **2002**, 31, 185.

[400] J. W. Jiang, S. I. Sandler, M. Schenk, and B. Smit, *Phy. Rev. B*, **2005**, 72.

[401] J. W. Jiang and S. I. Sandler, *J. Chem. Phys*, **2006**, 124.

[402] J. W. Jiang, *J. Phys. Chem. B*, **2006**, 110, 8670.

[403] P. S. Barcia, F. Zapata, J. A. C. Silva, A. E. Rodrigues, and B. L. Chen, *J. Phys. Chem. B*, **2007**, 111, 6101.

[404] K. H. Li, J. Y. Lee, D. H. Olson, T. J. Emge, W. H. Bi, M. J. Eibling, and J. Li, *Chem. Commun.*, **2008**, 46, 6123.

[405] J. P. Ryckaert and A. Bellemans, *Faraday Discuss. Chem. Soc.*, **1978**, 66, 95.

[406] M. D. Macedonia and E. J. Maginn, *Fluid Phase Equilib.*, **1999**, 158-160, 19.

[407] M. G. Martin and J. I. Siepmann, *J.Phys. Chem. B*, **1999**, 103, 4508.

[408] J. B. Klauda, B. R. Brooks, A. D. MacKerell, R. M. Venable, and R. W. Pastor, *J. Phys. Chem. B*, **2005**, 109, 5300.

[409] J. B. Klauda, R. W. Pastor, and B. R. Brooks, *J. Phys. Chem. B*, **2005**, 109, 15684.

[410] J. I. Siepmann and D. Frenkel, *Mol. Phys.*, **1992**, 75, 59.

[411] D. Frenkel, G. Mooij, and B. Smit, *J. Phys. Condens. Matter*, **1992**, 4, 3053.

[412] J. J. de pablo, M. Laso, and U. W. Suter, *J. Chem. Phys*, **1992**, 96, 2395.

[413] K. Esselink, L. D. J. C. Loyens, and B. Smit, *Phys. Rev. E*, **1995**, 51, 1560.

[414] J. A. Greathouse, T. L. Kinnibrugh, and M. D. Allendorf, *Ind. Eng. Chem. Res*, **2009**, 48, 3425.

[415] R. Krishna, S. Calero, and B. Smit, *Chem. Engg. J*, **2002**, 88, 81.

[416] R. Krishna, B. Smit, and T. J. H. Vlugt, *J. Phys. Chem. A*, **1998**, 102, 7727.

[417] B. Smit and R. Krishna, *Chem. Eng. Sci.*, **2003**, 58, 557.

[418] G. Ferey, C. Mellot-Draznieks, C. Serre, F. Millange, J. Dutour, S. Surble, and I. Margiolaki, *Science*, **2005**, 309, 2040.

[419] M. Latroche, S. Surble, C. Serre, C. Mellot-Draznieks, P. L. Llewellyn, J. H. Lee, J. S. Chang, S. H. Jhung, and G. Ferey, *Angew. Chem. Inter. Ed.*, **2006**, 45, 8227.

[420] D. Y. Hong, Y. K. Hwang, C. Serre, G. Ferey, and J. S. Chang, *Advan. Funct. Mater.*, **2009**, 19, 1537.

[421] L. S. Goodman and A. Gilman, The Pharmacological Bases of Therapeutics, ed. t. ed., Pergamom Press: New York, 1990.

[422] T. Duren, F. Millange, G. Ferey, K. S. Walton, and R. Q. Snurr, *J. Phys. Chem. C*, **2007**, 111, 15350.

[423] A. Lam and A. Rivera, *Microporous Mesoporous Mater.*, **2006**, 91, 181.

[424] J. A. Greathouse and M. D. Allendorf, *J. Am. Chem. Soc.*, **2006**, 128, 10678.

[425] M. Tafipolsky, S. Amirjalayer, and R. Schmid, *J. Comp. Chem.*, **2007**, 28, 1169.

[426] F. X. Coudert, C. Mellot-Draznieks, A. H. Fuchs, and A. Boutin, *J. Am. Chem. Soc.*, **2009**, 131, 3442.

[427] F. X. Coudert, M. Jeffroy, A. H. Fuchs, A. Boutin, and C. Mellot-Draznieks, *J. Am. Chem. Soc.*, **2008**, 130, 14294.

[428] S. Watanabe, H. Sugiyama, H. Adachi, H. Tanaka, and M. T. Miyahara, *J. Chem. Phys.*, **2009**, 130.

[429] R. Vaidhyanathan, D. Bradshaw, J. N. Rebilly, J. P. Barrio, J. A. Gould, N. G. Berry, and M. J. Rosseinsky, *Ang. Chem. Int. Ed.*, **2006**, 45, 6495.

[430] W. B. Lin, *MRS Bulletin*, **2007**, 32, 544.

[431] X. Y. Bao, L. J. Broadbelt, and R. Q. Snurr, *Mol. Sim.*, **2009**, 35, 50.

[432] D. Bradshaw, T. J. Prior, E. J. Cussen, J. B. Claridge, and M. J. Rosseinsky, *J. Am. Chem. Soc.*, **2004**, 126, 6106.

[433] S. Choomwattana, T. Maihom, P. Khongpracha, M. Probst, and J. Limtrakul, *J. Phys. Chem. C.*, **2008**, 112, 10855.

PUBLICATIONS

Babarao, R., Jiang, JW. Unraveling the Energetics and Dynamics of Ibuprofen in Mesoporous Metal-Organic Frameworks, ***The Journal of Physical Chemistry C,*** **2009**, 113, 18287-18291.

Babarao, R**., Jiang, JW. Upgrade of Natural Gas in *rho* Z**eolite-like Metal-Organic Framework and Effect of Water: A Computational Study**,** 2009**,** *Energy and Environmental Science***, 2, 1088-1093.** ***(Selected as Cover Art)***

Babarao, R., Jiang, JW. Unprecedentedly High Selective Adsorption of Gas Mixtures in a Zeolite-like Metal-Organic Framework: A Molecular Simulation Study, ***Journal of the American Chemical Society***, **2009**, 131, 11417-11425.

Babarao, R., Jiang, JW., Sandler, SI. Adsorptive Separation of CO_2/CH_4 Mixture in Metal Exposed, Catenated and Charged Metal-Organic Frameworks: Insight from Molecular Simulation, ***Langmuir***, **2009**, 25, 5239-5247. ***(Selected as Cover Art)***

Babarao, R., Tong, YH., Jiang, JW. Molecular Insight into Adsorption and Diffusion of Alkane Isomer Mixtures in Metal-Organic Frameworks**,** ***Journal of Physical Chemistry B,*** **2009,** 113, 9129-9136.

Babarao, R., Jiang, JW. Exceptionally High CO_2 storage in Covalent-Organic Frameworks: Atomistic Simulation Study, ***Energy and Environmental Science***, **2008**, 1,139-143.

Babarao, R., Jiang, JW. Molecular Screening of Metal-Organic Frameworks for CO_2 Storage, ***Langmuir***, **2008**, 24, 6270-6278.

Babarao, R., Jiang, JW. Diffusion and Separation of CO_2 and CH_4 in Silicalite, C_{168} schwarzite, and IRMOF-1: A Comparative Study from Molecular Dynamics Simulation, ***Langmuir***, **2008**, 24, 5474-5484.

Babarao, R., Hu, ZQ., Jiang, JW., Chempath, S., Sandler, SI. Storage and Separation of CO_2 and CH_4 in Silicalite, C_{168} schwarzite, and IRMOF-1: A Comparative Study from Monte Carlo Simulation, ***Langmuir***, **2007**, 23, 659-666 ***(Most Cited Article in Langmuir 2007)***.

PRESENTATIONS

Charged Metal-Organic Framework for Highly Selective Adsorption of Gas Mixtures: A Molecular Simulation Study, **Babarao, R**., Jiang, JW. *5th Pacific Basin Conference on Adsorption Science and Technology*, May 25-27, 2009, Singapore.

Storage of CO_2 in Hybrid Open Frameworks: A Computational Study, **Babarao, R.**, Jiang, JW. *International Conference on Environment*, Dec 15-17, 2008, Penang, Malaysia.

Metal-Organic Framework for CO_2 storage and CO_2/CH_4 Separation, **Babarao, R**., Jiang, JW. (2008), *AIChE Annual Meeting*, Nov 16-21, 2008, Philadelphia, USA.

Exploring the Distribution and Mobility of Nonframework ions in Charged Metal-Organic Frameworks Using Atomistic Simulations, **Babarao, R.**, Nalaparaju, A., Jiang, JW. *AIChE Annual Meeting*, Nov 16-21, 2008, Philadelphia, USA.

Adsorption and Diffusion of H_2 in Metal-Organic Frameworks: Atomistic Simulation Study, **Babarao, R.**, Chen, Y., Jiang, JW. *Asian Conference on Nanoscience and Nanotechnology* (AsiaNano), Nov 3-7, 2008, Singapore.

Molecular Screening of Metal-Organic Frameworks for CO_2 Storage, **Babarao, R.**, Jiang, JW. *International Congress on Membrane and Membrane Processes*, July 12-18, 2008, Hawaii, USA.

Atomistic Simulation for Adsorption and Separation of CH_4 and CO_2 in Silicalite, C_{168} schwarzite and IRMOF-1, **Babarao, R**., Jiang, JW. *13th Regional Symposium on Chemical Engineering*, Nanyang Technological University, Oct 3-5, 2007, Singapore.

A Comparative Study on Separation of CO_2/CH_4 in Nanoporous Materials from Atomistic Simulation, **Babarao, R.**, Jiang, JW. *4th Annual Graduate Student Symposium*, National University of Singapore, Singapore, Sep 22nd, 2008. ***(Best Poster Award)***

APPENDIX A
COPYRIGHT CLEARANCE

THE AMERICAN ASSOCIATION FOR THE ADVANCEMENT OF SCIENCE LICENSE TERMS AND CONDITIONS

FIGURE- 1.1

Jun 02, 2010

This is a License Agreement between Ravichandar Babarao ("You") and The American Association for the Advancement of Science ("The American Association for the Advancement of Science") provided by Copyright Clearance Center ("CCC"). The license consists of your order details, the terms and conditions provided by The American Association for the Advancement of Science, and the payment terms and conditions.

All payments must be made in full to CCC. For payment instructions, please see information listed at the bottom of this form.

License Number	2440841154920
License date	Jun 02, 2010
Licensed content publisher	The American Association for the Advancement of Science
Licensed content publication	Science
Licensed content title	Systematic Design of Pore Size and Functionality in Isoreticular MOFs and Their Application in Methane Storage
Licensed content author	Mohamed Eddaoudi, Jaheon Kim, Nathaniel Rosi, David Vodak, Joseph Wachter, Michael O'Keeffe, Omar M. Yaghi
Licensed content date	Jan 18, 2002
Type of Use	Thesis / Dissertation
Requestor type	Other Individual
Format	Print and electronic
Portion	Figure
Number of figures/tables	1
Order reference number	
Title of your thesis / dissertation	Computational Study of Adsorption and Diffusion in Metal-Organic Frameworks
Expected completion date	Jun 2010
Estimated size(pages)	240
Total	0.00 USD
Terms and Conditions	

American Association for the Advancement of Science TERMS AND CONDITIONS

Regarding your request, we are pleased to grant you non-exclusive, non-transferable permission, to republish the AAAS material identified above in your work identified above, subject to the terms and conditions herein. We must be contacted for permission for any uses other than those specifically identified in your request above.

The following credit line must be printed along with the AAAS material: "From [Full Reference Citation]. Reprinted with permission from AAAS."

All required credit lines and notices must be visible any time a user accesses any part of the AAAS material and must appear on any printed copies and authorized user might make.

FIGURE - 1.2

Babarao, Ravichandar

From: CONTRACTS-COPYRIGHT (shared) [Contracts-Copyright@rsc.org]
Sent: Friday, June 04, 2010 6:30 AM
To: Babarao, Ravichandar
Subject: RE: Permission Request Form: Ravichandar Babarao

Dear Ravichandar Babarao

The Royal Society of Chemistry hereby grants permission for the use of the material specified below in the work described and in all subsequent editions of the work for distribution throughout the world, in all media including electronic and microfilm. You may use the material in conjunction with computer-based electronic and information retrieval systems, grant permissions for photocopying, reproductions and reprints, translate the material and to publish the translation, and authorize document delivery and abstracting and indexing services. The Royal Society of Chemistry is a signatory to the STM Guidelines on Permissions (available on request).

Please note that if the material specified below or any part of it appears with credit or acknowledgement to a third party then you must also secure permission from that third party before reproducing that material.

Please ensure that the published article carries a credit to The Royal Society of Chemistry in the following format:

[Original citation] - Reproduced by permission of The Royal Society of Chemistry

and that any electronic version of the work includes a hyperlink to the article on the Royal Society of Chemistry website. The recommended form for the hyperlink is http://dx.doi.org/10.1039/DOI suffix, for example in the link http://dx.doi.org/10.1039/b110420a the DOI suffix is 'b110420a'. To find the relevant DOI suffix for the RSC paper in question, go to the Journals section of the website and locate your paper in the list of papers for the volume and issue of your specific journal. You will find the DOI suffix quoted there.

Regards

Dr Sharon Bellard, Manager Contracts & Copyright Royal Society of Chemistry, Thomas Graham House Science Park, Milton Road, Cambridge CB4 0WF, UK Tel +44 (0) 1223 432383, Fax +44 (0) 1223 423623 www.rsc.org

-----Original Message-----
From: babaraor@ornl.gov [mailto:babaraor@ornl.gov]
Sent: 02 June 2010 17:29
To: CONTRACTS-COPYRIGHT (shared)
Subject: Permission Request Form: Ravichandar Babarao

Name : Ravichandar Babarao
Address :

100 Erskine Lane Apt E36,
Oak Ridge, Tennessee, USA-37830

Tel : 18656855777

Fax : 18655765235
Email : babaraor@ornl.gov

I am preparing the following work for publication:

Article/Chapter Title : Compuational Study of Adsorption and Diffusion in Metal-Organic Frameworks
Journal/Book Title :
Editor/Author(s) : Ravichandar Babarao
Publisher : University-NUS

I would very much appreciate your permission to use the following material:

Journal/Book Title : Chemical Society Review
Editor/Author(s) : Jeffrey R. Long and Omar M. Yaghi,
Volume Number : 38
Year of Publication : 2009
Description of Material : Figure 1
Page(s) : 1214

Any Additional Comments :

Request permission to reprint in my thesis

FIGURE-1.3

AMERICAN CHEMICAL SOCIETY LICENSE TERMS AND CONDITIONS

Jun 02, 2010

This is a License Agreement between Ravichandar Babarao ("You") and American Chemical Society ("American Chemical Society") provided by Copyright Clearance Center ("CCC"). The license consists of your order details, the terms and conditions provided by American Chemical Society, and the payment terms and conditions.

All payments must be made in full to CCC. For payment instructions, please see information listed at the bottom of this form.

License Number	2440851474739
License Date	Jun 02, 2010
Licensed content publisher	American Chemical Society
Licensed content publication	Journal of the American Chemical Society
Licensed content title	Quest for Zeolite-like Metal−Organic Frameworks: On Pyrimidinecarboxylate Bis-Chelating Bridging Ligands
Licensed content author	Dorina F. Sava et al.
Licensed content date	Mar 1, 2008
Volume number	130
Issue number	12
Type of Use	Thesis/Dissertation
Requestor type11	Not specified
Format	Print and Electronic
Portion	Table/Figure/Micrograph
Number of Table/Figure/Micrographs	2
Author of this ACS article	No
Order reference number	
Title of the thesis / dissertation	Computational Study of Adsorption and Diffusion in Metal-Organic Frameworks
Expected completion date	Jun 2010
Estimated size(pages)	240
Billing Type	Invoice
Billing Address	100 Erskine Lane Apt E36 Oak ridge, TN 37830 United States
Customer reference info	
Total	0.00 USD

Terms and Conditions

Thesis/Dissertation